



Universidad  
del País Vasco

Euskal Herriko  
Unibertsitatea

**Manuscript Copyright**

**LIUBACHKO VITALII**

**Thermal transport and phase transitions in  $MM'P_2(S,Se)_6$  ( $M, M' =$   
 $Cu, Ag, In, Bi, Sn, Pb$ ) phosphorus chalcogenides**

Presented for obtaining the degree of PhD in Physics

Tutors:

**Dr. Yulian Vysochanskii**

Uzhhorod National University

Department of Semiconductor Physics

**Dr. Alberto Oleaga**

University of the Basque Country UPV/EHU

Department of Applied Physics

Ukraine, Uzhhorod - 2020

## **Acknowledgements**

First and foremost I would like to take this opportunity to thank to my dear scientific supervisors Dr. Alberto Oleaga and Dr. Yulian Vysochanskii. It has been an honor to be your PhD-student. I appreciate all your efforts to make my PhD experience very productive and spectacular. All the time you spent helping me on this work is invaluable.

It was very pleasant to have the opportunity to work on my research at the Department of Applied Physics at the UPV/EHU and have access to the laboratory and research facilities. Without this possibility none of this work would have been realized. I would also pay my sincere gratitude to Dr. Agustin Salazar, Dr. Arantza Mendioroz and other members from the Department for their helpful suggestions and moral support to me.

A very special gratitude goes out to all research funds especially Erasmus Mundus ACTIVE program for providing the funding of my work in Bilbao.

## Index

<b>Introduction .....</b>	<b>6</b>
<b>Chapter 1. The phenomenon of heat transfer and thermal properties of solids .....</b>	<b>16</b>
1.1. Mechanisms of heat transfer: conduction, convection and radiation .....	16
1.2. Determination of the thermal properties of materials .....	19
1.3. Electrons and phonons as heat carriers in semiconductor materials.....	22
1.4. Heat propagation in isotropic and anisotropic materials .....	26
1.4.1 <i>Conductivity matrix for crystal systems</i> .....	27
1.5. Temperature field in a medium. Thermal wave physics.....	28
1.5.1. <i>Parabolic and hyperbolic heat diffusion equation</i> .....	29
1.5.2. <i>Reflection and refraction of thermal waves</i> .....	31
<b>Chapter 2. Photopyroelectric calorimetry in solids.....</b>	<b>35</b>
2.1. Basic theory of pyroelectricity .....	35
2.2. Photopyroelectric calorimetry. Back-detection configuration BPPE .....	38
2.2.1 <i>Experimental conditions for experimental setups</i> .....	42
2.3. Description of experimental setups.....	46
2.3.1. <i>At room temperature as a function of frequency</i> .....	46
2.3.2. <i>Temperature measurements between 18K and 325K</i> .....	48
2.3.3. <i>Temperature measurements between 80 K and 350 K</i> .....	50
<b>Chapter 3. Phase transitions and critical phenomena in ferroelectrics .....</b>	<b>53</b>
3.1. Landau's classical theory of phase transitions for ferroelectric transitions.	53
3.2. Modern Theory of critical behavior. Fluctuations effects .....	57
3.3. Critical behavior studies of $(\text{Pb}_x\text{Sn}_{1-x})_2\text{P}_2(\text{Se}_y\text{S}_{1-y})_6$ uniaxial ferroelectrics prior to this work.....	62

3.3.1. $\text{Sn}_2\text{P}_2(\text{Se}_y\text{S}_{1-y})_6$ .....	62
3.3.2. $(\text{Pb}_x\text{Sn}_{1-x})_2\text{P}_2(\text{Se}_{1-y}\text{S}_y)_6$ .....	64
<b>Chapter 4. Structure and physical properties of <math>\text{CuInP}_2\text{S}_6</math> family of 2D layered crystals</b> .....	<b>66</b>
4.1. $\text{CuInP}_2(\text{S},\text{Se})_6$ compounds.....	68
4.1.1 <i>Substituting the cation sublattice</i> .....	75
4.2. Physical properties of $\text{M}^{1+}\text{M}^{3+}[\text{P}_2\text{X}_6]^{4-}$ multiferroics.....	82
4.2.1. <i>Dielectric measurements</i> .....	82
4.2.2. <i>Piezoelectric and ultrasonic measurements</i> .....	88
4.2.3. <i>Thermal properties</i> .....	91
<b>Chapter 5. Structure and physical properties of <math>(\text{Pb}_x\text{Sn}_{1-x})_2\text{P}_2(\text{Se}_y\text{S}_{1-y})_6</math> chalcogenide crystals</b> .....	<b>93</b>
5.1. Crystalline structure of $(\text{Pb},\text{Sn})_2\text{P}_2(\text{Se},\text{S})_6$ compounds .....	94
5.1.1. $\text{Sn}_2\text{P}_2\text{S}(\text{Se})_6$ compounds.....	94
5.1.2. $\text{Pb}_2\text{P}_2\text{S}(\text{Se})_6$ compounds .....	97
5.2. Compositional phase diagram study of the $(\text{Pb}_x\text{Sn}_{1-x})_2\text{P}_2(\text{Se}_y\text{S}_{1-y})_6$ system	100
5.2.1. <i>General shape of the phase diagram of <math>\text{Sn}(\text{Pb})_2\text{P}_2\text{S}(\text{Se})_6</math> compounds</i> .....	100
5.2.2. <i>Phase diagram of the <math>\text{Sn}_2\text{P}_2(\text{Se}_y\text{S}_{1-y})_6</math> crystals. Lifshitz point on the state diagram</i> .....	102
5.2.3. <i>Phase diagram of <math>(\text{Pb}_x\text{Sn}_{1-x})_2\text{P}_2\text{S}_6</math> crystals</i> .....	107
5.2.4. <i>Phase diagram of <math>(\text{Pb}_x\text{Sn}_{1-x})_2\text{P}_2\text{Se}_6</math> crystals</i> .....	110
5.2.5. <i>TCP and TCLP in <math>\text{Sn}(\text{Pb})_2\text{P}_2\text{S}(\text{Se})_6</math> mixed compounds</i> .....	111
5.3. Thermal properties .....	114
5.3.1. <i>Influence of Ge on the thermal properties in SPS chalcogenides</i> ..	119
<b>Chapter 6. Experimental results and discussion on layered ferroelectric compounds</b> .....	<b>122</b>
6.1. Introduction .....	122

6.2. Samples and experimental techniques .....	122
6.3. Experimental results and discussion .....	125
6.3.1. <i>Thermal Diffusivity</i> .....	125
6.3.2. <i>Heat Capacity</i> .....	131
6.3.3. <i>Thermal Conductivity</i> .....	134
6.4. Conclusions .....	153
<b>Chapter 7. Experimental results and discussion on <math>(\text{Pb}_x\text{Sn}_{1-x})_2\text{P}_2(\text{Se}_y\text{S}_{1-y})_6</math> ferroelectrics.....</b>	<b>154</b>
7.1. Introduction .....	154
7.2. Samples, experimental techniques and fitting methods.....	155
7.3. Experimental results and discussion .....	156
7.4. Conclusions .....	165
<b>Chapter 8. Phase diagram of <math>(\text{Pb},\text{Sn})_2\text{P}_2(\text{Se},\text{S})_6</math> ferroelectrics with multicritical points at coupling between polar and antipolar fluctuations.....</b>	<b>166</b>
8.1. Introduction .....	166
8.2. Phase diagram with tricritical Lifshitz point.....	166
8.3. Polar and antipolar fluctuations coupling .....	172
8.4. Conclusions .....	176
<b>Chapter 9. Ferroelectricity induced by germanium dopants in quantum paraelectrics <math>\text{Sn}(\text{Pb})_2\text{P}_2\text{S}(\text{Se})_6</math>.....</b>	<b>178</b>
9.1. Introduction .....	178
9.2. Samples and experimental techniques .....	178
9.3. Thermal diffusivity anomalies in $(\text{Pb}_x\text{Sn}_{1-x})_2\text{P}_2(\text{Se}_y\text{S}_{1-y})_6$ chalcogenides with Ge impurity.....	179
9.4. Quantum paraelectric state and critical behavior in $\text{Sn}(\text{Pb})_2\text{P}_2\text{S}(\text{Se})_6$ ferroelectrics.....	181
9.5. Conclusions .....	194
<b>Conclusions.....</b>	<b>195</b>
<b>Bibliography .....</b>	<b>197</b>
<b>Summary in Spanish / Resumen en Castellano .....</b>	<b>225</b>

## Introduction

### Interest of the study

Experimental and theoretical studies of different physical properties of chalcogenide crystals which have bulk and layered structure and present spontaneous polarization, are important for the study of physical principles and for the creation of a technology for manufacturing low-dimensional ferroics for integration into heterostructures with graphene-like materials that can be applied in essentially new bistable functional elements for electronics with ultra-high density and high-speed.

In  $\text{Sn}_2\text{P}_2\text{S}_6$  ferroelectric semiconductor, the structural phase transition (PT) is accompanied by a restructure of the chemical bonds. For chalcogenide materials which belongs to the group of  $(\text{Pb},\text{Sn})_2\text{P}_2(\text{Se},\text{S})_6$  crystals, the substitution of atoms in cation and anion sublattices can significantly change the nature of chemical bonds and determine the presence and features of the structural PT [1, 2]. The established changes in chemical bonds in ferroelectric crystals  $(\text{Pb},\text{Sn})_2\text{P}_2(\text{Se},\text{S})_6$  as well as in solid solutions with germanium dopant allow possible modifications of ferroelectric and semiconducting properties for these phosphorus chalcogenides.

Over the past years, there was a special interest among different scientific groups in layered two-dimensional materials of the  $\text{CuInP}_2\text{S}_6$  family of crystals which are narrow-band semiconductors with ionic conductivity and numerous ferroic properties [3]. In such materials, the phenomena of superconductivity, magnetism and ferroelectricity may be manifested [4, 5, 6]. These properties greatly enrich the number of functional 2D materials, especially when the phase transition occurs at temperatures close to room temperature. Also, such two-dimensional layered materials combined with their van der Waals heterostructures may be promising for advanced highly-integrated low-power-consumption logic devices [7].

The current interest of the topic of the dissertation is determined by the need to obtain new knowledge about physical and thermodynamic properties, which in turn have a fundamental value, allowing to obtain information on internal electron-phonon and phonon-phonon processes to describe the phenomenon of heat propagation in these ferroelectric crystals.

### **Relationship with academic programs, plans, themes**

This PhD thesis has been performed within the frame of a special cotutelle PhD agreement between Spain (The University of the Basque Country, Bilbao) and Ukraine (Uzhhorod National University, Uzhhorod). The financial support for the research in Bilbao has been provided by a grant provided by the European Union, through the ERASMUS MUNDUS ACTIVE programme (September 2016 - July 2017) as well as a grant provided by The University of the Basque Country (January – October 2018). The research study has also been supported by the Spanish funding programme UPV/EHU (GIU16/93).

### **Purpose and objectives of the study**

**Object:** The family of two dimensional layered  $M^{1+}M^{3+}[P_2X_6]^{4-}$  multiferroics and three dimensional  $(Pb_xSn_{1-x})_2P_2(Se_yS_{1-y})_6$  chalcogenides.

**Subject:** A study on the thermal properties and ultralow thermal conductivity in layered phosphorus compounds, as well as the critical behavior of anomalies of thermal diffusivity in the vicinity of the structural phase transitions for solid solutions of  $Sn(Pb)_2P_2S(Se)_6$ .

**Purpose:** To study the temperature evolution of the thermal properties of  $M^{1+}M^{3+}[P_2X_6]^{4-}$  and  $(Pb_xSn_{1-x})_2P_2(Se_yS_{1-y})_6$  chalcogenides, covering a wide temperature range and study the critical behavior of the second order phase transitions in the phase diagram, mainly focusing on the study of the influence of Sn by Pb substitution in  $(Pb_xSn_{1-x})_2P_2(Se_yS_{1-y})_6$  solid solutions. To investigate the influence of

germanium doping on the ferroelectric and thermal properties of the uniaxial  $\text{Sn}_2\text{P}_2\text{S}_6$  crystal, studying possible changes in the critical behavior.

**Methods:** In order to study the thermodynamic properties of crystals, high resolution *ac* photopyroelectric calorimetry (PPE) has been used. The analysis of the critical anomalies has been carried out by means of the theoretical predictions of the Landau classical theory and the Modern theory, which takes into account the influence of the order parameter fluctuations in the close vicinity of phase transitions (PT).

### Scientific novelty of the results

1. It is shown that the thermal conductivity of the layered  $\text{Cu,Ag}^{1+}\text{In,Bi}^{3+}\text{P}_2(\text{S,Se})_6$  compounds strongly depends on the cation sublattice. Significant anisotropy of thermal diffusivity and thermal conductivity in these crystals is found, where heat flows more efficiently along the layers than perpendicular to them. Different mechanisms of the anharmonicity of the crystalline lattice (strong phonon-phonon interaction, relaxation of the lone electron pair, the second order Jahn-Teller effect) and their influence on the thermodynamical properties are described. It was found that the studied crystals have very low thermal conductivity in comparison with other ferroelectric crystals, the lowest value is about  $0.2 \text{ W m}^{-1} \text{ K}^{-1}$  in disordered high-temperature phase obtained for a  $\text{CuBiP}_2\text{Se}_6$  crystal.
2. The phase transition crossover for  $(\text{Pb}_x\text{Sn}_{1-x})_2\text{P}_2(\text{Se}_{0.2}\text{S}_{0.8})_6$  crystals with a concentration of lead in cation sublattice at concentration of lead higher than  $x \approx 0.2$  was experimentally confirmed. The results of the critical behavior studies in  $(\text{Pb}_x\text{Sn}_{1-x})_2\text{P}_2(\text{Se}_{0.2}\text{S}_{0.8})_6$  crystals have confirmed the predictions for the Blume-Emery-Griffith model, taking into account the random field defects. It is shown that the critical behavior for  $\text{Sn}_2\text{P}_2\text{S}_6$  can be described as a crossover between Ising and 3D-XY universality classes.

3. Based on the results of thermal diffusivity studies and on available data of the thermodynamic and dynamic properties of ferroelectric crystals  $(\text{Pb},\text{Sn})_2\text{P}_2(\text{Se},\text{S})_6$  the  $T - x - y$  phase diagram was built. Such diagram contains tricritical points and Lifshitz points lines which meet at tricritical Lifshitz point. The topology of this diagram is compared with the calculated phase diagram within the combined BEG-ANNI model: Ising model with spin  $S = 1$ , taking into account the interaction between the first and second nearest neighbors.
4. The introduction of germanium in the cation sublattice induces the dipole glass state in  $(\text{Pb}_{0.7}\text{Sn}_{0.25}\text{Ge}_{0.05})_2\text{P}_2\text{S}_6$  and  $(\text{Pb}_{0.7}\text{Sn}_{0.25}\text{Ge}_{0.05})_2\text{P}_2\text{Se}_6$  mixed crystals in the region of quantum fluctuations (at  $T < 50$  K).

#### **Practical interest of the study**

1. The obtained ultra-low thermal conductivity in  $(\text{Cu},\text{Ag})(\text{In},\text{Bi})\text{P}_2(\text{S},\text{Se})_6$  layered crystals and the established mechanisms of lattice anharmonicity can be important for the design and production of promising thermoelectric materials.
2. The results on thermal diffusivity in  $(\text{Pb}_y\text{Sn}_{1-y})_2\text{P}_2(\text{Se}_x\text{S}_{1-x})_6$  solid solutions can be used in different phenomenological and microscopic models in order to describe the structural phase transitions in the vicinity of polycritical points.

#### **Contribution of the PhD candidate**

All thermal measurements have been performed by the PhD student personally at the laboratories of the Department of Applied Physics at the University of Basque Country, UPV/EHU (Bilbao, Spain), as well as completed the analysis of the research results. The author was directly involved in the preparation of samples for research, interpretation and discussion of all the results of experimental studies, has performed a complete theoretical analysis of the critical anomalies, has formulated the conclusions of the work and scientific novelty of the thesis.

## Publications and contribution to the conferences

### Publications in scientific journals:

1. Anisotropic thermal properties and ferroelectric phase transitions in layered  $\text{CuInP}_2\text{S}_6$  and  $\text{CuInP}_2\text{Se}_6$  crystals / V. Liubachko, V. Shvalya, A. Oleaga, A. Salazar, A. Kohutych, A. Pogodin and Yu. M. Vysochanskii // *Journal of Physics and Chemistry of Solids* – 2017. – V. 111. – P. 324–327.
2. Thermal diffusivity and thermal conductivity in layered ferrielectric materials  $\text{M}^{1+}\text{M}^{3+}\text{P}_2(\text{S,Se})_6$  ( $\text{M}^{1+} = \text{Cu, Ag}$ ;  $\text{M}^{3+} = \text{In, Bi}$ ) / V. Liubachko, A. Oleaga, A. Salazar, A. Kohutych, K. Glukhov, A. Pogodin and Yu. Vysochanskii // *Phase Transitions* – 2019. – V.92, No.5. – P. 494–499.
3. Inducing a Tricritical point in  $\text{Sn}_2\text{P}_2(\text{Se}_y\text{S}_{1-y})_6$  ferroelectrics by Pb addition / A. Oleaga, V. Liubachko, A. Salazar, Yu. Vysochanskii // *Thermochimica Acta* – 2019. – V. 675. – P. 38–43.
4. Cation role in the thermal and electric properties of layered ferroelectric materials  $\text{M}^{1+}\text{M}^{3+}\text{P}_2(\text{S,Se})_6$  ( $\text{M}^{1+} = \text{Cu, Ag}$ ;  $\text{M}^{3+} = \text{In, Bi}$ ) / V. Liubachko, A. Oleaga, A. Salazar, A. Kohutych, K. Glukhov, A. Pogodin and Yu. Vysochanskii // *Physical Review Materials* – 2019. – V. 3. – P. 104415(1-9).
5. Phase diagram of ferroelectrics with tricritical and Lifshitz points at coupling between polar and antipolar fluctuations / V. Liubachko, A. Oleaga, A. Salazar, R. Yevych, A. Kohutych, Yu. Vysochanskii // *Physical Review B*. – 2020. – V. 101. – P. 224110(1-10).
6. Quantum paraelectric state and critical behavior in  $\text{Sn}(\text{Pb})_2\text{P}_2\text{S}(\text{Se})_6$  ferroelectrics / I. Zamaraitė, V. Liubachko, R. Yevych, A. Oleaga, A. Salazar, A. Dziaugys, J. Banys, Yu. Vysochanskii // Under review at *Journal of Applied Physics*. – 2020. [<https://arxiv.org/abs/2003.09966>].

### Contribution to the conferences and seminars:

1. Influence of dopants and vacancies of chalcogenide atoms on possible deviation from Lifshitz behavior of  $\text{Sn}_2\text{P}_2(\text{S}_{0.72}\text{Se}_{0.28})_6$  crystal. / A. Oleaga, V. Shvalya, A. Salazar, V. Lyubachko, A. Kohutysh, I. Stoika, M. Danko, Yu. Vysochanskii. // 7<sup>th</sup> Seminar “Properties of ferroelectric and superionic systems”. Uzhhorod (Ukraine), April 24 2017.
2. Anisotropic thermal properties and ferrielectric phase transitions in layered  $\text{CuInP}_2\text{S}_6$  and  $\text{CuInP}_2\text{Se}_6$  crystals. / V. Liubachko, V. Shvalya, A. Oleaga, A. Salazar, A. Kohutysh, A. Pogodin, Yu. M. Vysochanskii. // 19th International Conference on Photoacoustic and Photothermal Phenomena in Bilbao (Spain), 16-20 July 2017.
3. Ferroelectric phase transitions and anisotropic thermal properties in layered  $\text{CuInP}_2(\text{S,Se})_6$  crystals. / V. Liubachko, A. Oleaga, V. Shvalya, A. Kohutysh, A. Pogodin, A. Salazar, Yu. M. Vysochanskii // Seminar “New multiferroics and superionic conductors for acoustoelectronics and solid state ionics”, Vilnius, (Lithuania), 10 October 2017.
4. Thermal diffusivity and thermal conductivity in layered ferroelectric materials  $\text{M}^{1+}\text{M}^{3+}\text{P}_2(\text{S,Se})_6$  ( $\text{M}^{1+} = \text{Cu, Ag}$ ;  $\text{M}^{3+} = \text{In, Bi}$ ) / V. Liubachko, A. Oleaga, A. Salazar, A. Kohutysh, K. Glukhov, A. Pogodin, Yu. Vysochanskii // V Ukrainian-Polish-Lithuanian Meeting on Physics of Ferroelectrics in Uzhhorod (Ukraine), 18-20 September 2018.
5. Cation role in the thermal and electric properties of layered ferrielectric materials  $\text{M}^{1+}\text{M}^{3+}\text{P}_2(\text{S,Se})_6$  ( $\text{M}^{1+} = \text{Cu, Ag}$ ;  $\text{M}^{3+} = \text{In, Bi}$ ) / V. Liubachko, A. Oleaga, A. Salazar, A. Kohutysh, K. Glukhov, A. Pogodin, Yu. Vysochanskii // International Meeting on Clusters and Nanomaterials (CNM'5-2018) in Uzhhorod (Ukraine), 22-26 October 2018.
6. Ultralow thermal conductivity in layered phosphorus chalcogenides  $\text{M}^{1+}\text{M}^{3+}\text{P}_2(\text{S, Se})_6$  ( $\text{M}^{1+} = \text{Cu, Ag}$ ;  $\text{M}^{3+} = \text{In, Bi}$ ) / V. Liubachko, A. Oleaga, A. Salazar, A. Kohutysh, K. Glukhov, A. Pogodin, Yu. Vysochanskii // The conference of

young scientist "Lashkaryov's readings – 2019" in Kyiv (Ukraine), 3-5 April 2019.

7. The effect of Pb doping on the critical behavior in  $(\text{Pb}_x\text{Sn}_{1-x})_2\text{P}_2(\text{Se}_{0.2}\text{S}_{0.8})_6$  ferroelectrics / V. Liubachko, A. Oleaga, A. Salazar, Yu. Vysochanskii // Conference of Young Scientists and Post-graduate Students IEP-2019 in Uzhhorod (Ukraine), 21-24 May 2019.
8. Thermal diffusivity and phase transitions in  $(\text{Pb}_x\text{Sn}_{1-x})_2\text{P}_2(\text{Se}_y\text{S}_{1-y})_6$  crystal / V. Liubachko, A. Oleaga, A. Salazar, Yu. Vysochanskii // School-conference of young scientists «Modern material science: physics, chemistry, technology» (MMSPCT-2019), in Uzhhorod (Ukraine), 27 - 31 May 2019.
9. Phonon spectrum and heat transport of  $[\text{Cu},\text{Ag}]^{1+}[\text{In},\text{Bi}]^{3+}\text{P}_2(\text{Se},\text{S})_6$  metal thio- and selenophosphates / V. Liubachko, A. Oleaga, A. Salazar, A. Kohutych, K. Glukhov, A. Pogodin, Yu. Vysochanskii // XXIV Galyna Puchkovska International School-Seminar "Spectroscopy of Molecules and Crystals" (XXIV ISSSMC), in Odesa (Ukraine), 25 - 30 August 2019.
10. Investigation of thermal transport in 2D layered  $[\text{Cu}, \text{Ag}]^{1+}[\text{In}, \text{Bi}]^{3+}\text{P}_2[(\text{Se}, \text{S})_6]^{4-}$  crystals / V. Liubachko, A. Oleaga, A. Salazar, K. Glukhov, A. Kohutych, Yu. Vysochanskii, A. Pogodin // VIII International seminar "Properties of ferroelectric and superionic systems", in Uzhhorod (Ukraine), 29-30 October 2019.
11. Phase diagram of ferroelectrics with tricritical Lifshitz point: paraelectric - modulated critical line end point and chaotic behavior / V. Liubachko, R. Yevych, A. Oleaga, A. Salazar, A. Kohutych, Yu. Vysochanskii // VIII International seminar "Properties of ferroelectric and superionic systems, in Uzhhorod (Ukraine), 29-30 October 2019.

### **Structure of the thesis**

The PhD thesis includes an introduction, nine chapters, general conclusions, bibliography, where 251 references are listed and a summary is written in Spanish. The total volume is 230 pages; the thesis contains 126 figures and 9 tables.

In the **first chapter**, the phenomenon of heat transfer and thermal properties of solids have been considered, in particular the main mechanisms of heat transfer: conduction, convection and radiation. Also, a brief description of four essential thermophysical properties which characterize the material: heat capacity, thermal diffusivity, thermal conductivity and thermal effusivity is given. After that the description of heat transfer by different carriers in semiconductor materials is considered. It has been explained how heat is transmitted in homogeneous, isotropic and anisotropic materials. Finally, the mathematical description of the heat propagation is shown through the parabolic and hyperbolic heat diffusion equations.

The **second chapter** contains a detailed description of the technique which was directly used in order to study the thermal properties of solids (*ac* photopyroelectric calorimetry (PPE) in the back-detection configuration). In order to better understand the nature of the phenomena which are the basis of this technique, the basic theory of pyroelectricity is considered. In the second part of the chapter the experimental techniques were considered, which allowed us to perform the thermal diffusivity measurements of the investigated ferroelectric crystals. Descriptions of the cryostats used are also presented in this chapter.

In the **third chapter**, the critical behavior and phase transition (PT) theory applied to the particular case of ferroelectrics, namely the classical Landau theory for ferroelectrics as well as the modern theory in the framework of the renormalization group theory is presented. Different mechanisms which can provoke a deviation from the mean-field behavior were considered in detail. For the ferroelectrics and magnets for which the classical Landau theory does not work properly we have presented a renormalization group theory development and have given information about the different universality classes which can appear while studying  $(\text{Pb}_x\text{Sn}_{1-x})_2\text{P}_2(\text{Se}_y\text{S}_{1-y})_6$  crystals. The second part of this chapter is devoted to the critical behavior studies of  $(\text{Pb}_x\text{Sn}_{1-x})_2\text{P}_2(\text{Se}_y\text{S}_{1-y})_6$  uniaxial ferroelectrics prior to this work.

The peculiarities of the crystalline structure, the influence on the physical properties on the substitution of atoms in the cation and anion sublattices in 2D thio- and selenophosphates were considered in **chapter four**. The second part of this

chapter is devoted to the description on the physical properties in two-dimensional layered crystals, namely dielectric, piezoelectric and ultrasonic as well as thermal properties.

In the **fifth chapter** a brief review of the literature on physical properties (thermal, optical, elastic, acoustic and dielectric) of solid solutions of the family of  $(\text{Pb},\text{Sn})_2\text{P}_2(\text{Se},\text{S})_6$  crystals has been made, which allows us to describe their complex temperature-concentration phase diagram. For a better understanding of the evolution of the nature of the PT at the substitution of chemical elements in the cation and anion sublattices, we have considered separately three diagrams  $\text{Sn}_2\text{P}_2(\text{Se}_y\text{S}_{1-y})_6$ ,  $(\text{Pb}_x\text{Sn}_{1-x})_2\text{P}_2\text{S}_6$  and  $(\text{Pb}_x\text{Sn}_{1-x})_2\text{P}_2\text{Se}_6$ . Special attention was paid to the multicritical points that appear on the phase diagram, depending on the change in the chemical composition or on compression. Here we consider the influence of lead atoms on the phase transition temperature position and on the critical anomalies shape in the  $\text{Sn}_2\text{P}_2\text{S}_6$  and  $\text{Sn}_2\text{P}_2\text{Se}_6$  crystals. Lastly, we present the physical properties studies of  $\text{Sn}_2\text{P}_2\text{S}_6$  compounds doped with Ge.

The next four chapters are fully devoted to the interpretation of the data obtained in this work. Thus, in **chapter six** the effect on physical properties of the substitution of atoms in the cation and anion sublattices has been studied, and a significant anisotropy of the thermal properties in these layered crystals has been distinguished. Also, the phase transitions (PT) in detail in crystals where they took place were considered. In this chapter we have presented the results of theoretical calculations of phonon spectra for each investigated crystal, a method for calculating the phonon spectrum using the theory of functional density is described, whose analysis allows us to completely understand the nature of low thermal conductivity. Also, the Debye temperatures, mean free paths and the average phonons group velocity have been calculated. Finally, the data obtained on the basis of experimental studies and theoretical calculations allow us to explain how the substitution of chemical elements in cation and anion sublattices affects the thermophysical properties.

In **chapter seven**, experimentally, the thermal diffusivity for  $(\text{Pb}_x\text{Sn}_{1-x})_2\text{P}_2(\text{Se}_{0.2}\text{S}_{0.8})_6$  with  $x = 0.1, 0.2, 0.3$  and for  $(\text{Pb}_{0.05}\text{Sn}_{0.95})_2\text{P}_2(\text{Se}_y\text{S}_{1-y})_6$  with  $y = 0.4$ ,

0.5 crystals have been studied. In order to obtain a tricritical point on the phase diagram the effect of lead by tin substitution is considered. The obtained critical exponents were compared with the theoretically predicted ones for this class of ferroelectrics. The approaching of the value of the critical exponent to the Mean Field model instead of the tricritical universality class has been explained on the basis of the Blume-Emery-Griffiths model (BEG model) with the influence of random field defects.

**Chapter eight** is devoted to the critical behavior study in  $\text{Sn}_2\text{P}_2\text{S}_6$  which can be described as a crossover between Ising and XY universality classes, what is expected near bicritical points with coupled polar and antipolar order parameters and competing instabilities in  $q - \text{space}$ . An enhanced,  $T - x - y$  phase diagram for  $\text{Sn}(\text{Pb})_2\text{P}_2\text{S}(\text{Se})_6$  ferroelectrics is proposed, which combines a Lifshitz point line, tricritical point line as well as a tricritical Lifshitz point. Such complex phase diagram can be described in a combined BEG – ANNNI model. Here the “chaotic” state accompanied by the coexistence of ferroelectric, metastable paraelectric and modulated phases can be expected.

Finally, **chapter nine** is devoted to the comparison of thermal and dielectric properties of  $(\text{Pb}_y\text{Sn}_{1-y})_2\text{P}_2(\text{Se},\text{S})_6$  crystals with germanium impurity. Here the temperature dependences of thermal diffusivity for  $(\text{Sn}_{0.95}\text{Ge}_{0.05})_2\text{P}_2(\text{Se}_{0.2}\text{S}_{0.8})_6$ ,  $(\text{Sn}_{0.95}\text{Ge}_{0.05})_2\text{P}_2(\text{Se}_{0.4}\text{S}_{0.6})_6$ ,  $(\text{Sn}_{0.95}\text{Ge}_{0.05})_2\text{P}_2(\text{Se}_{0.5}\text{S}_{0.5})_6$ ,  $(\text{Pb}_{0.7}\text{Sn}_{0.25}\text{Ge}_{0.05})_2\text{P}_2\text{S}_6$  and  $(\text{Pb}_{0.7}\text{Sn}_{0.25}\text{Ge}_{0.05})_2\text{P}_2\text{Se}_6$  crystals are presented. The analysis of temperature dependences of the dielectric susceptibility, together with calorimetric data have shown the presence of a quantum paraelectric state in  $\text{Pb}_2\text{P}_2\text{S}_6$  type crystals. The temperature dependences of thermal conductivity for the crystals which contain germanium was also studied and compared with the pure crystals.

**Key words:** ferroics, ferroelectric crystals, phase transitions, photopyroelectric calorimetry, thermal diffusivity, thermal conductivity, critical behavior, anharmonicity.

## Chapter 1. The phenomenon of heat transfer and thermal properties of solids

All matter consists of molecules and atoms. These atoms are always in different types of motion (vibrational, rotational or translational). The motion of atoms and molecules creates thermal energy (heat). All matter has this thermal energy. The more motion the atoms or molecules have, the more heat or thermal energy they will have.

Thermodynamics is the study of the relationship between heat and other forms of energy. Thermodynamics is applicable to systems that are in thermal equilibrium. The phenomenon of heat transfer deals with systems that are not in thermal equilibrium.

Heat transfer is based on the following fundamental laws:

- Law of conservation of mass-energy;
- Newton's laws of motion;
- Laws of Thermodynamics.

In this chapter we will focus on the heat transfer mechanisms in solids. Special attention will be paid to the main thermophysical properties (heat capacity, thermal conductivity, thermal diffusivity and thermal effusivity).

### 1.1. Mechanisms of heat transfer: conduction, convection and radiation

In a medium or between bodies heat can be transferred from one place to another in three ways: **conduction** is the transfer of heat between substances that are in direct contact with each other, **convection** is the transfer of heat from hot places to cold places by means of an intermediate fluid and **radiation** is a heat transfer that does not rely upon any contact between the heat source and the heated object. Both conduction and convection are significantly different from radiation transfer at macroscales and require matter to transfer heat. At atomic levels they have similar equations based on

statistical thermodynamics. In all cases there is a quantitative relation between the heat flow  $\vec{q}$  and the temperature gradient  $\vec{\nabla}T$ .

For heat conduction in an isotropic and homogeneous material with temperature distribution  $T$  and constant thermal conductivity  $\kappa$ , the energy equation is derived by applying the macroscopic empirical Fourier's conduction law in any direction

$$q_{cond} = -\kappa \frac{dT}{da}, \quad (1.1)$$

where  $a$  is the direction of the heat flow.

If heat is produced within the solid, equation (1.1) must be modified. For an elementary cube within a solid as depicted in figure 1.1, the time-dependent energy change in cubical element  $dV$  due to a volumetric heat source term  $A$  is

$$\rho c \frac{\partial T}{\partial t} \partial V + \nabla(\kappa \nabla T) dV = A dV, \quad (1.2)$$

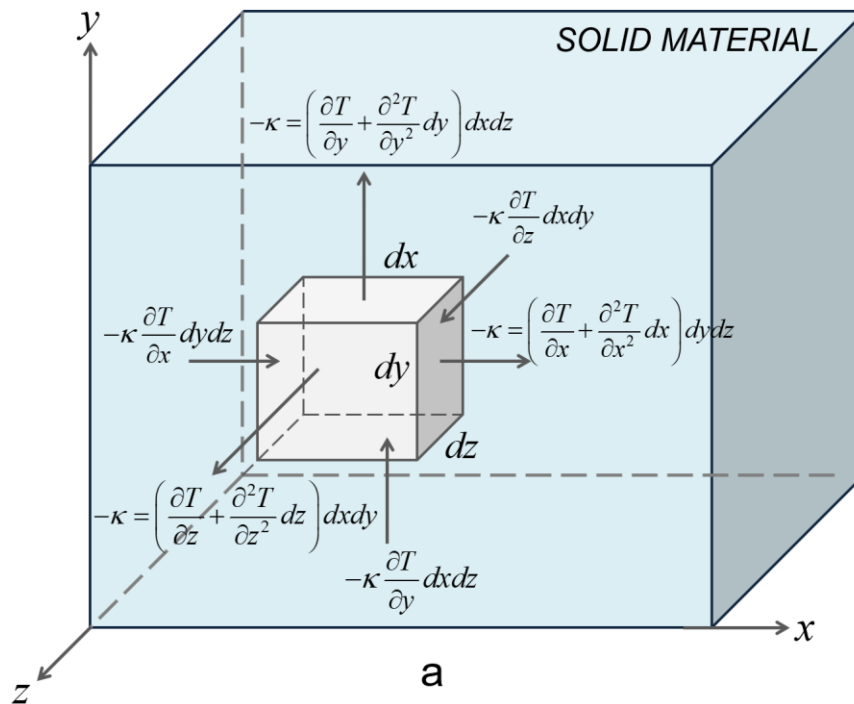


**Fig. 1.1.** Energy conduction for a volume element in a solid

where  $\partial$  is partial differentiation. For a homogenous stationary system, only the heat conduction in and out of all the faces of the cubic element needs to be considered, which yields Laplace's equation governing the heat conduction within the material:

$$\frac{A}{\kappa} = \frac{\partial^2 T}{\partial x^2} + \frac{\partial^2 T}{\partial y^2} + \frac{\partial^2 T}{\partial z^2}. \quad (1.3)$$

Equation 1.3 is written for a medium with uniform thermal conductivity [8].

Convection is the form of heat transfer, by real movement of matter, which mainly takes place in fluids whose molecules move freely from one place to another, such as liquids and gases.

The heat flow between a body surface  $T_{surface}$  and a fluid  $T_{fluid}$  with a boundary layer of thickness  $\delta$  (fig.1.2) has the next form

$$q = -\kappa \frac{T_{fluid} - T_{surface}}{\delta} = -\kappa \frac{\Delta T}{\delta}. \quad (1.4)$$

As  $\delta$  cannot be estimated independently we combine it with  $\kappa$  to give

$$q = -\frac{\kappa}{\delta} * \Delta T = -h * \Delta T, \quad (1.5)$$

where  $h$  is the heat transfer coefficient [9].

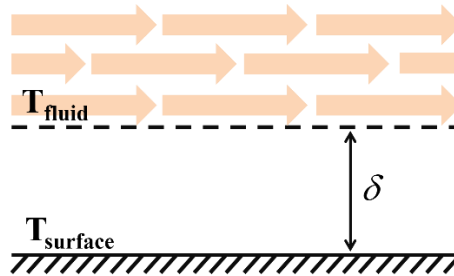


**Fig. 1.2.** Heat transfer by convection

Radiation occurs from all objects, at temperature higher than 0 K. In radiation, energy is transmitted between separated bodies without the need of a medium between the bodies. Radiation energy exchange between two surfaces depends on the geometry, shape, area, orientation, and effusivity of the two surfaces. In addition, it depends on the absorptivity  $\alpha$  of each surface. Absorptivity is a surface property defined as the fraction of radiation energy incident on a surface which is absorbed by the surface. Although the determination of the net heat exchange rate by radiation between two surfaces,  $Q_{12}$ , can be complex, the analysis is simplified for an ideal

model for which the absorptivity  $\alpha$  is equal to the effusivity  $\varepsilon$ . Such an ideal surface is called a gray surface. For the special case of a gray surface which is completely enclosed by a much larger surface,  $Q_{12}$  is given by Stefan-Boltzmann radiation law

$$Q_{12} = \varepsilon_1 \sigma A_1 (T_1^4 - T_2^4), \quad (1.6)$$

where  $\varepsilon_1$  is the emissivity of the small surface,  $A_1$  its area,  $T_1$  its absolute temperature, and  $T_2$  is the absolute temperature of the surrounding surface,  $\sigma = 5,67 \cdot 10^{-8} \text{ Wm}^{-2} \text{ K}^{-4}$  is the Stefan-Boltzmann's constant. It is worth noting that for this special case neither the area of the large surface nor its emissivity  $\varepsilon_2$  affects the result [9]. The mechanism of heat transfer by radiation is depicted in fig. 1.3.

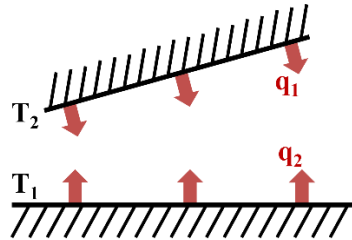


**Fig. 1.3.** Heat transfer by radiation

## 1.2. Determination of the thermal properties of materials

There are four essential thermal properties to characterize a material: heat capacity, thermal diffusivity, thermal conductivity and thermal effusivity.

**Heat capacity** ( $\text{J K}^{-1} \text{ mol}^{-1}$ ) as a basic thermal property is one of the main parameters for evaluation, calculation and design of thermal system. Heat capacity expresses the ability of a material to store heat. In its equation form, heat capacity  $C$  is

$$C = mc_p, \quad (1.7)$$

where  $m$  is mass and  $c_p$  is specific heat. Heat capacity is closely related to the concept of **specific heat**. The specific heat is the amount of heat per unit mass required to raise the temperature by one degree Celsius. At constant pressure the specific heat can be higher than at constant volume, because additional energy is required to bring about a volume change against external pressure. The equation for heat transfer  $Q$  is

$$Q = mc_p \Delta T. \quad (1.8)$$

**Thermal conductivity** ( $\text{W m}^{-1} \text{K}^{-1}$ ) is one of the most important intrinsic parameters to exhibit the potential of heat transfer in materials. Thermal conductivity is the property which indicates the capacity of a material to conduct heat. Different materials conduct heat at different rates. The general conduction equation for thermal conductivity for an isotropic and homogeneous material has the next form

$$\vec{q} = -\kappa \vec{\nabla} T, \quad (1.9)$$

where  $\vec{q}$  is the heat flow taking place in the material. Thermal conductivity measures the heat that flows in unit time through a unit area of a layer of the material of unit thickness with unit temperature difference between its faces.

**Thermal diffusivity**  $D$  ( $\text{m}^2 \text{s}^{-1}$ ) is the property that determines how fast heat is propagated through the medium. It measures the temperature change created in the unit volume of a material produced by a heat flow transported through a unit area per unit time, in a material with unit thickness, whose opposite surfaces have the temperature gradient equal to 1 K. Thermal diffusivity is an important parameter to be taken into account; a high value does not necessarily mean that heat is better dissipated, since it is the ratio between the thermal conductivity and the volumetric heat capacity at constant pressure. It provides information about the competition between heat conduction and storing, and both can be useful to keep temperature as low as possible:

$$D = \frac{\kappa}{\rho c_p}, \quad (1.10)$$

Where  $D$  is the thermal diffusivity,  $\kappa$  is the thermal conductivity,  $\rho$  is density, and  $c_p$  is the heat capacity.

For a homogeneous and isotropic medium with temperature-independent thermal properties and no heat generation inside it, the differential equation of heat conduction is [10]

$$\nabla^2 T(\vec{r}, t) - \frac{1}{D} \frac{\partial T(\vec{r}, t)}{\partial t} = 0. \quad (1.11)$$

The relationship between thermal conductivities and thermal diffusivities in condensed matters and gases is depicted in fig. 1.4.

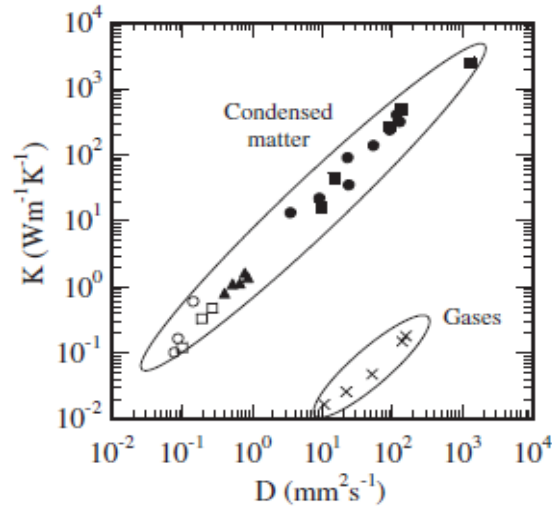


**Fig. 1.4.** Thermal conductivity compared with thermal diffusivity in solids and gases. Closed circles represent metals, squares - ceramics, triangles - glasses, open squares - polymers and open circles - liquids [11]

**Thermal effusivity** ( $\text{W s}^{1/2} \text{m}^{-2} \text{K}^{-1}$ ) tells us about the behavior of the heat storing or dissipating capability of materials. Thermal effusivity can be found as

$$e = \sqrt{\rho c_p K} = \frac{K}{\sqrt{D}} = \rho c_p \sqrt{D}. \quad (1.12)$$

Thermal effusivity is used to outline heat transfer behavior between two bodies (solids or fluids), when the two bodies are in contact with each other. When the two materials have the same thermal effusivity, the heat transfer behavior will equal to a unique object as if there were no junction between the two objects.

Table 1.1 contains the measured values of the specific heat, thermal conductivity, thermal diffusivity and thermal effusivity for some selected materials [11].

Table 1.1

Thermophysical properties of some materials [11]

<b>Material</b>	$\rho c_p,$ ( $\times 10^{-6} \text{ Jm}^{-3}\text{K}^{-1}$ )	$\kappa,$ ( $\text{Wm}^{-1}\text{K}^{-1}$ )	$D,$ ( $\times 10^{-6} \text{ m}^2 \text{ s}^{-1}$ )	$e,$ ( $\text{Jm}^{-2}\text{K}^{-1}\text{s}^{-1/2}$ )
Diamond	1.78	2300	1290	64040
Glass	1.98	1.11	0.56	1480
Air	0.0012	0.026	22	5.5
He	0.0011	0.15	137	12.8
Water	4.16	0.6	0.144	1580
AISI 304	3.62	14.5	4	7250
PC	1.33	0.2	0,15	515
Cu	3.45	400	116	37140
Ni	3.95	91	23	19400
K	0.65	102	158	8150
Pb	1.52	35	23	7300
Co	4.05	102	24.6	20150

### 1.3. Electrons and phonons as heat carriers in semiconductor materials

Heat energy is the result of the microscopic motions of the various electronic carriers (electrons and holes, lattice waves, heat transport due to excitons, electromagnetic waves, spin waves, or other excitations) at finite temperature, which induces a thermal distribution of the energies of the particles [12]. The motion of atoms in the sites in the solid bodies forms lattice oscillations - *phonons*, which transfer heat. Electron energies are also broadened by heat and give an electronic thermal conductivity. In metals, the thermal conductivity is mainly governed by the electrons, while in semiconductors and insulators it is mainly due to the phonons.

Lattice thermal conductivity is dominant for semiconductors. There are acoustic phonons and optical phonons in a crystal. The acoustic phonons are low frequency acoustic branches in which atoms are in phase. Unlike the acoustic phonons the optical phonons are high frequency branches with atoms out of phase. Nevertheless, the optical phonons turn out to be ineffective as heat carriers due to their low group velocities. But, they interact with the acoustic phonons which are the main contributors to the thermal conductivity.

The thermal conductivity is expressed as

$$\kappa = \frac{1}{3} c_p v \Lambda, \quad (1.13)$$

where  $c_p$  is the specific heat per volume,  $v$  is the phonons velocity in the crystal,  $\Lambda$  is the phonon mean free path.

As the phonon mean free path depends strongly on temperature, let's consider the dependence of thermal conductivity on temperature. The phonon mean free path is the average distance travelled by the phonons between two sequential clashes. Hence  $\Lambda$  depends on the next significant mechanisms:

1. Phonon – phonon interaction;
2. Phonon – impurity interaction;
3. Phonon – external boundaries of the sample.

Foremost phonon – phonon interaction is dominant at high temperatures, at which the atomic displacements are large. Therefore at high temperature,  $\Lambda$  is inversely proportional to temperature and more phonons take part in the interaction at high temperatures reducing mean free path and hence conductivity. When there is a greater number of impurities, the phonon scattering increases and, therefore, the phonon mean free path is shorter. At low temperatures, phonon – phonon and phonon – impurity interactions become ineffective. On the contrary, the primary scattering mechanism is the external boundary of the crystal due to the comparable size of the crystal and the wavelength of the excited phonon. Therefore,  $\Lambda$  is nearly equal to the

diameter of the crystal and is independent of temperature. According to the above the dependence of mean free path with temperature is as follows:

1. At low temperatures, the optical branch phonons have energies higher than  $k_B T$ , as consequence, optical branch waves are not excited. At temperatures close to 0 K the phonon mean free path is a constant (equal to the size of the crystal) and does not depend on temperature. Here the thermal conductivity is determined by specific heat as  $\sim T^3$ .

2. At low temperatures ( $T < \theta_{Debye}$ ) the Debye approximation is best suited because almost all excited phonons belong to the long-wavelength waves in the acoustic branches and the crystal behaves like a continuum.

3. In the high temperature region, the phonon mean free path decreases with the inverse of temperature as  $1/T$ .

Figure 1.5 represents the temperature dependence of the phonon thermal conduction.

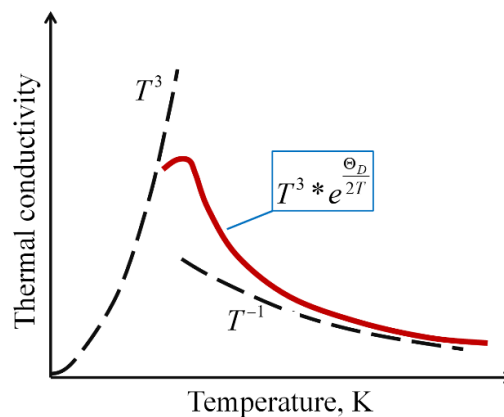


**Fig. 1.5.** Dependence of the phonon thermal conductivity on temperature

Let's consider the mechanism of the phonon-phonon interactions. In quantum mechanics perturbation theory, the crystal potential is expanded as a power of displacement and the Hamiltonian can be written as:

$$\hat{H} = H_0 + \alpha H_3 + \alpha^2 H_4 + \alpha^3 H_5 + \dots = \sum_{n=0}^{\infty} H_n + \alpha^n H_{n+2}, \quad (1.14)$$

where  $H_0$  is the harmonic Hamiltonian and  $H_3, H_4, H_5, \dots, H_n$  are the perturbation terms involving three, four, five ...,  $n$  interacting phonons,  $\alpha$  is a dimensionless parameter [13].

Figure 1.6 represents the interactions of four phonons in solid materials. In such interactions, one phonon splits into three; or two phonons form two new phonons; or three phonons combine into one. These quantum-mechanical phenomena are related to the effects of heat conduction in solid materials [14].

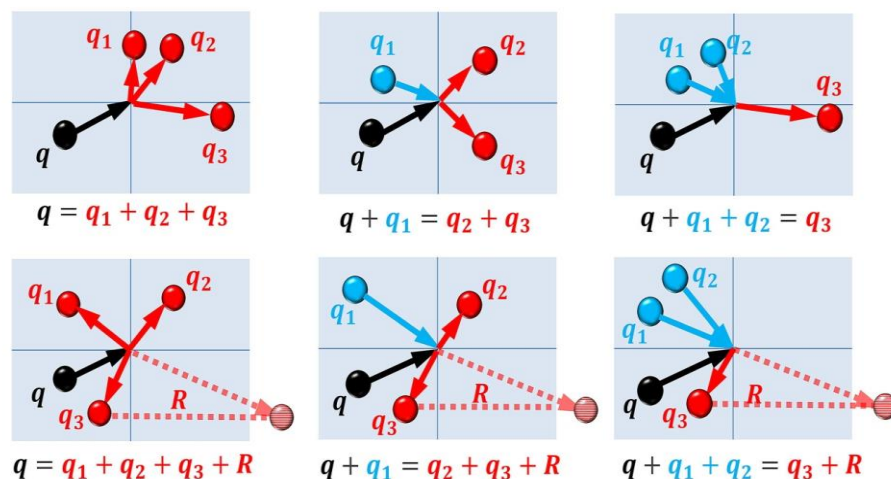


**Fig. 1.6.** The diagrams of four-phonon interactions in condensed matters [14]

Considering the *electrons* as the heat carriers, in semiconductors the electronic contribution to the thermal conductivity is much smaller than the contribution of phonons. Nevertheless heat transport in semiconductors is more complex than in dielectrics or metals and the electron component is quite important for them. In cases when the number of the free electrons or holes is quite large ( $\sim 10^{20} \text{ cm}^{-3}$ ),  $\kappa_{\text{electrons}}$  could be as important as  $\kappa_{\text{phonons}}$ .

Accordingly, the thermal conduction caused by the free electrons and holes can be found as a function of the temperature of a material and its electronic conductivity [15]:

$$\frac{\kappa}{\sigma T} = \frac{k^2}{e^2} \left[ \left( \frac{5}{2} + \alpha \right) + \left( 5 + 2\alpha + \frac{\zeta_G}{kT} \right)^2 \frac{n_e \mu_e^* n_h \mu_h}{(n_e \mu_e + n_h \mu_h)^2} \right], \quad (1.15)$$

where  $\sigma$  is an electric conductivity,  $\zeta_G$  is the width of the energy gap,  $n_e$  and  $\mu_e$  are the mobilities of electrons and holes respectively.

#### 1.4. Heat propagation in isotropic and anisotropic materials

In *isotropic* materials the thermal conductivity is not dependent on the direction. As opposed to isotropic system, the thermal conductivity in an *anisotropic* case has two important differences. The first one is that the thermal conductivity of anisotropic materials is different in different directions, it is a tensor. The second one is that the magnitude of heat transfer rate of an anisotropic material in one direction not only depends on the temperature gradient in this direction, but also on the temperature gradient which is normal to the direction [16].

Isotropic thermal conductivity specifies that the heat flux  $q_i$  depends linearly and isotropically on the gradient of the temperature field

$$q_i = -\kappa \frac{\partial T}{\partial x_i}. \quad (1.16)$$

For a homogeneous isotropic solid heat fluxes  $q_x$ ,  $q_y$  and  $q_z$  the equation of conduction of heat may be expressed as

$$\frac{\partial^2 T}{\partial x^2} + \frac{\partial^2 T}{\partial y^2} + \frac{\partial^2 T}{\partial z^2} = \frac{1}{D} \frac{\partial T}{\partial t}, \quad (1.17)$$

where  $D$  is the thermal diffusivity.

For an anisotropic case the heat flux will depend on the direction

$$\begin{aligned} q_x &= -\left( \kappa_{xx} \frac{\partial T}{\partial x} + \kappa_{xy} \frac{\partial T}{\partial y} + \kappa_{xz} \frac{\partial T}{\partial z} \right); \\ q_y &= -\left( \kappa_{yx} \frac{\partial T}{\partial x} + \kappa_{yy} \frac{\partial T}{\partial y} + \kappa_{yz} \frac{\partial T}{\partial z} \right); \\ q_z &= -\left( \kappa_{zx} \frac{\partial T}{\partial x} + \kappa_{zy} \frac{\partial T}{\partial y} + \kappa_{zz} \frac{\partial T}{\partial z} \right). \end{aligned} \quad (1.18)$$

The differential equation of conduction heat for an anisotropic solid has the next form

$$\rho c_p \frac{\partial T}{\partial t} = \kappa_{xx} \frac{\partial^2 T}{\partial x^2} + \kappa_{yy} \frac{\partial^2 T}{\partial y^2} + \kappa_{zz} \frac{\partial^2 T}{\partial z^2} + 2\kappa_{xy} \frac{\partial^2 T}{\partial x \partial y} + 2\kappa_{xz} \frac{\partial^2 T}{\partial x \partial z} + 2\kappa_{yz} \frac{\partial^2 T}{\partial y \partial z}, \quad (1.19)$$

provided that the medium is homogeneous and that heat is not produced in it [10].

#### 1.4.1 Conductivity matrix for crystal systems

Thermal conductivity and thermal diffusivity are second rank tensors. Second rank tensor can be written as 3x3 matrix. Let's consider all the possible crystal systems for solids.

**Cubic** crystal system ( $a = b = c$ ,  $\alpha = \beta = \gamma = 90^\circ$ ) has one independent component:  $\kappa_{xx} = \kappa_{yy} = \kappa_{zz}$ .

$$\kappa = \begin{pmatrix} \kappa_{xx} & 0 & 0 \\ 0 & \kappa_{yy} & 0 \\ 0 & 0 & \kappa_{zz} \end{pmatrix}. \quad (1.20)$$

**Tetragonal** ( $a = b \neq c$ ,  $\alpha = \beta = \gamma = 90^\circ$ ), **trigonal** ( $a = b = c$ ,  $\alpha = \beta = \gamma \neq 90^\circ$ ) and **hexagonal** ( $a = b \neq c$ ,  $\alpha = \beta = 90^\circ$ ,  $\gamma = 120^\circ$ ) have two independent components:

$$\kappa_{xx} = \kappa_{yy} \neq \kappa_{zz}$$

$$\kappa = \begin{pmatrix} \kappa_{xx} & 0 & 0 \\ 0 & \kappa_{yy} & 0 \\ 0 & 0 & \kappa_{zz} \end{pmatrix}. \quad (1.21)$$

For **orthorhombic** ( $a \neq b \neq c$ ,  $\alpha = \beta = \gamma = 90^\circ$ ) all components are different

$$\kappa_{xx} \neq \kappa_{yy} \neq \kappa_{zz}.$$

$$\kappa = \begin{pmatrix} \kappa_{xx} & 0 & 0 \\ 0 & \kappa_{yy} & 0 \\ 0 & 0 & \kappa_{zz} \end{pmatrix}. \quad (1.22)$$

**Monoclinic** ( $a \neq b \neq c$ ,  $\alpha = \gamma = 90^\circ \neq \beta$ ) has four independent components

$$\kappa_{xx} \neq \kappa_{yy} \neq \kappa_{zz} \text{ and } \kappa_{xz} = \kappa_{zx}$$

$$\kappa = \begin{pmatrix} \kappa_{xx} & 0 & \kappa_{zx} \\ 0 & \kappa_{yy} & 0 \\ \kappa_{xz} & 0 & \kappa_{zz} \end{pmatrix}. \quad (1.23)$$

*Triclinic* is the system with a lowest symmetry ( $a \neq b \neq c$ ,  $\alpha \neq \beta \neq \gamma$ ), hence all nine components of  $\kappa_{ij}$  can be nonzero, the number of independent components six:  $\kappa_{xx} \neq \kappa_{yy} \neq \kappa_{zz}$ ,  $\kappa_{yx} = \kappa_{xy}$ ,  $\kappa_{zy} = \kappa_{yz}$  and  $\kappa_{zx} = \kappa_{xz}$ .

$$\kappa = \begin{pmatrix} \kappa_{xx} & \kappa_{xy} & \kappa_{xz} \\ \kappa_{yx} & \kappa_{yy} & \kappa_{yz} \\ \kappa_{zx} & \kappa_{zy} & \kappa_{zz} \end{pmatrix}. \quad (1.24)$$

All the above is also applicable to the thermal diffusivity tensor.

### 1.5. Temperature field in a medium. Thermal wave physics

As we have already discussed above, conducted heat in semiconductors is mainly transported by lattice vibrations - phonons and free electrons or holes. We can describe these vibrations as highly damped waves, which we are commonly called *thermal waves*. Many photothermal techniques such as thermal wave interferometry (TWI), piezoelectric optothermal window (POW), photopyroelectric (PPE) calorimetry are based on the diffusion of thermal energy in heated matter by a periodically modulated light beam (PPE techniques will be discussed in more detail in chapter 2) [17, 18, 19, 20, 21, 22, 23, 24, 25, 26, 27]. Thermal waves inside the matter are generated by means of a periodically varying heat source.

Although the diffusion of thermal energy in a periodically heated material is well described in terms of thermal waves, the latter do not transport energy. Thermal waves cannot be considered as real travelling waves because they do not show wave fronts [28, 29]. However, temperature oscillations inside the sample have the same mathematical expression as highly damped waves, the so-called thermal waves, which will be shown in detail in the next section.

### 1.5.1. Parabolic and hyperbolic heat diffusion equation

From the classical Fourier's law (1.1) whenever there is a temperature gradient  $\vec{\nabla}T$  in a material and a heat flow  $\vec{q}$ , the law of energy conservation leads to the **parabolic heat diffusion equation**, which in the absence of internal heat sources takes the form (1.11).

Let's consider an opaque and semi-infinite solid whose surface is uniformly illuminated by a periodically modulated light beam with intensity

$$I = \frac{I_0}{2}(1 + \cos(\omega t)) = \text{Re} \left[ \frac{I_0(1 + e^{i\omega t})}{2} \right],$$

where  $I_0$  is the source intensity of the beam and  $\omega = 2\pi f$  is the angular modulation frequency [30]. Fig. 1.7 exhibits the geometry of the solid whose surface is uniformly illuminated.

The temperature at any point can be found as

$$T(x, t) = T_E + T_{DC}(x) + T_{AC}(x, t), \quad (1.25)$$

where  $T_E$  is the temperature of the environment,  $T_{DC}$  is a time-independent temperature rise above  $T_E$  and  $T_{AC}$  is a periodic temperature oscillation with the same frequency as the illumination which has the next form:

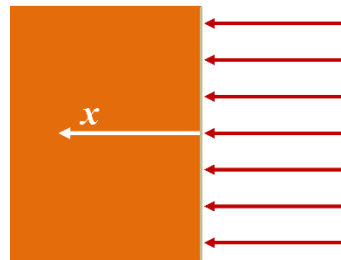


**Fig. 1.7.** An opaque, semi-infinite solid illuminated by a modulated light beam

$$T_{AC}(x, t) = T_{AC}(x)e^{i\omega t}. \quad (1.26)$$

Substituting (1.26) into (1.11), the spatial component of  $T_{AC}$  satisfies Helmholtz's equation.

$$\frac{d^2 T_{AC}(x)}{dx^2} - \sigma^2 T_{AC}(x) = 0, \quad (1.27)$$

where  $\sigma = \sqrt{i\omega/D}$ . Hence, the general solution of (1.23) can be written as

$$T_{AC}(x) = A e^{-\sigma x} + B e^{\sigma x}, \quad (1.28)$$

where  $A$  and  $B$  are constants. When  $x \rightarrow \infty$ ,  $T(x)$  is finite, therefore  $B = 0$ . Constant  $A$  can be found by applying the flux continuity boundary conditions, when  $x = 0$

$$-\kappa \left. \frac{dT_{AC}}{dx} \right|_{x=0} = \kappa \sigma A e^{-\sigma x} \Big|_{x=0} = \frac{I_0}{2}. \quad (1.29)$$

Hence,  $A = \frac{I_0}{2\kappa\sigma}$  and the time-dependent component of the temperature has the

next form

$$T_{AC}(x,t) = \frac{I_0}{2\kappa\sigma} e^{-\sigma x} e^{i\omega t} = \frac{I_0}{2\varepsilon\sqrt{\omega}} e^{-\frac{x}{\mu}} \cos\left(\frac{x}{\mu} - \omega t + \frac{\pi}{4}\right). \quad (1.30)$$

Here the thermal effusivity of the material  $\varepsilon$  can be written as  $\varepsilon = \kappa/\sqrt{D}$  and the thermal diffusion length (the distance at which the propagated wave amplitude decays  $e$  times its value at  $x = 0$ ) is  $\mu = \sqrt{2D/\omega}$ .

The disadvantage of the parabolic heat diffusion equation is its inability to consider heat transport with a propagation speed. To solve this issue a **hyperbolic heat diffusion equation** which includes a delay  $\tau$  between the temperature gradient  $\vec{\nabla}T$  and the heat flow  $\vec{q}$  has been proposed in [31]:

$$\nabla^2 T(\vec{r},t) - \frac{1}{D} \frac{\partial T(\vec{r},t)}{\partial t} - \frac{\tau}{D} \frac{\partial T(\vec{r},t)}{\partial t} = 0. \quad (1.31)$$

Following the same process to obtain the time-dependent component of the temperature for the hyperbolic heat diffusion equation as described above for parabolic case, we obtain

$$T'_{AC}(x,t) = \text{Re} \left[ \frac{I_0}{2\kappa q'} (1 + i\omega\tau) e^{-\sigma'x} e^{i\omega t} \right] = \frac{I_0 \sqrt{\tau}}{2\varepsilon} \sqrt[4]{\frac{1 + (\omega\tau)^2}{(\omega\tau)^2}} e^{-x\sqrt{\frac{\omega}{2D}} \sqrt{\sqrt{1 + (\omega\tau)^2} - \omega\tau}} \times \quad (1.32)$$

$$\times \cos \left( x\sqrt{\frac{\omega}{2D}} \sqrt{\sqrt{1 + (\omega\tau)^2} - \omega\tau} - \omega\tau - \frac{\text{arctg}(\omega\tau)}{2} + \pi/4 \right),$$

$$\text{where } \sigma' = \sqrt{\frac{i\omega}{D} - \frac{\tau\omega^2}{D}} = \frac{i\omega}{D} (1 + i\omega\tau).$$

We can distinguish two frequency regions:

1. If  $\omega\tau \ll 1$ , therefore we have that (1.32) becomes (1.30). Hence, solutions for the parabolic and the hyperbolic cases coincide.

2. If  $\omega\tau \gg 1$ , equation (1.32) has the next form:

$$T'_{AC}(x,t) = \frac{I_0 \sqrt{\tau}}{2\varepsilon} e^{\left(-x\sqrt{\frac{\omega}{2D\tau}}\right) \cos\left(\sqrt{\frac{\tau}{D}}\omega x - \omega t\right)}. \quad (1.33)$$

This means that this hyperbolic description does not depend on the time scale.

### 1.5.2. Reflection and refraction of thermal waves

As other kinds of waves (electromagnetic or acoustic) the thermal waves can also be reflected and refracted. Thermal waves propagate across the surface of two media with different thermal effusivity, giving rise to the same interference phenomena as electromagnetic, acoustic or mechanical waves do. Figure 1.8 shows a time-periodic heat wave  $AO$  which encounters the interface between two media at point  $O$  and separates in two waves: a reflected  $OB$  with the angle of reflection  $\varphi$  and a transmitted  $OC$  with the angle of transmission  $\theta$ . According to the reflection law, the angle of incidence is equal to the angle of reflection. Therefore the expression for these three waves can be written in the form [32]

$$\begin{aligned} T_i &= A e^{-\sigma_1 x \cos \varphi - \sigma_1 y \sin \varphi + i\omega t}, \\ T_r &= A R e^{\sigma_1 x \cos \varphi - \sigma_1 y \sin \varphi + i\omega t}, \\ T_t &= A T e^{-\sigma_2 x \cos \theta - \sigma_2 y \sin \theta + i\omega t}. \end{aligned} \quad (1.34)$$

where  $A$  is the amplitude of the incident wave,  $R$  and  $T$  are the reflection and transmission coefficients at  $x = 0$  and  $y = 0$  respectively,  $\sigma = \sqrt{\omega / 2D}$ . Given the continuity of temperature at the interface the values of these coefficients can be determined:

$$Ae^{-\sigma_1 y \sin \varphi} + AR e^{-\sigma_1 y \sin \varphi} = AT e^{-\sigma_2 y \sin \theta} . \quad (1.35)$$

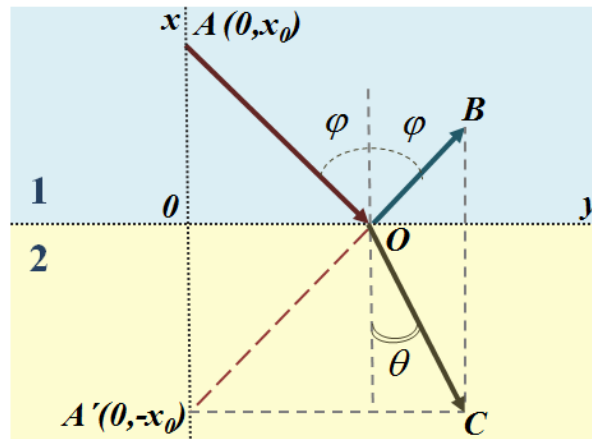


**Fig. 1.8.** Geometry of the model of reflection and refraction of the thermal waves in two media

Applying the Snell's law:  $\sigma_1 \sin(\varphi) = \sigma_2 \sin(\theta)$  and in the case of continuity of flow at  $x = 0$ , by differentiating the equation (1.35) we will obtain the coefficients  $R$  and  $T$

$$R = \frac{\cos(\varphi) - b \cos(\theta)}{\cos(\varphi) + b \cos(\theta)}, \text{ and } T = \frac{2 \cos(\theta)}{\cos(\theta) + b \cos(\theta)}, \quad (1.36)$$

where,  $b = \frac{\kappa_2 \sigma_2}{\kappa_1 \sigma_1} = \frac{\sqrt{\rho_2 c_2 \kappa_2}}{\sqrt{\rho_1 c_1 \kappa_1}} = \frac{\varepsilon_2}{\varepsilon_1}$ ,  $\varepsilon = \sqrt{\rho c \kappa}$  is the thermal effusivity.

For a normal incidence beam  $\varphi = 0$ , hence, the equations (1.36) are reduced to

$$R = \frac{1-b}{1+b} = \frac{\varepsilon_1 - \varepsilon_2}{\varepsilon_1 + \varepsilon_2}, \text{ and } T = \frac{2}{1+b} = \frac{2\varepsilon_1}{\varepsilon_1 + \varepsilon_2}. \quad (1.37)$$

As seen above the coefficients  $R$  and  $T$  depend on the thermal effusivity  $\varepsilon$ . Let's consider two possible situations: steady (fig.1.9 (1, 2)) and non-steady (fig.1.9 (3, 4))

in which the thermal effusivities and conductivities are very different. For an steady situation when  $\varepsilon_1 \gg \varepsilon_2$ ,  $T_1 > T_2$  and  $\kappa_1 \gg \kappa_2$  nearly no heat will be transferred from medium 1 to medium 2. At  $\varepsilon_1 \ll \varepsilon_2$ ,  $T_1 > T_2$  and  $\kappa_1 \ll \kappa_2$  heat will be efficiently transferred to medium 2.

In a non-steady situation when  $\varepsilon_1 \gg \varepsilon_2$ ,  $T_1 > T_2$  and  $\kappa_1 \gg \kappa_2$  we have  $b \sim 0$ ,  $R \sim 1$  and  $T \sim 2$ . Introducing these  $R$  and  $T$  in equation (1.34) gives that  $T_{transmitted} \neq 0$  meaning that the thermal wave propagates into the medium. In the case of  $\varepsilon_1 \ll \varepsilon_2$ ,  $T_1 > T_2$  and  $\kappa_1 \ll \kappa_2$ ,  $b \sim \infty$  that, in turn, modifies the reflection and transmission coefficients  $R \sim 1$ ,  $T \sim 0$ . Substituting these values into equation (1.34) gives  $T_{transmitted} \sim 0$ , which means that the thermal wave does not propagate along medium 2 [33]. In this case the thermal mirror effect is observed, when the phase of the reflected wave is shifted  $180^\circ$  with respect to the incident one.

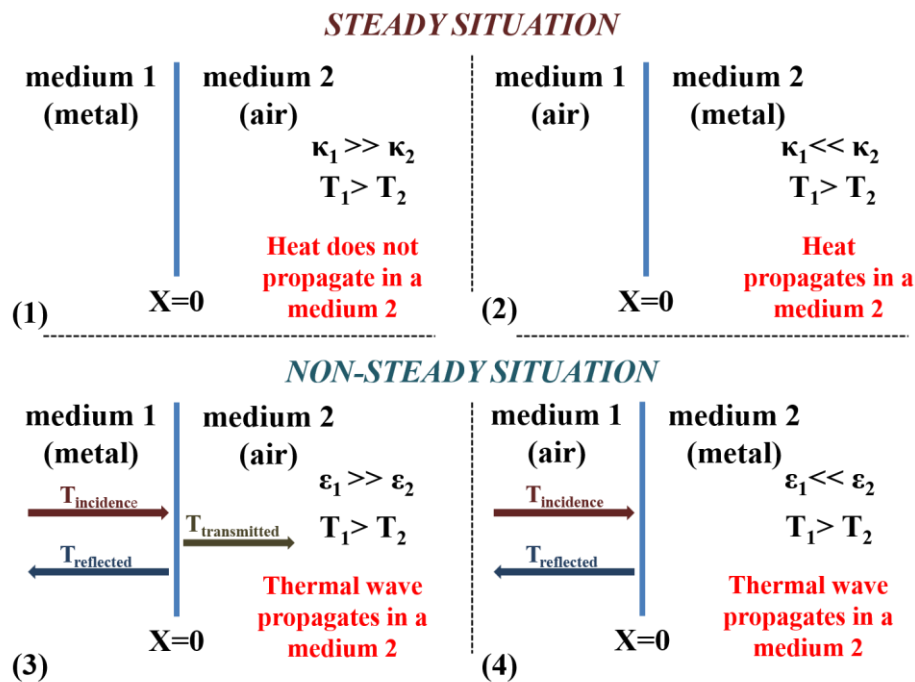


**Fig. 1.9.** Thermal wave propagation through the two media

Both of them, steady and non-steady situation, must be taken into consideration. In the steady case thermal conductivity tells us what will happen. In the second case, thermal effusivity governs what happens in the interface. This is

related to the fact that thermal waves lack an important wave-like feature: they do not transport energy, as already mentioned in the previous section. This is why both thermal magnitudes have equal importance when considering thermal physics.

## Chapter 2. Photopyroelectric calorimetry in solids

### 2.1. Basic theory of pyroelectricity

Pyroelectric effects appear only in crystals that are characterized by spontaneous polarization  $P_s$  and can only be in solids which do not have more than one axis of symmetry and there is not a center of symmetry. As a consequence, all pyroelectrics are also piezoelectrics. Pyroelectricity implies that the polarization of a material is a function of temperature. The pyroelectric coefficient is equal to the negative derivative of spontaneous polarization with respect to the temperature. The equation for pyroelectric coefficient  $p$  has the next form:

$$p = \frac{-dP_s}{dT} \quad (2.1)$$

where  $p$  is pyroelectric coefficient,  $P_s$  - spontaneous polarization.

As a whole, the pyroelectric coefficient of a free sample consists of three components:

1. The real coefficient which depends on the derivative of spontaneous polarization with respect to the temperature (see eq. (2.1.)).
2. The second one is derived from the temperature expansion and can be calculated based on mechanical parameters.
3. The third component is related to the piezoelectric effect and is due to the temperature gradient that exists along the polar axis of the crystal. In cases when the specimen is relatively small the third coefficient can be neglected.

The measured pyroelectric coefficient is the sum of the first coefficient  $p_i^{T,E}$  and the second one, which depends on the piezoelectric constant  $d_{ij}$ , the thermal expansion coefficient  $\alpha_{ij}^E$  and the elastic compliance coefficient  $s_{ij}^E$  [34]:

$$p_i^{T,E} = p_i^{S,E} + \frac{d_{ij} \alpha_{ij}^E}{s_{ij}^E} \quad (2.2)$$

The nature of the pyroelectricity can be explained as follows. Pyroelectric crystals have special axes, where the properties of such crystals are different in the positive and negative directions. As a result of temperature changes, minor alterations occur in the position of atoms within the crystals, hence, the polarization of the crystal changes. This creates a voltage across the crystal. Nevertheless, the voltage that develops across the crystal is not stable and when the temperature change stops, the voltage gradually disappears due to leakage of current. This may be due to the movement of electrons in the crystals. On heating, one part is charged positively while the other one is negatively due to the thermal expansion, therefore charge compensation is violated (fig. 2.1). The appearance of charges on the surface of the pyroelectrics is due to the additional displacement of dipoles along the electric axis under the influence of temperature.

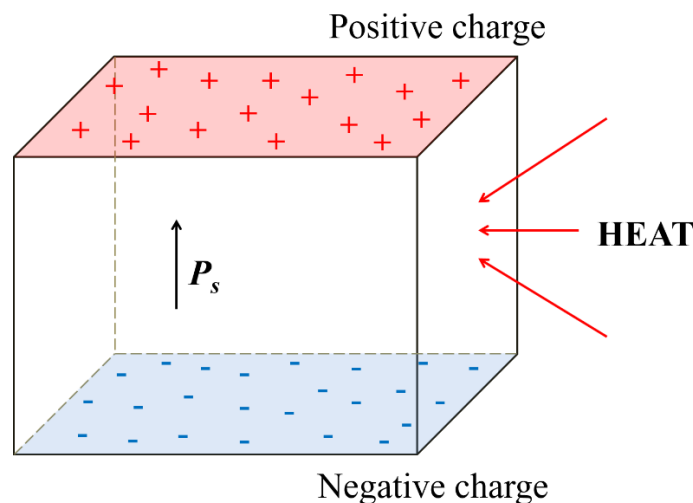


**Fig. 2.1.** Polarized pyroelectric crystal

The most known pyroelectrics are ferroelectrics: triglycine sulfate, niobium and lithium tantalate (polarized by the bias current when the crystal is growing), thin films of potassium nitrate in the ferroelectric phase, as well as ceramic lead titanate and lead zirconate-titanate with various impurities. To provide and increase pyroelectric properties, ferroelectric ceramics are subjected to the following

procedure: the sample is electrically poled by heating above  $T_C$  and then slowly cooled down to room temperature under some electric field applied (about 1 kV/cm) along the x-direction.

*Lithium Niobate (LiNbO<sub>3</sub>) and Lithium Tantalate (LiTaO<sub>3</sub>)* possess a combination of unique electro-optical, acoustic, pyroelectric, piezoelectric and non-linear optical properties making it an appropriate material for applications in acoustic, electro-optical and non-linear optical devices, etc. As seen from table 1.1 these two materials have similar physical properties but, in the application as photopyroelectric sensors, lithium tantalate is more desirable due to a higher pyroelectric coefficient [34, 36].

Table 1.1

Physical properties of lithium tantalate (LiTaO<sub>3</sub>) and lithium niobate (LiNbO<sub>3</sub>) [34, 36]

<b>Material</b>	<b>LiNbO<sub>3</sub></b>	<b>LiTaO<sub>3</sub></b>
<b>Chemical formula weight</b>	147.8	235.9
<b>Cell parameters</b>	Trigonal	Trigonal
<b>Space group</b>	R3c	R3c
<b>a (Å)</b>	5.148	5.154
<b>b (Å)</b>	5.148	5.154
<b>c (Å)</b>	13.863	13.783
<b><math>\alpha</math> (°)</b>	90.000	90.000
<b>V (Å<sup>3</sup>)</b>	318.2	317.1
<b>Z</b>	6	6
<b><math>\epsilon</math></b>	30	47
<b>tg <math>\delta</math></b>	< 0.01	0.01

<b>Density, g/cm<sup>3</sup></b>	4.65	7.46
<b><math>c_p</math> (10<sup>6</sup> J m<sup>-3</sup> K<sup>-1</sup>)</b>	3.2	3.2
<b>Curie temperature (°C)</b>	1410	620
<b>Melting temperature (°C)</b>	1257	1650
<b>Pyroelectric coefficient (10<sup>-6</sup> C m<sup>-2</sup> K<sup>-1</sup>)</b>	71	230

## 2.2. Photopyroelectric calorimetry. Back-detection configuration BPPE

The photothermal techniques are based on the generation of a temperature field in the specimen, as a consequence of the absorption of electromagnetic radiation; this process depends on the specimen optical and thermal properties. Photopyroelectric (PPE) calorimetry is a high resolution *ac* technique which allows to determine thermal properties such as thermal diffusivity ( $D$ ), specific heat ( $c_p$ ), thermal effusivity ( $e$ ) and thermal conductivity ( $\kappa$ ) with a high temperature resolution, both in a wide temperature range as well as close to the phase transitions in solid, gas, and fluid materials.

For the last years different techniques have evolved to study the behavior of the system in the vicinity of phase transitions with the highest accuracy. Among them, the most used are: Differential Scanning Calorimetry (Adiabatic Scanning Calorimetry [20], Nonadiabatic Scanning Calorimetry [21]), and several *ac*-Calorimetry (ACC) configurations [23, 24, 25, 37]. Not all of these techniques permit to obtain a high signal-to-noise ratio in the detector because not all of them induce small temperature gradients in the material or can be applied in a wide temperature region hence the thermal parameters cannot be studied with great detail in the close vicinity of the phase transition (PT). Some of the *ac* PPE calorimetry techniques can fulfill these requirements and show very high efficiency in the study of PT [26, 27].

In order to perform this kind of studies, an *ac* PPE calorimetry technique must fulfill the next requirements:

- the possibility to work in a broad temperature range;
- sub-millikelvin temperature resolution;
- the small sample size;
- measuring enthalpy changes near phase transitions.

These PPE techniques can be divided in two large groups depending on the signal detection:

1. Back-detection configuration (BPPE) if the sample is illuminated.
2. Front-detection configuration (FPPE) if the sensor is illuminated.

All the calorimetric measurements of this work are based on BPPE-configuration *ac* PPE calorimetry so let's consider it in detail.

As depicted on fig. 2.2 back-detection multilayer system consists of: a gas at the front (f), an opaque sample (s), thermal grease (used to improve the thermal contact between the pyroelectric sensor and the sample) (g), the pyroelectric detector (p) and a backing environment (b). A solid sample is illuminated by a monochromatic modulated light beam with an angular frequency  $\omega$ , intensity  $I_0$  (W/m<sup>2</sup>) and wavelength  $\lambda$ . All thicknesses are taken into account.

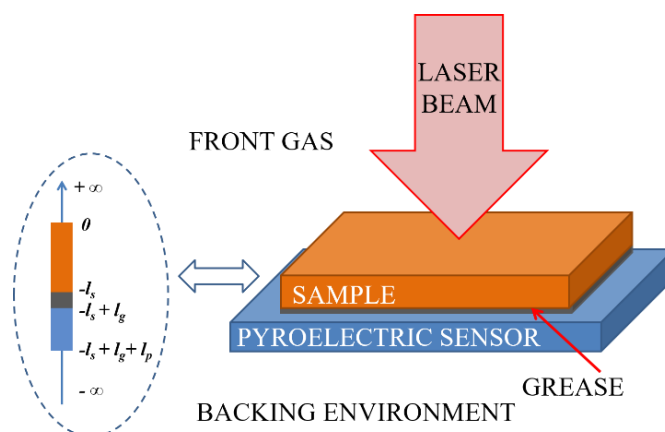


**Fig. 2.2.** Scheme of the PPE in back detection configuration with opaque sample

The light absorbed by the sample transforms into heat. Then this heat wave propagates from the sample to the pyroelectric sensor and creates a temperature field distribution in the sensor:

$$\langle T_p \rangle = \frac{l}{l_p} \int_{-(l_s+l_g)}^{-(l_s+l_g+l_p)} T_p(x) dx. \quad (2.3)$$

A potential difference  $\Delta\varphi$  between the sensor surfaces is produced by this temperature field and has the next form [38]:

$$\Delta\varphi = \frac{i\omega\tau_\varepsilon p l_p}{\varepsilon(1+i\omega\tau_\varepsilon)} \langle T_p \rangle e^{i\omega t}, \quad (2.4)$$

where  $\tau_\varepsilon$  is the electrical time constant,  $p$  the pyroelectric coefficient and  $\varepsilon = \varepsilon_0\varepsilon_r$  the dielectric constant of the pyroelectric.

As seen from figure 2.2. the system consists of five component:  $f$  – front gas,  $s$  – sample,  $g$  – thermal grease,  $p$  – pyroelectric detector,  $b$  – backing environment. An important requirement for this technique is the use of opaque samples. In case the sample is (semi)transparent, its surface is coated with carbon paint. As the thickness of the carbon covering is extremely small (less than 10  $\mu\text{m}$ ) we will not take into account its effect on the system. To find the solution for the whole system we need to apply to each component using the heat diffusion equation [38]:

$$\frac{\partial^2 T_i}{\partial x^2} - \frac{1}{D_i} \frac{\partial T_i}{\partial t} = 0, \quad (2.5)$$

where  $D_i$  is thermal diffusivity ( $i = f, s, g, p$  or  $b$ ). Therefore the general solution for this system has the next form [33]:

$$\begin{aligned} - \textit{front gas}: \quad T_f &= A e^{-\sigma_f x}; & x &\geq 0; \\ - \textit{sample}: \quad T_s &= B e^{\sigma_s x} + C e^{-\sigma_s x}; & -l_s &\leq x \leq 0; \\ - \textit{grease}: \quad T_g &= D e^{\sigma_g(x+l_s)} + E e^{-\sigma_g(x+l_s)} & -(l_s+l_f) &\leq x \leq -l_s;; \\ - \textit{detector}: \quad T_p &= F e^{\sigma_f(x+l_s+l_g)} + G e^{-\sigma_f(x+l_s+l_g)}; & -(l_s+l_g+l_p) &\leq x \leq -(l_s+l_g); \end{aligned} \quad (2.6)$$

- **backing environment:**  $T_b = H e^{\sigma_f(x+l_s+l_g+l_p)}$ ;  $x \leq -(l_s+l_f+l_p)$ .

$A, B, C, D, E, F, G, H$  are constants which can be found after taking into account the boundary conditions of temperature continuity and heat flux between layers. The boundary conditions of temperature continuity are written in the form:

$$\begin{aligned} T_f \Big|_{x=0} &= T_s \Big|_{x=0}; & T_s \Big|_{x=-l_s} &= T_g \Big|_{x=-l_s}; \\ T_g \Big|_{x=-(l_s+l_g)} &= T_p \Big|_{x=-(l_s+l_g)}; & T_p \Big|_{x=-(l_s+l_g+l_p)} &= T_b \Big|_{x=-(l_s+l_g+l_p)}; \end{aligned} \quad (2.7)$$

and for the heat flux

$$\begin{aligned} \frac{I_0}{2} + \kappa_f \frac{\partial T_f}{\partial x} \Big|_{x=0} &= \kappa_s \frac{\partial T_s}{\partial x} \Big|_{x=0}; & \kappa_s \frac{\partial T_s}{\partial x} \Big|_{x=-l_s} &= \kappa_g \frac{\partial T_g}{\partial x} \Big|_{x=-l_s}; \\ \kappa_g \frac{\partial T_g}{\partial x} \Big|_{x=-(l_s+l_g)} &= \kappa_p \frac{\partial T_p}{\partial x} \Big|_{x=-(l_s+l_g)}; & \kappa_p \frac{\partial T_p}{\partial x} \Big|_{x=-(l_s+l_g+l_p)} &= \kappa_b \frac{\partial T_b}{\partial x} \Big|_{x=-(l_s+l_g+l_p)}. \end{aligned} \quad (2.8)$$

The expression for the temperature distribution can be found by substituting (2.6) and (2.7) into (2.3)

$$\langle T_p \rangle = \frac{4I_0(1-R_s)b_{sf}}{2k_s l_p} \frac{1}{\sigma_s \sigma_p (1+b_{pg})(1+b_{gs})(1+b_{sf})} \left[ \frac{e^{\sigma_p l_p} + R_{bp} e^{-\sigma_p l_p} - (1+R_{bp})}{e^{\sigma_s l_s} \Lambda + R_{fs} e^{-\sigma_s l_s} \Sigma} \right], \quad (2.9)$$

where  $R_{12} = (b_{12} - 1)/(b_{12} + 1)$ , and  $b_{12} = e_1/e_2$  are the thermal effusivities ratio of layers,  $1, 2 = f, s, g, p, b$ ;  $R_s$  is the reflection coefficient of the sample. The constants  $\Lambda$  and  $\Sigma$  are defined as

$$\begin{aligned} \Lambda &= \left( e^{\sigma_p l_p} + R_{bp} R_{pg} e^{-\sigma_p l_p} \right) e^{\sigma_f l_f} + R_{gs} \left( R_{pg} e^{\sigma_p l_p} + R_{bp} e^{-\sigma_p l_p} \right) e^{-\sigma_g l_g}, \\ \Sigma &= R_{gs} \left( e^{\sigma_p l_p} + R_{bp} R_{pg} e^{-\sigma_p l_p} \right) e^{\sigma_f l_f} + \left( R_{pg} e^{\sigma_p l_p} + R_{bp} e^{-\sigma_p l_p} \right) e^{-\sigma_g l_g}. \end{aligned} \quad (2.10)$$

Now we are able to find the signal  $U$  produced in the photopyroelectric sensor which has the next form:

$$U = \frac{i\omega\tau_\varepsilon p l_p}{\varepsilon} \frac{4I_0(1-R_s)b_{sf}}{2k_s l_p} \frac{1}{\sigma_s \sigma_p (1+b_{pg})(1+b_{gs})(1+b_{sf})} \left[ \frac{e^{\sigma_p l_p} + R_{bp} e^{-\sigma_p l_p} - (1+R_{bp})}{e^{\sigma_s l_s} \Lambda + R_{fs} e^{-\sigma_s l_s} \Sigma} \right]. \quad (2.11)$$

In order to avoid the electronic influence in the final result, a normalization procedure is proposed, which consists of dividing the signal obtained by equation (2.11) by the signal of a bare pyroelectric. In order to do this, it is necessary to find out the temperature field in the sensor without the sample  $\langle T_p \rangle_{bare}$ . When a sensor is directly

illuminated, we have  $e^{\sigma_s l_s} \sim e^{-\sigma_s l_s} \sim 1$ . Therefore, the denominator in the square brackets of the equation (2.8) is reduced, hence we have

$$\langle T_p \rangle_{bare} = \frac{4I_o (1-R_p) b_{pf}}{2k_p l_p} \frac{1}{\sigma_p \sigma_p} \frac{1}{(1+b_{pg})(1+b_{gp})(1+b_{pf})} \left[ \frac{e^{\sigma_p l_p} + R_{bp} e^{-\sigma_p l_p} - (1+R_{bp})}{\Lambda + R_{fp} \Sigma} \right]. \quad (2.12)$$

The photopyroelectric signal in this case is

$$U_{bare} = \frac{i\omega \tau_\varepsilon p l_p}{\varepsilon} \frac{4I_o (1-R_p) b_{pf}}{2k_p l_p} \frac{1}{\sigma_p \sigma_p} \frac{1}{(1+b_{pg})(1+b_{gp})(1+b_{pf})} \left[ \frac{e^{\sigma_p l_p} + R_{bp} e^{-\sigma_p l_p} - (1+R_{bp})}{\Lambda + R_{fp} \Sigma} \right]. \quad (2.13)$$

By dividing (2.11) over (2.13) the normalized PPE signal will have the following form

$$U_n = \frac{U}{U_{p\ bare}} = \frac{(1-R_s)(1+b_{gp})(1+b_{pf})}{(1-R_p)(1+b_{gs})(1+b_{sf})} \left[ \frac{\Lambda + R_{fp} \Sigma}{e^{\sigma_s l_s} \Lambda + R_{fs} e^{-\sigma_s l_s} \Sigma} \right] \quad (2.14)$$

### 2.2.1 Experimental conditions for experimental setups

Frequency scan at a **fixed temperature**. In order to apply the theory described in the previous section to our experimental setups we need to introduce some additional conditions. As we are going to work with a thermally thick LiTaO<sub>3</sub> sensor, we can consider  $e^{-\sigma_p l_p} \simeq 0$ . Then we will not take into account the thickness of the thermal grease layer because its thickness is very small hence  $l_g = 0$ ,  $e^{-\sigma_g l_g} \sim e^{\sigma_g l_g} \simeq 1$ . Finally, the front gas and the backing environment are going to be the same, so  $f = b$ . Besides, it is well known that the gases possess low effusivity values so we can

consider  $R_{fp} \sim R_{fs} \sim -1$  and  $\frac{(1+b_{pf})}{(1+b_{sf})} \sim e_p / e_s$ . Given these approximations and after some calculations, (2.14) is modified to obtain

$$U_n = 2 \frac{e_p}{e_p + e_s} e^{-\sigma_s l_s} \quad (2.15)$$

Consider  $U_n$  as a function of the illumination frequency for the case study of Ni as a sample and LiTaO<sub>3</sub> as sensor, for which  $D_s = 22 \text{ mm}^2/\text{s}$ ,  $e_s = 19000 \text{ Wm}^{-2}\text{K}^{-1}\text{s}^{1/2}$ ,  $e_p = 3750 \text{ Wm}^{-2}\text{K}^{-1}\text{s}^{1/2}$ ,  $l_s = 1 \text{ mm}$ ,  $R_s = R_p = 0$ , and let's represent equation (2.14) as a function of the square root of the modulation frequency (see fig. 2.3) [33]. As it is a complex number, we will represent both the natural logarithmic of the normalized amplitude and phase.

The natural logarithm of the amplitude and the phase can be extracted to get

$$\begin{aligned} \ln(U_n) &= \ln\left(2e_p / (e_s + e_p)\right) - \sqrt{\pi f / D} l_s; \\ \text{phase}_n &= -\sqrt{\pi f / D} l_s; \end{aligned} \quad (2.16)$$

In figure 2.3 we can highlight three different frequency regions:

**Useless zone.** At low frequencies the sample is not thermally thick, and there is neither linearity nor parallelism.

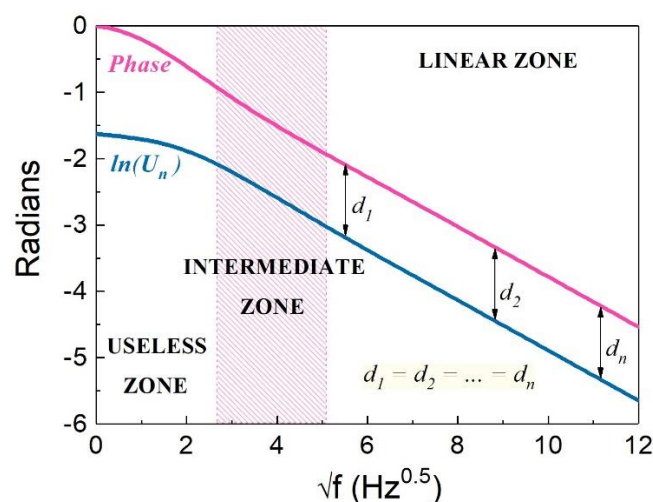


**Fig. 2.3.** Phase and natural logarithm of the normalized PPE signal as a function of the square root of the frequency [33]

**Intermediate zone.** Here linearity and parallelism are beginning but still impossible to obtain good enough information about the thermal properties of the sample.

**Linear zone.** This region has a fairly good parallelism between amplitude and phase to retrieve proper information on the sample properties.

As expected from (2.16), in the last zone, the amplitude and the phase are linearly depending on  $\sqrt{f}$  with the same slope  $m$ , where the thermal diffusivity  $D$  of the sample can be obtained

$$D_s = \frac{\pi l_s^2}{m^2}. \quad (2.17)$$

Also, one detail should nevertheless be emphasized. Since the presence of the thermal grease is not taken into account, we only have a sample-sensor configuration. If we introduce nonzero thickness for grease, the slopes of the curves on figure 2.3 increase and, as a consequence, the thermal diffusivity of the sample will be underestimated [39]. To solve the issue induced by the coupling grease, the use of a transparent pyroelectric sensor and transparent thermal grease has been proposed in combination with a self-normalization procedure [40]. In work [32], possible effects which might affect the linearity and parallelism of the curves and the value of the thermal diffusivity as a whole are described, namely electronic noise, possible influence of a parasitic light, piezoelectric contribution of the sensor and others. It is worth noting that our experimental setups are designed to work under conditions in which the influence of these effects can be neglected.

**Continuous temperature measurements.** Once we have already obtained the values of diffusivity and effusivity at  $T_{ref}$  by using a linear fitting of the experimental data using equations (2.16), we proceed to obtain thermal diffusivity and thermal effusivity as a function of temperature by using the following equations obtained in [41, 42]

$$D(T) = \left[ \frac{1}{\sqrt{D_{ref}}} - \frac{\Delta(T)}{l_s \sqrt{\pi f}} \right]^{-2}; \quad e(T) = e_p(T) \left( \frac{1 + (e_{ref} / e_p(T_{ref}))}{\exp[\Delta''(T)]} - 1 \right), \quad (2.18)$$

where  $\Delta(T) = \psi(T) - \psi(T_{ref})$  is the normalized phase;  $\Delta'(T) = \ln U(T) - \ln U(T_{ref})$  is the normalized amplitude;  $\Delta''(T) = \Delta'(T) - \Delta(T)$ . It is also possible to obtain the heat capacity  $c_p(T)$  and the thermal conductivity  $\kappa(T)$  data, using the next interrelations

$$c_p(T) = \frac{e(T)}{\rho \sqrt{D(T)}}, \quad (2.19)$$

$$\kappa(T) = e(T) \sqrt{D(T)}. \quad (2.20)$$

where  $\rho$  is the density of the sample under study. As seen from these four equations the thermal diffusivity depends solely on the phase of the PPE signal while the three other quantities (conductivity, effusivity and specific heat) are obtained by using both the amplitude and the phase of the pyroelectric signal. This is an important advantage, because the performance of a continuous temperature run enables to obtain the temperature evolution of all thermal parameters. In spite of this possibility, at the same time two undesirable problems can appear. From the experimental point of view the phase is always more stable in time than the amplitude of the signal due to laser instabilities or electronic problems; thus, in general, the thermal diffusivity curves are less noisy than the others. A second problem which sometimes arises has to do with the use of equations (2.19 and 2.20) to extract the thermal parameters of a phase transition of a particular material, around a critical point. It might happen that the combination of amplitude and phase to obtain specific heat and thermal conductivity gives some artifacts in the shape of these last variables in the critical region, making it impossible to retrieve reliable curves of  $e(T)$ ,  $c_p(T)$ ,  $\kappa(T)$ . In these cases, the physics of the transition is more complicated than the model used and, so far, there is no theory developed to cover those cases.

### 2.3. Description of experimental setups

In this section we consider the experimental setups which have been used in this work.

#### 2.3.1. At room temperature as a function of frequency

In order to perform the measurement of the sample under study as a function of the modulation frequency in the back-detection configuration, the following has been done. We have used a thermally thick lithium tantalate slab with metallic electrodes Ni-Cr as a pyroelectric sensor which could be connected to a *lock-in* amplifier. The thermal contact between the sample and the sensor has been provided by a silicon thermal grease a few microns thick. The setup is depicted on fig. 2.4 schematically.

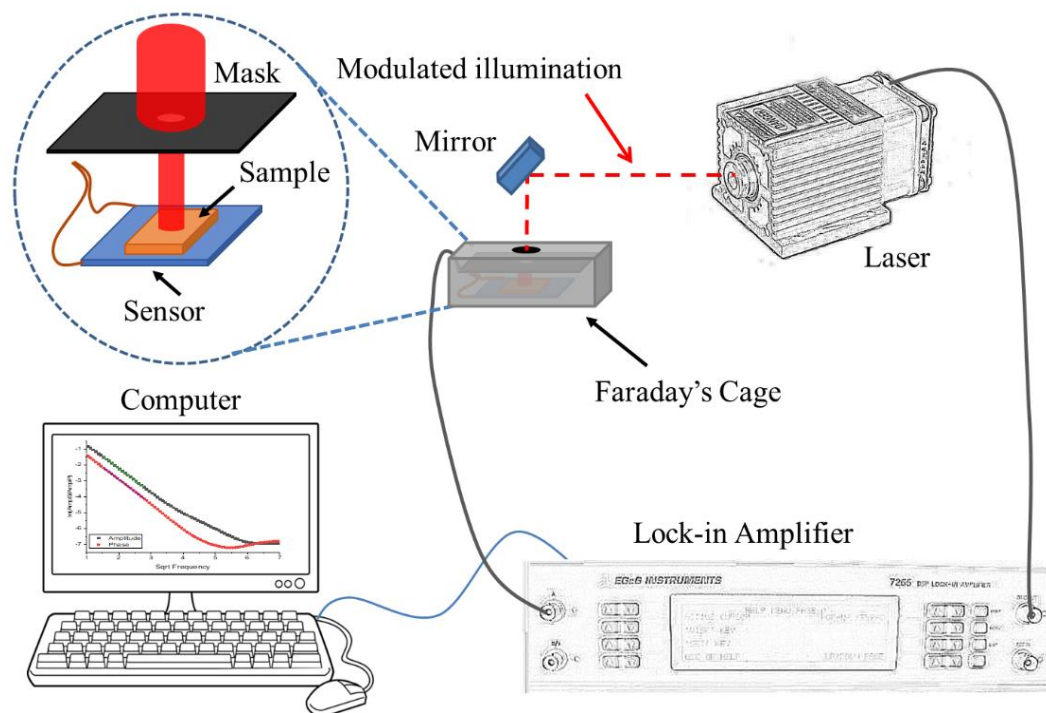


**Fig. 2.4.** Working scheme of frequency measurements in BPPE configuration at room temperature. Lock-in Amplifier: 7265 Dual Phase DSP

An opaque and thermally thick sample is illuminated by an about 5mW low power modulated diode laser beam at a wavelength  $\lambda = 632\text{nm}$ . In that way the thermal energy deposited on the sample is small and also the induced temperature

gradient. This will help to quickly achieve thermal equilibrium when the temperature is changed and be able to do very slow temperature runs with a high signal to noise ratio. This is because the temperature oscillations in the sample are of the order of 1 mK, while the dc contribution is estimated at about 2 mK [49].

The photopyroelectric signal was processed by a *lock-in* amplifier in the current mode. The *lock-in* amplifier performs two very important functions. It modulates the illumination frequency of the laser; at the same time, it amplifies and processes the signal from the pyroelectric sensor whose frequency is the same as the modulation of the laser. The working principle of the amplifier is based on a bandpass filter synchronized with the frequency of the PPE signal. This line will make the frequencies outside the bandwidth automatically filtered. Moreover, it provides gain, amplifying the received signal [44].

In order to avoid unwanted disturbance in an electrical signal of the same frequency as the one of the collected signal, the *lock-in* also has a variable integration time. A Faraday's cage connected to the earth can be used to prevent external electronic noise of the environment. The *lock-in* amplifier sends the PPE signal to a computer for further analysis. To avoid possible parasitic light effects (which appear when some amount of radiation falls on the pyroelectric surface), a matte black mask with a hole smaller than the sample size has been used [33].

In fig. 2.5 we present a frequency scan at room temperature for a layered  $\text{AgInP}_2\text{Se}_6$  crystal with the surface parallel to the layers. Three different regions can be distinguished: the first one is the *useless zone* without linearity and parallelism, the second region *with linearity* in a range about 2-8 Hz where the thermal properties of sample can be extracted and the last one is the region where the generated pyroelectric signal also has the *contribution of a piezoelectric component*. When the impact of the piezoelectric contribution is very significant and it masks the region with linearity, a multiparametric fitting must be applied as described in [44] to retrieve the thermal diffusivity from such kind of curves.

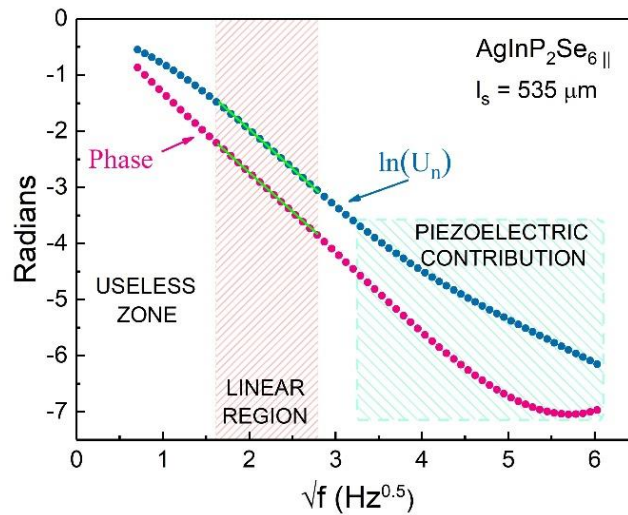


**Fig. 2.5.** Frequencies scan at room temperature for 2D layered crystal  $\text{AgInP}_2\text{Se}_6$

### 2.3.2. Temperature measurements between 18K and 325K

After the measurements performed at room temperature we increase the temperature range of the research to perform the measurements as a function of temperature. In this regard we should use the cryostat in cooling/heating mode. Depending on the temperature interval we were interested in, two different cryostat systems have been used: a closed cycle He cryostat for extremely low temperatures and a liquid  $\text{N}_2$  cryostat if we are interested in ranges higher than room temperature.

First of all, we consider the experimental setup which works in 18 - 325 K temperature range. A modified conventional closed cycle He cryostat with a vertical configuration by Janis Research Company has been used. Temperature control has been performed by using of a rhodium/iron temperature sensor RF-100T/U.

The main parts of the cooling system are given below:

- **Helium Compressor:** provides a supply of high-pressure helium gas to the cooling head.
- **Cooling Head:** expands the helium gas to cool the sample holder.

- **Lines for He gas:** these lines are connected between the compressor and cooling head supply and return fitting, and transfer the helium gas between the two components.
- **Internal chamber:** which is screwed to the cooling head. It includes an evacuation valve, safety pressure relief, electrical feedthroughs, and a clamped vacuum seal for easy access to the sample space.
- **External chamber:** which is screwed to the cooling head first stage. It is used to intercept room temperature radiation before it reaches the sample, allowing the lowest possible sample temperature to be achieved.
- **Temperature controller:** needful for monitoring and controlling the sample temperature.

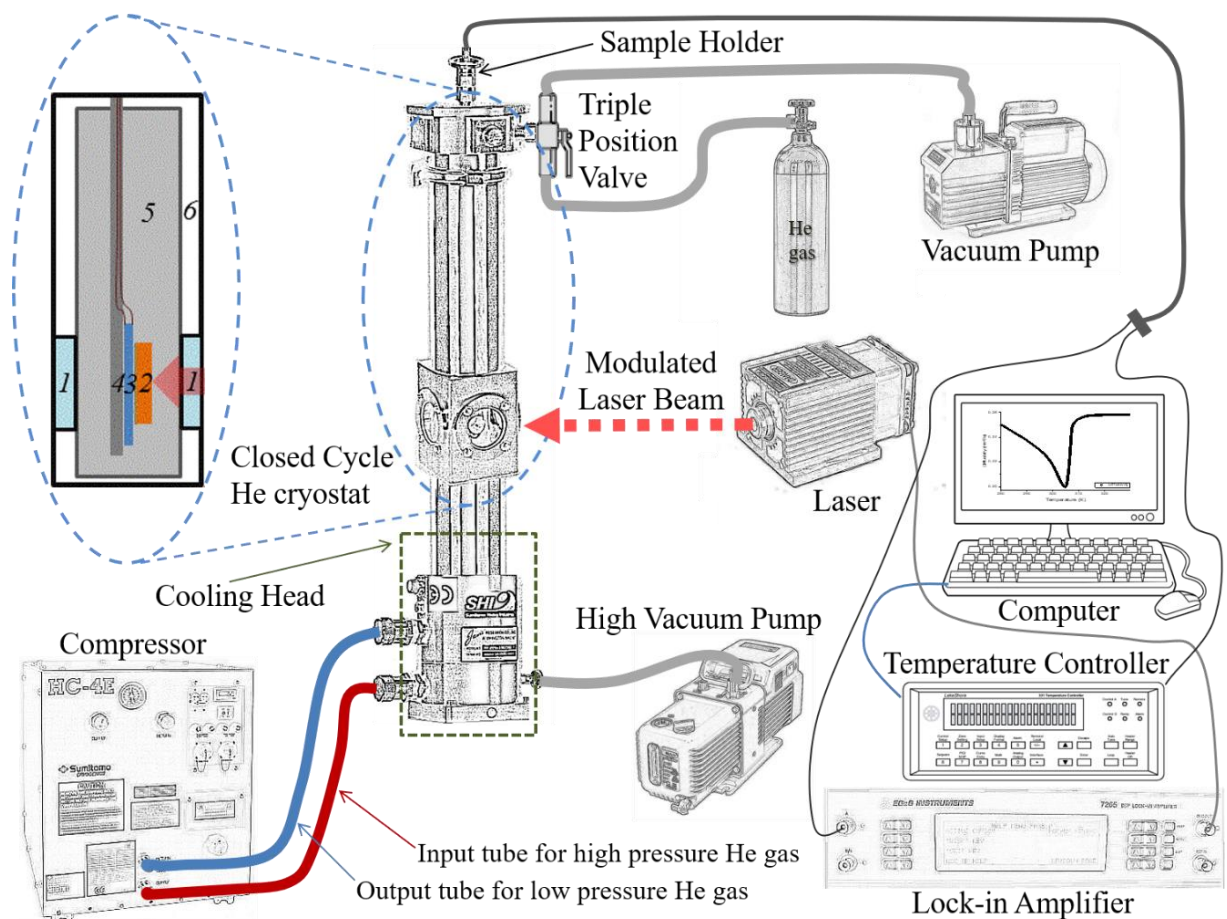


**Fig. 2.6.** Scheme of experimental setup for measurements as a function of temperature in the range 18 - 325 K. Scheme of the Closed cycle He cryostat in vertical configuration: 1 – optical window; 2 – sample; 3 – pyroelectric sensor; 4 – sample holder; 5 – internal chamber; 6 – external chamber. Lock-

in Amplifier: 7265 Dual Phase DSP. Temperature Controller: Lake Shore 332

The cryostat is mounted on a massive table residing on pumped air pillows which eliminate possible vibration of the system which might introduce a piezoelectric component in the PPE signal [33]. High vacuum turbomolecular pump creates a high vacuum (HV) (about  $5 * 10^{-6}$  mbar) in the external chamber, isolating the internal chamber from the external environment. The stable gas condition inside of the chamber provides a homogeneous distribution of gases and temperature. In order to attain it we introduce *He-gas* inside the internal chamber. A triple position valve provides alternate access to the internal camera. The scheme of experimental setup for measurements in the temperature range 18 - 325 K is depicted in fig. 2.6. This experimental setup has an important advantage as there is no refrigerant consumption because here a closed loop of helium gas is compressed and expanded, based on the Gifford-McMahon thermodynamic cycle. This system permits to work with very small changes in temperature. Cooling and heating rates can be down to 2 mK per minute for high resolution runs.

### ***2.3.3. Temperature measurements between 80 K and 350 K***

To perform high temperature measurements we have used a liquid nitrogen cryostat. The working scheme of this setup is presented on fig. 2.7.

Work principle of the N<sub>2</sub> cryostat can be described as follows. The sample holder is placed in an internal chamber in a vertical position. The cooling process is performed through a reservoir placed on top of a central camera and filled by liquid nitrogen. Liquid nitrogen flows through the capillaries into the sample space and evaporates on the heat exchanger. The nitrogen gas temperature is controlled by the electric power of the heat exchanger. During the measurements it is important to optimize the flow by a controlling valve to obtain a smooth temperature control, for which the PID (proportional-integral-derivative) of the controller has been optimized.

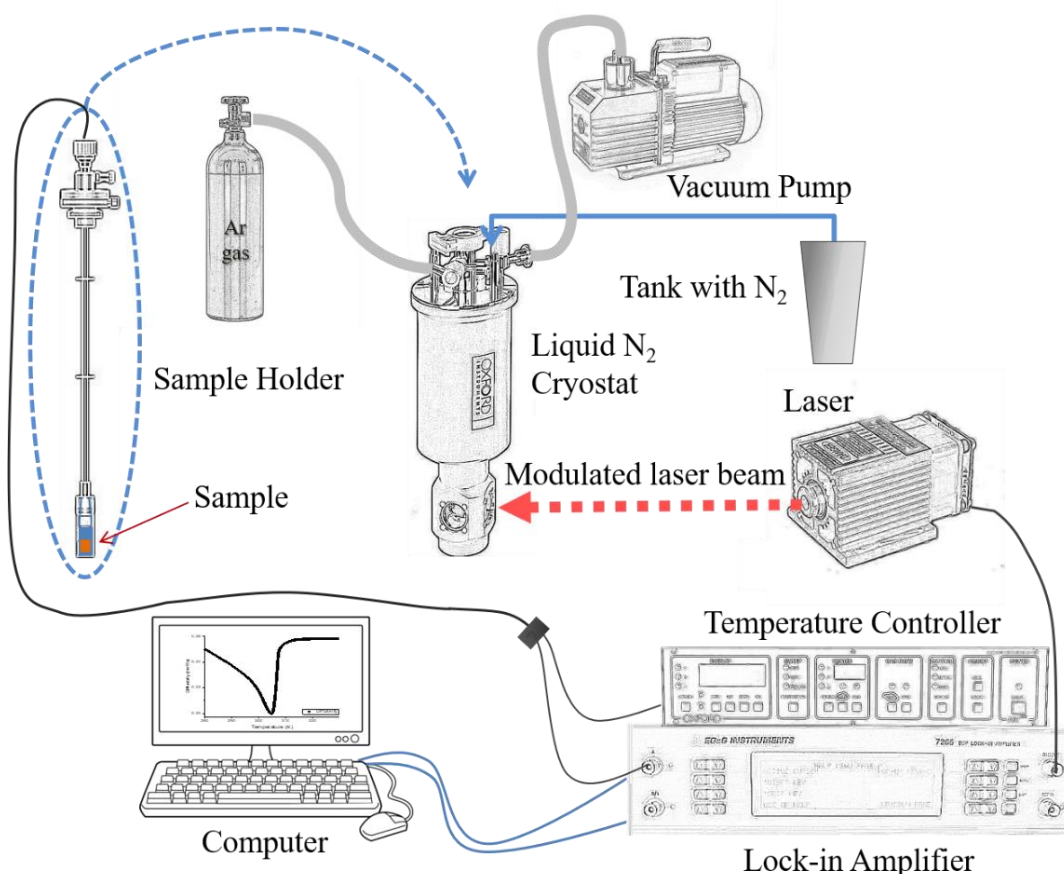


**Fig. 2.7.** Scheme of experimental setup for measurements as a function of temperature in the range 80 - 350 K. Temperature Controller: Oxford Instruments Mod ITC 502. Lock-in Amplifier: 7265 Dual Phase DSP. Cryostat: Oxford Instruments Optistat<sup>DN</sup>

Thermal contact in the cryostat occurs by means of the gas which surrounds the sample and acts as a heat exchanger. The minimum temperature possible to achieve is 78 K, due to the use of liquid nitrogen as a refrigerant. The temperature ramps are made via the temperature controller with an accuracy of  $\pm 0.01$  K in temperature range between 78 K and 200 K and  $\pm 0.1$  K if we measure between 200 and 400 K. The system permits to work with temperature rates from 100 mK/min measuring in a wide temperature range and down to 2mK/min for high resolution runs. The nitrogen hold time is approximately 6-10 hours (depending on the temperature) before refilling is required, nevertheless the nitrogen can be refilled as often as desired without the need to return the system to the initial conditions. The air inside the internal chamber is replaced by the inert gas argon. In order to isolate the

internal chamber from the environment it is important to make vacuum in the external chamber which acts as a thermal insulator and promotes the optimization of the temperature control. In our case, we perform vacuum with a rotary pump, reaching approximately  $10^{-3}$  mbar [33].

## Chapter 3. Phase transitions and critical phenomena in ferroelectrics

This chapter is dedicated to the critical behavior and phase transition (PT) theory applied to the particular case of ferroelectrics, namely the classical Landau theory for ferroelectrics as well as the modern theory in the framework of the renormalization group theory.

### 3.1. Landau's classical theory of phase transitions for ferroelectric transitions

Ferroelectrics are promising materials due to the spontaneous electric polarization, polarization switching effect, hysteresis loop and polarization absence for temperatures higher than  $T_c$ . In order to understand the physical nature of ferroelectrics, it is interesting to explore the phase transition phenomena in these materials, the electron-phonon interactions effects and other physical mechanisms and properties. The phenomenological theory of ferroelectrics and the phase transition theory have been developed by Landau, Khalatnikov, Ginzburg, Lifshitz, Levanyuk, Strukov, Devonshire and others [45, 46, 47, 48, 49, 50, 51, 52, 53, 54, 55].

The order parameter  $\eta$  is a quantity characterizing the transition which arises from symmetry breaking.  $\eta=0$  above the critical temperature (the one at which the PT takes place) and  $\eta \neq 0$  below. In a first order PT the order parameter will change in an abrupt way while in a second order/continuous PT, it will change in a continuous way (fig. 3.1). In these transitions, as opposed to the first order ones, there will be no latent heat and no hysteresis in the variation of the physical variables. As follows from the Landau theory the order parameter  $\eta$  has the same transformation properties as polarization vector  $\vec{P}$ .

Let's consider a one-component order parameter and expand the thermodynamic potential density in the vicinity of the phase transition for an isotropic medium or a crystal with cubic symmetry. It can be written as a standard Taylor's series form [56]

$$\phi = \phi_0 + \frac{A}{2}P^2 + \frac{B}{4}P^4 + \frac{C}{6}P^6 + \dots + \frac{\delta}{2}(\vec{\nabla}P)^2 + \frac{g}{2}(\vec{\nabla}P)^2 + \lambda P^2(\vec{\nabla}P)^2 + \dots, \quad (3.1)$$

where  $\phi_0$  is the free energy density in the paraelectric phase.

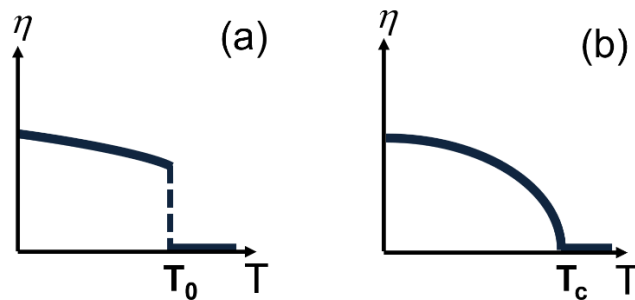


**Fig. 3.1.** Order parameter  $\eta$  as a function of temperature  $T$ : first order PT (a), second order PT (b)

The thermodynamic potential density for proper uniaxial ferroelectrics  $\text{Sn}_2\text{P}_2(\text{Se}_x\text{S}_{1-x})_6$  type can be written in the next form [57]

$$\phi = \phi_0 + \frac{\alpha}{2}P^2 + \frac{\beta}{4}P^4 + \frac{\gamma}{6}P^6, \quad (3.2)$$

where  $\alpha = \chi(T - T_c)$ ,  $\chi$  is related to the Curie-Weiss constant,  $T_c$  is the transition temperature (critical temperature),  $\beta$ ,  $\gamma$  and  $\delta$  are phenomenological coefficients which do not depend on temperature and are positive (negative  $\beta$  is an evidence of a first order PT). The ferroelectric-paraelectric PT temperature is the so called Curie temperature; hence, all properties depend on the temperature difference of the crystal from  $T_c$ . Some particular values of certain phenomenological coefficients will involve particular phase transitions. For a tricritical point (tricritical points (TCP) separating continuous and discontinuous symmetry breaking transitions)  $\alpha = 0$  and  $\beta = 0$ , while for a Lifshitz point  $\alpha = 0$  and  $\delta = 0$ . In ferroelectric materials, a Lifshitz point splits two regions in the phase diagram: one with a direct second order PT from the paraelectric to the ferroelectric phase and another one in which there is a second order PT from the paraelectric phase to an incommensurate one (IC) at  $T_i$  and then a first order PT from the IC phase to the ferroelectric phase at  $T_c$ .

The classical theory also includes the possibility of the coupling of the order parameter to some other variables, such as deformation, which is useful in the case of uniaxial ferroelectrics, such as [57]

$$\phi = \phi_0 + \frac{\alpha}{2} P^2 + \frac{\beta}{4} P^4 + \frac{\gamma}{6} P^6 + \frac{1}{2} c_{ijkl} u_{ij}^2 + r_{ijkl} u_{ij} P^2, \quad (3.3)$$

where  $c_{ijkl}$  is the elastic module matrix,  $u_{ij}$  is the deformation tensor,  $r_{ijkl}$  is the electrostriction coefficient, and elements of higher order are neglected. This is a short version of the Landau-Khalatnikov potential which includes even more terms [48, 57].

In order to obtain a measurable quantity such as specific heat, the free energy must be minimized with respect to the order parameters, in order to obtain the equilibrium value of the order parameter in the ferroelectric phase, and the isobaric heat capacity of the body at  $T < T_c$  and taking into account expression (3.3) will have the next form [57]

$$C_p = -T \left( \frac{\partial^2 \phi}{\partial T^2} \right)_p = C_p^0 + \frac{\alpha^2}{2\beta'} \frac{T}{\sqrt{1-4At}}, \quad (3.4)$$

where  $C_p^0$  is the heat capacity above the Curie point,  $t = \frac{T-T_c}{T_c}$  is reduced temperature.

$$\beta' = \beta - \frac{2r_{ijkl}}{c_{ijkl}^2} \text{ and } A = \frac{\gamma\alpha}{\beta'^2}. \quad (3.5)$$

So equation which will express the anomalous part of the heat capacity takes the form

$$\Delta C_p = \frac{\alpha^2}{2\beta'} \frac{T}{\sqrt{1-4At}}. \quad (3.6)$$

Unfortunately this approach (with or without couplings) can not be applied for most of the materials. In a real physical system, when  $t$  ends to zero, fluctuations of the order parameter start to appear which are stronger and stronger as  $t$  decreases till

they dominate the transition. This does not lie within Landau's theory, where it is established that the order parameter remains homogeneous within the material, and is the main cause of the deviations from it [51, 47].

The phenomenological Landau theory is valid in a range of reduced temperature  $t$  out of which the first fluctuational correction can be used and within which a new approach must be developed. This criterion for the applicability of Landau theory is often referred to as the Ginzburg criterion  $E_{LG}$  [51]. In addition, it is very important to take into account that the range must not be larger than the correlation length  $\xi$  which shows how far fluctuations of the order parameters are sensed in the material or, in another way, the size of those fluctuations. Thus, the Ginzburg criterion can be defined as follows [51]

$$E_{LG} = \frac{\left| \int_V d^d r G(r) \right|}{\int_V d^d r \eta(r)^2}, \quad (3.7)$$

where  $V$  is taken to be the correlation volume  $V = \xi(T)^d$ ,  $G(r)$  is the two-point correlation function,  $d$  is the dimensionality of the system ( $d = 1, 2, 3, 4, \dots$ ), and  $\eta(r)$  takes into account that the order parameter is allowed to vary in space  $\eta = \eta(r)$ .

Some theoretical works [52, 56] have been used to extend Landau's theory including first-order fluctuations of the order parameter, and the dependence of specific heat can be described as

$$\Delta c_p \sim t^{-1/2}. \quad (3.8)$$

But in ferroelectrics, in general, this approach can not be applied. In the case of uniaxial ferroelectric materials, the spatially inhomogeneous polarization distributions are closely related to the appearance of a macroscopic electric field, which can affect on fluctuations [56]. In fact, dipole-dipole interaction decreases these fluctuations effects and the singularity in specific heat has the next behavior [52, 56]

$$\Delta c_p \sim \ln t. \quad (3.9)$$

This logarithmic correction to the classical Landau theory has proven to be very useful for various uniaxial ferroelectrics. Also, it is possible to use the combination of eqs. 3.8 and 3.9 when the attenuation of fluctuations is small enough and only a small logarithmic correction is needed

$$\Delta c_p \sim t^{-1/2} |\ln t|^b \quad (3.10)$$

with  $\frac{1}{10} < b < \frac{1}{3}$  [82].

Defects also could play an essential role in ferroelectric phase transitions which was confirmed in work [58]. In general, defects introduce a certain rounding of the anomalies but in [59, 60, 61] have established that in the case of charged defects in ferroelectrics they may lead to stronger anomalies as they can induce long-range perturbations of the order parameter. The anomaly of the specific heat will have the form

$$\Delta c_p \sim t^{-3/2}. \quad (3.11)$$

For magnetic systems, the Landau classical theory does not work properly, Landau theory only describes the universal behavior of a system. Thus a modern theory of critical behavior has been developed, pursuing new ideas and establishing new approaches.

### **3.2. Modern Theory of critical behavior. Fluctuations effects**

Scaling analysis within the framework of renormalization group theory (RG) has predicted that the critical behavior of second order phase transitions in the near vicinity to  $T_c$  is characterized by a set of critical exponents associated with different physical properties, with interrelated values [62]. RG theory is effective in the study of materials with phase transitions owing to the following advantages [63]:

- It explains the variety of power laws at critical points and near them;
- It explains the values of the leading thermodynamic and correlation exponents;

- It clarifies why and how the classical values are not correct;
- It gives the understanding of universality with nontrivial exponents;
- It allows to understand the breakdown of universality and scaling under certain circumstances.

In this critical region the specific heat often presents a singularity following the law

$$c_p \sim A^\pm |t|^{-\alpha}, \quad (3.12)$$

where  $t$  is the reduced temperature,  $A^+$  and  $A^-$  are critical amplitudes above and below  $T_c$  respectively. The critical amplitudes  $A^+$  and  $A^-$  are nonuniversal, but their dimensionless ratio  $\frac{A^+}{A^-}$  is universal.

However,  $c_p$  is not the only physical magnitude with such behavior. In magnetic systems, for instance, the spontaneous magnetization ( $M_s$ ), the inverse of initial magnetic susceptibility ( $\chi_0^{-1}$ ) and the critical isotherm ( $M(H)$  at  $T = T_c$ ) fulfill analogous equations with different critical exponents.

$$M_s(T) \sim |t|^\beta, \quad (T < T_c), \quad (3.13)$$

$$\chi_0^{-1} \sim |t|^\gamma, \quad (T > T_c), \quad (3.14)$$

$$M(H) \sim H^{\frac{1}{\delta}}, \quad (T = T_c). \quad (3.15)$$

The following scaling laws give the relations among the critical exponents [56, 64]

$$\alpha + 2\beta + \gamma = 2, \quad (3.16)$$

$$\delta = 1 + \gamma/\beta. \quad (3.17)$$

Different sets of values of those exponents correspond to different models called universality classes which have been theoretically developed taking as a starting point a particular form of the Hamiltonian describing the physical system. The renormalization group theory predicts the particular values of these critical exponents [65, 66, 67].

The particular values of the critical exponents and parameters are contained in table 3.1 for a mean-field model, an isotropic 3-dimensional Heisenberg model, a planar 3 dimensional XY model and a uniaxial 3-dimensional Ising model, referring to the ordering of the spins and the number of spin components needed to describe it. Mean-field model implies long-range order interactions, equivalent to a Landau approach while Heisenberg, Ising and 3D XY models correspond to short range interactions. A strong theoretical effort has been developed for magnetic systems (e.g. Landau theory is not valid for a system whose specific heat diverges to infinity) but also for many other systems.

Table 3.1

Main universality classes for magnetic systems [65, 66, 67]

<i>Universality class</i>	$\alpha$	$\beta$	$\gamma$	$\delta$	$\frac{A^+}{A^-}$	<i>Interaction range</i>
Mean-field Model	0	0.5	1.0	3.0	-	Long range
3D-Ising	0.11	0.33	1.24	4.76	0.52	Short range
3D-XY	-0.014	0.34	1.30	4.82	1.06	Short range
3D-Heisenberg	-0.134	0.36	1.39	4.86	1.52	Short range

Many scientific papers are devoted to universality classes [68, 69, 70, 71, 72, 73, 74, 75, 76, 77, 78, 79]. In particular, for ferroelectric systems, the theoretical framework of the different universality classes which might appear depending on the properties of the Hamiltonian has also been developed [69, 70, 80, 81, 82, 83, 84]. Besides  $c_p$ , the equivalent magnitudes to study their critical behavior are the spontaneous polarization  $P_s$  (eq. 3.18) and the inverse of dielectric susceptibility  $\chi^{-1}$  (eq. 3.19). Between the values of these critical exponents there exists a relation established by scaling theory which is called Rushbrooke's scaling law and has the form of eq. 3.16. The values of the universality classes found so far for ferroelectric systems are listed in table 3.2 [69, 80, 81, 82, 83, 84].

$$P_s(T) \sim |t|^\beta, (T < T_c), \quad (3.18)$$

$$\chi^{-1} \sim |t|^\gamma, (T > T_c), \quad (3.19)$$

Table 3.2

Values of the critical exponents for ferroelectrics. S: usual critical point isotropic short-range interaction, U with uniaxial dipolar interactions, T tricritical point, L Lifshitz point. Those exponents with an asterisk \* have a logarithmic correction with exponent  $x$ .  $m$  is the number of components of the order parameter [69, 80, 81, 82, 83, 84].

	Universality class						
	Mean- field model	S	U	T	UT	L, m=1	L, m=2
$\alpha$	0	$\frac{1}{6}$	0*	$\frac{1}{2}$ *	$\frac{1}{2}$	$\frac{1}{4}$	$\frac{1}{3}$
$\beta$	$\frac{1}{2}$	$\frac{1}{3}$	$\frac{1}{2}$ *	$\frac{1}{4}$ *	$\frac{1}{4}$	$\frac{1}{4}$	$\frac{1}{6}$
$\gamma$	1	$1\frac{1}{6}$	1*	1*	1	$1\frac{1}{4}$	$1\frac{1}{3}$
$x$	-	-	$\frac{1}{3}$	$\frac{1}{3}$	-	-	-
	<b>L, m=3</b>	<b>LT, m=1</b>	<b>LT, m=2</b>	<b>UL, m=1</b>	<b>UL, m=2</b>	<b>ULT, m=1</b>	<b>ULT, m=2</b>
$\alpha$	$\frac{5}{12}$	$\frac{9}{14}$	$\frac{31}{40}$	$\frac{1}{6}$	$\frac{1}{4}$	$\frac{1}{2}$ *	$\frac{19}{48}$
$\beta$	$\frac{1}{12}$	$\frac{1}{7}$	$\frac{3}{80}$	$\frac{1}{3}$	$\frac{1}{4}$	$\frac{1}{4}$ *	$\frac{13}{48}$
$\gamma$	$1\frac{5}{12}$	$1\frac{1}{28}$	$1\frac{3}{40}$	$1\frac{1}{6}$	$1\frac{1}{4}$	1*	$1\frac{1}{16}$
$x$	-	-	-			$\frac{1}{10}$	$\frac{1}{8}$

The ratios of the critical amplitudes  $\frac{A^+}{A^-}$  for specific heat for ferroelectric systems are not included because it is very difficult to predict those values within the framework of the RG theory. However, the analysis of those critical amplitudes [85] revealed that, for the L class ( $m = 1$ ) in first-order approximation, it is 0.30 and rises up to 0.35 in second-order approximation. On the other hand, in the Gaussian approximation (Gaussian approximation allows fluctuations about the spatially uniform mean-field, but assumes, in effect, that the fluctuations are distributed normally about the uniform mean-field; in this approximation, the fluctuations turn out to be non-interacting i.e. independent random variables [63]), at a Lifshitz point with long-range interactions this value is 0.25, while if they are neglected, it is increased to 0.42 [85].

It is worth noting that the particular values for critical exponents within a certain universality class might be quite different depending on the particular mathematical methods used to obtain it. For instance, some authors [86, 87, 88] have obtained the values of critical exponent smaller than the ones given in table 3.2.

In addition, it should be mentioned that when the modern treatment of critical behavior theory is applied, fully taking into account the contribution of fluctuations till  $t \rightarrow 0$ , both branches of the experimentally measured specific heat anomaly (paraelectric as well as ferroelectric) should be fitted by the well-known equation

$$c_p = B + Ct + A^\pm |t|^{-\alpha} \left(1 + E^\pm |t|^{0.5}\right) \quad (3.20)$$

where  $\alpha$ ,  $A^\pm$ ,  $B$ ,  $C$  and  $E^\pm$  are adjustable parameters. Superscripts  $^+$  and  $^-$  stand for  $T > T_c$  and  $T < T_c$ , respectively. The linear term represents the background contribution to the specific heat, while the last term represents the anomalous contribution at the second order PT. The factor under parenthesis is the correction to scaling that represents a singular contribution to the leading power as known from theory and experiments [89, 90] but which must be small and which is not always necessary and can be neglected. Scaling laws require that there is a unique critical exponent  $\alpha$  for both branches and rigorous application states that constant  $B$  needs also be the same

[91]. These conditions have sometimes been relaxed in literature due to the difficulty of obtaining good fittings to the experimental data with those constraints, but this only makes the interpretation of results more complicated. Strict application of scaling theory must respect these rules.

### 3.3. Critical behavior studies of $(\text{Pb}_x\text{Sn}_{1-x})_2\text{P}_2(\text{Se}_y\text{S}_{1-y})_6$ uniaxial ferroelectrics prior to this work

#### 3.3.1. $\text{Sn}_2\text{P}_2(\text{Se}_y\text{S}_{1-y})_6$

In calorimetric investigations of  $\text{Sn}_2\text{P}_2\text{S}_6$  and  $\text{Sn}_2\text{P}_2\text{Se}_6$  compounds performed by Vysochanskii and co-workers [92], the first fluctuational correction has been found of the anomalous part of heat capacity in the paraelectric phase:  $\Delta C_p \sim \tau^{-0.5}$  which corresponds to eq. 3.8. The temperature dependence of the dielectric permittivity of  $\text{Sn}_2\text{P}_2\text{S}_6$  crystal in the paraelectric phase exhibits a slight deviation from the Curie-Weiss law [93], which is described by the multiplicative logarithmic correction  $\chi^{-1} = \tau(|\ln\tau|)^{0.1}$  which is related to eq. 3.10.

Ultrasonic measurements of the hypersound velocity in a ferroelectric phase for  $\text{Sn}_2\text{P}_2(\text{S}_{0.72}\text{Se}_{0.28})_6$  compound by Brillouin-scattering and ultrasonic pulse-echo techniques revealed strong anomalies near the PT. Here the authors observed that the temperature dependence of the hypersound velocity is well approximated by a Landau-Khalatnikov approach based on the mean-field model [94].

At the temperature evolution of the optical birefringence measurements, performed by Vysochanskii *et al* [95], it was found that the behavior of the heat capacity in the paraelectric phase can be well described by eq. 3.10 with a small logarithmic correction ( $b = 0.1$ ). Sequentially, the value of the critical exponent  $\beta$  for polarization has been observed to be close to 0.25. This value is well-coordinated with the universality class UTL,  $m = 1$  given in table 3.2. A partial substitution of sulphur atoms by selenium in the anion sublattice in  $\text{Sn}_2\text{P}_2(\text{Se}_y\text{S}_{1-y})_6$  with  $y = 0, 0.15, 0.28$  and  $0.29$  demonstrates a clear evolution of the anomalous part of the

birefringence in [95]. The analysis of this evolution by the combination of two models such as those shown in eqs. 3.8 and 3.11 shows that the amplitude  $A$  of the fluctuational contribution significantly increases when substituting S by Se, indicating a possible crossover of the critical behavior.

The thermal diffusivity measurements (inverse of thermal diffusivity is proportional to specific heat for such type of crystals [96]) of  $\text{Sn}_2\text{P}_2\text{S}_6$  single crystals by Oleaga *et al* show that the ferroelectric phase of those compound can be well described within the framework of the Landau model (eq. 3.6) while this model fails to describe the temperature dependence of thermal diffusivity in the paraelectric phase [96]. To describe the critical behavior near the PT in the paraelectric phase, it is necessary to take into account the superposition of the effect of first-order fluctuations and the contribution of defects, corresponding to eq. 3.8 and eq. 3.11.

The thermal studies in  $\text{Sn}_2\text{P}_2(\text{Se}_y\text{S}_{1-y})_6$  ferroelectric compounds performed by Oleaga and co-workers show a deviation from a mean-field model and a crossover to a more specific Lifshitz one [43]. For pure and lightly doped ( $y = 0.15$ , and  $y = 0.2$ ) crystals, no meaningful fittings were found, pointing that at those concentrations there is not a clear dominant effect yet (fluctuations, short or long-range dipolar interactions, charged defects...). On the other hand, good fittings with meaningful adjustable parameters were obtained (eq. 3.20) when increasing Se concentration from 0.2 up to 0.30. Obtained values of critical exponents  $\alpha$  and the amplitude ratios  $c$  support the universality class L for uniaxial ferroelectrics, indicating that the close presence of the Lifshitz point is more relevant when explaining critical behavior than other effects such as charged defects, first-order fluctuations or closeness to a TCP.

Moreover, the amplitude ratio  $\frac{A^+}{A^-}$  was found to be in the range 0.42 - 0.51. This is also close to the theoretically estimated value (0.35) for a Lifshitz system without taking into account strong dipolar interactions. These findings reveal that for selenium concentrations around the Lifshitz point, long-range dipole interactions do not play a significant role and that the critical parameters are close to those of the Lifshitz universality class L [43].

For the compositions with concentrations exceeding the Lifshitz point  $y > 0.28$ , RG theoretically predicted that the critical behavior of the second order paraelectric to incommensurate PT should correspond to the 3D-XY universality class. Indeed, the critical behavior study of  $\text{Sn}_2\text{P}_2\text{Se}_6$  ferroelectric crystal confirms the applicability of the 3D-XY universality class. The detailed review on the critical study for this compound will be considered at the end of the next section [97].

### 3.3.2. $(\text{Pb}_x\text{Sn}_{1-x})_2\text{P}_2(\text{Se}_{1-y}\text{S}_y)_6$

Investigations of the temperature dependence of the birefringence using eq.3.9 and eq.3.12 to study the paraelectric phase showed that a small substitution of Sn atoms by Pb (0.5% Pb) does not exert a significant influence on the temperature dependence of the effective value of the critical exponent  $\beta$  for the order parameter in the ferroelectric phase. On the other hand, in the same work, there is a strong influence on the amplitude of the defect contribution to the critical anomaly, whose value considerably increases [95].

Besides,  $(\text{Pb}_x\text{Sn}_{1-x})_2\text{P}_2\text{S}_6$  ferroelectric compounds have been studied by means of hypersound and ultrasound investigation [2]. The analysis of the temperature dependencies of the hypersound velocity for concentrations  $x = 0, 0.2, 0.3$ , and  $0.45$  reveal that the anomalies around the second order PT are well described by the Landau-Khalatnikov model based on the mean-field approach. The same results have been observed when studying ultrasound velocity. Moreover, from the fitted parameters, the thermodynamic coefficients in the Landau expansion series (eq. 3.2) were extracted. These coefficients are slightly reduced when lead concentration is increased; it is worth noting that all values are positive, indicating a continuous character in the transition in this concentration range [2].

Critical behavior study of  $(\text{Pb}_x\text{Sn}_{1-x})_2\text{P}_2\text{S}_6$  ferroelectric semiconductors from thermal diffusivity measurements in [98] shows a crossover from a clear non-mean-field model at  $x = 0.1$  (where the first-order fluctuations as well as the presence of defects must be taken into account) to a mean field one at  $x = 0.3$ . The sample with  $x$

$x = 0.1$  has the same critical behavior as  $\text{Sn}_2\text{P}_2\text{S}_6$  where there are several competing mechanisms. On the one hand, the closeness to a Lifshitz point enhances the fluctuations of the order parameter while on the other one, the closeness to a tricritical point reduces them. Besides, point defects are responsible for inducing long-range perturbations of the order parameter. The combination of all of them is needed to take into account a clear deviation from a mean field model, which has been discarded by the appropriate fittings. As lead concentration is increased, a crossover to other universality classes starts, shown by the fact that the critical behavior of the sample with  $x = 0.2$  can be explained by two models. In the first place, by a similar combination of mechanisms as for  $x = 0.1$  shown by the fitting of the paraelectric phase by the superposition of fluctuation effects (eq. 3.9) and the contribution of defects (eq. 3.12); secondly, the fitting to eq. 3.23 using both the paraelectric and the ferroelectric phase gave a critical exponent  $\alpha = -0.07$  close to the mean field model 0. At  $x = 0.3$ , the fitting to eq. 3.23 gave a very good fitting, with  $\alpha = -0.04$ , very close to the mean field model, while it was not possible to fit it to any model with had any relation to the nearness to Lifshitz or tricritical points or the contribution of point defects. To all effects,  $x = 0.3$  behaves as a common uniaxial ferroelectric. So, we see a crossover from a non-mean field model to it.  $x = 0.2$  is an intermediate case in which the predominance of the long-range perturbations is not settled yet as it is in  $x = 0.3$  [98].

In work [97] the thermal diffusivity of  $(\text{Pb}_x\text{Sn}_{1-x})_2\text{P}_2\text{Se}_6$  ferroelectric crystals with  $x = 0, 0.05, 0.2$  and  $0.47$  has been measured where a second order PT has been found which corresponds to the paraelectric commensurate to IC phase. The critical behavior of this transition has been studied for  $x = 0, 0.05$  and it confirms the theoretical prediction that this kind of PT belongs to the 3D-XY universality class. The application of eq. 3.22 for the fittings has given the critical parameters  $\alpha = -0.019 \pm 0.008$  for  $x = 0$  and  $\alpha = -0.026 \pm 0.018$  for  $x = 0.05$  (the theoretical value is  $-0.014$ ).

The ratio of the critical amplitudes  $\frac{A^+}{A^-}$  gives 1.00 and 1.03 respectively, while the theoretical value for 3D-XY universality class is 1.06.

## Chapter 4. Structure and physical properties of $\text{CuInP}_2\text{S}_6$ family of 2D layered crystals

The first part of this chapter focuses on the structure of metalthio- and selenophosphates, while the second one does on their physical properties. A wide range of 2D layered crystals of  $\text{Fe}_2\text{P}_2\text{S}_6$  family has been studied from the 1970s to the present day.  $\text{M}^{1+}\text{M}^{3+}[\text{P}_2\text{X}_6]^{4-}$  compounds are promising materials for functional electronics and piezoelectronics because they exhibit ferro-, ferri-, antiferroelectric, ferro- or antiferromagnetic as well as piezoelectric properties, possess mixed electronic conductivity and extremely high elastic nonlinearity, own promising optical properties, show resistive switching characteristics and an important thermal anisotropy has been observed [99, 100, 101, 102, 103, 104, 105, 106, 107, 108]. These ferroelectric and multiferroic materials have electronic properties as well as memory effects which strongly depend on temperature [109, 110]. The substitution of certain chemical elements allows to obtain new compounds demonstrating a rich variety of physical properties, photosensitivity etc.

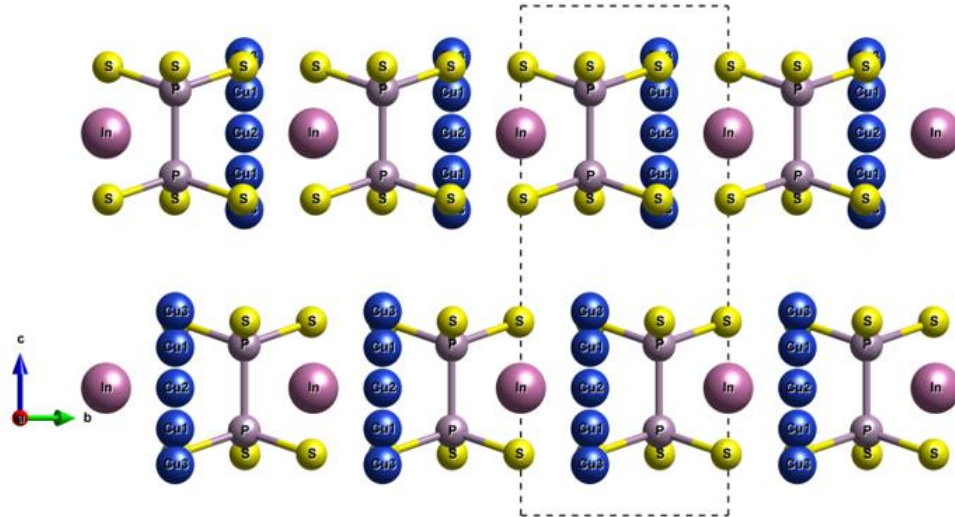
From the structural point of view, all of the members of 2D layered hexachalcogenohypodiphosphates have a common feature: a common  $[\text{P}_2\text{X}_6]^{4-}$  anion sublattice (where  $\text{X} = \text{S}, \text{Se}$ ) within each lamella of the layered crystal. On the cation side, they can accommodate most of group I and group II elements, most of the transition metals of the fourth period, and some heavier ones, such as Pd, Ag, and Cd, or a combination thereof. The most interesting ones are compounds with vanadium, chromium, manganese, iron, nickel, copper, indium and bismuth because of their magnetic or ferroelectric ordering, electrochemistry and catalysis. A few compositions with lanthanides and actinides are also known, which may suggest that more lanthanides will be compatible with this family of 2D layered materials [111, 112]. In table 4.1 some structural information for layered seleno- and thiophosphates is given.

Table 4.1

Crystalline lattice parameters of 2D layered compounds [113, 114, 115, 116, 117, 118, 119]

	Compound	Symmetry	Lattice parameters			$\beta$ [°]	Cell volume [Å <sup>3</sup> ]
			a [Å]	b [Å]	c [Å]		
$M^{1+}M^{3+}[P_2Se_6]^{4-}$ (disordered)	AgCrP <sub>2</sub> Se <sub>6</sub>	<i>C2/m</i>	6.305	10.917	6.991	107.7	458.4
$M^{1+}M^{3+}[P_2Se_6]^{4-}$	CuInP <sub>2</sub> Se <sub>6</sub>	$\bar{P}31c$	6.392	6.392	13.338	-	472.0
	AgInP <sub>2</sub> Se <sub>6</sub>	$\bar{P}31c$	6.483	6.483	13.330	-	485.2
	CuCrP <sub>2</sub> Se <sub>6</sub>	<i>C2/m</i>	6.193	10.724	6.909	107.2	438.3
	CuBiP <sub>2</sub> Se <sub>6</sub> (rt)	$\bar{P}31c$	6.541	6.541	13.263	-	491.4
	CuBiP <sub>2</sub> Se <sub>6</sub> (lt2)	$\bar{R}3h$	6.553	6.553	39.762	-	1487.9
	CuBiP <sub>2</sub> Se <sub>6</sub> (lt1)	$\bar{R}3h$	6.559	6.559	79.385	-	2957.7
	AgBiP <sub>2</sub> Se <sub>6</sub>	$\bar{R}3h$	6.652	6.652	39.615	-	1518.3
$M^{1+}M^{3+}[P_2S_6]^{4-}$	CuInP <sub>2</sub> S <sub>6</sub>	<i>Cc (lt)</i>	6.096	10.565	13.623	107.10	838.5
	AgInP <sub>2</sub> S <sub>6</sub>	<i>C2/c (ht)</i>	6.182	6.182	12.957	-	428.8
	CuCrP <sub>2</sub> S <sub>6</sub> (ht)	<i>C2/c</i>	5.916	10.246	13.415	107.09	777.3
	CuCrP <sub>2</sub> S <sub>6</sub> (lt)	<i>Pc</i>	5.935	10.282	13.368	106.78	781.0
$M^{1+}M^{3+}[P_2S_6]^{4-}$ (buckled)	AgCrP <sub>2</sub> S <sub>6</sub>	<i>P2/a</i>	5.892	10.632	6.745	105.82	483.7

$\text{CuM}^{3+}\text{P}_2\text{S}_6$  ( $\text{M}^{3+} = \text{In, Cr}$ ) crystal consists of lamellae defined by a sulfur framework in which metal cations and P–P pairs occupy the octahedral cages and the copper, the other cations, and P–P pairs form separate triangular networks within the layer (fig. 4.1).



**Fig. 4.1.** Layers of the  $\text{CuInP}_2\text{S}_6$  crystal along  $[001]$  axis. Dashed line surrounds  $\text{CuInP}_2\text{S}_6$  unit cell, where blue, rose, violet and yellow spheres are Cu, In, P, and S atoms respectively [120]

#### 4.1. $\text{CuInP}_2(\text{S,Se})_6$ compounds

In  $\text{CuInP}_2\text{X}_6$  ( $\text{X} = \text{S, Se}$ ) each lamella is chained with another layer by weak van der Waals bonding, forming a lamellar crystallographic structure with negligible transverse (along the  $c$ -axis) structural and electronic coupling.  $\text{CuInP}_2\text{S}_6$  is the essential compound of this family, and shows a well defined first-order order–disorder ferroelectric phase transition (PT) at  $T_c \approx 315$  K (there is a decrease in the symmetry group from monoclinic space group  $C2/c$  to  $Cc$ ) as a consequence of the ordering of the Cu ions in a polar sublattice, together with a small displacement of the In ions, forming a second polar sublattice; both ions are displaced from the layers plane. As the off centering of the Cu ions is much greater than that of In, the result is an uncompensated two-dimensional ferroelectric arrangement with total polarization normal to the layer (along the  $c$ -axis). [100, 120].

As shown from powder diffraction data in  $\text{CuInP}_2\text{S}_6$  by Simon *et al.* [121] the  $\text{Cu}^{1+}$  probability density shows a twofold-symmetric shape relative to the centre of the octahedral  $\text{CuS}_6$  group in the paraelectric phase. This dynamic disorder has been crystallographically modeled by three types of partially filled copper sites with large thermal factors: a distinctly off-center and quasi-trigonal Cu1, a nearly central or octahedral Cu2, and a tetrahedral one in the interlayer space Cu3 (fig. 4.2).

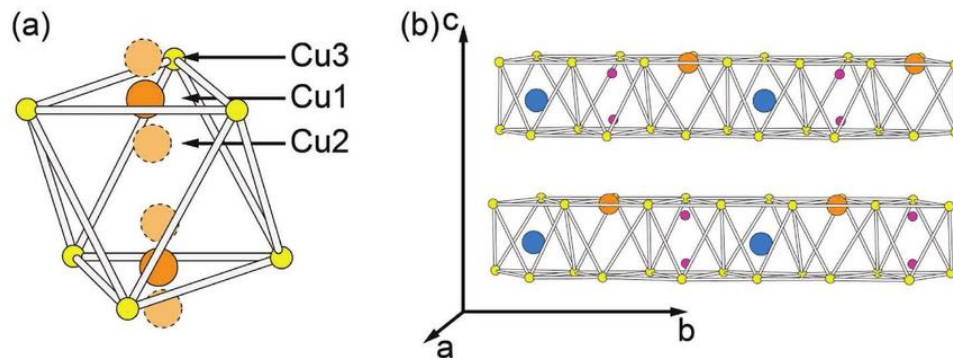


**Fig. 4.2.** (a) The position of three “up” copper positions labeled Cu1, Cu2, Cu3 at paraelectric phase. The corresponding “down” positions are also shown. (b) An in-plane view of the layers in the ferrielectric state, showing Cu in the Cu1-up position and the In shifted downward. Orange, blue, pink, and yellow circles represent Cu, In, P and S atoms respectively [4]

The phase transition is triggered by the cooperative freezing of intersite copper motions. For  $\text{Cu}^{1+}$  cations there are two possible positions:  $\text{Cu}^{up}$  is displaced upwards from the middle of the layer while  $\text{Cu}^{down}$  is displaced downwards. Below 315 K the upper site is preferentially occupied. The  $\text{Cu}^{1+}$  ions are shifted upward from the midplane of the lamella by  $\approx 1.58 \text{ \AA}$  [100]. In [115, 122] it has been shown that a twofold axis through the octahedral center and in the plane of the layer doubles the number of positions per  $\text{CuS}_6$  unit, the quasitrigonal Cu1 being mostly occupied in both  $\text{CuCrP}_2\text{S}_6$  and  $\text{CuVP}_2\text{S}_6$  at room temperature [122].

Figure 4.3 demonstrates how the S atoms lattice and the top and bottom of the lamella are distorted when the cation order into this arrangement. Although the P–P bonds are rigid, the sulfur triangles are complacent to ionic displacements and, as a

consequence, the coupling between the  $\text{Cu}^{1+}$  and  $\text{In}^{3+}$  displacements occurs in a simple way through the anion sublattice.

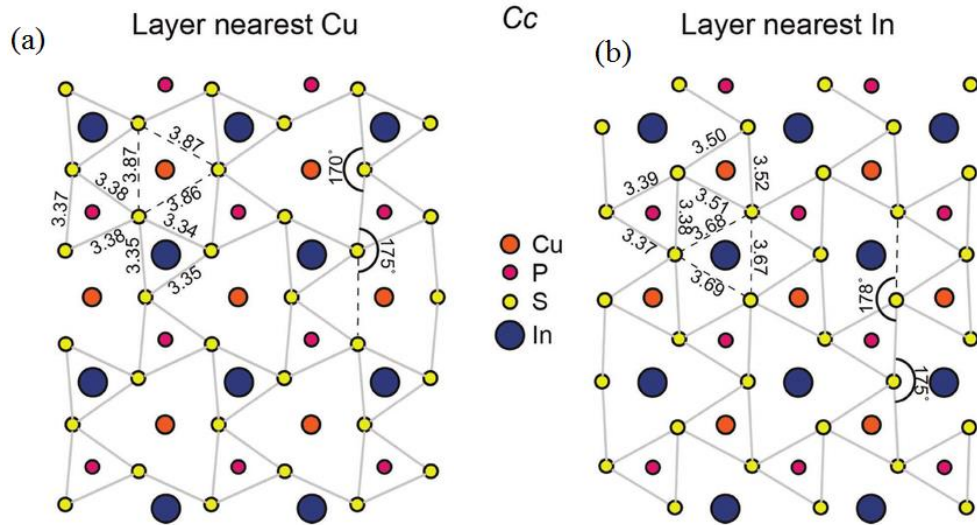


**Fig. 4.3.** The distorted close packed sulfur lattice nearest the Cu atoms (a) and the In atoms (b). S–S distances are reported in Angstroms [4]

At 298 K, 90% of the  $\text{Cu}^{1+}$  ions occupy a site  $\text{Cu}^{\text{up}}$  shifted upward by 1.58 Å from the center of the layer (figure 4.4). The  $\text{In}^{3+}$  cations are also shifted but in opposite position and by only 0.2 Å from the middle of the layer, forming a second polar sublattice [100].

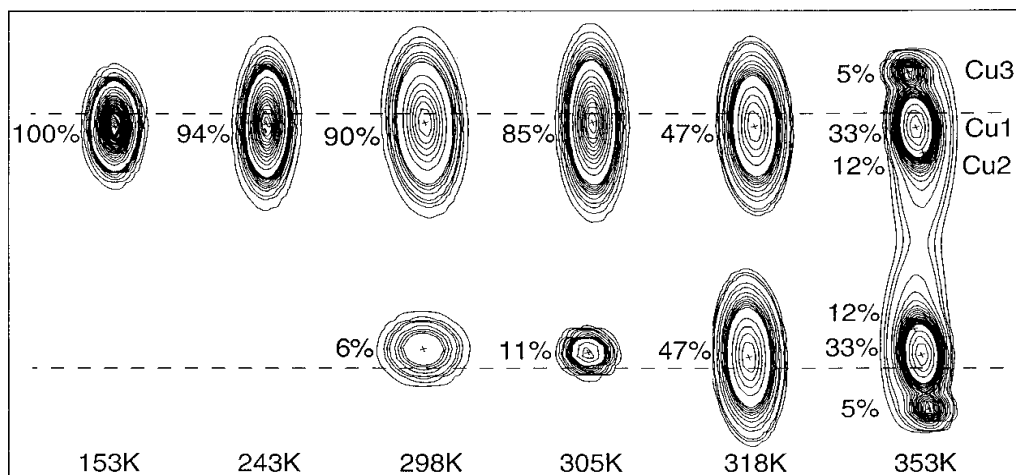


**Fig. 4.4.** Thermal evolution of the different copper site occupancies and the corresponding probability density contours in  $\text{CuInP}_2\text{S}_6$ . The small crosses indicate the refined positions, and the dashed lines denote the upper and lower sulfur planes marking a single lamella [100]

Because the  $\text{Cu}^{1+}$  off centering is much greater than that of  $\text{In}^{3+}$ , a pretty large spontaneous polarization may be expected to appear normal to the layers. Calorimetric and dielectric permittivity measurements on  $\text{CuInP}_2\text{S}_6$  confirmed it [121]. Dipole ordering in  $\text{CuMP}_2\text{S}_6$  ferroelectric compounds appears by the availability of two effects: an off-centering instability caused by an electronic instability in the form of a second order Jahn–Teller effect related to the  $d^{10}$  electronic configuration of the cations ( $3d^{10} \text{Cu}^{1+}$  and  $4d^{10} \text{In}^{3+}$ ), and the cations being constrained by the layered morphology to undergo antiparallel displacements. As a consequence, in  $\text{CuInP}_2\text{S}_6$  crystal, ferrielectric ordering appears [123].

A second order Jahn–Teller coupling, involving the localized  $d^{10}$  states forming the top of the valence band and the S–P states of the bottom of the conduction band, is predicted with such instability [124]. This has been showed for the Cu tetrahedral site in  $\text{CuCl}$  [125].

Maisonneuve *et al.* have obtained electronic densities of copper site occupancies using the Fourier maps which could be calculated to locate the copper atom. The electron densities gave the evidence of the degree of polarity of the copper sublattice at several temperatures. In the paraelectric phase, the  $\text{Cu}1^{up}$  and  $\text{Cu}1^{down}$  sites become equivalent to Cu1, i.e., the structure becomes centrosymmetric with the appearance of a twofold axis through the octahedral center. At 353 K a three-copper-site model was observed with Cu1, Cu2 and Cu3 occupancies of 33%, 12%, 5% respectively. For  $T = 315$  K, the densities were dominated by a maximum around the upper off-center site  $\text{Cu}1^{up}$ . At 318 K, density maxima of equal height were detected at the upper and lower off-center sites, giving hints of a twofold axis through the center of the  $\text{CuS}_6$  octahedral unit, parallel to the  $b$  axis [100]. On decreasing the temperature, a cooperative freezing of the motions of Cu cations takes place. At 298 and 248 K the  $\text{Cu}1^{up}$  occupancy increases to 90% and 94% respectively. At 153 K, the  $\text{Cu}1^{up}$  site above the middle of the layer is 100% filled, which has also been confirmed by dielectric measurements in [99].

In  $\text{CuInP}_2\text{S}_6$ , the ionic conductivity studies along the  $c$ -axis and the possibility for Cu atoms to be in off-centred quasi-trigonal distorted sites even above  $T_c$  led to

the discovery of the role of the second order Jahn-Teller effect in that phenomena. Despite numerous studies, there is still a need to quantify the modifications of the electronic structure with respect to this polar ordering and its relation to the off-centred cationic shifts in the crystal [126].

DFT-based *ab initio* calculations of band structure and density of states of the  $\text{CuInP}_2\text{S}_6$  crystal (figure 4.5.) by Bercha *et al.* confirmed the Jahn-Teller effect and its ferroelectric ordering [127].

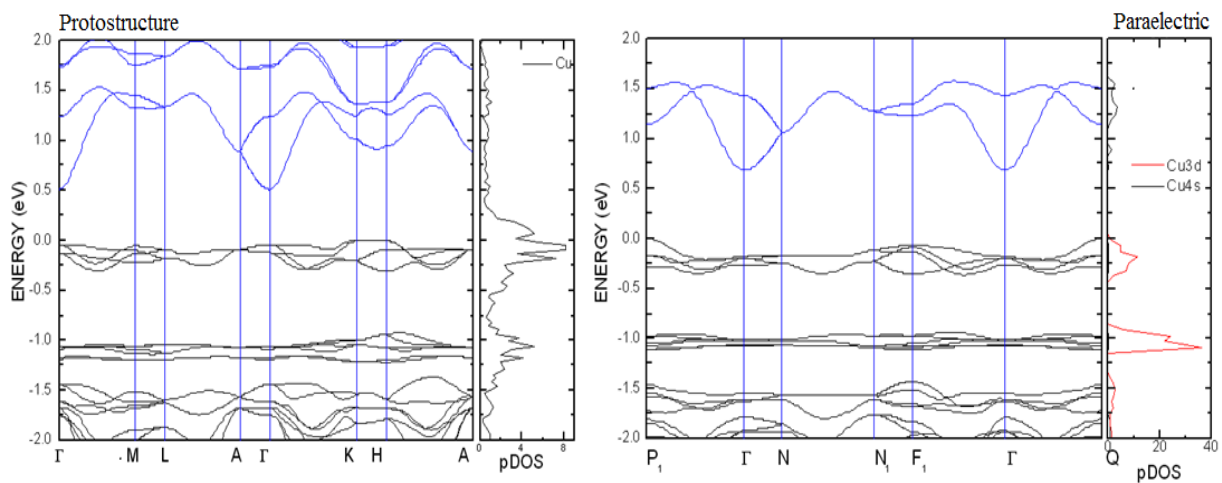


**Fig. 4.5.** Band structures and density of states of the  $\text{CuInP}_2\text{S}_6$  compound protostructure and paraelectric phase [127]

Concerning the In sites there was no residual electronic densities indicative of upshifted  $\text{In}^{3+}$  [100]. The  $\text{In}^{3+}$  downward displacement decreases from 0.24 Å at 153 K to 0.18 Å at 305 K and disappears at  $T = 315$  K.

Compounds of  $\text{CuInP}_2\text{Se}_6$  are very similar to those of  $\text{CuInP}_2\text{S}_6$  which also have high and low temperature structures (the reduction in symmetry is from  $P\bar{3}1c$  to  $P31c$  but takes place at a much lower temperature (236 vs. 315 K)) [128, 129]. Differences between these two compounds may exist due to increased P–Se bond distances and Se–P–Se bond angles indicating that selenides are much more structurally sensitive than sulphides [4]. Diffraction analysis has shown that the ferroelectric transition in materials containing selenium is also due to an ordering of the Cu cations but they are displaced only by 1.17 Å from the middle of the structure

layers while it is 1.58 Å in the case of  $\text{CuInP}_2\text{S}_6$  [100]. As a consequence, the double-well potential for copper ions in selenide compound will be shallower than for its sulfide analog, and the structural PT in  $\text{CuInP}_2\text{Se}_6$  is observed at lower temperature than for the sulfide one. Furthermore, in the selenide compound, the calculated values of activation energies were smaller than in the sulphides ( $E_A = 0.8$  eV in the paraelectric phase and  $E_A = 0.59$  eV in the ferroelectric one for  $\text{CuInP}_2\text{Se}_6$  and  $E_A = 0.92$  eV in paraphase and  $E_A = 1.16$  eV in ferrophase for  $\text{CuInP}_2\text{S}_6$  compound) which confirms the shallower potential of  $\text{Cu}^{1+}$  ions in the selenide compound [130, 131].

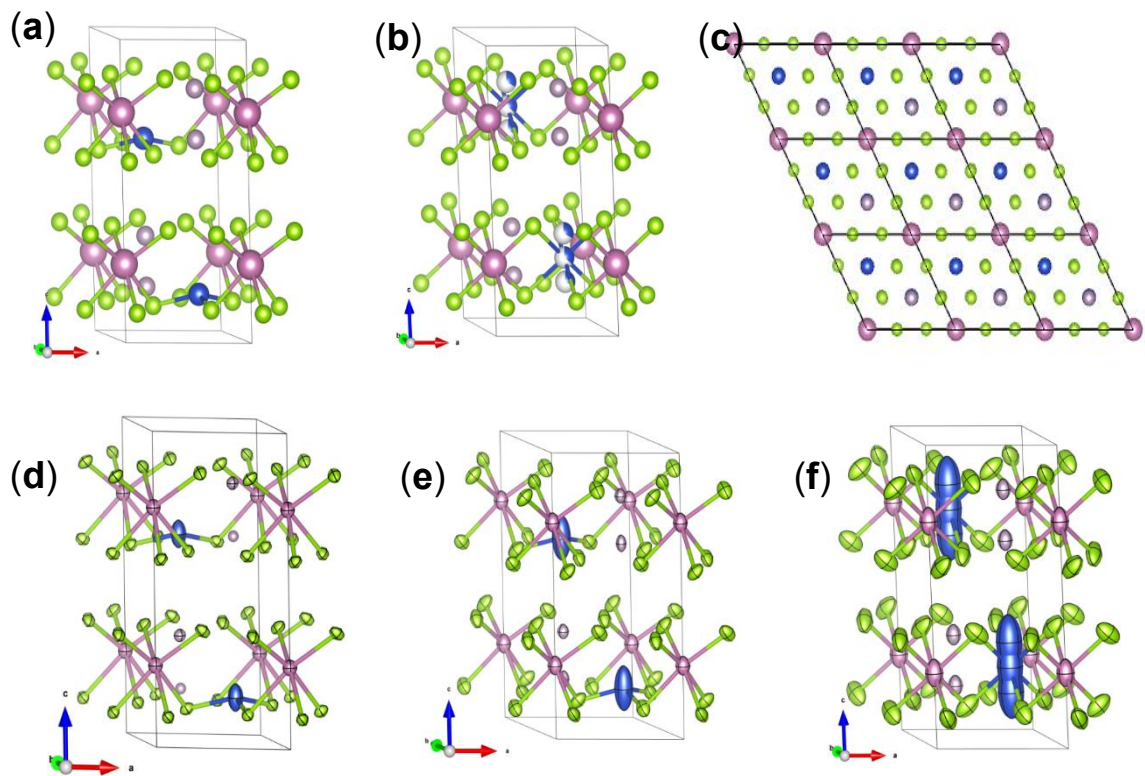


**Fig. 4.6.** Representation of  $\text{CuInP}_2\text{Se}_6$  lamellas at a) 100 K and b) 293 K ([011] direction). c) View ([110] direction) of a single  $\text{CuInP}_2\text{Se}_6$  layer showing the arrangement of Cu (blue), In (pink), P (grey) and Se (green). Atomic displacements of individual atoms of  $\text{CuInP}_2\text{Se}_6$  at d) 100 K, e) 180 K and f) 250K [132]

In works [104, 130], measurements of DC conductivity have been performed which showed much higher values for compounds with sulphur ( $\sigma_0 = 5.6 \cdot 10^{12}$  S/m in the ferroelectric phase and  $\sigma_0 = 2.66 \cdot 10^7$  S/m in the paraelectric one) than for

selenides ( $\sigma_0 = 2.35$  S/m in the ferroelectric and  $\sigma_0 = 1.21$  S/m in the paraelectric phase, respectively). The higher conductivity in the case of sulphides is most likely due to the dynamic hopping of the  $\text{Cu}^{1+}$  cations in the lattice down to low temperatures [99] while in the selenide the  $\text{Cu}^{1+}$  cations are almost frozen at the off-centre positions in the ferroelectric ordering because of the double-well minimum potential [129].

The structures of  $\text{CuInP}_2\text{Se}_6$  crystal at  $T = 100$  K and at room temperature are depicted in fig. 4.6 (a) and fig. 4.6 (b), respectively. Figure 4.6. (c) shows the single layer in [110] direction. Figure 4.6. (d, e, f) exhibits the ordering of  $\text{Cu}^+$  cations in  $\text{CuInP}_2\text{Se}_6$  at different temperatures.

As in the case of  $\text{CuInP}_2\text{S}_6$  compounds, in selenides the second-order Jahn–Teller effect is the driving force of the ferroelectric transition. The calculated partial densities of states of Cu cation (fig. 4.7) have showed that with decreasing  $T$ , low-energy Cu  $3d$  levels have clearly shifted to higher binding energy (the peak A merges into the peak B) and the gap has slightly increased [126].

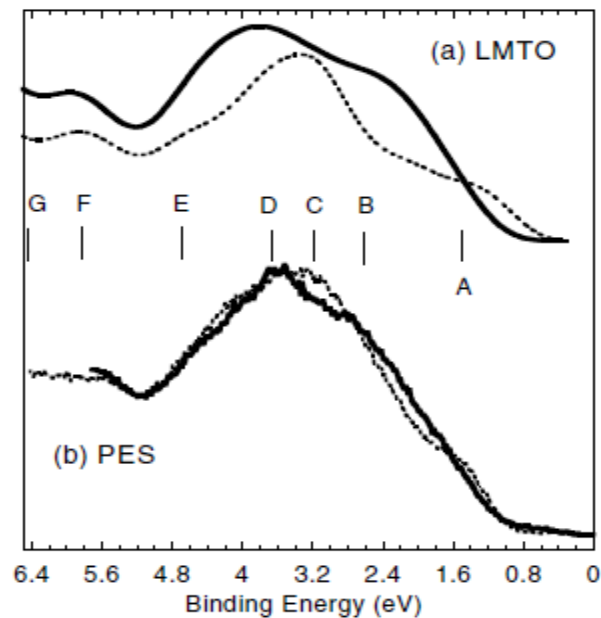


**Fig. 4.7.** (a) The LMTO densities of states obtained at  $T = 298$  K (dashed curve) and  $T = 150$  K (solid curve); (b) the corresponding UV photoemission spectra measured at  $T = 298$  K (dashed curve) and  $T = 190$  K (solid curve) [126]

In figure 4.8 the splitting of peak A into two contributions is exhibited clearly in the calculated Cu partial densities of states. The new binding energy for the last occupied states (assumed to be the  $3d_{z^2}$  orbital) is higher, consistent with a second order Jahn-Teller effect accompanied by a substantial energetic gain (around 0.3 eV). This is corroborated by the simultaneous increase in the binding energy of the unoccupied Cu  $4s$  states observed in LMTO calculations for  $T \ll T_c$ .

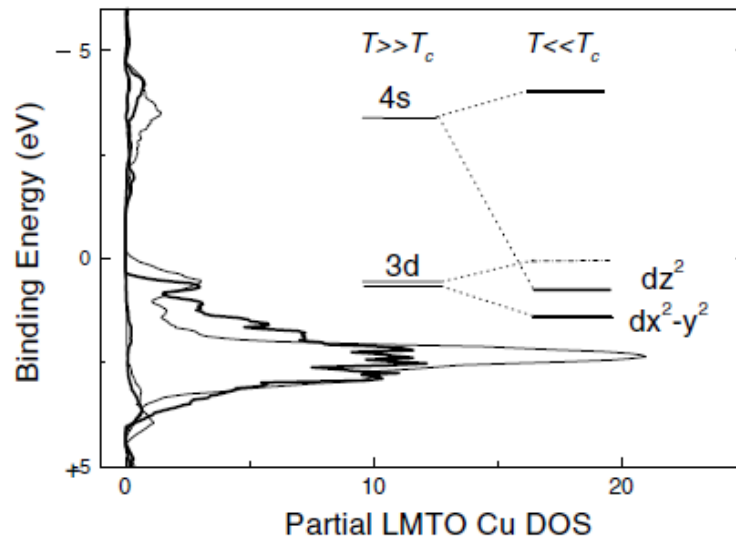


**Fig. 4.8.** The  $\text{Cu}^{1+}$  partial densities of states at  $T = 298$  and  $150$  K compared with energy diagram, showing the second order Jahn-Teller effect mechanism in  $\text{CuInP}_2\text{Se}_6$  compound [126]

#### 4.1.1 Substituting the cation sublattice

In general, it becomes interesting to explore the effect of cation substitution on ferroic properties. For example, replacing the copper cation by silver vanishes the ferroelectric phase ( $\text{AgInP}_2\text{S}_6$ ,  $\text{AgInP}_2\text{Se}_6$ ) [103, 133]. Several materials in the selenide family with the trivalent cation of bismuth have antiferroelectric ordering ( $\text{AgBiP}_2\text{Se}_6$  and  $\text{CuBiP}_2\text{Se}_6$ ) [119]. As a starting point in our analysis we consider the structure and their peculiarities of some of the 2D layered compounds which belong to  $\text{M}^{1+}\text{M}^{3+}[\text{P}_2\text{S}_6]^{4-}$  and  $\text{M}^{1+}\text{M}^{3+}[\text{P}_2\text{Se}_6]^{4-}$  subgroups and which have similar structure, namely:  $\text{AgInP}_2\text{S}_6$ ,  $\text{AgInP}_2\text{Se}_6$ ,  $\text{AgBiP}_2\text{S}_6$ ,  $\text{AgBiP}_2\text{Se}_6$  and  $\text{CuBiP}_2\text{Se}_6$ . It worth noting that the crystal growth processes are quite complicated and it was impossible to obtain

good samples for our studies in some cases like, for instance,  $\text{CuBiP}_2\text{S}_6$ , as well as compounds with chromium; therefore, we will not consider these compounds here.

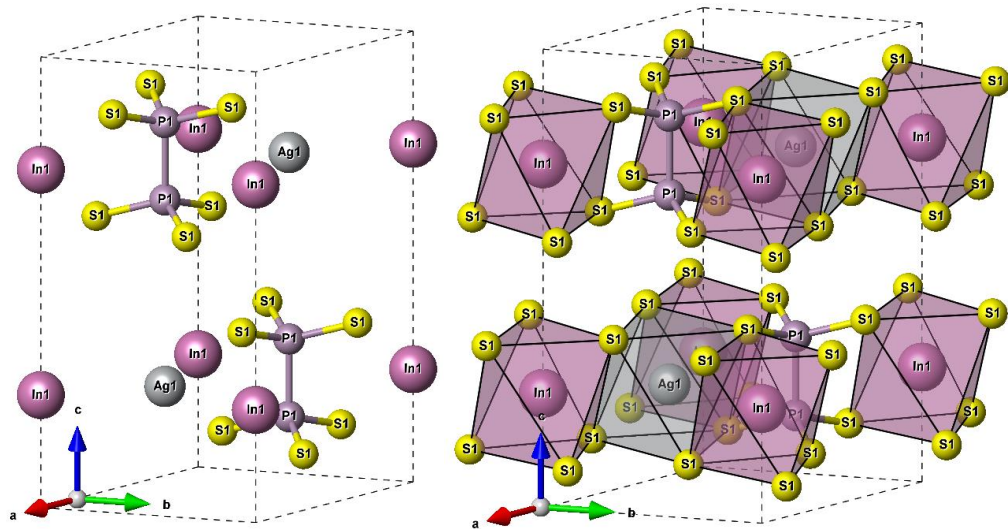


**Fig. 4.9.** The unit cell of the  $\text{AgInP}_2\text{S}_6$  crystal structure (a) and topology of the Ag- and In-centered polyhedrons (b) [134]

The  $\text{AgInP}_2\text{S}_6$  is a 2D layered crystal with trigonal symmetry and  $\overline{P3}1c$  space group at room temperature [114]. The crystal structure of the  $\text{AgInP}_2\text{S}_6$  compound (fig. 4.9.) is closely related to the  $\text{CdI}_2$ -type structure. There is no confirmation about any type of ferroelectric ordering down to 110 K in these compounds [103]. Partial changing of the chemical elements in the cation sublattice (e.g.,  $\text{Ag}_{0.1}\text{Cu}_{0.9}\text{InP}_2\text{S}_6$ ) reduces the  $T_c$  by 30 K [99]. This effect is attributed to the larger size of the  $\text{Ag}^{1+}$  cation where lower temperatures are needed to stop the static hopping of the system. The calculated electronic and phonon properties of the  $\text{AgInP}_2\text{S}_6$  crystal structure [134] have shown big covalence of the bonds between the silver cation and  $[\text{P}_2\text{S}_6]^{4-}$  anion and thus Ag–S polyhedral is harder. This information tells about the realization or absence of the second order Jahn-Teller effect mechanism.

The crystal structure of the  $\text{AgInP}_2\text{Se}_6$  compound (fig. 4.10.) is very similar to the structure of  $\text{AgInP}_2\text{S}_6$ . The selenium atoms form a hexagonal close packed structure arrangement with the layer sequence ABAB running along c-axis. The cell parameters for the  $\text{AgInP}_2\text{Se}_6$  crystal are as follows:  $a = 6.483 \text{ \AA}$ ,  $b = 6.483 \text{ \AA}$ ,  $c = 1.333 \text{ \AA}$  and the angle  $\beta = 90^\circ$ . At room temperature the crystalline structure of

$\text{AgInP}_2\text{Se}_6$  may be described by the  $P\bar{3}1/c$  space group [118]. Dielectric measurements in [133] have shown that  $\text{AgInP}_2\text{Se}_6$  crystal does not have any evidence of phase transitions; moreover, it is not a ferroelectric material.

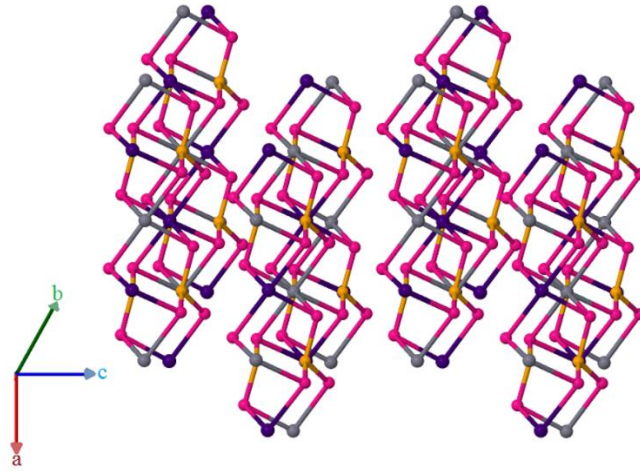


**Fig. 4.10.** The layered structure of  $\text{AgInP}_2\text{Se}_6$  where grey, violet, orange and purple spheres are silver, indium, phosphorus and selenium atoms, respectively [135]

$\text{AgBiP}_2\text{S}_6$  crystallizes in the triclinic space group  $P\bar{1}h$  with  $a = 6.3833 \text{ \AA}$ ,  $b = 7.1439 \text{ \AA}$ ,  $c = 9.5366 \text{ \AA}$ ,  $\alpha = 91.89^\circ$ ,  $\beta = 91.45^\circ$  and  $\gamma = 94.05^\circ$  [119]. In work [144] the temperature dependence of longitudinal relative ultrasonic velocity has shown the indication of a phase transition near 220 K.

As showed in fig. 4.11, one half of the  $[\text{P}_2\text{S}_6]^{4-}$  anions lie with their P–P axis normal to the layer, whereas the other ones are rotated so their P–P bond axis is nearly parallel to the layer. The P–P distance ranges from 2.212 to 2.225  $\text{\AA}$ , and the P–S distances range from 1.993 to 2.044  $\text{\AA}$ . The  $[\text{P}_2\text{S}_6]^{4-}$  anion normal to the layer coordinates to four silver and two bismuth cations. The anions lying parallel coordinate to four  $\text{Bi}^{3+}$  and two  $\text{Ag}^+$  cations. Silver cations are instead coordinated by a highly distorted tetrahedron of S atoms within the same layer and have only weak Ag–S interactions across the van der Waals gap. The  $\text{Bi}^{3+}$  cations are coordinated by six S atoms with bond distances ranging from 2.752 to 3.106  $\text{\AA}$ . This is a highly distorted coordination environment for Bi, and clearly there is one side of the

coordination sphere that is devoid of S atoms. This suggests that the inert lone pair ( $6s^2$ ) of bismuth is strongly stereochemically expressed [119]. The ultrasonic measurements have found a phase transition near 220 K in layered  $\text{AgBiP}_2\text{S}_6$  crystals [136].

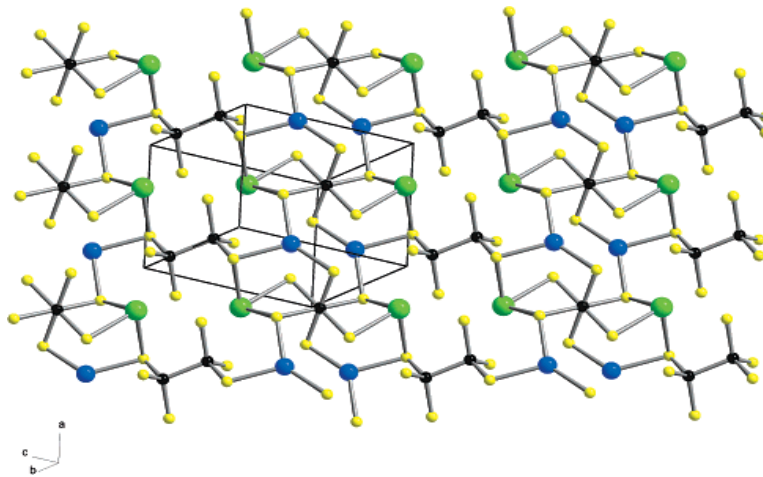


**Fig. 4.11.** View of a single layer of  $\text{AgBiP}_2\text{S}_6$ . Blue spheres are silver atoms, green - bismuth, red - selenium, and black are phosphorus atoms [119]

At room temperature the  $\text{AgBiP}_2\text{Se}_6$  compound is an anti-ferroelectric semiconductor, however, there exists an intra-layer ferroelectric ordering as shown in figure 4.12. The purple and blue arrows represent the polarizations contributed by the bismuth and silver ions, respectively. The green arrow represents the total polarization of the monolayer  $\text{AgBiP}_2\text{Se}_6$  [137].

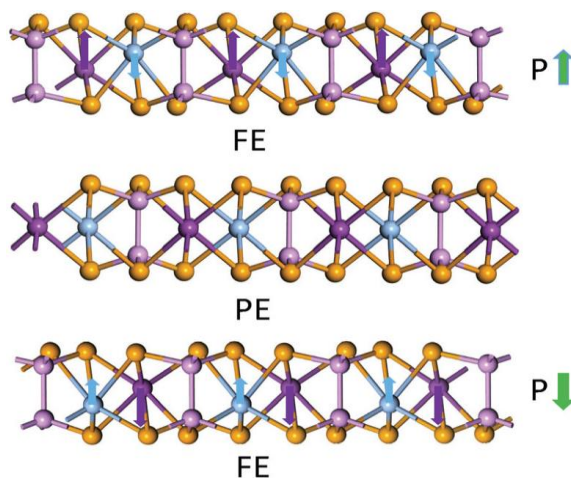


**Fig. 4.12.** Schematic side-views of the two distorted ferroelectric phases with different polarization directions (upper and lower images) and the high

symmetry paraelectric phase (centre image). The Brown, pink, purple and blue spheres are Se, P, Bi and Ag atoms, respectively [137]

The positions of the silver cations are distorted from an octahedral environment by the elongation of three of the Ag–Se bonds displacing the silver cations along the *c*-axis away from the center of the layer by 0.4 Å. The bismuth cations are shifted only 0.2 Å off the center of the octahedron in the opposite direction along the layer normal of the silver cations. AgBiP<sub>2</sub>Se<sub>6</sub> crystal has a lamellar MPSe<sub>3</sub> structure type with weakly interacting layers packed by van der Waals interactions. In each layer, the cations and P–P bonds fill the octahedral holes defined by the selenium framework. The [P<sub>2</sub>Se<sub>6</sub>]<sup>4-</sup> anions are bridged by an ordered arrangement of alternating Ag<sup>1+</sup> and Bi<sup>3+</sup> metal centers [119, 137]. Figure 4.13 exhibits the structure of a monolayer in AgBiP<sub>2</sub>Se<sub>6</sub>. The lattice parameters obtained by DFT calculations are:  $a = b = 6.752$  Å. The AgBiP<sub>2</sub>Se<sub>6</sub> compounds crystallize in the space group  $R\bar{3}$  [137].

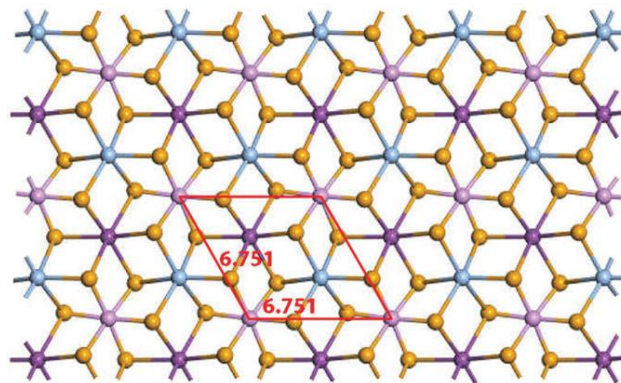


**Fig. 4.13.** Top-view of the structure of monolayer AgBiP<sub>2</sub>Se<sub>6</sub>. The Brown, pink, purple and blue balls represent Se, P, Bi and Ag atoms, respectively. The red line describes the unit cell [137]

The calculated phonon dispersion of the paraelectric phase (fig. 4.14) for AgBiP<sub>2</sub>Se<sub>6</sub> monolayer shows an imaginary frequency at the  $\Gamma$  point, demonstrating the instability of the paraelectric phase [137]. The unstable mode at the  $\Gamma$  point mostly

corresponds to the off-centering displacements of the silver and bismuth cations with opposite directions, which leads to a lower symmetric, ferroelectric phase.

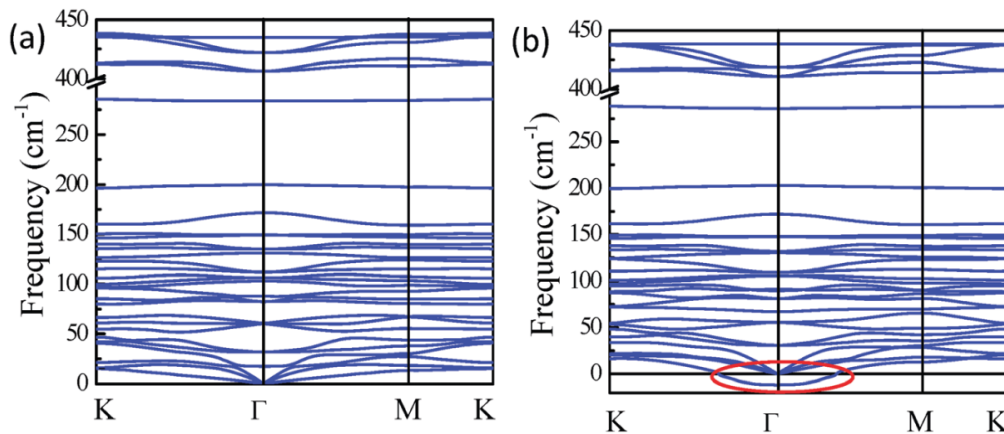


**Fig. 4.14.** The phonon spectra of the ferroelectric (a) and paraelectric (b) phases of monolayer  $\text{AgBiP}_2\text{Se}_6$  [137]

Comparing sulphates with selenides, the structural differences between  $\text{AgBiP}_2\text{Se}_6$  and its sulphide analogue could have their origins in the size of Bi for the available Se-based octahedral cage as well as its decreased trend to stereochemically express its lone pair of electrons.

$\text{CuBiP}_2\text{Se}_6$  compounds (fig. 4.15 (A)) have the lamellar  $\text{CuInP}_2\text{Se}_6$  structure with the same  $[\text{P}_2\text{Se}_6]^{4-}$  anion lattice connected by the metal cations, crystallizing in the space group  $R\bar{3}$  with  $a = 6.5532 \text{ \AA}$  and  $c = 39.762 \text{ \AA}$ . At room temperature, the  $[\text{P}_2\text{Se}_6]^{4-}$  anions structure of  $\text{CuBiP}_2\text{Se}_6$  is bridged by an ordered arrangement of alternating coinage metal and bismuth metal centers [119]. Each  $[\text{P}_2\text{Se}_6]^{4-}$  anion has three coinage metal ions and three  $\text{Bi}^{3+}$  ions as its nearest metal neighbors (fig. 4.15 (B)). As it was shown by the authors in ref. [119], the structure at three different temperatures (298, 173, and 97 K) confirmed the ordering in the form of two well-defined antiferroelectric transitions as the copper cations move and settle off-center of the octahedral sites. Partial antiferroelectric ordering is observed below 173 K, with 85% of  $\text{Cu}^+$  cations found in well-defined off-center positions below 97 K. The increased displacement of the bismuth cations compared to the indium ones may be

an indication of stereoactive lone pair electrons, which could be present in  $\text{Bi}^{3+}$  but not  $\text{In}^{3+}$ . The same mechanism is observed in  $\text{AgBiP}_2\text{Se}_6$  crystals at room temperature.

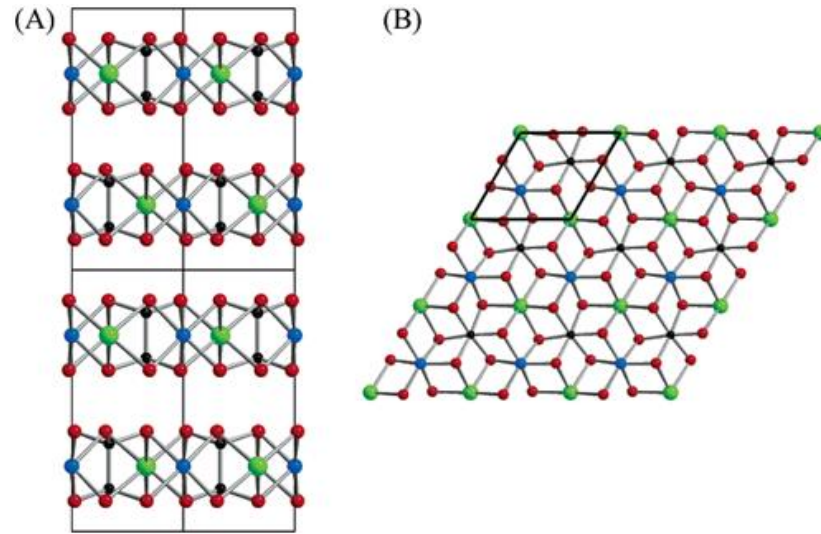


**Fig. 4.15.** (A) The layered structures of  $\text{CuBiP}_2\text{Se}_6$  at room temperature in  $[110]$  direction. (B) View of a single  $\text{CuBiP}_2\text{Se}_6$  layer down the  $c$ -axis showing the ordered arrangement of the  $\text{Bi}^{3+}$  and  $\text{Cu}^+$  ions. Blue spheres are  $\text{Cu}(\text{Ag})$ , green -  $\text{Bi}$ , red -  $\text{Se}$ , and black are atoms  $\text{P}$  [119]

The information about the ordering in  $\text{CuInP}_2\text{S}_6$ -type compounds is listed in table 4.2.

Table 4.2.

Information on availability of phase transitions in  $\text{M}^{1+}\text{M}^{3+}[\text{P}_2\text{X}_6]^{4-}$  crystals [100, 119, 129, 141]

Compound	Order Type	Ordering Temperature
$\text{CuInP}_2\text{S}_6$	Ferrielectric	315K
$\text{CuInP}_2\text{Se}_6$	Ferrielectric	$T_c = 235.5\text{K}$ and $T_i = 248.5\text{K}$
$\text{AgInP}_2\text{S}_6$	No PT	—
$\text{AgInP}_2\text{Se}_6$	No PT	—
$\text{AgBiP}_2\text{S}_6$	?	220K
$\text{AgBiP}_2\text{Se}_6$	Antiferroelectric	$T_c < 298\text{K}$
$\text{CuBiP}_2\text{Se}_6$	Antiferroelectric	145K and 220K

## 4.2. Physical properties of $M^{1+}M^{3+}[P_2X_6]^{4-}$ multiferroics

In this section we consider some physical properties in two-dimensional layered crystals, namely dielectric, piezoelectric and ultrasonic as well as thermal properties.

### 4.2.1. Dielectric measurements

The temperature dependence of complex dielectric permittivity is presented as  $\varepsilon^* = \varepsilon' - i\varepsilon''$ . According to the dielectric studies in  $\text{CuInP}_2\text{S}_6$  the first order phase transition was observed at  $T = 315$  K [138]. The increasing of the dielectric permittivity at 1 kHz showed in fig. 4.16 above 330 K is related to the ionic conductivity of the Cu cations [121]. In the same work [138], the authors have studied the impact of high hydrostatic pressure on the dielectric properties of  $\text{CuInP}_2\text{S}_6$  compound. The pressure behavior of the phase transition temperature confirmed the order-disorder type of phase transition in these crystals.

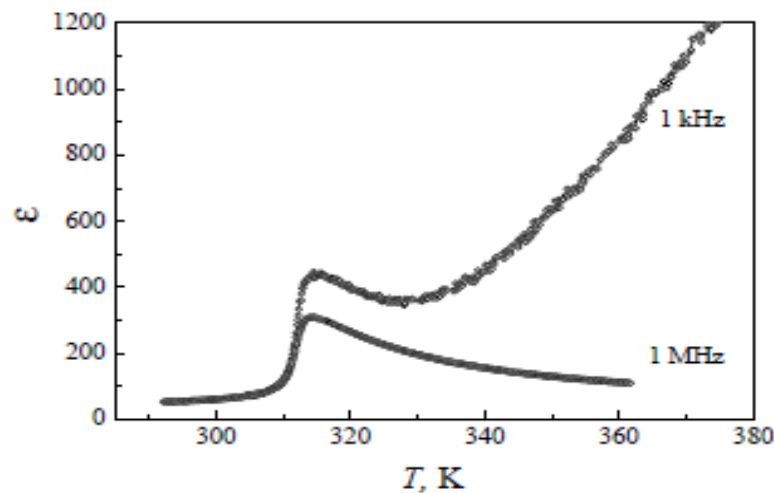


**Fig. 4.16.** Temperature dependences of  $\text{CuInP}_2\text{S}_6$  crystals dielectric permittivity in the heating mode at the measuring field frequencies of 1 kHz and 1 MHz [138]

As seen from fig. 4.17, substituting copper with silver changes the position of the ferroelectric phase transition to lower temperatures (from  $T = 315$  K in  $\text{CuInP}_2\text{S}_6$  to  $T = 283$  K in  $\text{Ag}_{0.1}\text{Cu}_{0.9}\text{InP}_2\text{S}_6$ ). Such a decrease can be interpreted as follows: the

size of the silver cations is bigger than for copper ions, hence, lower temperatures are needed to stop the static hopping motions of the system [139].

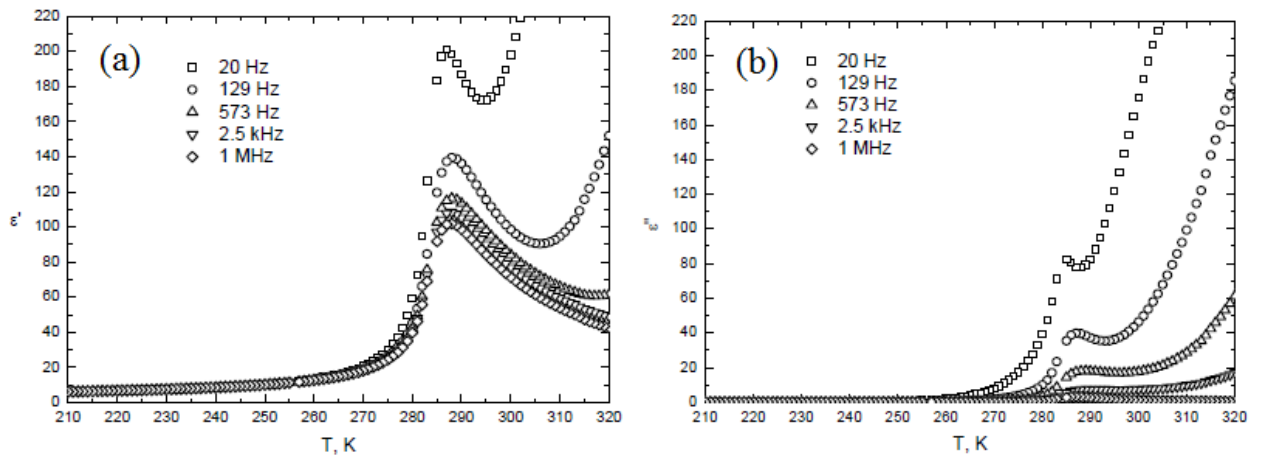


**Fig. 4.17.** Temperature dependence of real (a) and imaginary (b) part of the complex dielectric permittivity in  $\text{Ag}_{0.1}\text{Cu}_{0.9}\text{InP}_2\text{S}_6$  crystals [139]

For the pure  $\text{AgInP}_2\text{S}_6$  compound, the dielectric permittivity strongly increases on heating (fig. 4.18), with a similar increase to the case of  $\text{CuInP}_2\text{Se}_6$  and  $\text{CuInP}_2\text{S}_6$  [133, 138]. As opposed to the case of  $\text{CuInP}_2\text{S}_6$ , no anomaly indicating polar phase transitions have been found in these crystals down to the lowest temperatures measured. Calculated electrical conductivity data has shown a high enough value of the conductivity which is also ionic, due to the silver cations. Therefore, the dielectric properties of these ferroelectrics are mainly caused by a high conductivity [103].

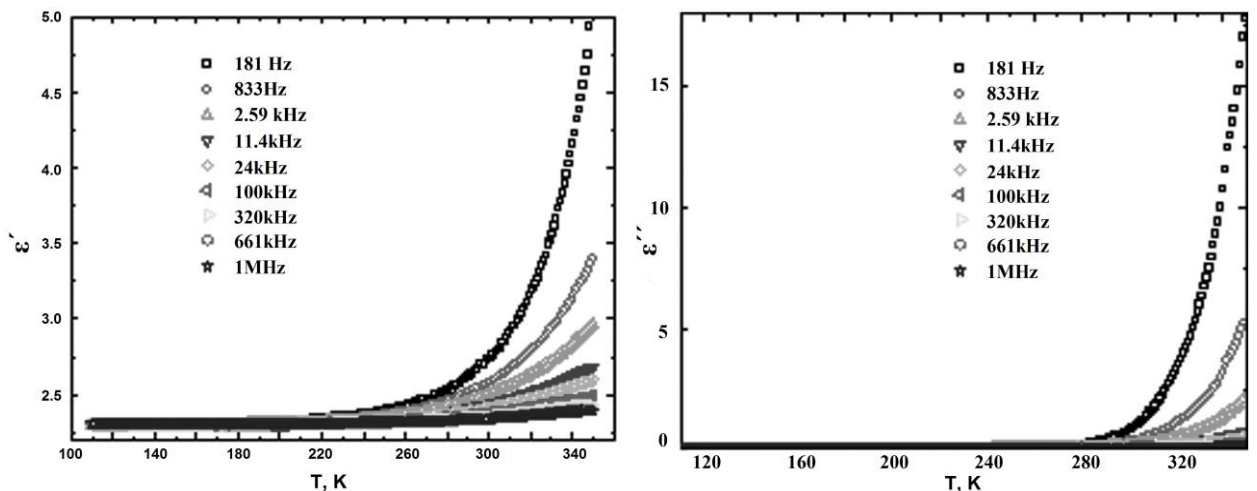


**Fig. 4.18.** Temperature dependence of real and imaginary part of the complex dielectric permittivity in  $\text{AgCuInP}_2\text{S}_6$  crystals [103]

Broadband dielectric studies of  $\text{AgInP}_2\text{Se}_6$  (fig. 4.19) show a strong increasing of the dielectric permittivity on heating, similar to  $\text{AgInP}_2\text{S}_6$ , as described in the previous paragraph. The dielectric properties in  $\text{AgInP}_2\text{Se}_6$  crystals are also due to a high conductivity. There is no indication of any ferroelectric phase transition down to 110 K [133].

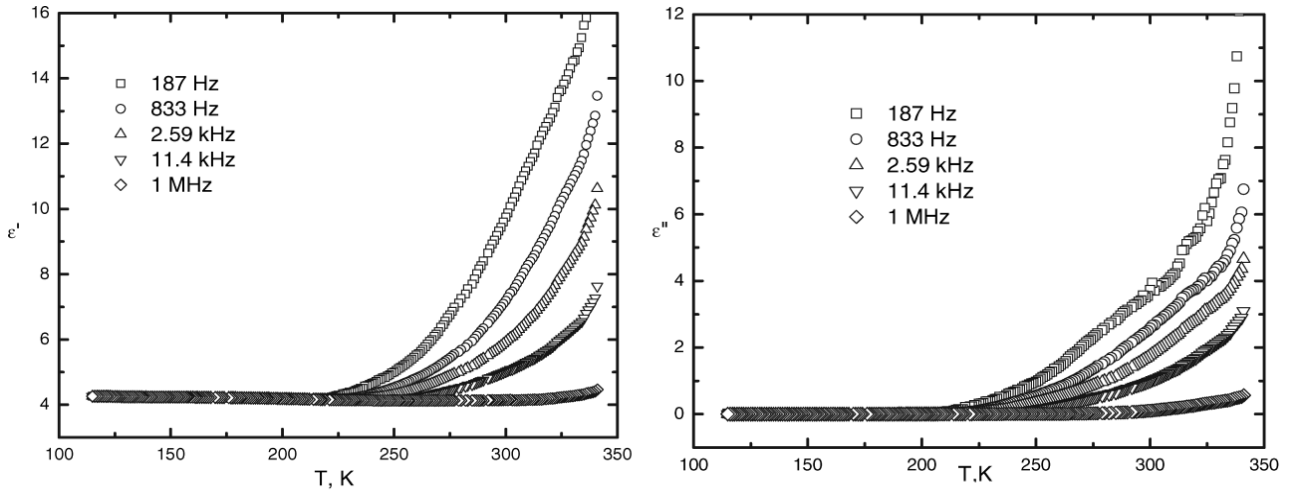


**Fig. 4.19.** Temperature dependence of the real and imaginary parts of the complex dielectric permittivity in  $\text{AgInP}_2\text{Se}_6$  crystals [141]

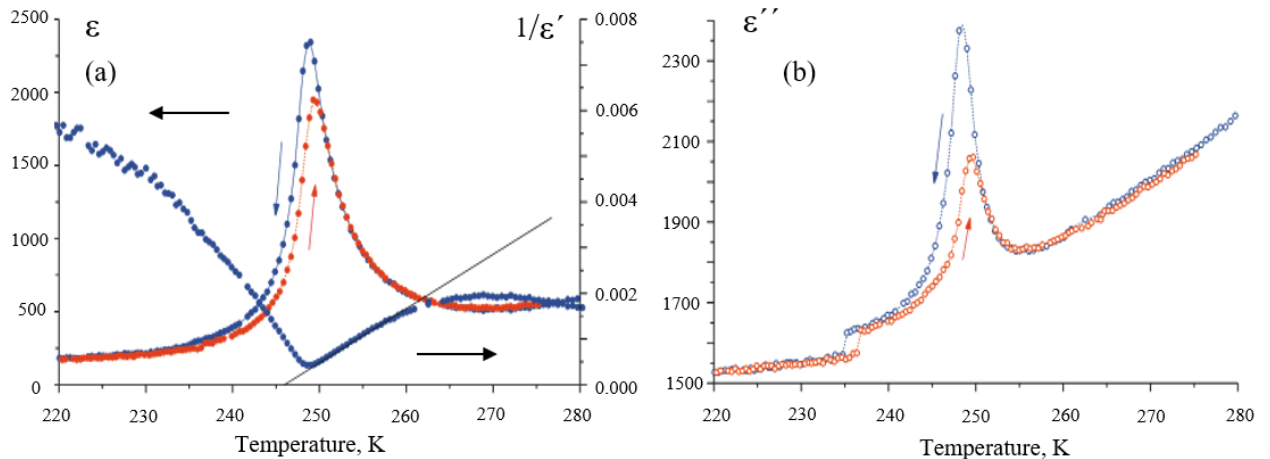


**Fig. 4.20.** Temperature dependence of the real (a) and imaginary (b) parts of the complex dielectric permittivity in  $\text{CuInP}_2\text{Se}_6$  crystals. Temperature dependence of  $1/\epsilon'$  is measured on cooling [129]

As it was shown by the authors in ref. [129], in the case of  $\text{CuInP}_2\text{Se}_6$  compounds there are two phase transitions: a second-order one at  $T_i = 248.5$  K and a first-order transition at  $T_c = 235.5$  K, in cooling mode, with incommensurate phase between

those (fig. 4.20). These two transitions in  $\text{CuInP}_2\text{Se}_6$  have hysteresis, implying that these phase transitions are first-order. On the other hand, the hysteretic effects involve not only an upward shift by  $\approx 1.5$  K of  $T_i$  but, more importantly, a rather large decrease in the values of the real and imaginary parts of the dielectric permittivity in almost the entire temperature range during the heating mode. The latter observation indicates that this PT into the intermediate phase may be second-order [129]. The values of the calculated Curie constants obtained from the dielectric data indicate an order–disorder type of the phase transitions [129].

The dielectric measurements of the  $\text{CuInP}_2\text{Se}_6$  compound by Macutkevic et al. [140] confirmed only one ferroelectric phase transition at  $T_c = 225$  K. This discrepancy with [129] may be related to the different preparation conditions of the  $\text{CuInP}_2\text{Se}_6$  compounds.

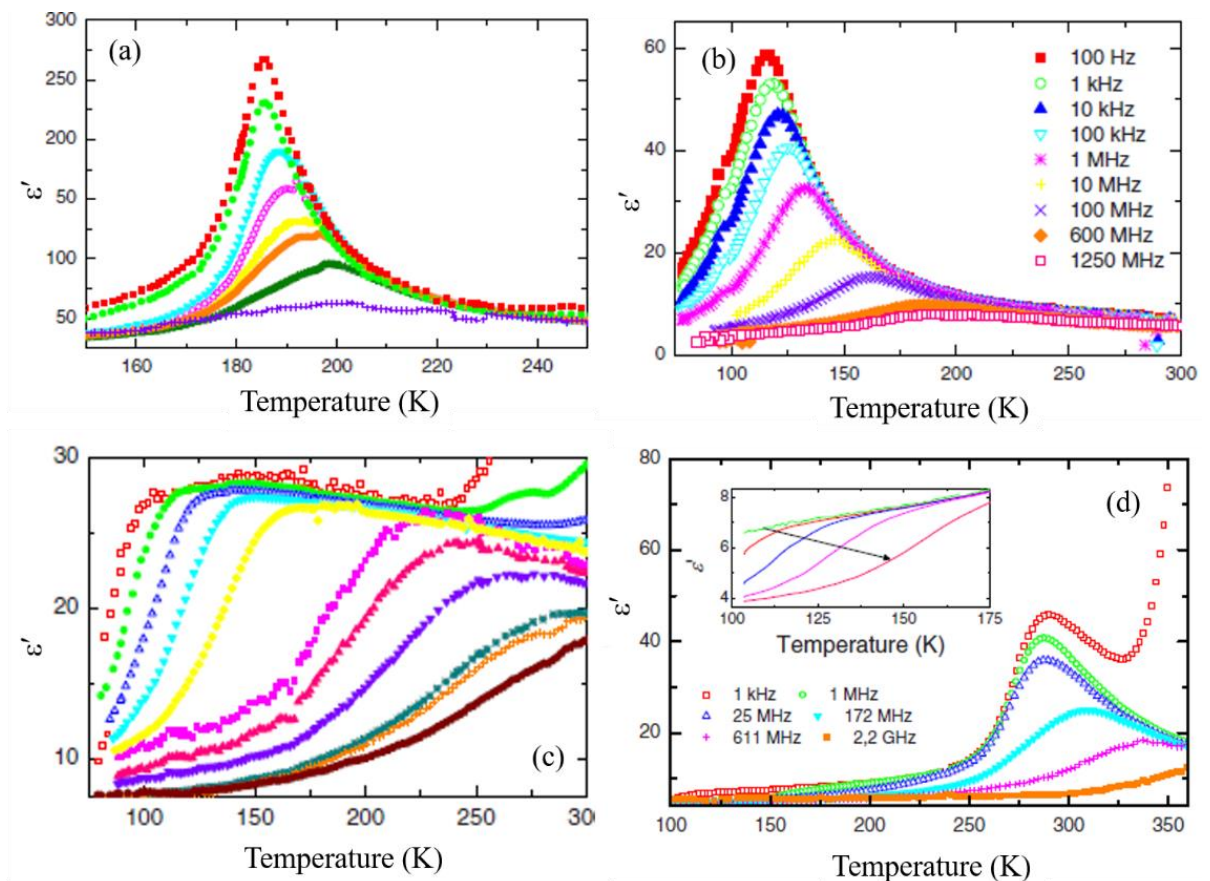


**Fig. 4.21.** Real part of dielectric permittivity of  $\text{CuInP}_2(\text{S}_x\text{Se}_{1-x})_6$  crystals measured at several frequencies: (a)  $x = 0.1$ ; (b)  $x = 0.25$ ; (c)  $x = 0.8$ ; (d)  $x = 0.98$  [141]

Let's consider a variation of the structural parameters when substituting S by Se in mixed  $\text{CuInP}_2(\text{S}_x\text{Se}_{1-x})_6$  crystals. Even a small amount of sulphur substitution by selenium can significantly change properties in these mixed two-dimensional ferroics. As observed in [141], a small amount of sulfur shifts the transitions to lower temperatures. For  $x = 0.02$  the PT temperature in mixed crystals decreases from  $T = 225$  K in the pure one [140] to 215.7 K, with 5% of Se to 208.2 K and with 10% to 185 K (Fig. 4.21 (a) and Fig. 4.22(a)).

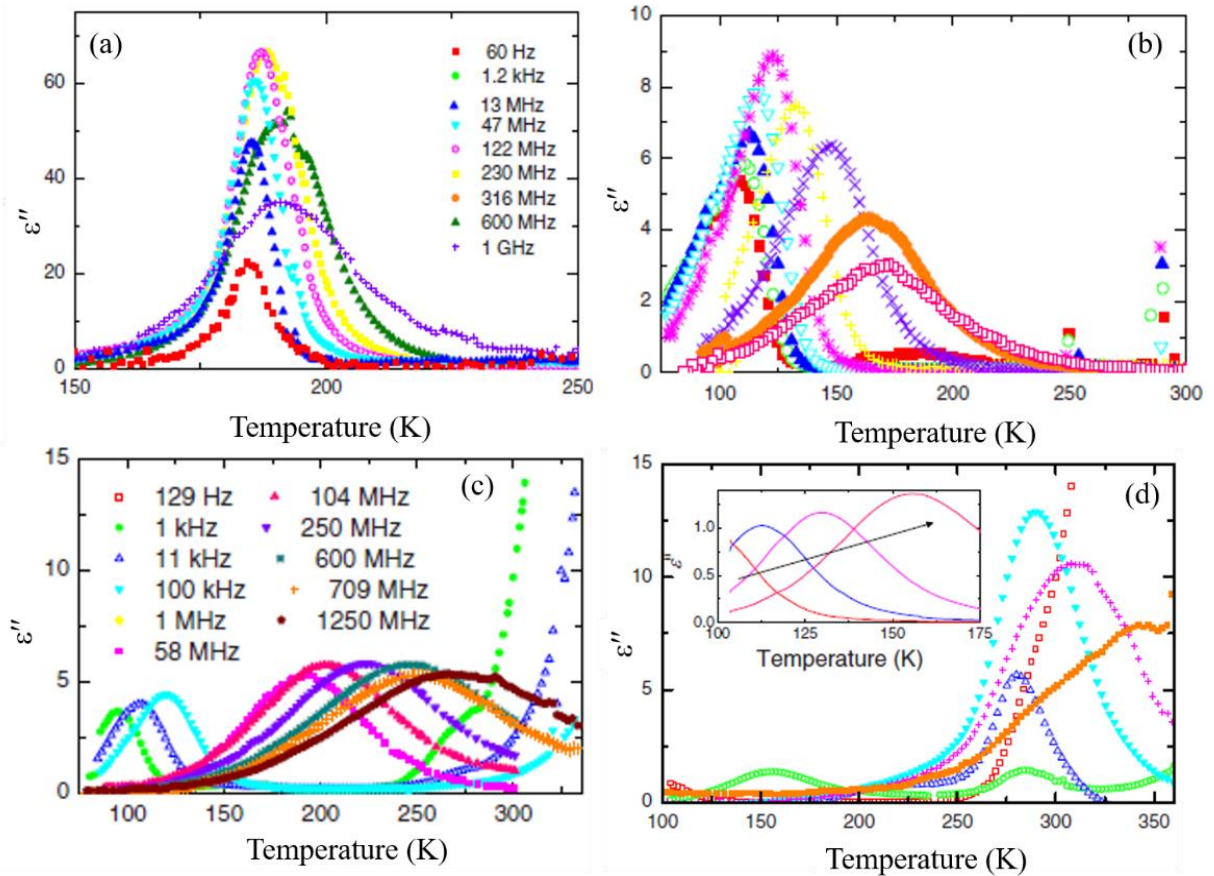


**Fig. 4.22.** Imaginary part of dielectric permittivity in  $\text{CuInP}_2(\text{S}_x\text{Se}_{1-x})_6$  compounds measured at several frequencies: (a)  $x = 0.1$ ; (b)  $x = 0.25$ ; (c)  $x = 0.8$ ; (d)  $x = 0.98$  [141]

At concentrations  $x = 0.2$  and  $x = 0.25$ , these mixed compounds show just one maximum in the real and imaginary parts of the dielectric permittivity in the temperature range of 110 and 145 K at a frequency of 10 kHz [101]. The temperature dependences of the complex dielectric permittivity at various frequencies of these crystals show a typical relaxor behavior, as can be seen in fig. 4.21 (b) and fig. 4.22

(b). The position of the maximum of dielectric permittivity is strongly frequency dependent. In  $\text{CuInP}_2(\text{S}_{0.8}\text{Se}_{0.2})_6$  (fig. 4.21 (c) and fig. 4.22 (c)), it is easy to see a broad dispersion of the complex dielectric permittivity starting from 260 K and extending to the lowest temperatures. The maximum of the real part of the dielectric permittivity shifts to higher temperatures with an increase in the frequency, together with the maximum of the imaginary part, and the typical behavior of dipolar glasses appears. A small amount of Se ( $x = 0.98$ ) changes dielectric properties of  $\text{CuInP}_2\text{S}_6$  crystals significantly: the temperature of the main dielectric anomaly shifts more than 20 degrees: from 315 K to 289 K (fig. 4.21 (d) and fig. 4.22 (d) [141]).

In the case of  $\text{CuBiP}_2\text{Se}_6$ , a first-order antiferroelectric PT was found at 136 K. From the dielectric permittivity data of the  $\text{CuBiP}_2\text{Se}_6$  crystal, the measured temperature region can be divided in three intervals: 1. At higher temperatures dielectric dispersion occurs due to the high electrical conductivity; 2. A frequency independent anomaly of  $\varepsilon'$  at 136 K indicates an antiferroelectric PT; 3. At temperatures lower than 40 K the dielectric dispersion effect can be observed [102]. No dielectric dispersion is observed about the antiferroelectric PT temperature ( $T = 136$  K), therefore the dielectric permittivity at 2 kHz corresponds to the static one as depicted in figure 4.23. Moreover, the value of the dielectric permittivity around the antiferroelectric phase transition temperature is low. Typically, such a low value of dielectric permittivity has a phononic origin; therefore, the phase transition is a displacive type and is driven by a resonant soft mode [102].

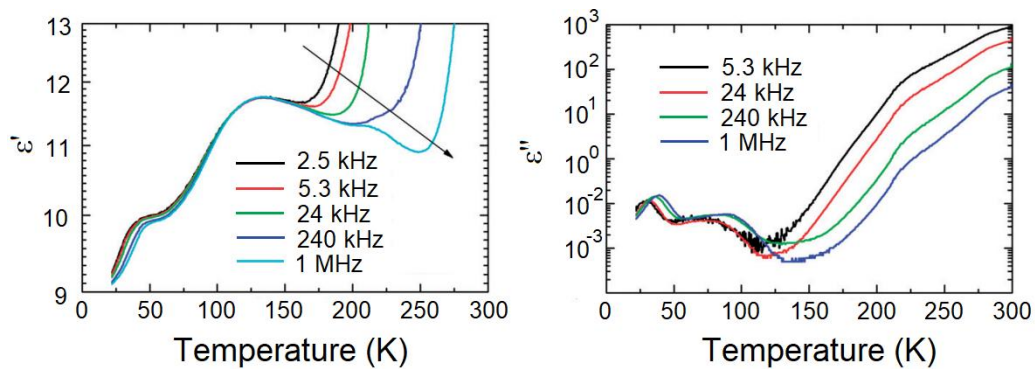


**Fig. 4.23.** Temperature dependence of the real and imaginary parts of the complex dielectric permittivity in  $\text{CuBiP}_2\text{Se}_6$  crystals [102]

As mentioned, the microscopic mechanism of the phase transition is antiparallel displacements in the copper and bismuth sublattices [119]. However, not all copper ions are ordered below the antiferroelectric PT temperature. Therefore, the non-ordered copper ions form a glassy phase at low temperatures [102].

#### 4.2.2. Piezoelectric and ultrasonic measurements

In pure  $\text{CuInP}_2\text{S}_6$  ferroelectric crystals ultrasonic and piezoelectric studies also confirm the existence of a PT around 315 K. The hysteresis in fig. 4.24 (a) has shown that a first order character can be attributed to this phase transition. In Fig. 4.24 (b), the temperature dependencies of the longitudinal ultrasonic attenuation coefficient are shown for different propagation directions and the longitudinal wave attenuation peak in direction [001] is more than one order of magnitude larger than in the direction parallel to the layers what could be explained with the argument that the electrostriction parameters along the layers are very small in comparison to those through the layers [142].

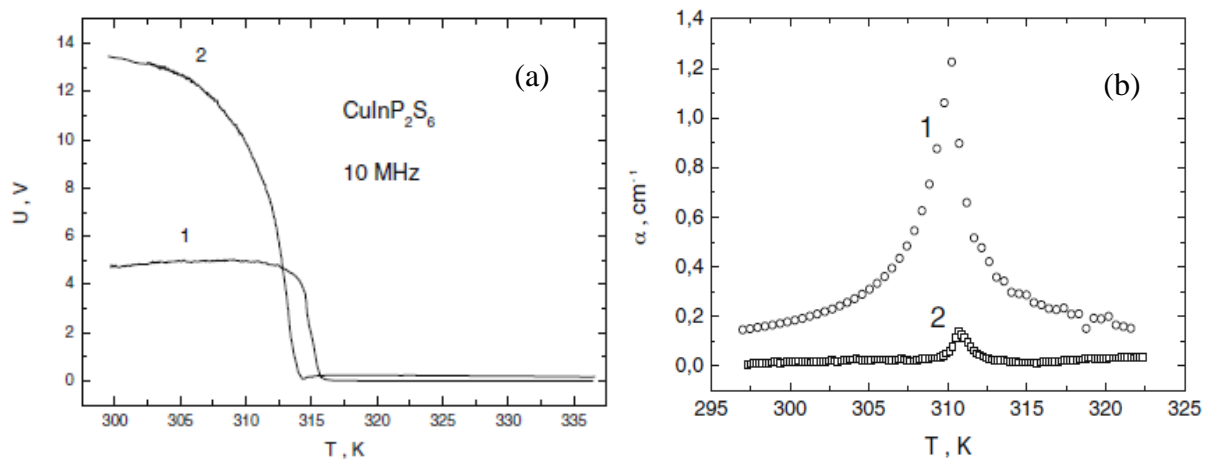


**Fig. 4.24** (a) Temperature dependences of ultrasonically detected piezoelectric signal in  $\text{CuInP}_2\text{S}_6$  c-cut plate in heating (1) and in cooling run (2). (b) Temperature dependences of longitudinal ultrasonic attenuation along (1) [001] and normal (2) to [001] [142]

Ultrasonic and piezoelectric studies of the phase transitions in 2D layered  $\text{CuInP}_2\text{S}_6$  crystals by Samulionis *et al.* have shown the possibility of tuning-off the

elastic piezoelectric and electronic properties by manipulations on the composition [142]. Substituting copper with silver changes the position of PT to lower temperatures (fig. 4.25 (a)), which is in good agreement with [139].

Similar piezoelectric sensitivity measurements by an ultrasonic method were carried out and in mixed  $\text{Ag}_{0.1}\text{Cu}_{0.9}\text{InP}_2\text{Se}_6$  and  $\text{Ag}_{0.2}\text{Cu}_{0.8}\text{InP}_2\text{Se}_6$  layered crystals. Substituting Cu by Ag leads to a decreasing PT from 225 K and 235 K in pure  $\text{CuInP}_2\text{Se}_6$  compound to 215 and 230 K for a sample with 10% of  $\text{Ag}^+$  and 210 and 225 K with 20% of silver respectively. As a consequence, piezoelectricity exists in these crystals only at comparatively low temperatures (Fig. 4.25 (b)) [143]. Other piezoelectric and ultrasonic measurements showed that, in polarized  $\text{CuInP}_2\text{Se}_6$  type compounds at room temperature, an electromechanical coupling constant as high as  $> 50\%$  could be obtained. In the paraelectric phase, the high electromechanical coupling can be induced by external DC bias field, because of electrostriction [144].

In pure  $\text{AgInP}_2\text{Se}_6$  and  $\text{AgInP}_2\text{Se}_6$  crystals, no PT was observed in the temperature range 100-300 K [143].

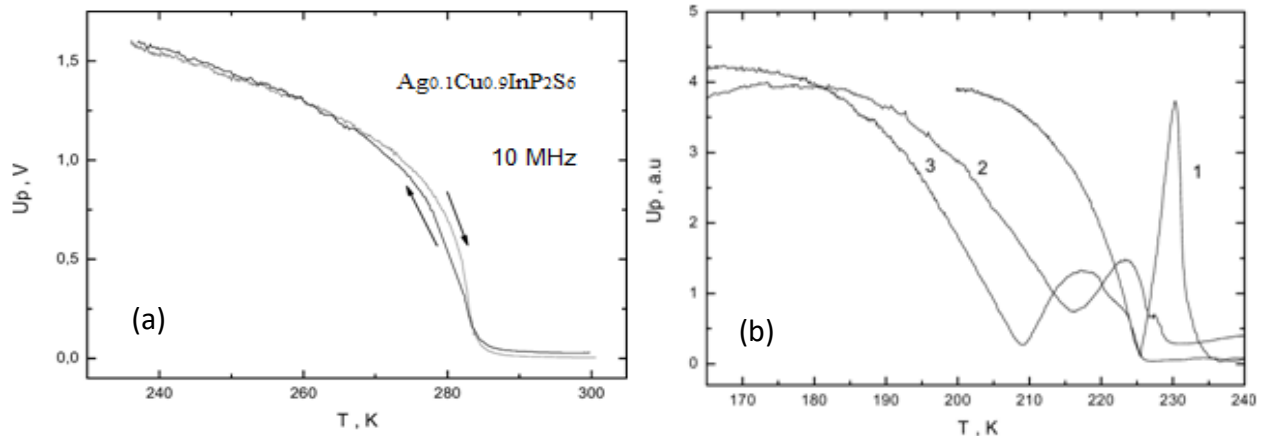


**Fig. 4.25.** Temperature dependencies of ultrasonically detected piezoelectric signal in  $\text{Ag}_{0.1}\text{Cu}_{0.9}\text{InP}_2\text{Se}_6$  crystal in heating and in cooling run (a). Temperature dependencies of ultrasonically detected piezoelectric signal in  $\text{CuInP}_2\text{Se}_6$  (1),  $\text{Ag}_{0.1}\text{Cu}_{0.9}\text{InP}_2\text{Se}_6$  (2),  $\text{Ag}_{0.2}\text{Cu}_{0.8}\text{InP}_2\text{Se}_6$  (3) crystals in heating run (b) [143]

The temperature dependence of ultrasonically detected piezoelectric signal of  $\text{CuBiP}_2\text{Se}_6$  crystal was measured in [136] and the result is shown in fig. 4.26 (a). In the high temperature region, the signal is absent and it turns out that the crystal has no piezoelectric sensitivity and it is in the centrosymmetric phase. On cooling, the onset of piezoelectric signal appeared near 220 K and reached a maximum; afterwards, when cooling down, the signal increased and at 150 K the change of slope was clearly seen in fig. 4.26 (b). It is worth noting that the amplitude of the piezoelectric signal was small in comparison with pure  $\text{CuInP}_2\text{S}_6$  crystal, what was determined by the difference in the electrical conductivity of the samples as well as by smaller piezoelectric parameters [142]. The presence of these two anomalies tells about the possibility of two phases: an antiferroelectric PT at  $T = 146$  K and intermediate one at 220 K [136].

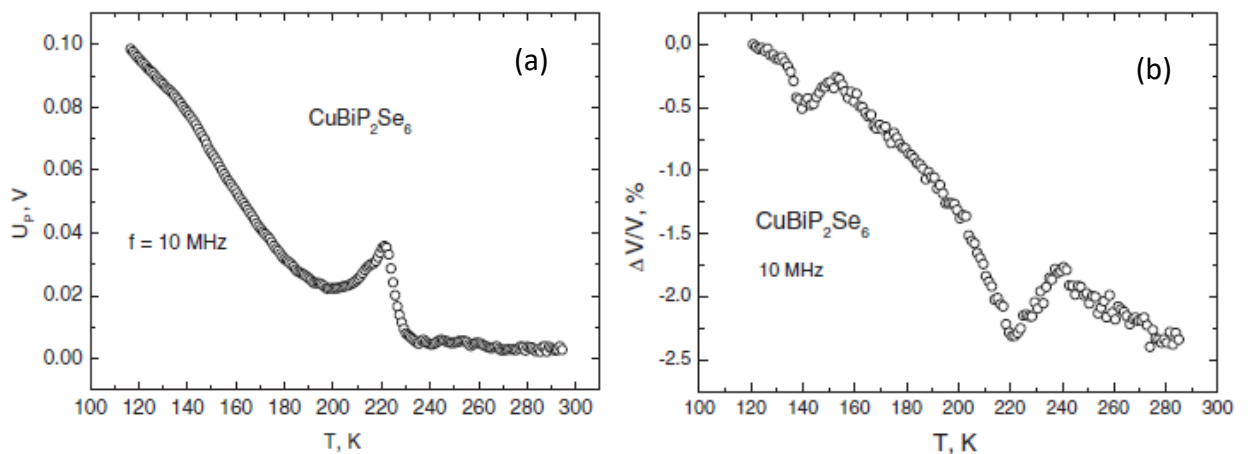


**Fig. 4.26.** Temperature dependence of the piezoelectric signal ultrasonically detected in  $\text{CuBiP}_2\text{Se}_6$  plate (a) and temperature dependence of the relative longitudinal ultrasonic velocity along c-axis (b) [136]

The piezoelectric sensitivity of  $\text{AgBiP}_2\text{S}_6$  compounds was very small in the temperature region between 120 and 300 K. As it seen in fig. 4.27 a, only a hint of a piezoelectric signal was observed at around 220 K, whose origin lies on the large electrical conductivity of  $\text{AgBiP}_2\text{S}_6$  crystals [136]. Ultrasonic frequency dependent attenuation  $\alpha = f(\omega)$  of both types (fig. 4.27 b) has been obtained by the following equation:

$$\alpha = A \frac{\omega^2 \tau}{1 + \omega^2 \tau^2}, \quad (4.1)$$

where  $A$  is the coefficient proportional to the relaxation strength,  $\tau$  - is the Maxwell relaxation time:  $\tau = \varepsilon \varepsilon_0 / \sigma$ ,  $\sigma = \sigma_{ion} + \sigma_{el}$  is the total ionic—electronic conductivity and  $\varepsilon$  is the dielectric constant.

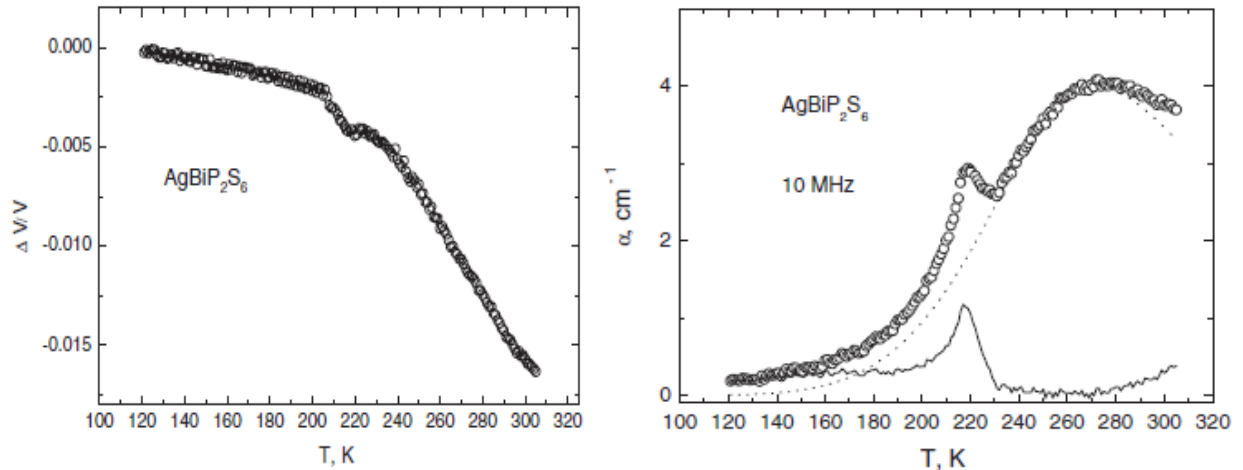


**Fig. 4.27.** Temperature dependence of longitudinal relative ultrasonic velocity measured along  $c$  axis in AgBiP<sub>2</sub>S<sub>6</sub> crystals at 10 MHz frequencies (a), temperature dependence of the longitudinal attenuation coefficient along  $c$  axis in AgBiP<sub>2</sub>S<sub>6</sub> samples (b) [136]

The obtained temperature dependence of the longitudinal attenuation has a large peak of ultrasonic attenuation below room temperature which is attributed to the ultrasonic interaction with silver ions [136].

### 4.2.3. Thermal properties

As shown in figure 4.28, the temperature dependence of the heat capacity  $C_p$  for CuInP<sub>2</sub>S<sub>6</sub> crystal shows two  $\lambda$ -shape anomalies, the first one at 309.35 K, signaling the presence of a first order transition, and the second one at 329.5 K, which has some retardation into the paraelectric phase [145].

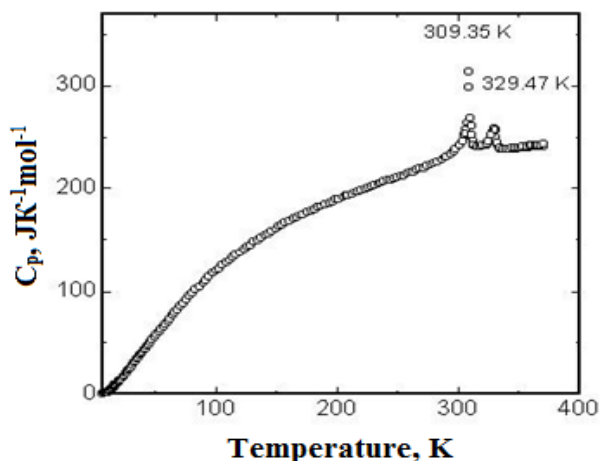


**Fig. 4.28.** Temperature dependence of heat capacity in  $\text{CuInP}_2\text{S}_6$  samples [145]

In the case of  $\text{CuInP}_2\text{Se}_6$  compound, the dependence of the molar heat capacity also exhibits a  $\lambda$ -shape anomaly. In contradistinction to the sulphide case there is only one phase transition at 226 K (fig. 4.29) [154].

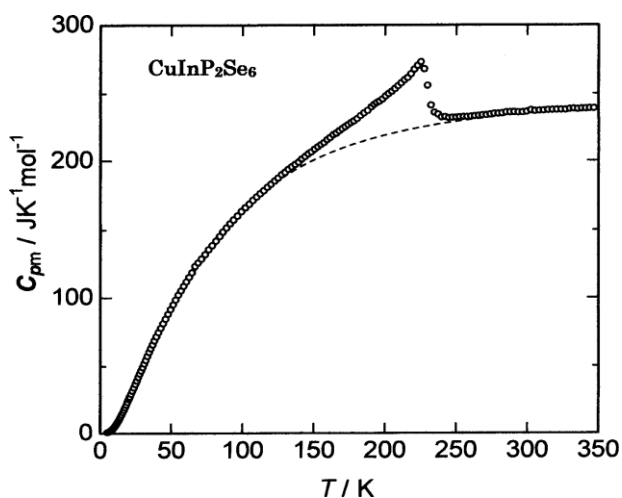


**Fig. 4.29.** Temperature dependence of heat capacity in  $\text{CuInP}_2\text{Se}_6$  samples [146]

For the rest compounds, there is no information on thermal measurements in literature prior to this work.

## Chapter 5. Structure and physical properties of $(\text{Pb}_x\text{Sn}_{1-x})_2\text{P}_2(\text{Se}_y\text{S}_{1-y})_6$ chalcogenide crystals

$(\text{Pb}_x\text{Sn}_{1-x})_2\text{P}_2(\text{Se}_y\text{S}_{1-y})_6$  ferroelectric compounds are a broad family of ferroelectric semiconductors specially interesting due to their promising photorefractive, acoustooptic, and electrooptic properties [147, 148] as well as for the complexity of their phase diagram, with the presence of a Lifshitz point (LP), incommensurate phases (IC), first and second order PT [56]. The presence of solid solutions among  $\text{Sn}_2\text{P}_2\text{S}_6$ ,  $\text{Sn}_2\text{P}_2\text{Se}_6$ ,  $\text{Pb}_2\text{P}_2\text{S}_6$  and  $\text{Pb}_2\text{P}_2\text{Se}_6$  allows to obtain ferroelectrics-semiconductors with different desirable physical properties. Hence, it is possible to design materials with different structural and electronic attributes and characteristics and the ultimate application of these semiconductors in various electronic devices. Figure 5.1 demonstrates the common model representing a crystal structure of  $M_2^{2+}[P_2X_6]^{4-}$  crystal.

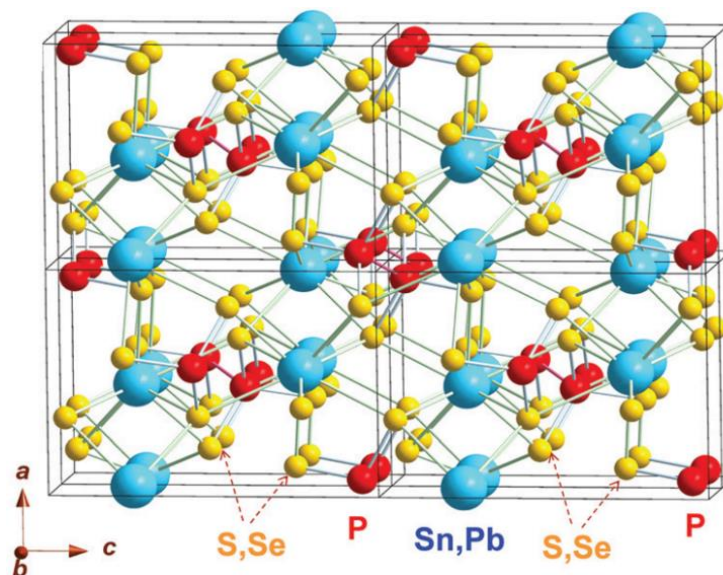


**Fig. 5.1.** Structure of  $M_2^{2+}[P_2X_6]^{4-}$  phosphorus chalcogenide crystals. Blue, red and yellow spheres represent  $M^{2+}$  (Pb, Sn), P and X (S, Se) atoms respectively [149]

This chapter consists of three parts: in the first part the crystalline structure of this type of materials will be described in detail, in the second one the general shape of the phase diagram will be comprehensively describe; finally, in the third part there is a consideration of some thermal properties of  $\text{Sn}(\text{Pb})_2\text{P}_2\text{S}(\text{Se})_6$  ferroelectrics.

## 5.1. Crystalline structure of $(\text{Pb},\text{Sn})_2\text{P}_2(\text{Se},\text{S})_6$ compounds

### 5.1.1. $\text{Sn}_2\text{P}_2\text{S}(\text{Se})_6$ compounds

$\text{Sn}_2\text{P}_2\text{S}(\text{Se})_6$  crystals, as well as any of the  $M_2^{2+}[\text{P}_2\text{X}_6]^{4-}$  compounds, are ion-covalent ferroelectrics with the common  $[\text{P}_2\text{S}(\text{Se})_6]^{4-}$  sublattice. In contrast to most industrially relevant ferroelectrics, which are insulators,  $\text{Sn}_2\text{P}_2\text{S}_6$  has pronounced semiconductor features due to its small band gap of 2.3 eV at room temperature [147]. For these specific compounds of the  $M_2^{2+}[\text{P}_2\text{X}_6]^{4-}$  type, two thirds of the octahedral centers are occupied by  $M^{2+}$  cations. The remaining one third are occupied by P–P bonds which covalently bond to the sulfur atoms, with each P atom having tetrahedral coordination with three S atoms and one P atom, forming an ethane-like  $(\text{P}_2\text{X}_6)^{4-}$  unit. Each S atom is bonded to a single P atom and coordinated by two sites of cation [56].

The crystallographic unit cell of  $\text{Sn}_2\text{P}_2\text{S}_6$  (SPS) comprises two formula units ( $Z = 2$ ). At room temperature the crystalline structure of  $\text{Sn}_2\text{P}_2\text{S}(\text{Se})_6$  can be described by the monoclinic space group Pc [150, 151]. The cell parameters at ambient conditions for the SPS crystal are as follows:  $a = 9.378 \text{ \AA}$ ,  $b = 7.488 \text{ \AA}$ ,  $c = 6.513 \text{ \AA}$ , and the angle  $\beta = 91.15^\circ$ . The unit cell volume is  $456 \text{ \AA}^3$  [152, 153]. The lengths of the Sn–S ionic bounds (2.77 - 3.451  $\text{ \AA}$ ) are considerably larger than for P–S and P–P. The P–S bonds in the pyramids have different lengths in the range 2.015 - 2.035  $\text{ \AA}$ . Tin atoms are located between the ions inside the polyhedron formed by 7 or 8 sulphur atoms. Above about 337 K the crystal undergoes a second order paraelectric PT into another monoclinic phase, possessing the center of inversion space group  $\text{P2}_1/\text{c}$  with “off-center” Sn displacement playing the role of the order parameter (fig.5.2 (a)) [154].

Electronic structure studies of  $\text{Sn}_2\text{P}_2\text{S}_6$  confirm that tin in SPS occurs as  $\text{Sn}^{2+}$  ions [155, 156]. The spectroscopy data has shown that the Sn ion is in the 2+ state with very high ionicity ( $\sim 1.6$ ) [157].

In fig. 5.2 (b) the cut is done through three consecutive Sn–S–P atoms, and their other neighbors almost in, or slightly off, this plane. In work [155], the charge-density plot has demonstrated a striking contrast between an ionized shape of Sn atoms (indicated by perfect sphericity of the electron density in its neighborhood) and a strong covalency along the S–P–P–S chains. One notices, moreover, an electron-density displacement from phosphorus to sulfur atoms. Away from the  $\text{P}_2\text{S}_6$  groups and Sn ions docked between them, there is hardly any charge density accumulated [155].

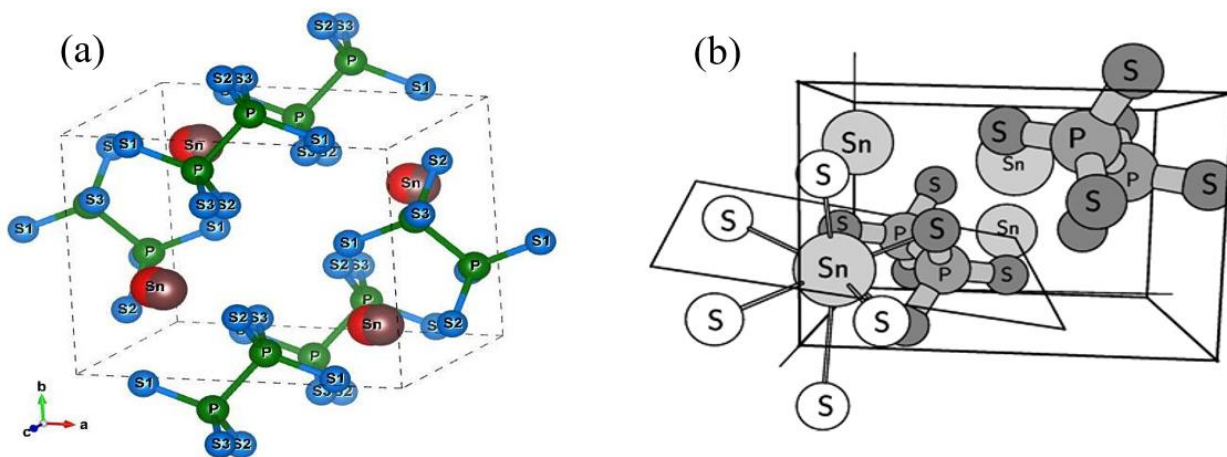


**Fig. 5.2.** Structure of  $\text{Sn}_2\text{P}_2\text{S}_6$  type crystals in paraelectric ( $P2_1/c$ ) phase with shown shifts of cation atoms in ferroelectric ( $Pc$ ) phase (a) [158], unit cell with 2 formula units (shown in gray) and some additional S atoms (in white) obtained by translation to complete the near-neighbor shell of a Sn atom (b) [155]

The tin selenide  $\text{Sn}_2\text{P}_2\text{Se}_6$  (SPSe) metal thiophosphate is similar in its structure to SPS. The divalent metal cation structures are similar as those represented in figure 5.2. However, differences may exist due to the increased P–Se bond distances and Se–P–Se bond angles reported for SPSe. At room temperature SPSe has the next cell parameters:  $a = 6.815 \text{ \AA}$ ,  $b = 7.671 \text{ \AA}$ ,  $c = 9.626 \text{ \AA}$ ,  $\beta = 91.01^\circ$ . Hence, the unit cell volume is here increased with a value of  $503.2 \text{ \AA}^3$  [159].

$\text{Sn}_2\text{P}_2\text{Se}_6$  exhibits three phases; at room temperature it is paraelectric ( $\text{P2}_1/\text{c}$ ), at  $T_i \approx 221$  K a second order transition takes place to a modulated incommensurate phase (IC), and at  $T_c \approx 193$  K the crystal shows a first order transition to the ferroelectric phase (Pc) [153, 160, 161]. The period of transverse wave modulation of spontaneous polarization in the IC phase is about 14 unit cells [162]. The  $\text{Sn}^{2+}$  atoms are surrounded by eight Se atoms forming a bicapped trigonal prism (BTP), which are depicted on fig. 5.3 a, b at low and room temperature. Octahedra containing a couple of phosphorus atoms are connected by empty octahedra and form chains along the [010] and [101] directions.

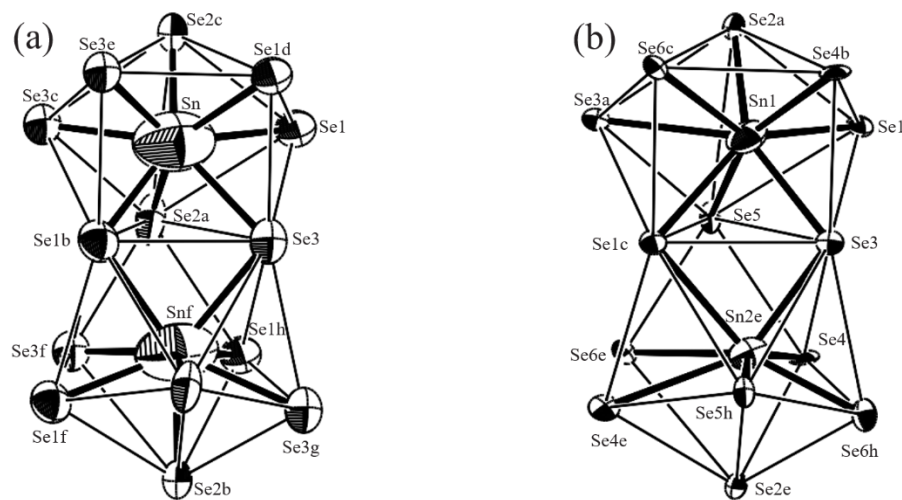


**Fig. 5.3.** Association of two  $\text{Sn}_2\text{Se}_8$  polyhedra along the [010] direction, a: paraelectric phase (293K), b: ferroelectric phase (150K) [159]

In the paraelectric phase, displacements of  $\text{Sn}^{2+}$  cations have been detected, two tin sites being separated by about  $0.34 \text{ \AA}$ . The comparison of the two crystal structures has showed that tin ions are shifted from the disordered state in the high-temperature phase (paraelectric) to the site appropriate for tin in the low-temperature phase (ferroelectric). The displacements of tin atoms are about  $0.13 \text{ \AA}$ . In general, the displacement from the average Sn-position in the paraelectric phase to the Sn-position in the ferroelectric phase is about  $0.30 \text{ \AA}$ . A spontaneous polarization of the structure obviously arises due to these displacements. Moreover, the average direction of these displacements is perpendicular to the modulation wave vector direction in the IC

phase, showing the prime importance of such movements on the incommensurate phase formation [161, 163].

The comparison of the atomic displacement parameters of the tin atom in the two phases shows that they are not proportional to the temperature [163]. A simple Debye approximation for the contribution of the acoustic phonon predicts a linear dependence with temperature. In fig. 5.4 the (equivalent) atomic displacement parameters of  $\text{Sn}^{2+}$  cations are plotted at the temperatures of the structure determinations for SPS and SPSe. The atomic displacement parameters of the tin atoms of both compounds in the ferroelectric phase are almost the same (dashed) lines. The atomic displacement parameter of Sn in the paraelectric phase is for both compounds significantly higher than the extrapolated lines of the ferroelectric phase.

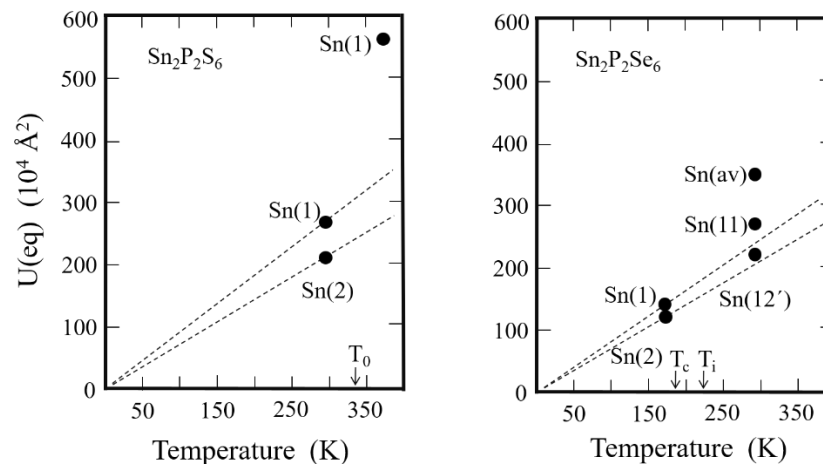


**Fig. 5.4.** Isotropic atomic displacement parameters for  $\text{Sn}^{2+}$  cations for  $\text{Sn}_2\text{P}_2\text{S}_6$  (left) and  $\text{Sn}_2\text{P}_2\text{Se}_6$  (right) versus temperature on X-ray data [163]

### 5.1.2. $\text{Pb}_2\text{P}_2\text{S}(\text{Se})_6$ compounds

At ambient conditions  $\text{Pb}_2\text{P}_2\text{S}_6$  crystallizes in a monoclinic  $\text{P2}_1/\text{c}$  structure and remains in this centrosymmetric phase till 0 K (fig. 5.5) [164]. The crystal lattice parameters are:  $a = 6.612 \text{ \AA}$ ,  $b = 7.466 \text{ \AA}$ ,  $c = 11.349 \text{ \AA}$ ,  $\beta = 124.09^\circ$ . The unit cell volume is  $462 \text{ \AA}^3$ . The difference in volumes for  $\text{Sn}_2\text{P}_2\text{S}_6$  and  $\text{Pb}_2\text{P}_2\text{S}_6$  compounds is quite small in view of the difference in the atomic radii of octa-coordinated tin and lead atoms:  $1.58 \text{ \AA}$  and  $1.75 \text{ \AA}$ . Thus, the  $\text{Sn}^{2+}$  ions are in a less “squeezed” state,

which is reflected in their ferroactivity, suggesting that compounds with  $\text{Sn}^{2+}$  cation should possess higher PT temperature [56].

As mentioned above, in the paraelectric phase all of the members of SPS uniaxial ferroelectric family compounds are characterized by the  $P2_1/c$  space group. For  $\text{Pb}_2\text{P}_2\text{Se}_6$  crystal  $\text{Pb}^{2+}$  cations are bonded to ethane-like  $[\text{P}_2\text{Se}_6]^{4-}$  anions [166]. The only difference between these compounds is due to the difference in the sizes of the ions which provoke a change in the crystal lattice parameters which are:  $a = 6.910 \text{ \AA}$ ,  $b = 7.660 \text{ \AA}$ ,  $c = 11.819 \text{ \AA}$ ,  $\beta = 124.38^\circ$ , the unit cell volume is  $513 \text{ \AA}^3$  [167, 168]. The structure of these compounds is shown in figure 5.6.

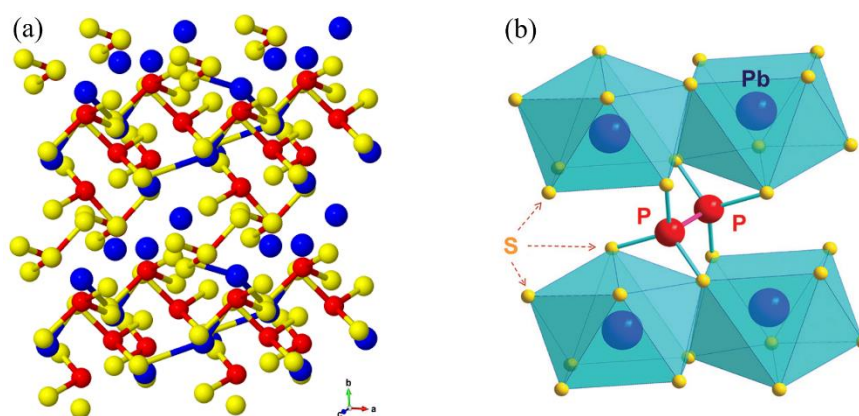


**Fig. 5.5.** The crystal structures of  $\text{Pb}_2\text{P}_2\text{S}_6$  at ambient conditions. (a) General view [165]; (b) The P–P bonds [149]. Blue, red and yellow spheres represent Pb, P and S respectively

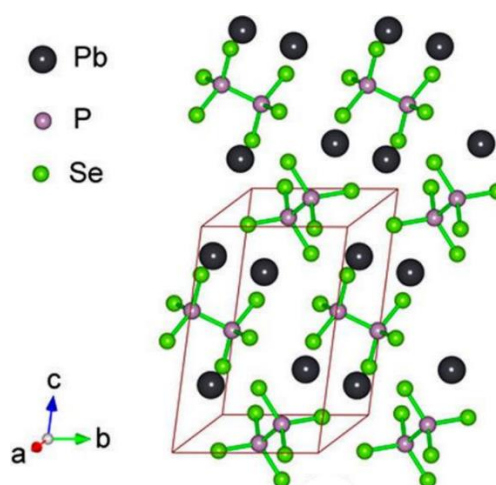


**Fig. 5.6.**  $\text{Pb}_2\text{P}_2\text{Se}_6$  crystal structure. Each P (pink) is attached to Se (green) in a distorted tetrahedral arrangement. Polarization arises from asymmetric displacements of Pb along the  $[101]$  direction [166]

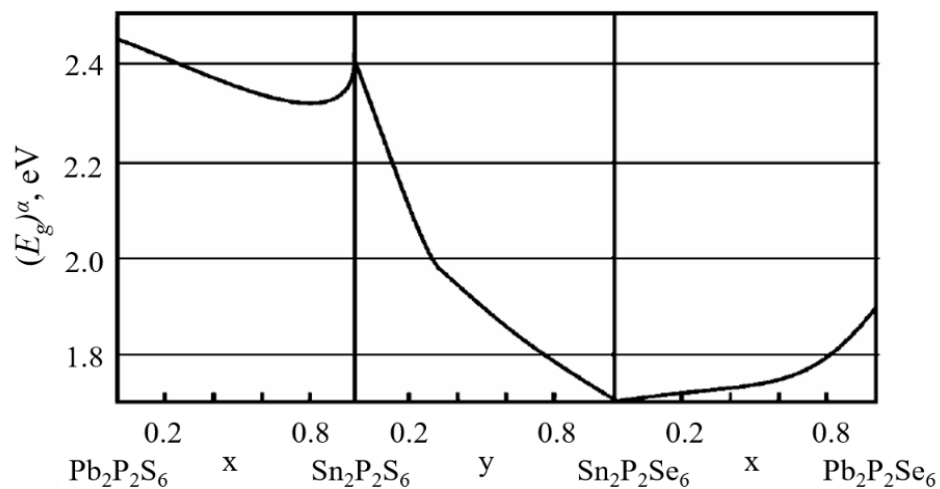
In table 5.1 the main structural parameters which characterize the monoclinic crystalline lattice of  $\text{Sn}(\text{Pb})_2\text{P}_2\text{S}(\text{Se})_6$  ferroelectric thiophosphates are given.

Table 5.1

Crystalline lattice parameters of  $\text{Sn}(\text{Pb})_2\text{P}_2\text{S}(\text{Se})_6$  ferroelectric compounds in ferroelectric (ferro) and paraelectric (para) phases [152, 153, 159, 164, 168]

Compound	Symmetry	Lattice parameters			$\beta$ [°]	Cell volume [Å <sup>3</sup> ]
		a [Å]	b [Å]	c [Å]		
$\text{Sn}_2\text{P}_2\text{S}_6$ (ferro)	Pc	9.378	7.488	6.513	91.15	456
$\text{Sn}_2\text{P}_2\text{S}_6$ (para)	$\text{P2}_1/\text{c}$	9.362	7.493	6.550	91.17	457
$\text{Sn}_2\text{P}_2\text{Se}_6$ (ferro)	Pc	6.805	7.708	9.616	91.03	504.4
$\text{Sn}_2\text{P}_2\text{Se}_6$ (para)	$\text{P2}_1/\text{c}$	6.815	7.671	9.626	91.01	503.2
$\text{Pb}_2\text{P}_2\text{S}_6$ (para)	$\text{P2}_1/\text{c}$	6.612	7.466	11.349	124.09	462
$\text{Pb}_2\text{P}_2\text{Se}_6$ (para)	$\text{P2}_1/\text{c}$	6.910	7.660	11.819	124.38	513

The absorption edge of SPS and its structural analogs has been studied in work [169]. The energy position of the absorption edge  $E_g^\alpha = h\nu_\alpha$  (with  $\alpha$  being the absorption coefficient) for  $\text{Sn}(\text{Pb})_2\text{P}_2\text{S}(\text{Se})_6$  mixed compounds is shown in Fig. 5.7.



**Fig. 5.7.** Concentration dependences of  $E_g^\alpha$  ( $\alpha = 150 \text{ cm}^{-1}$ ) for the solid solutions based on  $\text{Sn}_2\text{P}_2\text{S}_6$  at  $T = 293 \text{ K}$  and  $p = p_{atm}$  [169]

It is clearly seen that the substitution of sulphur by selenium in the anion sublattice decreases the  $E_g^\alpha$  value, while the substitution tin by lead produces the contrary effect [169].

## 5.2. Compositional phase diagram study of the $(\text{Pb}_x\text{Sn}_{1-x})_2\text{P}_2(\text{Se}_y\text{S}_{1-y})_6$ system

### 5.2.1. General shape of the phase diagram of $\text{Sn}(\text{Pb})_2\text{P}_2\text{S}(\text{Se})_6$ compounds

Over the last decades various scientific studies on dielectric, thermal, optical, elastic and acoustic properties of these solid solutions have been conducted, which makes it possible to comprehensively describe the complex phase diagram of these solid compounds [2, 43, 94, 95, 96, 97, 98, 170, 171, 172, 173, 174, 175, 176, 177, 178, 179, 180, 181, 182, 183, 184, 185, 186, 187].

Let's consider the main features of the “temperature-concentration” phase diagram of  $(\text{Pb}_x\text{Sn}_{1-x})_2\text{P}_2(\text{Se}_y\text{S}_{1-y})_6$  ferroelectric compounds by substituting S atoms by Se in the anion sublattice and Sn by Pb in the cation one (fig. 5.8). Replacing Se ions instead of S for  $y < 0.28$  leads to a smooth splitting of the second order PT line (dashed line on fig. 5.8) into a first order (solid curves) and second order (dashed curves) phase transition lines at  $y = 0.28$ . Consequently, in the crystal SPSe two phase transitions take place: a second-order PT at  $T_i = 221$  K and a first-order one at  $T_c = 193$  K [160, 176]. Substituting Sn by Pb in the  $(\text{Pb}_x\text{Sn}_{1-x})_2\text{P}_2\text{S}_6$  series sharply reduces the temperature of the ferroelectric PT which becomes as low as 4.2 K for  $x = 0.61$ . In this case, the PT does not change its character and remains continuous [164].

Tin by lead substitution in the cation sublattice in  $(\text{Pb}_x\text{Sn}_{1-x})_2\text{P}_2\text{Se}_6$  gives the same effect as in compounds with sulphur. Pb ions lower the temperatures of the transitions  $T_i$  and  $T_c$ . At the same time, substitution lead by tin increases the width of the IC phase. For instance, the temperature region where the IC phase exists broadens out; it is larger than 100 K at  $x = 0.4$ . It should be noted that the first-order and second-order PT lines approach 0 K at  $x = 0.40$  and  $x = 0.61$ , respectively [164].

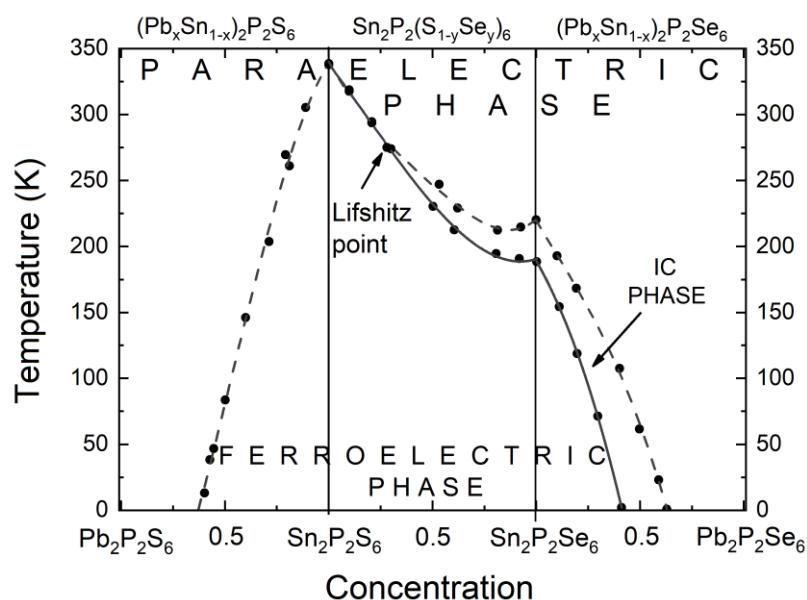


**Fig. 5.8.** Phase diagram of  $Sn(Pb)_2P_2S(Se)_6$  mixed compounds: The dashed lines show the second-order phase transitions: from the paraelectric phase to the ferroelectric one in  $(Pb_xSn_{1-x})_2P_2S_6$  and in  $Sn_2P_2(Se_yS_{1-y})_6$  with  $y < 0.28$ , while in  $Sn_2P_2(Se_yS_{1-y})_6$  with  $y > 0.28$  and  $(Pb_xSn_{1-x})_2P_2Se_6$  it demonstrates the transition to an IC phase. The continuous lines indicate the first order transition from the IC to the ferroelectric phase [56]

Based on heat capacity and dielectric studies data [187], the evolution of the character of the PT and the shape of the compositional phase diagram in  $Sn(Pb)_2P_2S(Se)_6$  compounds has been determined. When lead and sulphur simultaneously substitute tin and selenium, respectively, the temperatures  $T_i$  and  $T_c$  decrease at the same concentration rates, i.e. the width of the IC phase is nearly constant (fig. 5.9).

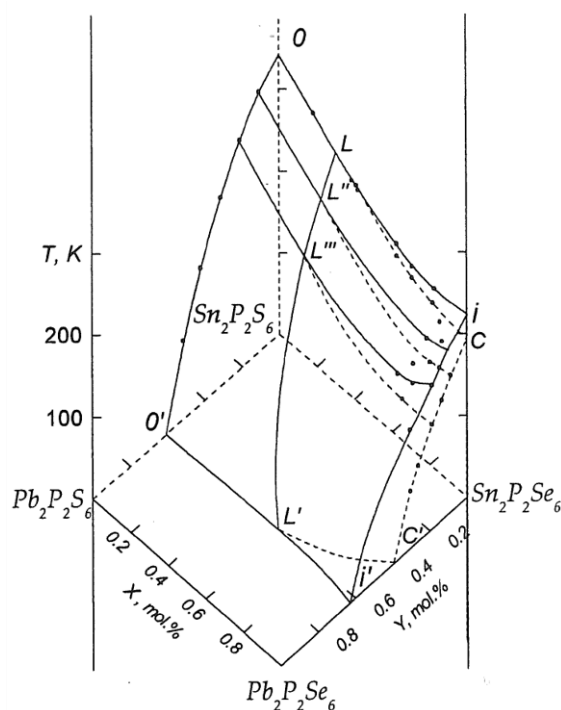


**Fig. 5.9.** Phase diagram for  $\text{Sn}(\text{Pb})_2\text{P}_2\text{S}(\text{Se})_6$  mixed compounds. Dotted lines: second-order PT. Solid lines: first-order PT [187]

### 5.2.2. Phase diagram of the $\text{Sn}_2\text{P}_2(\text{Se}_y\text{S}_{1-y})_6$ crystals. Lifshitz point on the state diagram

Considered in its general form (fig. 5.7), the phase diagram can be divided in three parts:  $\text{Sn}_2\text{P}_2\text{S}_6 - \text{Sn}_2\text{P}_2\text{Se}_6$ ,  $\text{Sn}_2\text{P}_2\text{Se}_6 - \text{Pb}_2\text{P}_2\text{Se}_6$  and  $\text{Pb}_2\text{P}_2\text{S}_6 - \text{Sn}_2\text{P}_2\text{S}_6$ . Foremost, we consider available data on temperature-concentration phase diagram of the SPS-SPSe compounds ( $\text{Sn}_2\text{P}_2(\text{Se}_y\text{S}_{1-y})_6$ ). X-ray diffraction [162, 172], ultrasound [94, 183], dielectric [173, 184] and calorimetric [43, 96, 176] data are collected on fig. 5.10. On replacing sulphur by selenium ions, a relatively slow reduction of the PT temperature occurs. It is also clearly seen that the PT line starts to be splitted up at  $y \sim 0.28$ ,  $T = 284$  K. This special splitting point is known as a Lifshitz point (LP) which separates the PT from the paraelectric phase into the ferroelectric or IC phases. The modulated IC phase is observed with the same space group as the paraelectric one ( $\text{P2}_1/\text{c}$ ).

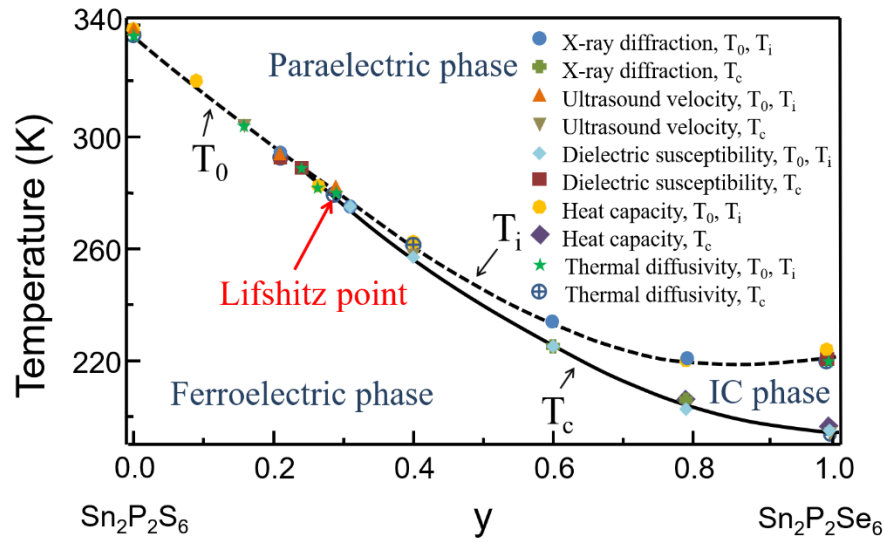


**Fig. 5.10.** Phase diagram of  $\text{Sn}_2\text{P}_2(\text{S}_{1-y}\text{Se}_y)_6$  crystals.  $T_0$  at  $y < 0.28$  and  $T_i$  at  $y > 0.28$  are the second order paraelectric-ferroelectric and paraelectric-IC transitions, respectively (dashed line).  $T_c$  is the first-order lock-in IC-ferroelectric transition at  $y > 0.28$  (solid line) [43, 94, 96, 162, 172, 173, 174, 183]

The position of the LP could also be appreciated from the evolution of the temperature dependence of the phonon spectra at different concentrations of S and Se in the cation sublattice. The results, obtained from the treatment of neutron scattering, revealed a linear interaction of low-energy soft optic and acoustic phonon branches in SPS<sub>y</sub> crystal [185]. This interaction was phenomenologically described as a Lifshitz-type invariant in the thermodynamic potential function for proper uniaxial ferroelectrics with type II IC phase [185, 186]. Such linear interaction near the LP results in a softening of acoustic phonons, which have been observed for the  $\text{Sn}_2\text{P}_2(\text{Se}_y\text{S}_{1-y})_6$  crystals in Brillouin scattering and ultrasound investigations [94].

The X-ray experiments have shown that there is no variation of the modulation wave-vector orientation which occurs in the IC phase with the composition variation. Thus, only the length of the wave-vector depends on the temperature, while its direction remains almost constant. The rate of the reduction of its value on cooling increases on approaching the Lifshitz point (fig. 5.11) [162]. In this manner, the modulation vector on the  $T_i(y)$  line is changing as  $y \rightarrow y_{LP}$  as  $q_i^2 \sim (y - y_{LP})$  (fig.5.12).

Such behavior agrees well with the one predicted within the framework of the mean-field model for the proximity to the LP [188].

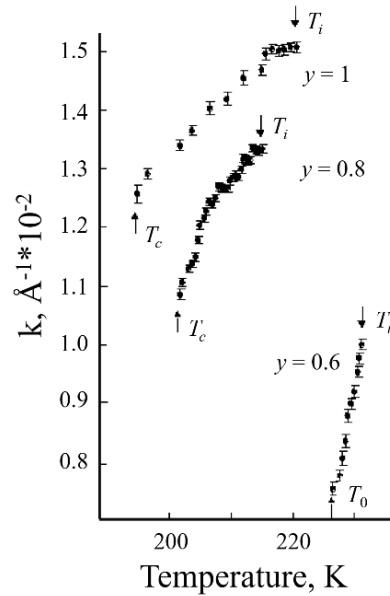


**Fig. 5.11.** Temperature behavior of the modulation wave vector for  $\text{Sn}_2\text{P}_2(\text{Se}_y\text{S}_{1-y})_6$  crystals in the IC phase [162]

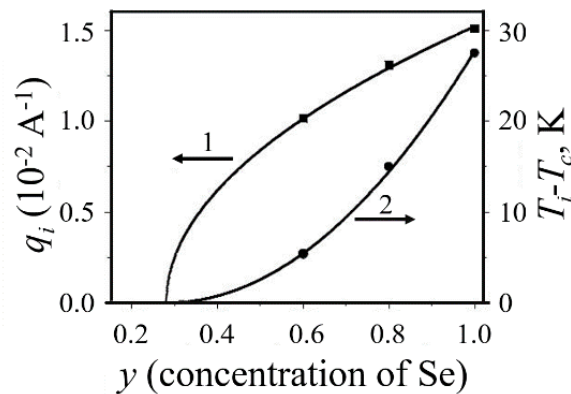


**Fig. 5.12.** The concentration dependencies of the IC phase temperature width  $T_i - T_c$  and modulation wave number for  $\text{Sn}_2\text{P}_2(\text{Se}_y\text{S}_{1-y})_6$  crystals  $q_i$ . Lines denote the fit by relations  $q_i \sim (y - y_{LP})^{0.5}$  and  $T_i - T_c \sim (y - y_{LP})^2$  [162]

Rushchanskii *et al* [194] have studied the temperature dependence of the hypersound velocity by means of Brillouin light scattering. For  $\text{Sn}_2\text{P}_2(\text{Se}_y\text{S}_{1-y})_6$  compounds, the temperature dependence of the longitudinal hypersound in [001] direction is presented in fig. 5.13. The temperature dependencies of the longitudinal ultrasound velocity show the sharpest shape for  $y = 0.22$ , reaching a minimal value

of about 3100 m/s (fig. 5.13 (d)). For the compound with 30% Se, the anomaly of ultrasound velocity becomes shallower due to temperature hysteresis of the IC phase and first-order lock-in transition.

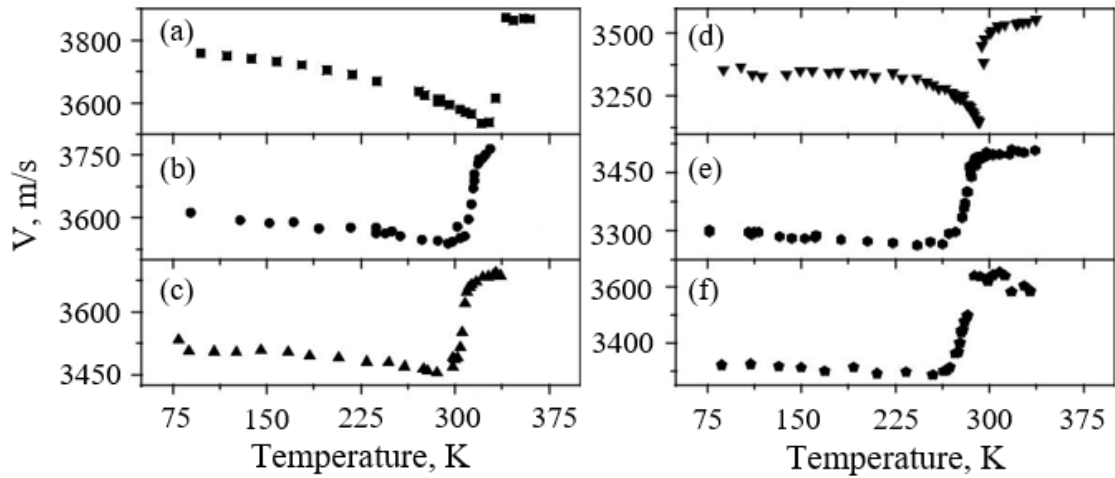
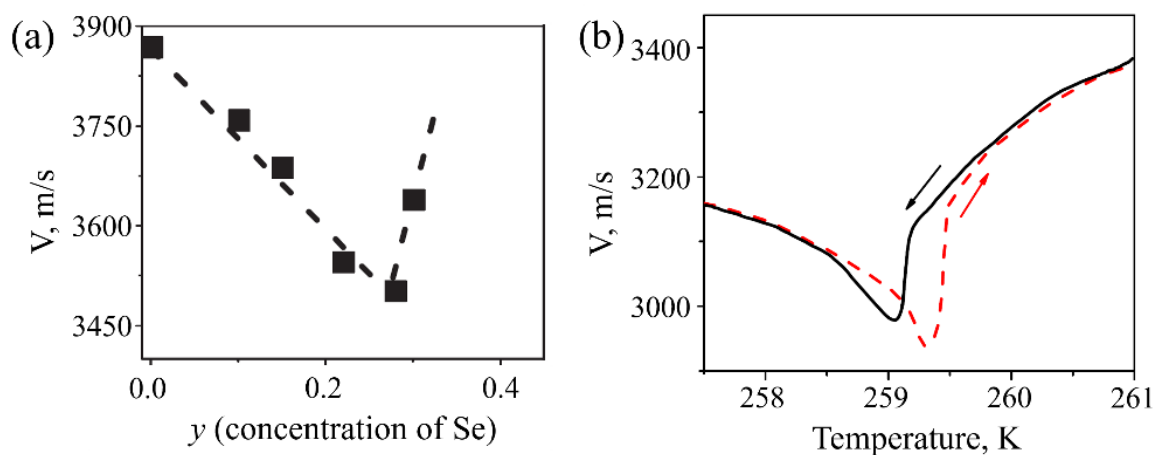


**Fig. 5.13.** Temperature dependence of longitudinal hypersound velocity obtained by Brillouin scattering in Z(X X)-Z geometry for  $\text{Sn}_2\text{P}_2(\text{Se}_y\text{S}_{1-y})_6$  mixed crystals with (a)  $y = 0$ , (b)  $y = 0.10$ , (c)  $y = 0.15$ , (d)  $y = 0.22$ , (e)  $y = 0.28$ , (f)  $y = 0.30$  [183]

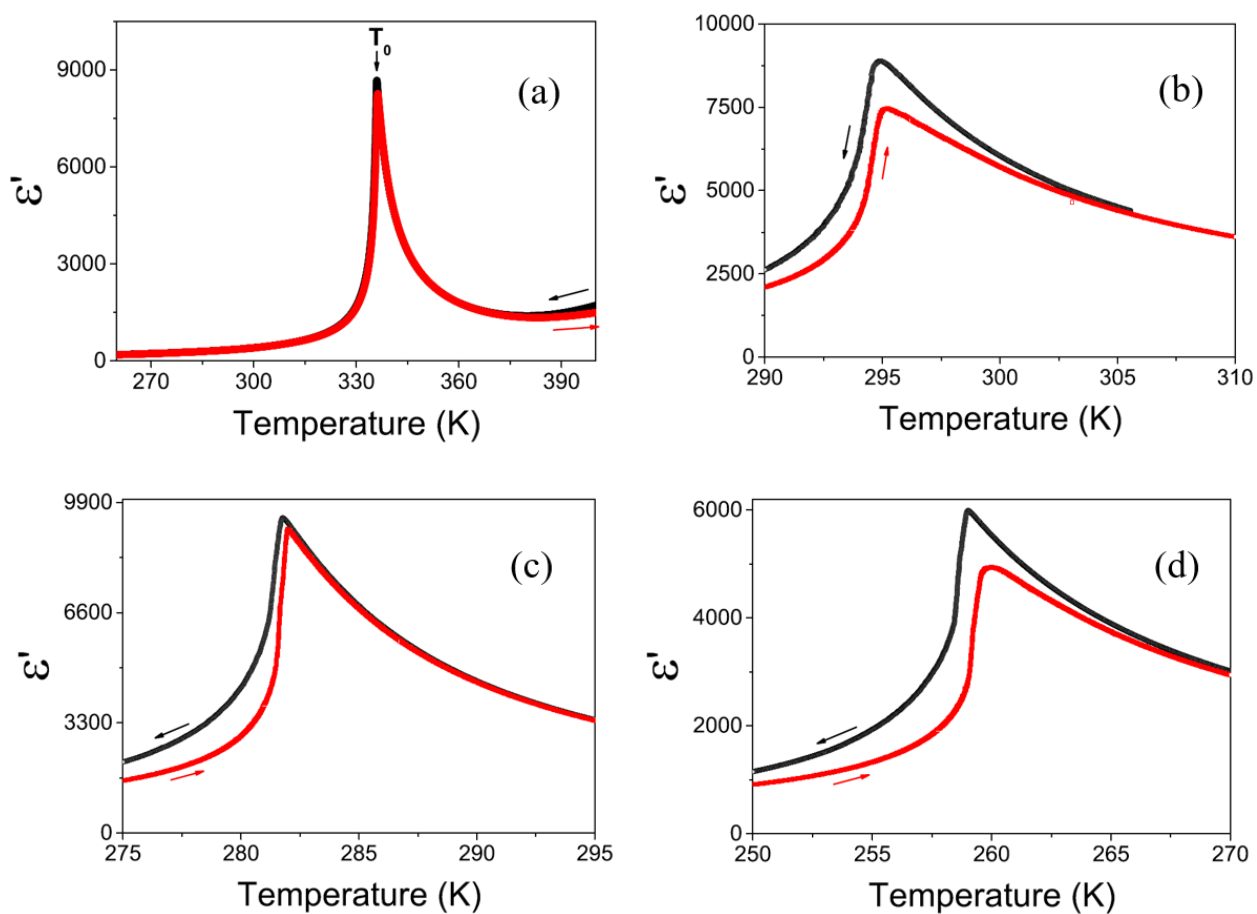
Figure 5.14 (a) shows the total amount of collected values of the hypersound velocity in the paraelectric phase according to data from fig. 5.13. The minimal value of velocity has been obtained near the expected composition  $y_{LP} = 0.28$ . The ultrasound data for  $\text{Sn}_2\text{P}_2(\text{Se}_{0.4}\text{S}_{0.6})_6$  (fig. 5.14 (b)) show a temperature hysteresis of about 0.3 K in cooling and heating modes. Hence, that is a hint of a first-order lock-in transition at  $T_c$ . This hysteresis is comparable with the temperature interval of the IC phase  $T_i - T_c$  for this composition [183].

At the same work [183] authors have studied dielectric properties of the  $\text{Sn}_2\text{P}_2(\text{Se}_y\text{S}_{1-y})_6$  ferroelectric crystals. From these studies it is well established that in the case of a crystal  $\text{Sn}_2\text{P}_2\text{Se}_6$  there are two PT ( $T_c \sim 195$  K and  $T_i \sim 223$  K) with the IC phase is ranged in temperature interval  $T_i - T_c \sim 28$  K (fig. 5.15 (e)), and the presence of a IC phase with temperature width of about 0.6 K for  $\text{Sn}_2\text{P}_2(\text{Se}_{0.4}\text{S}_{0.6})_6$

(fig. 5.15 (d)), while for the rest of concentrations only one PT was found (fig. 5.14 (a, b, c)).



**Fig. 5.14.** Temperature dependence of: (a) the concentration behavior of the hypersound velocity in a paraelectric phase; (b) the longitudinal ultrasound velocity in  $\text{Sn}_2\text{P}_2(\text{Se}_{0.4}\text{S}_{0.6})_6$  [183]



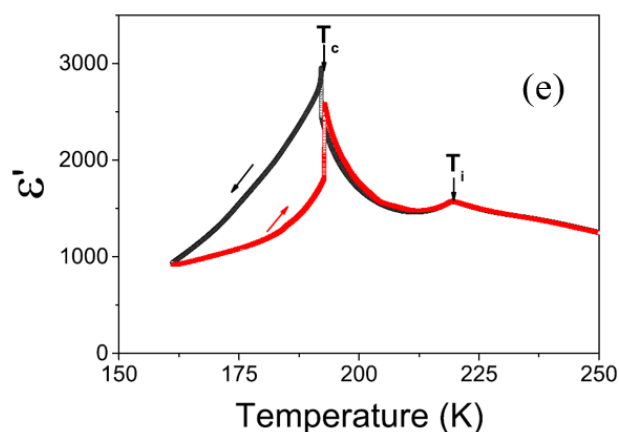


**Fig. 5.15.** Temperature dependencies of dielectric susceptibility for  $\text{Sn}_2\text{P}_2(\text{Se}_y\text{S}_{1-y})_6$  crystals measured at 0.005 K/min cooling and heating rate. (a)  $y = 0$ ; (b)  $y = 0.22$ ; (c)  $y = 0.28$ ; (d)  $y = 0.4$ ; (e)  $y = 1$  [183]

### 5.2.3. Phase diagram of $(\text{Pb}_x\text{Sn}_{1-x})_2\text{P}_2\text{S}_6$ crystals

Let's consider the phase diagram for  $(\text{Pb}_x\text{Sn}_{1-x})_2\text{P}_2\text{S}_6$  phosphorous chalcogenide ferroelectrics. The PT temperatures obtained by dielectric [171] and calorimetric [44] measurements versus lead concentration are shown in fig. 5.16.

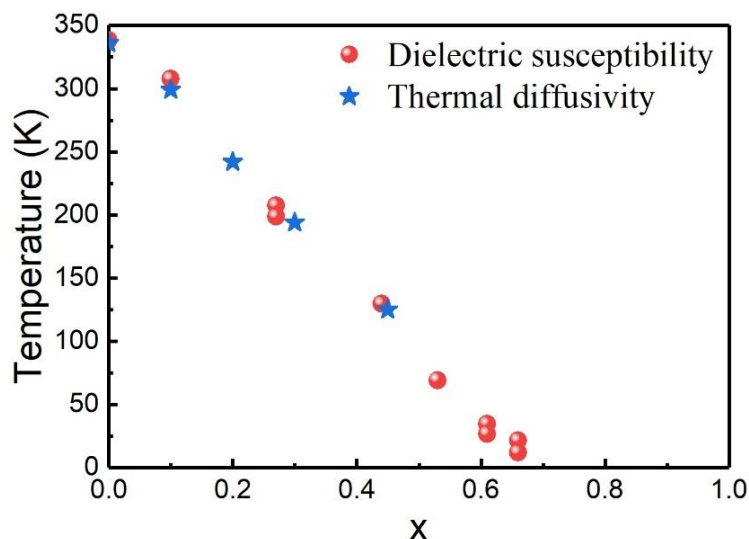


**Fig. 5.16.** Phase diagram of  $(\text{Pb}_x\text{Sn}_{1-x})_2\text{P}_2\text{S}_6$  crystals. For the compositions with  $x = 0.27$ ,  $0.61$ , and  $0.66$ , the positions of the dielectric anomalies are shown. Red spheres - dielectric data [171], blue stars exhibit thermal diffusivity data [98]

Increasing the lead concentration leads to a decrease PT temperature in a linear dependence with  $x$  between  $x = 0$  and  $x = 0.27$ . This can be explained as follows: the ionic radius of the  $\text{Pb}^{2+}$  ion is larger than that of the  $\text{Sn}^{2+}$  ion, and so the addition of lead increases the space available for tin ions. But due to the fluctuations in the concentration of a particular sample the discrepancy takes place after reaching  $x = 0.3$ , the line bends showing a slight upward curvature and achieves 4.2 K at concentrations  $x = 0.66$ . It is recognized that the tin ion is mobile; whereas, the lead ion is not so mobile in the crystal. In the region after  $x = 0.66$  the PT is frozen. Indeed, in the case of  $x = 0.8$  and  $x = 1.0$ , calorimetric measurements have been performed down to 18 K, confirming the absence of the PT [98].

Rushchanskii *et al.* have also performed dielectric measurements for  $x = 0, 0.1, 0.2, 0.3$ , and  $0.45$  (fig. 5.17) [2]. At  $x = 0.2$ , there might be a crossover phenomena when the ferroelectric PT changes its character to first order and that tricritical point (TCP) could be reached at  $x > 0.2$  and that some phase coexistence takes place there, which can be seen from the transformation of the low-frequency dielectric susceptibility temperature anomalies (fig. 5.17 (a)). For the sample with  $x = 0.3$ , the anomalies of the dielectric susceptibility curves become broader and have a clear temperature hysteresis. For these compositions, the temperature behavior of the anomalies is smeared into the ferroelectric phase. For  $x = 0.45$ , the dielectric losses have the highest value near the first-order PT and their temperature dependence has a shape of an almost symmetric maximum (fig. 5.17 (b)), and the shape of curve is also different in heating or cooling runs which could be the evidence of a first-order PT [2].

The ultrasonic studies performed in the same work [2] show that for the sample with 30 % of lead the shape of the anomaly differs; there is an additional contribution on the step of sound velocity (fig. 5.18). Such singularities could be explained as follows: a first-order PT is already reached for  $x = 0.3$  and phase coexistence produces those changes and makes the anomaly more complex in shape.

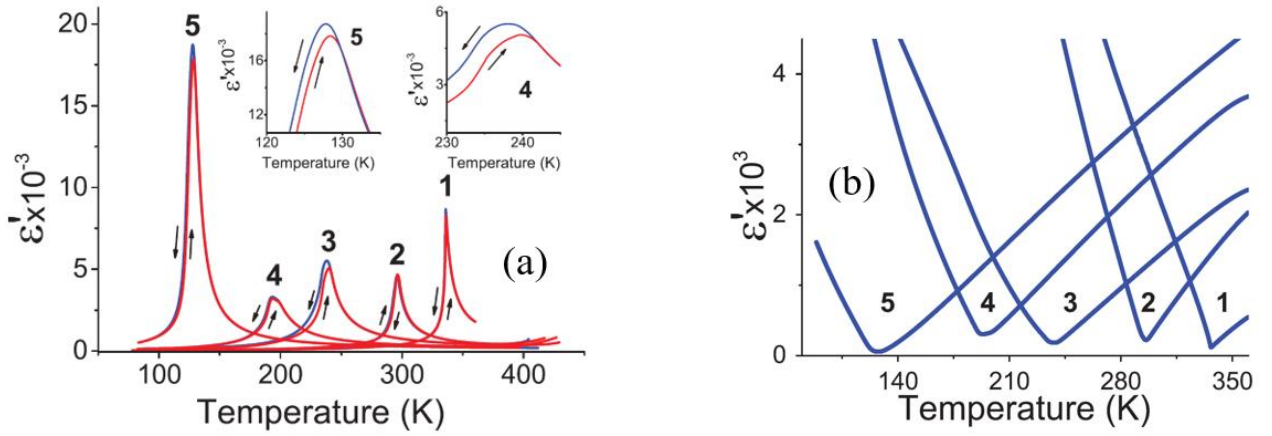


**Fig. 5.17.** Temperature dependence of the real part of the dielectric susceptibility at  $10^4$  Hz on cooling (blue lines) and heating (red lines) (a), reciprocal real part of the dielectric susceptibility on cooling at  $10^4$  Hz for  $(\text{Pb}_x\text{Sn}_{1-x})_2\text{P}_2\text{S}_6$  mixed crystals for different concentrations of lead: (1) 0; (2) 0.1; (3) 0.2; (4) 0.3; (5) 0.45 (b) [2]

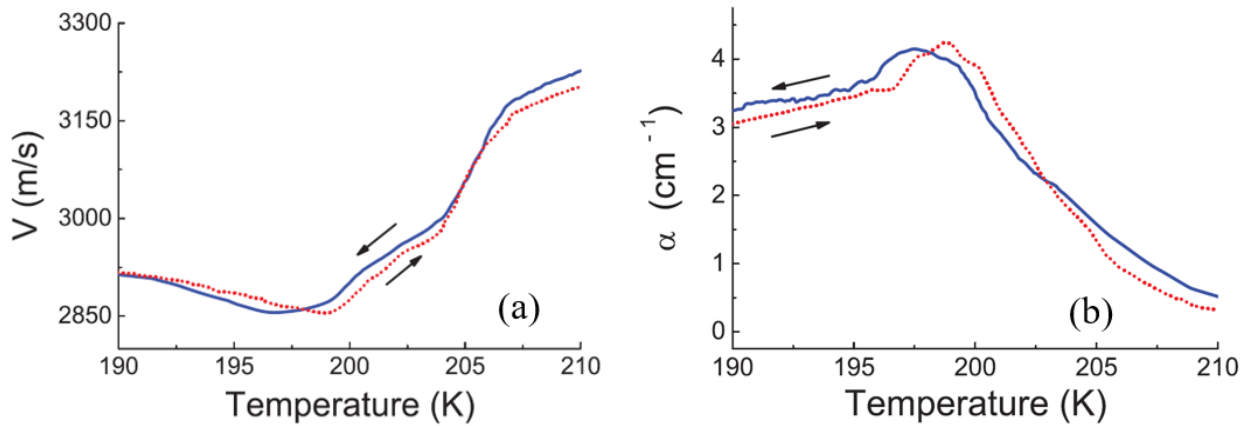


**Fig. 5.18.** Temperature dependences of ultrasound velocity (a) and attenuation (b) on cooling (blue solid lines) and heating (red dotted lines) in close vicinity of PT for a  $(\text{Pb}_{0.3}\text{Sn}_{0.7})_2\text{P}_2\text{S}_6$  crystal [2]

For  $(\text{Pb}_{0.45}\text{Sn}_{0.55})_2\text{P}_2\text{S}_6$  crystal [2], the temperature hysteresis of the sound velocity is clearly seen (fig. 5.19) which is related to the first-order character of the ferroelectric PT at about 132 K.

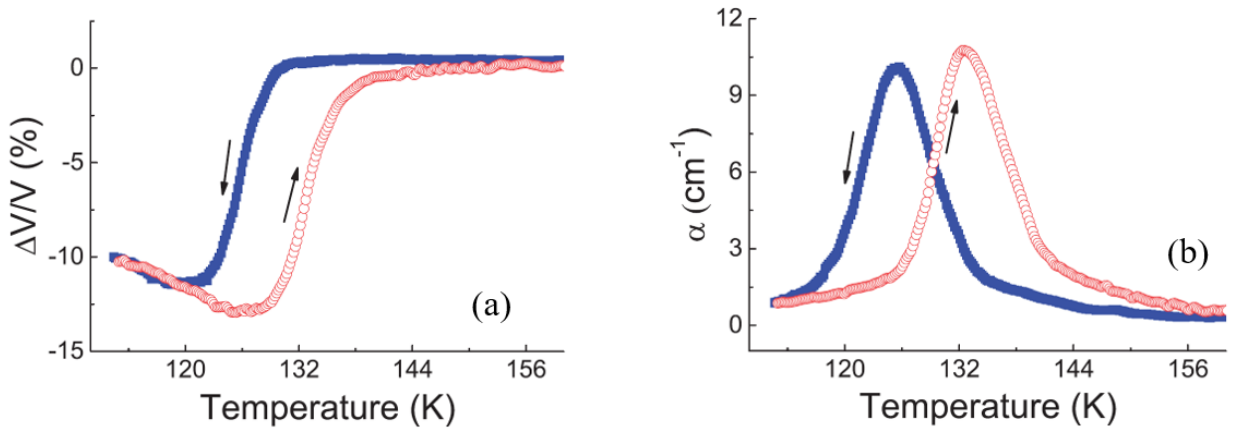


**Fig. 5.19.** Temperature dependences of ultrasound velocity (a) and attenuation (b) on cooling (blue squares) and heating (red dots) in the close vicinity of PT for a  $(\text{Pb}_{0.45}\text{Sn}_{0.55})_2\text{P}_2\text{S}_6$  crystal [2]

#### 5.2.4. Phase diagram of $(\text{Pb}_x\text{Sn}_{1-x})_2\text{P}_2\text{Se}_6$ crystals

In figure 5.20, light transmission [164] and calorimetric [97, 175] data are collected. As mentioned in the previous section, there are two PT for the  $\text{Sn}_2\text{P}_2\text{Se}_6$  crystal with the width of IC phase of about 28 K between them. Further substitution of Sn by Pb in  $(\text{Pb}_x\text{Sn}_{1-x})_2\text{P}_2\text{Se}_6$  ferroelectrics increases this width to 65 K at  $x = 0.3$  [164].

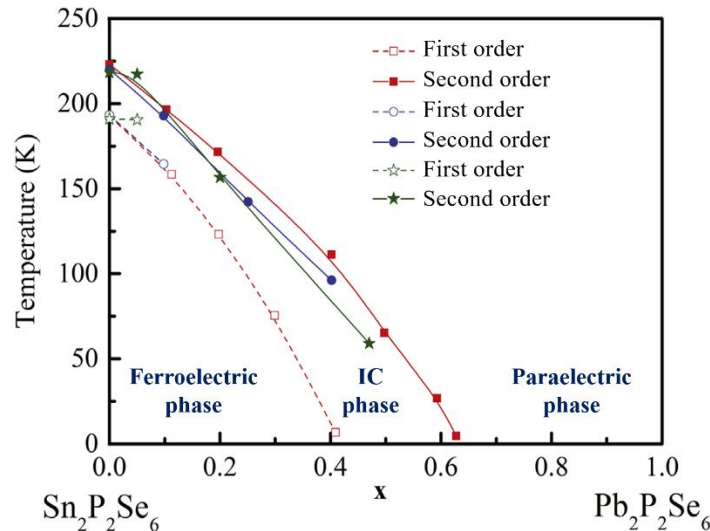


**Fig. 5.20.** Phase diagram for  $(\text{Pb}_x\text{Sn}_{1-x})_2\text{P}_2\text{Se}_6$  mixed crystals [97]. Solid symbols represent high-temperature Paraelectric-IC PT (second-order) and empty symbols the lock-in IC-ferroelectric ones, which are first-order. Stars correspond to data [97], circles to [164] and squares to [175]

Besides, with increasing Pb content the temperature of the transitions decreases. Such a decrease can be interpreted as follows: the ionic radius of  $\text{Pb}^{2+}$  ions is bigger than for  $\text{Sn}^{2+}$  ones, hence, the addition of lead increases the space available for tin in  $(\text{Pb}_x\text{Sn}_{1-x})_2\text{P}_2\text{Se}_6$  crystals. As a result, the motion of Sn becomes easier and ions can move with smaller thermal energy which leads to the lowering of the PT temperatures [175]. Increasing lead to  $x = 0.47$  leads to a stronger smearing of the continuous transition without hysteresis. In  $\text{Pb}_2\text{P}_2\text{Se}_6$  crystal, there was not any evidence of a PT [97].

### 5.2.5. TCP and TCLP in $\text{Sn}(\text{Pb})_2\text{P}_2\text{S}(\text{Se})_6$ mixed compounds

In previous sections we have considered the complex phase diagram of  $(\text{Pb}_x\text{Sn}_{1-x})_2\text{P}_2(\text{Se}_y\text{S}_{1-y})_6$  mixed compounds using concentration ( $x$  or  $y$ ) as a variable, thus we can distinguish three different phases bounded by first and second order PT lines as well as the presence of LP. In this section we will consider the possibility of the appearance of a tricritical point (TCP) and a tricritical Lifshitz point (TCLP) in  $\text{Sn}(\text{Pb})_2\text{P}_2\text{S}(\text{Se})_6$  mixed compounds while adding a new variable - pressure  $p$ . It is well known that the SPS crystal is a uniaxial ferroelectric with a three-well local potential for spontaneous polarization fluctuations [189]. The thermodynamics of such system could be well described within the framework of the Blue-Emery-Griffiths (BEG) model which plays an important role in the development of the theory of multicritical points, where pseudospins can have three different values  $S_i = 0, +1$  and  $-1$  [190]. Another important feature of the BEG model is the possible appearance of a TCP on the phase diagram at which the second-order PT turns into a first-order type transition. As it is known from work [43], replacing sulphur by selenium causes random field effects but their influence does not play an essential role, because they do not provoke any smearing in the critical anomaly. Nevertheless, to properly describe the case of the BEG model with random field it is necessary to combine it with ANNNI (axial-next-nearest-neighbor Ising) model [2]. Such model combination assumes the possible existence of a TCP and also an intermediate IC existence on the phase diagram of  $\text{Sn}_2\text{P}_2(\text{Se}_{1-y}\text{S}_y)_6$  at  $y > y_{LP}$ . Unlike  $\text{Sn}_2\text{P}_2(\text{Se}_{1-y}\text{S}_y)_6$ , in the

$(\text{Pb}_x\text{Sn}_{1-x})_2\text{P}_2\text{S}(\text{Se})_6$  solid solution, the introduction of lead essentially alters the total electronic orbitals hybridization, which causes, in its turn, the appearance of strong random-field defects. For this case a diluted BEG model is appropriated [80].

For  $\text{Sn}_2\text{P}_2(\text{S}_{1-y}\text{Se}_y)_6$  a TCP has been theorized to be at  $y = 0.6$  but it is a virtual point as the Lifshitz point takes precedence. A TCP has been found in SPS applying pressure. Under the pressure, the temperature of the ferroelectric PT decreases to  $T_c \sim 110$  K at  $p = 1.2$  GPa [192]. The observed TCP ( $p$ ) dependence at linear extrapolation reaches 0 K at the pressure of about 1.5 GPa. For  $(\text{Pb}_x\text{Sn}_{1-x})_2\text{P}_2\text{S}_6$  compounds the paraelectric phase becomes stable till 0 K above  $x \sim 0.7$  [171]. Comparison of TCP ( $p$  and  $x$ ) dependencies (fig. 5.21) demonstrates, that the stability of the paraelectric state in  $\text{Pb}_2\text{P}_2\text{S}_6$  compound could be compatible with the behavior of SPS crystal under compression of 2.2 GPa.

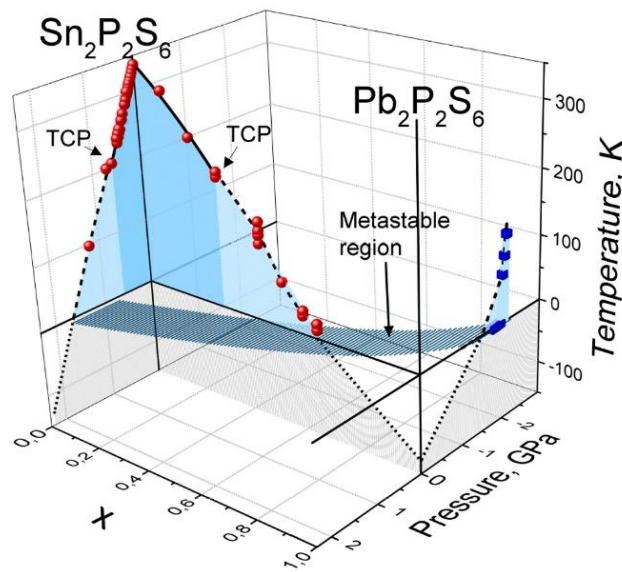


**Fig. 5.21.** Temperature-pressure phase diagram for  $\text{Sn}_2\text{P}_2\text{S}_6$  crystal and temperature-composition phase diagram for  $(\text{Pb}_x\text{Sn}_{1-x})_2\text{P}_2\text{S}_6$  mixed crystals. The TCP are located near 220 K for pressure  $p \approx 0.6$  GPa [192] or for concentration  $x \approx 0.3$  [2]. For  $\text{Pb}_2\text{P}_2\text{S}_6$  crystal the calculated temperature-pressure phase diagram is shown. The metastable region in the ground state ( $T = 0$  K) with possible coexistence of paraelectric and ferroelectric phases is shaded [158]

Regarding TCLP on the state diagram, as seen from the theoretical estimations in fig. 5.22, it could be found for  $(\text{Pb}_{0.12}\text{Sn}_{0.88})_2\text{P}_2(\text{Se}_y\text{S}_{1-y})_6$  compound at  $T = 225$  K,  $p = 0.28$  GPa as well as in  $(\text{Pb}_{0.12}\text{Sn}_{0.88})\text{P}_2\text{S}_6$  crystal at  $T = 295$  K at atmospheric pressure [193].

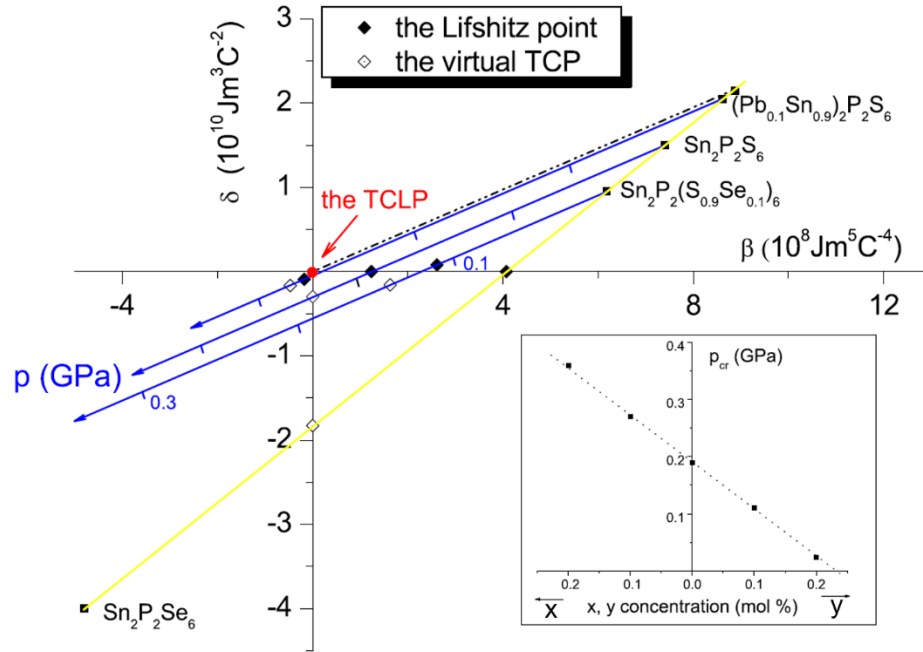


**Fig. 5.22.** Concentration and baric “thermodynamic trajectory” in the  $\delta$ - $\beta$  plane for  $(\text{Pb}_x\text{Sn}_{1-x})_2\text{P}_2(\text{Se}_y\text{S}_{1-y})_6$  mixed compounds [193]

In a critical behavior study of  $\text{Sn}_2\text{P}_2(\text{Se}_y\text{S}_{1-y})_6$  metal thiophosphates doped with lead cations by Oleaga *et al.*, a TCLP has been experimentally confirmed for  $(\text{Pb}_{0.05}\text{Sn}_{0.95})\text{P}_2(\text{Se}_{0.28}\text{S}_{0.72})_6$  crystal at  $T_c = 259.12$  K with the critical exponent  $\alpha = 0.638$ , fulfilling the predictions of the BEG model with random field for systems with local three-well potential for the order parameter fluctuations [191].

Special attention should be paid to the optical birefringence measurements for pure  $\text{Sn}_2\text{P}_2\text{S}_6$  and  $\text{Sn}_2\text{P}_2(\text{Se}_{0.28}\text{S}_{0.72})_6$  compounds under high hydrostatic pressures, performed in work [197]. For  $\text{Sn}_2\text{P}_2\text{S}_6$ , it is shown that the critical exponent  $\beta$  decreases gradually with increasing pressure down to  $0.25 \pm 0.01$  in the pressure range 4.1 – 4.5 kbar (fig. 5.23(a)). This corresponds to thermodynamic conditions of the TCP. The critical exponent acquires the values less than 0.25 under the pressures

above  $\sim 4.5$  kbar. Obviously, pressures higher than the above value should correspond to thermodynamic conditions under which a first-order PT occurs.

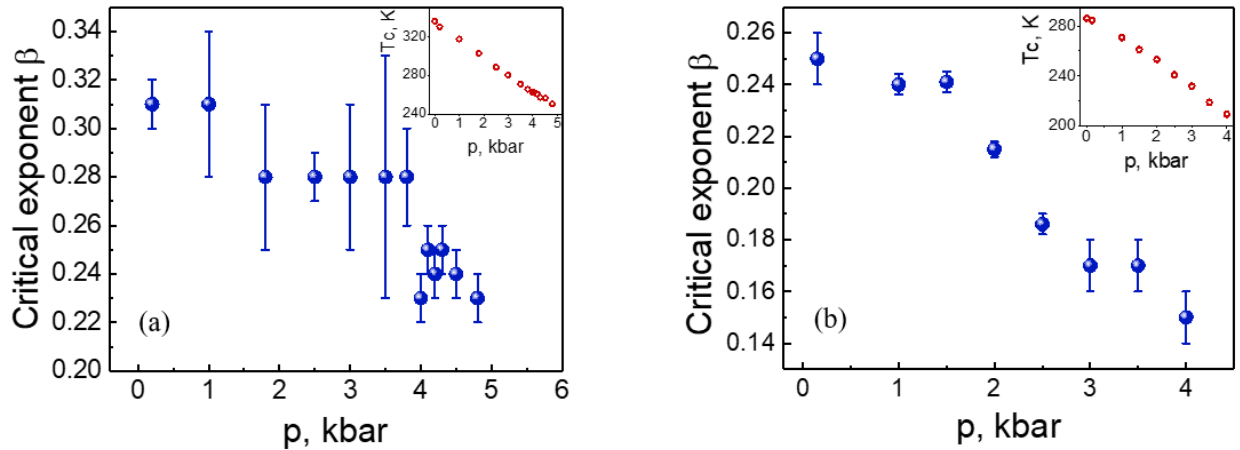


**Fig. 5.23.** Dependence of the critical exponent  $\beta$  on the hydrostatic pressure for  $\text{Sn}_2\text{P}_2\text{S}_6$  (a) and  $\text{Sn}_2\text{P}_2(\text{Se}_{0.28}\text{S}_{0.72})_6$  (b) crystals. The insert exhibits dependence of PT temperature  $T_c$  on pressure [197]

For  $\text{Sn}_2\text{P}_2(\text{Se}_{0.28}\text{S}_{0.72})_6$  (fig. 5.23(b)) the critical exponent  $\beta$  also decreases with increasing pressure and becomes less than 0.25. This may be caused by passing, in the phase space, into the region of first-order PT, as well as by splitting of the paraelectric–ferroelectric PT [52]. These results might suggest the conclusion that the pressure point  $\sim 2.5$  kbar corresponds to the thermodynamic coordinate at which the first-order ferroelectric–paraelectric PT splits into two transitions: the second-order paraelectric–IC PT and the first-order IC – ferroelectric one.

### 5.3. Thermal properties

As seen on figure 5.24 (a) the temperature dependence of the heat capacity  $C_p$  for  $\text{Sn}_2\text{P}_2\text{S}_6$  ferroelectric crystal shows a  $\lambda$ -shape anomaly at about  $T_c = 337.25$  K, pointing to the presence of a second order PT from a high symmetry state to a low symmetry one [178]. With the substitution of S by Se in the anion sublattice, two anomalies appear at lower temperatures: a ferroelectric commensurate - intermediate incommensurate (C-IC) lock-in PT at  $T_c = 193.24$  K which has latent heat and,

therefore, a first-order character; and another one at  $T_i = 220.27$  K characterized by the absence of latent heat, implying a second order character (fig. 5.24 (b)) [186].

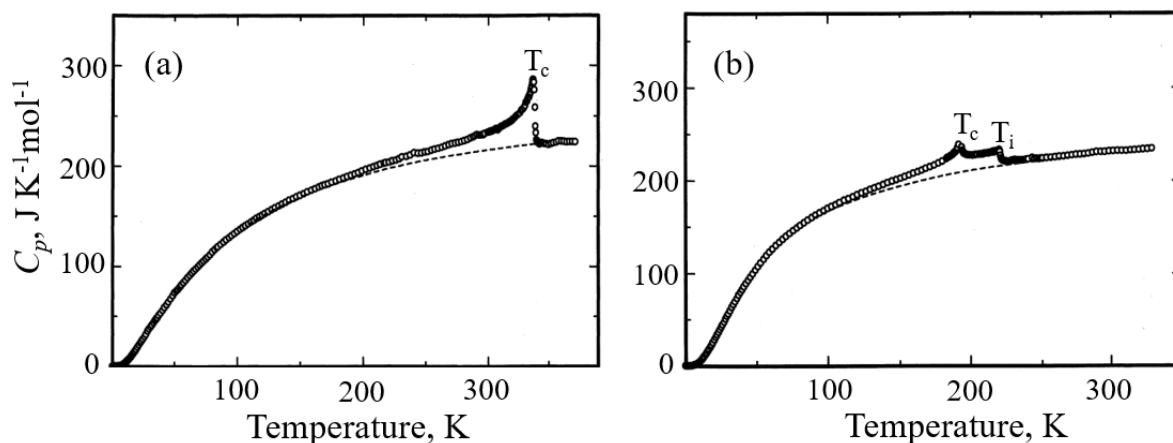


**Fig. 5.24.** Heat capacity data for  $\text{Sn}_2\text{P}_2\text{S}_6$  (a) and  $\text{Sn}_2\text{P}_2\text{Se}_6$  (b) ferroelectric crystals. Dashed line represents the vibrational heat capacity at constant pressure [178]

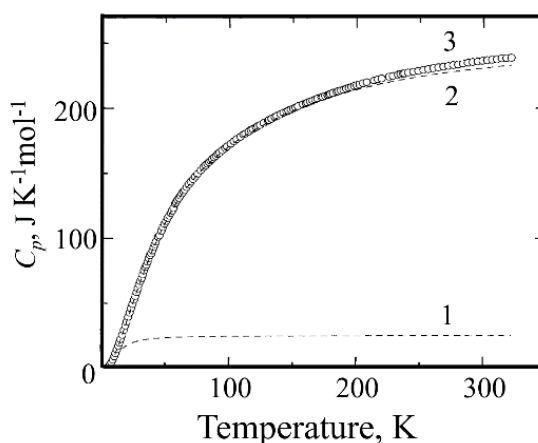


**Fig. 5.25.** Molar heat capacities of  $\text{Pb}_2\text{P}_2\text{Se}_6$ . The curves represent the calculated heat capacities. (1) Optimized Debye term. (2) Optimized Debye and Einstein terms. The calculated vibrational heat capacities at constant pressure. (3) Experimental molar heat capacities, open circles [176]

Thermal studies have been performed prior to this work on the thermal diffusivity of  $(\text{Pb},\text{Sn})_2\text{P}_2(\text{Se},\text{S})_6$  mixed compounds using an *ac* photopyroelectric calorimetry technique, focused on the critical behavior of the phase transitions [43, 96, 97, 98, 191, 195]. According to the data depicted on fig. 5.26 (a) the thermal

diffusivity of  $\text{Sn}_2\text{P}_2(\text{Se}_y\text{S}_{1-y})_6$  solid solutions in the paraelectric phase decreases while increasing the amount of Se present in the sample [43].

In  $(\text{Pb}_x\text{Sn}_{1-x})_2\text{P}_2\text{S}_6$  compounds (fig. 5.26 (b)) the evolution of the critical behaviour has shown that there is a crossover from a non-mean-field model at  $x = 0.1$  to a mean field one at  $x = 0.3$  [98]. For  $(\text{Pb}_x\text{Sn}_{1-x})_2\text{P}_2\text{Se}_6$  mixed ferroelectrics (fig. 5.26 (c)) a second-order PT has been found for  $x = 0, 0.05, 0.2$  and  $0.47$  which corresponds to the paraelectric C-IC phase and confirms the affiliation to the 3D-XY universality class for samples with the lead concentration  $x = 0, 0.05$  [97].

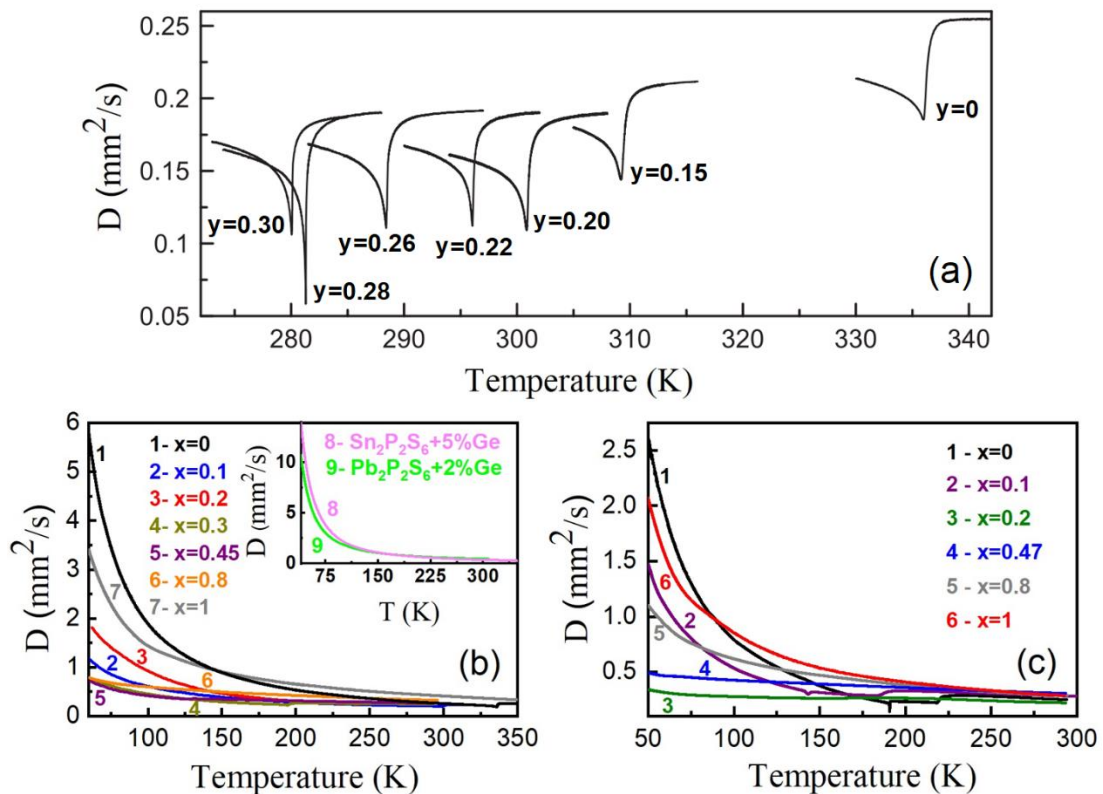


**Fig. 5.26.** Thermal diffusivity data for  $\text{Sn}_2\text{P}_2(\text{Se}_y\text{S}_{1-y})_6$  (a) [43],  $(\text{Pb}_x\text{Sn}_{1-x})_2\text{P}_2\text{S}_6$  (b) and  $(\text{Pb}_x\text{Sn}_{1-x})_2\text{P}_2\text{Se}_6$  (c) mixed compounds. The inset shows the thermal diffusivity curves for  $\text{Sn}_2\text{P}_2\text{S}_6 + 5\% \text{ Ge}$  and  $\text{Pb}_2\text{P}_2\text{S}_6 + 2\% \text{ Ge}$  [195]

In order to study the expected anisotropic behavior in the thermal diffusivity due to the peculiarities of the crystal structure in  $\text{Sn}_2\text{P}_2\text{S}_6$  (as it was mentioned in the first section of this chapter, the structure of this family compounds is characterized by a monoclinic crystalline lattice), samples in three orientations have been cut parallel to the unit cell vectors [100], [010] and [001]. In figure 5.27 it is shown, that

heat transfer is easier in the [100] plane, where polarization vector lies, than in a direction perpendicular to it [96].

In work [195], thermal conductivity data has been calculated in the full temperature range through the well known equation  $\kappa = CD$ , where  $D$  is the measured thermal diffusivity and  $C$  is the heat capacity (fig. 5.28). The regions where there is any PT have been removed as different techniques have been used to measure  $D$  and  $C_p$ , so the exact position and width of the transitions do not coincide, hence it would lead to artifacts in the PT region.

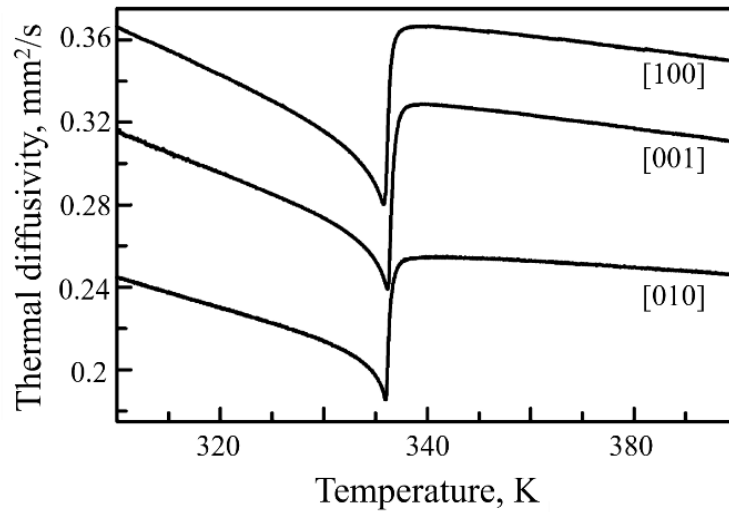


**Fig. 5.27.** Thermal diffusivity as a function of temperature for the SPS samples cut in the directions [100], [010] and [001] [102]

For  $\text{Pb}_2\text{P}_2\text{S}_6$  and  $\text{Pb}_2\text{P}_2\text{Se}_6$  crystals the thermal conductivity decreases on heating satisfying the Eiken law  $\kappa = T^{-1}$  in the interval 100-190K with experimental exponents obtained  $\kappa = T^{-n}$  between  $n = -1.2$  and  $-0.8$ , confirming the dominant role of the phonon scattering above the Debye temperature, which is  $T_D \approx 85$  K for the sulfide crystal and  $T_D \approx 55$  K for the selenide compound [176, 178]. Above  $2T_D$ , the dependencies are weakly dependent on temperature and deviate to almost constant values [195].

For the paraelectric phases of SPS and SPSe ferroelectric crystals at  $T_c > 337$  K and at  $T_i > 221$  K, respectively, the  $\kappa(T)$  dependencies are also characterized by constant values (the Debye temperatures for SPS and SPSe are  $T_D \approx 83$  K and  $T_D \approx$

74 K respectively) [178, 196]. Inside the ferroelectric phase, at low temperatures, the thermal conductivity of SPS and SPSe compounds exceed the values of the corresponding lead containing compounds [195].

Partial substitution of Sn by Pb in  $(\text{Pb}_x\text{Sn}_{1-x})_2\text{P}_2\text{S}_6$  and  $(\text{Pb}_x\text{Sn}_{1-x})_2\text{P}_2\text{Se}_6$  solid solutions strongly changes the temperature dependencies of the thermal conductivity because the mass fluctuations induce additional phonon scattering, which is clearly observed at low temperatures (fig. 5.29). At 60 K, in the middle of the concentration interval, for both sulfide and selenide ferroelectric crystals the thermal conductivity decreases several times, almost till 0.5 W/m K. At above 250 K, additional phonon scattering in mixed crystals doesn't decrease the thermal conductivity. Here evidently the lattice anharmonicity is so strong that additional scattering by mass fluctuations doesn't play an important role [195].

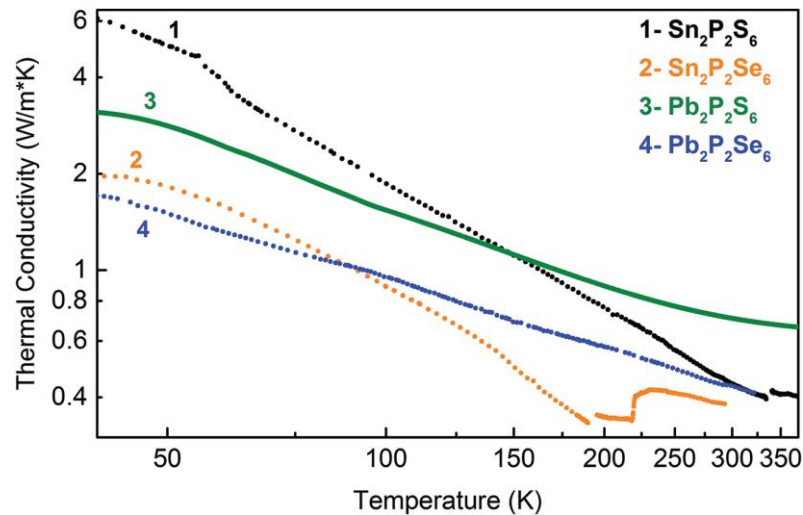


**Fig. 5.28.** Log–log scaled temperature dependence of thermal conductivity for  $\text{Sn}_2\text{P}_2\text{S}_6$ ,  $\text{Sn}_2\text{P}_2\text{Se}_6$ ,  $\text{Pb}_2\text{P}_2\text{S}_6$ , and  $\text{Pb}_2\text{P}_2\text{Se}_6$  crystals [195]

One more important thermodynamic property of solids is the thermal expansion coefficient  $\alpha_V(T)$ , which gives a hint on the accuracy of the harmonic approximation for the description of atomic vibrations in a medium. The corresponding coefficients for different crystallographic directions can be obtained experimentally with dilatometric studies. For the  $\text{Sn}_2\text{P}_2(\text{Se}_y\text{S}_{1-y})_6$  ferroelectrics with  $y = 0, 0.10$  and  $0.20$  for the three main directions parallel to the unit cell vectors [100], [010], [001] the

linear thermal expansion coefficients  $\alpha_{11}$ ,  $\alpha_{22}$  and  $\alpha_{33}$  are positive in the paraelectric phase, and negative in ferroelectric PT signaling clear "negative" anomalies [174].

The temperature dependencies of the volume  $\alpha_V(T)$  for  $\text{Sn}_2\text{P}_2\text{S}_6$ ,  $\text{Sn}_2\text{P}_2\text{Se}_6$  and  $\text{Pb}_2\text{P}_2\text{Se}_6$  compounds are depicted in fig. 5.30. For SPS and SPSe compounds the dips correspond to the PT, while in the case of  $\text{Pb}_2\text{P}_2\text{Se}_6$  no anomaly was observed; only a slight reduction with temperature was found [177, 197].

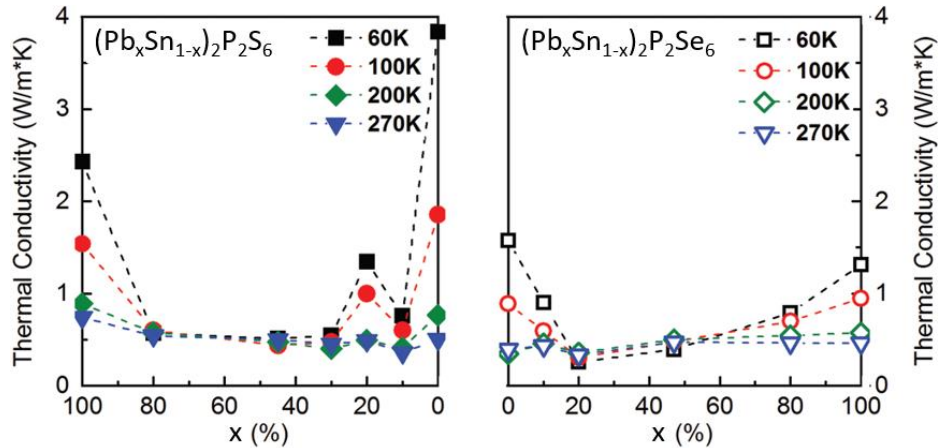


**Fig. 5.29.** Composition dependence of thermal conductivity for  $(\text{Pb}_x\text{Sn}_{1-x})_2\text{P}_2\text{S}_6$  and  $(\text{Pb}_x\text{Sn}_{1-x})_2\text{P}_2\text{Se}_6$  mixed crystals at different temperatures [195]

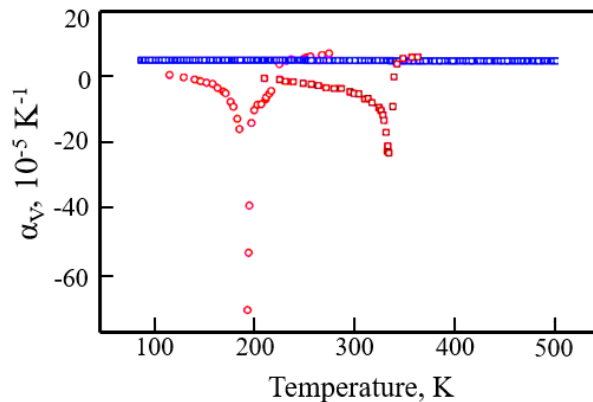


**Fig. 5.30.** Temperature dependence of the volume thermal expansion coefficient: red squares –  $\text{Sn}_2\text{P}_2\text{S}_6$ , red circles –  $\text{Sn}_2\text{P}_2\text{Se}_6$ , blue squares –  $\text{Pb}_2\text{P}_2\text{Se}_6$  [177, 197]

### 5.3.1. Influence of Ge on the thermal properties in SPS chalcogenides

The thermal properties of SPS compound doped with Ge have been studied in the vicinity of the ferroelectric to paraelectric second-order PT by means of an *ac*

photopyroelectric calorimetry, measuring thermal diffusivity [198]. Introducing  $\text{Ge}^{2+}$  into the cation sublattice (fig. 5.31) increases the transition temperature (336.2 K and 349.2 K for undoped SPS and SPS + 5% Ge, respectively) and the sharpening of the transition; this is due to the strengthening of the  $sp^2$  electronic orbitals hybridization. Both the increase in  $T_c$  and in the sharpness of the transitions in the doped compounds illustrate the fact that the ferroelectric PT is favored with respect to the pure one, which suggests that the stereoactivity of the cation sublattice has been improved with the substitution of  $\text{Sn}^{2+}$  by  $\text{Ge}^{2+}$  [198].

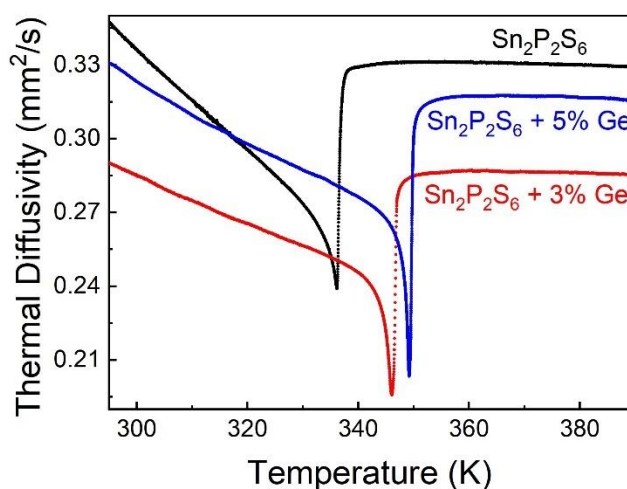


**Fig. 5.31.** Thermal diffusivity in the [001] direction of SPS doped with Ge: pure SPS [8]; SPS + 3% Ge; SPS + 5% Ge [198]

Indeed, X-ray photoelectron spectroscopy studies [199] have shown that doping with Ge improves the stereoactivity in the  $\text{Sn}^{2+}$  cation sublattice, what leads to the displacement of the ferroelectric PT to higher temperatures. In work [200] the authors have studied the possible effect of Ge doping on pyroelectric and piezoelectric properties. It was suggested that the distribution of the dopants over the sample is homogeneous and that the induced defects in the crystal lattice cannot be considered to be defects of a random local field type. Due to the interaction between the defects' mode (assumed to be of a relaxation type) and the critical lattice vibration, the latter is softened and causes an increase in  $T_c$ . One may suggest that Ge can occupy two or more quasi-equilibrium states in the crystal lattice of SPS in the paraelectric phase. A transition from one state to another can occur in a thermally activated way [200].

Finally, according to what has been mentioned above, we can conclude that germanium plays a role opposite to that of lead when it substitutes tin, the effect of the latter being a reduction in the stereoactivity of the cation sublattice, lowering the PT temperature and even frustrating it at high concentrations [56, 98].

## Chapter 6. Experimental results and discussion on layered ferroelectric compounds

### 6.1. Introduction

This chapter is focused on the thermal and electric properties of layered ferroelectric materials  $M^{1+}M^{3+}P_2(S,Se)_6$  ( $M^{1+}$  – Cu, Ag;  $M^{3+}$  – In, Bi). After chapter 4, it is established that the substitution of S by Se atoms in  $CuInP_2(S,Se)_6$  series leads to a decrease in the temperature of the ferroelectric PT. Partial substitution of Cu by Ag in  $(Ag_xCu_{1-x})InP_2(S,Se)_6$  leads to a bigger covalency of the Ag– $[P_2S_6]$  bonds [99]; these properties make the silver compounds more stable. Besides, silver ions have a bigger size which implies that the freezing of the hopping motion of the  $Cu^+$  ions which leads to the ordered, ferroelectric phase is much more difficult to happen [119]. All these reasons add up to explain the lowering of the PT temperature with small amounts of Ag and its full frustration when the substitution is completed. Differences in thermal properties when substituting In by Bi are due to the lone pair of bismuth being stereochemically active as opposed to indium. Combining thermal diffusivity and heat capacity data it is possible to obtain thermal conductivity in the full temperature range. The analysis of the evolution of the thermal conductivity curves gives us an insight on how the substitution of the chemical elements changes the physical properties in these layered compounds. Finally, we explain the very low values obtained for the thermal conductivity on the basis of the phonon scattering and different mechanisms of anharmonicity.

### 6.2. Samples and experimental techniques

Single 2D layered ferroelectric crystals of  $Cu_{1-x}Ag_xInP_2(S,Se)_6$  with  $x = 0, 0.1,$  and 1,  $AgBiP_2(S,Se)_6$  and  $CuBiP_2Se_6$  were grown for thermal studies. Initial purity of the different elements is as follows: Cu (99.999%), Ag (99.999%), In (99.999%), Bi (99.9999%), P (99.9999%), S (99.999%), Se (99.9996%). The directed melt

crystallization method was used because of the congruent melting character of the compounds and the comparatively low dissociation vapor pressure.

The synthesis regime for  $\text{Cu}_{1-x}\text{Ag}_x\text{InP}_2\text{S}_6$  crystals involved a stepwise heating up to 673 K (pressure of sulphur vapor 101.325 kPa) at 50 K/hour rate and temperature stabilization for 24 hours for Cu–In bonding ( $\text{CuInP}_2\text{S}_6$ ) or Ag–In bonding ( $\text{AgInP}_2\text{S}_6$ ) correspondingly with formation of binary, ternary and tetrary intermediate phases. Further temperature increase for 50 K above melting temperature (1145 K for  $\text{CuInP}_2\text{S}_6$  and 1115 K for  $\text{AgInP}_2\text{S}_6$  crystal) at 50 K/hour rate and temperature stabilization for 48 hours for melt homogenization, and then decrease temperature down to room temperature at 50 K/hour rate [201].  $\text{CuInP}_2\text{S}_6$  2D layered chalcogenide crystallizes in a monoclinic *Cc* system [113].  $\text{AgInP}_2\text{S}_6$  crystallizes in a trigonal system [114]. According to the results of the combination of XRF spectroscopy analysis with the mathematical package EXPO 2014 [202, 203],  $\text{Cu}_{1-x}\text{Ag}_x\text{InP}_2\text{S}_6$  ( $x = 0.1$ ) solid solutions crystallize in the monoclinic *Cc* system.

In order to grow  $\text{CuInP}_2\text{Se}_6$ ,  $\text{AgInP}_2\text{Se}_6$ ,  $\text{AgBiP}_2\text{Se}_6$  and  $\text{CuBiP}_2\text{Se}_6$  crystals the temperature of synthesis was raised up to 873 K (pressure of selenium vapor ~ 101.325 kPa) at 50 K/hour rate and temperature stabilization for 24 hours for P and Se bonds formation with Cu and In ( $\text{CuInP}_2\text{Se}_6$ ), Ag and In ( $\text{AgInP}_2\text{Se}_6$ ), and Cu and Bi ( $\text{CuBiP}_2\text{Se}_6$ ) with formation of binary, ternary and tetrary intermediate phases, correspondingly. Then temperature increase for 50 K above melting temperature (970 K for  $\text{CuInP}_2\text{Se}_6$ , 1000 K for  $\text{AgInP}_2\text{Se}_6$ , and 860 K for  $\text{CuBiP}_2\text{Se}_6$  crystals respectively) at 50 K/hour rate and temperature stabilization for 48 hours for homogenization of melt, and then decrease temperature to room temperature at 50 K/hour rate [201]. As a result,  $\text{CuInP}_2\text{S}_6$ ,  $\text{AgInP}_2\text{S}_6$ ,  $\text{CuInP}_2\text{Se}_6$ ,  $\text{AgInP}_2\text{Se}_6$ , and  $\text{CuBiP}_2\text{Se}_6$  single crystals of 14–16 mm diameter and 40–60 mm length were obtained. As already mentioned in chapter 4,  $\text{CuBiP}_2\text{S}_6$  crystal was impossible to grow, this is why it is not present here.

From the single crystal boules, samples were cut and prepared as thin plane parallel slabs (450–700  $\mu\text{m}$ ) and polished either parallel to the layers or perpendicular to them, obtaining two orientations per sample in order to study possible thermal

anisotropies. A high-resolution ac photopyroelectric calorimeter in the back-detection configuration has been used to measure thermal diffusivity ( $D$ ) as a function of temperature, where it is measured in the direction perpendicular and parallel to the surface of the sample. For thermal diffusivity measurements both a closed cycle helium cryostat and a liquid  $N_2$  cryostat have been used in order to cover a whole temperature region. The detailed description of the technique as well as of the experimental setups are well described in chapter 2. The measured temperature range has been 30-350 K in order to check the possible ferroelectric orderings in a broad temperature range, seldom used in literature. The phase transitions are generally signalled in  $D$  as dips or jumps superimposed to a monotonic increase as temperature decreases, typical for thermally insulating materials, where heat is mainly transferred by phonons. Measurements have been performed in two steps: first there was a quick run with a rate of 100 mK/min in order to cover a wide temperature range, and a second step consisted of high-resolution heating/cooling runs when verifying the possible hysteresis of the transitions, even down to 10 mK/min for particular cases.

The heat capacities of the considered crystals have been calculated through the evaluation of the phonon spectra using density-functional perturbation theory [204]. The ABINIT software code [205] has been used to estimate specific heat within the harmonic approximation [206]. The calculation has been performed in generalized gradients approximation (GGA) [207] for the exchange-correlation part of density functional with dispersion (DFT-D) correction by Grimme. The latter correction has been used because of the layered structure of considered crystals. The plane-wave basis set has been restricted by the cut-off energy of 850 eV which provides convergence in energy and forces equal to  $5 \cdot 10^{-7}$  eV/atom and 0.01 eV/Å, respectively. Integration over Brillouin zone has been performed at the  $3 \cdot 3 \cdot 2$  mesh of the special k-points generated by Monkhorst-Pack algorithm [208]. The symmetry of the system has been totally preserved while geometry optimization. Linear response, or density functional perturbation theory (DFPT), has been used for ab initio calculation of lattice dynamics [209]. In this approach, the electronic second

order energy is minimized and the dynamical matrix for a given wavevector  $q$  is then evaluated from the converged 1st order wavefunctions and densities.

Having calculated the phonon spectra, one can obtain the corresponding density of phonon states, and then the heat capacity, by means of the well-known expression [210]:

$$C_v = 3nNk_B \int_0^{\omega_L} \left( \frac{\hbar\omega}{2k_B T} \right)^2 \operatorname{csch}^2 \left( \frac{\hbar\omega}{2k_B T} \right) g(\omega) d\omega, \quad (6.1)$$

where  $n$  is the number of atoms per unit cell,  $N$  is the number of unit cells,  $\omega_L$ , is the largest phonon frequency, and the density of phonon states  $g(\omega)d\omega$  is defined to be the fractional number of phonon frequencies in the range  $d\omega$  in the vicinity of  $\omega$ .

Finally, thermal conductivity has been calculated by combining the experimental thermal diffusivity  $D$  and the calculated heat capacity  $C$  following the well-known equation

$$\kappa = C * D. \quad (6.2)$$

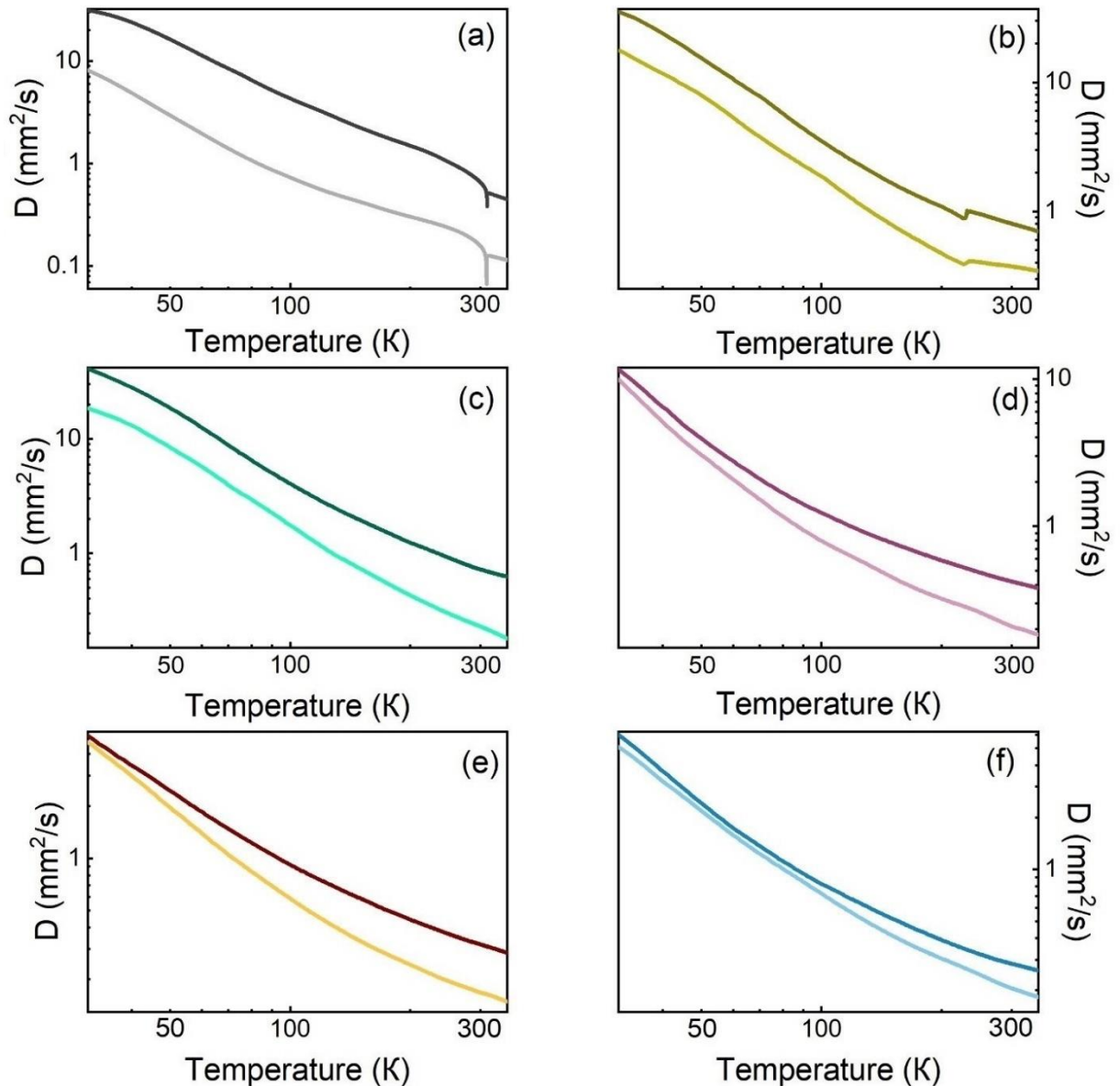
It is worth mentioning, that the regions where there is any PT have been removed from  $D$  as only the background heat capacity has been calculated, hence, the width and the shape of the transitions could be different, so we would obtain artefacts in the PT region.

### 6.3. Experimental results and discussion

#### 6.3.1. Thermal Diffusivity

Thermal diffusivity curves for 2D metalthiophosphates and metalselenophosphates are presented in a temperature range from 30 K till 350 K in fig. 6.1 in a log-log scale, which allows a better observation of their features. It is worth pointing out that, though the uncertainty in the measurement of thermal diffusivity at a fixed temperature is  $\pm 3\%$ , in the continuous measurements as a function of temperature the thermal diffusivity is obtained from the difference in the

phase of the pyroelectric signal, which is extremely stable (the phase is obtained with an uncertainty of  $\pm 0.01$ ), allowing us to present curves with very smooth changes. In each case, both orientations have been studied, retrieving the thermal diffusivity along the layers and perpendicular to them. There are common trends shared by all the samples: At high temperature the values are small, typical for insulating materials, where heat is mainly transferred by phonons. As the temperature decreases there is a monotonic increase in the value of  $D$  (as the phonon mean free path increases) which quickly grows at low temperature, starting at very close temperatures among the samples. This sudden growth should start at temperatures close to the Debye temperature (calculated afterwards in this discussion) and which coincides well with the experiment.



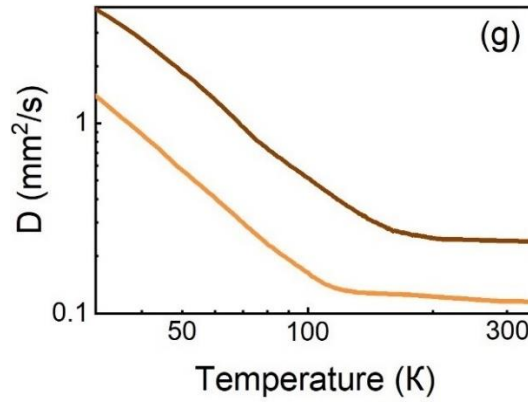


**Fig. 6.1.** Thermal diffusivity  $D$  as a function of temperature for:  $\text{CuInP}_2\text{S}_6$  (a),  $\text{CuInP}_2\text{Se}_6$  (b),  $\text{AgInP}_2\text{S}_6$  (c),  $\text{AgInP}_2\text{Se}_6$  (d),  $\text{AgBiP}_2\text{S}_6$  (e),  $\text{AgBiP}_2\text{Se}_6$  (f) and  $\text{CuBiP}_2\text{Se}_6$  (e) 2D layered ferroelectric compounds. Dark colour denotes that  $D$  is measured along the layers while light implies that it is measured perpendicular to them

Thermal anisotropy is present in all compounds: heat is much more easily transferred along the layers, as proved by the values of  $D$  being between twice and four times higher along the layers than perpendicular to them. The relevant values of thermal diffusivity at 50 K as well as at room temperature for all samples are gathered in table 6.1.

Table 6.1.

Values of thermal diffusivity at 50 K and at room temperature for  $\text{Cu}_{1-x}\text{Ag}_x\text{InP}_2(\text{S,Se})_6$  with  $x = 0, 0.1, \text{ and } 1$ ,  $\text{AgBiP}_2(\text{S,Se})_6$  and  $\text{CuBiP}_2\text{Se}_6$  compounds. Labels  $\parallel$  for the thermal diffusivity measured along the layers and as  $\perp$  when it is measured perpendicular to them

Compound	Thermal Diffusivity $\text{mm}^2/\text{s}$		Compound	Thermal Diffusivity $\text{mm}^2/\text{s}$	
	295K	50K		295K	50K
$\text{CuInP}_2\text{S}_6\perp$	0.167	2.93	$\text{CuInP}_2\text{Se}_6\perp$	0.376	7.93
$\text{CuInP}_2\text{S}_6\parallel$	0.695	16.2	$\text{CuInP}_2\text{Se}_6\parallel$	0.815	15.41
$\text{AgInP}_2\text{S}_6\perp$	0.236	8.405	$\text{AgInP}_2\text{Se}_6\perp$	0.214	3.054

$\text{AgInP}_2\text{S}_6 \parallel$	0.738	18.612	$\text{AgInP}_2\text{Se}_6 \parallel$	0.427	4.92
$\text{AgBiP}_2\text{S}_6 \perp$	0.17	1.962	$\text{AgBiP}_2\text{Se}_6 \perp$	0,208	2.177
$\text{AgBiP}_2\text{S}_6 \parallel$	0.322	2.455	$\text{AgBiP}_2\text{Se}_6 \parallel$	0.288	2.412
			$\text{CuBiP}_2\text{Se}_6 \perp$	0.116	0.567
			$\text{CuBiP}_2\text{Se}_6 \parallel$	0.241	1.859

Concerning phase transitions, these are marked on the thermal diffusivity curves as dips of different sharpness but only in some compounds. The ferrielectric ordering is signalled as a sharp and narrow dip typical of first order phase transitions for  $\text{CuInP}_2\text{S}_6$  and a shallow and wider one appears at the ferroelectric ordering of  $\text{CuInP}_2\text{Se}_6$ , which we have published in work [108]. The hysteresis for these two cases is shown in Fig. 6.2. In the case of  $\text{CuInP}_2\text{S}_6$  there is a clear hysteresis, signalled not only by the different position of the minimum in heating and cooling rates but also by the different shape of the transition.

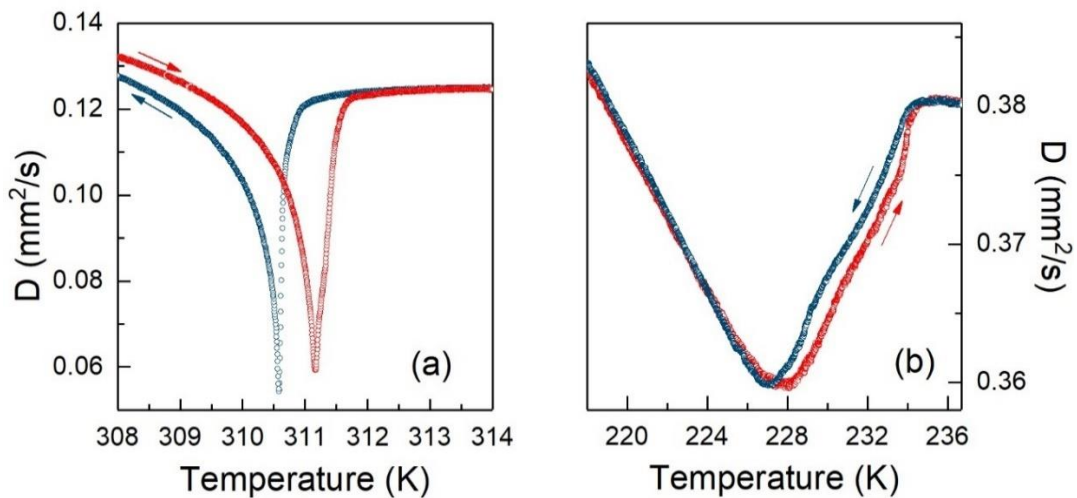


**Fig. 6.2.** Hysteresis of the phase transitions at a rate of 50 mK/min in  $\text{CuInP}_2\text{S}_6$  (a) and  $\text{CuInP}_2\text{Se}_6$  (b), measured in the direction perpendicular to the layers

On the other hand, in  $\text{CuInP}_2\text{Se}_6$ , there is a slight hysteresis on the upper temperature part of the dip, signalling that it could have a weak first order character or be composed of two transitions very close to each other with a small

incommensurate region between of them (less than 10 K); this term is used to describe a transition which appears to be second order but which has a very small latent heat and hysteresis, not easily shown unless using high resolution techniques.

The substitution of Cu by Ag alters completely this scenario. At low concentrations the transition is shifted to lower temperatures and it is less sharp and wider; moreover, from our results it turns out that the character of the PT has changed to second order for  $\text{Ag}_{0.1}\text{Cu}_{0.9}\text{InP}_2\text{S}_6$ , as it was also observed with ultrasonic measurements in [143] as opposed to dielectric measurements which supported that the transition was still first order [99]. At full substitution the transition is frustrated, there is no hint of any transition down to 30 K. The detailed comparison of the evolution at the substituting Ag by Cu is given in fig. 6.3a. The reduction of the PT temperature is not so pronounced in  $\text{Cu}_{0.9}\text{Ag}_{0.1}\text{InP}_2\text{Se}_6$  but the transition is severely smeared. At full substitution of Cu by Ag in  $\text{AgInP}_2\text{Se}_6$  the transition is also completely frustrated as it happens with sulphide compounds (fig. 6.3 b).

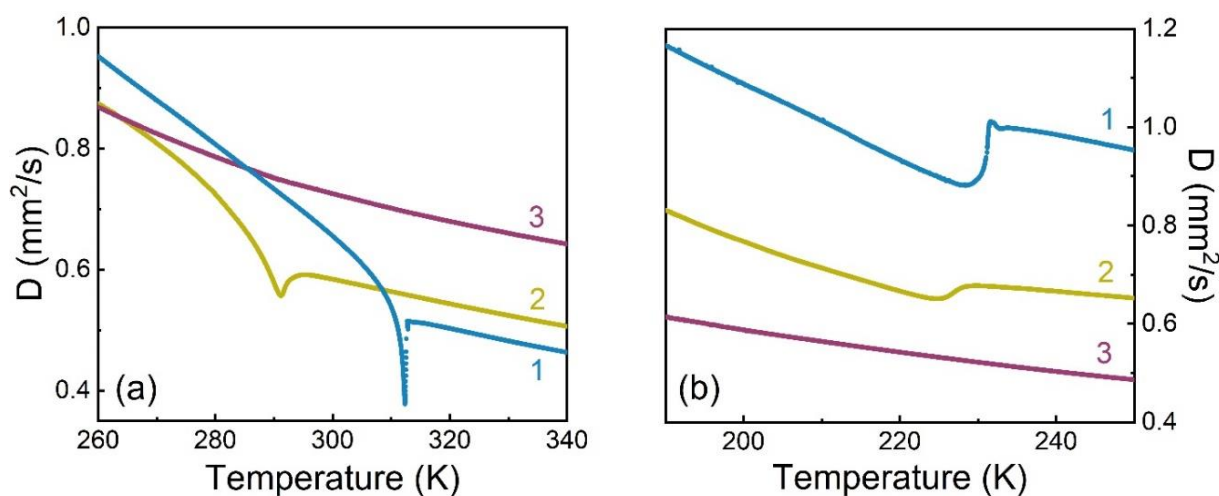


**Fig. 6.3.** Thermal diffusivity as a function of temperature for: (1)  $\text{CuInP}_2\text{S}_6$ , (2)  $\text{Ag}_{0.1}\text{Cu}_{0.9}\text{InP}_2\text{S}_6$ , (3)  $\text{AgInP}_2\text{S}_6$  (a) and (1)  $\text{CuInP}_2\text{Se}_6$ , (2)  $\text{Ag}_{0.1}\text{Cu}_{0.9}\text{InP}_2\text{Se}_6$ , (3)  $\text{AgInP}_2\text{Se}_6$  (b), measured in the direction parallel to the layers measured in the direction parallel to the layers

As the PT in  $\text{CuInP}_2(\text{S,Se})_6$  is explained on the basis of a second order Jahn Teller (SOJT) effect induced by the local dynamic hopping of  $\text{Cu}^+$  ions [100, 126], it

is important to establish what happens when Cu is substituted by Ag. The presence or absence of this SOJT effect is severely dependent on the covalency of the bonds and the hybridization of the s and d orbitals of the  $M^{1+}$  cation. The latter is more efficient in silver doped compounds in the paraelectric phase, leading to a bigger covalency of the Ag–[P<sub>2</sub>S<sub>6</sub>] bonds; these properties make the silver compounds more stable. Besides, silver ions have a bigger size which implies that the freezing of the hopping motion of the Cu<sup>+</sup> ions which leads to the ordered, ferrielectric phase is much more difficult to happen [119]. All these reasons add up to explain the lowering of the phase transition temperature with small amounts of Ag and its full frustration when the substitution is completed.

The substitution of In by Bi has the general consequence of making heat transfer more difficult, as the values of  $D$  in all directions are smaller than the corresponding with In. Starting with CuBiP<sub>2</sub>Se<sub>6</sub>, there is a faint first order phase transition at about 140 K, thus altering the ordering which happened in CuInP<sub>2</sub>Se<sub>6</sub>. Figure 6.4 exhibits the detail of this transition and its hysteresis while heating and cooling, confirming the antiferroelectric transition (see Chapter 4). The origin of this change lies on the different behaviour of the ions while reducing the temperature. In CuBiP<sub>2</sub>Se<sub>6</sub>, the copper ions in the paraelectric phase are distributed in a disordered arrangement of several off-centre positions while in the ordered phase they are settled off-centre the octahedral sites promoted by a SOJT effect associated with the d-p states hybridization [119]. The bismuth ions are displaced in the opposite direction, tending to cancel the intralayer dipole moment and thus creating an antiferroelectric state; this displacement is driven by the stereochemical expression of its s<sup>2</sup> lone pair. The main difference with CuInP<sub>2</sub>Se<sub>6</sub> is that indium ions do not present that lone pair and can only have small displacements to oppose the Cu shifts; therefore, the low temperature phase is ferroelectric.

AgBiP<sub>2</sub>Se<sub>6</sub> is ferroelectric at room temperature and has many structural similarities with CuBiP<sub>2</sub>Se<sub>6</sub> in the ordered phase [119], the main difference being that the lone pair of bismuth is not stereochemically expressed. The origin of the ferroelectricity is the ordered displacement of the silver ions along the c-axis. In

agreement with those results, no phase transition has been found in the thermal properties, not even up to 350K, looking for a potential paraelectric phase.

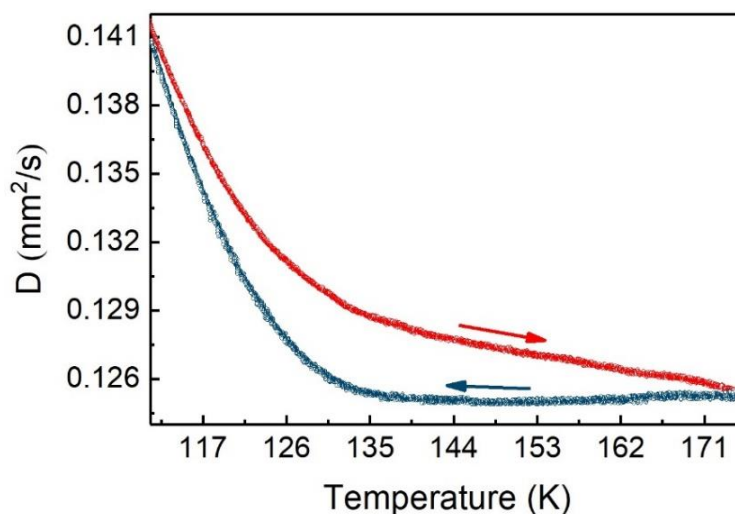
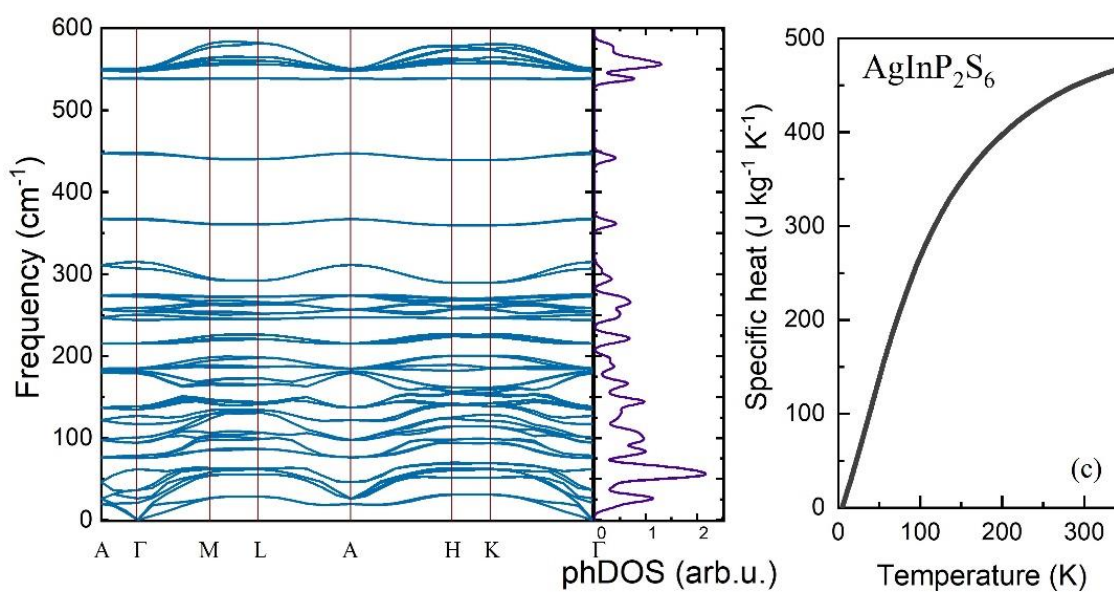
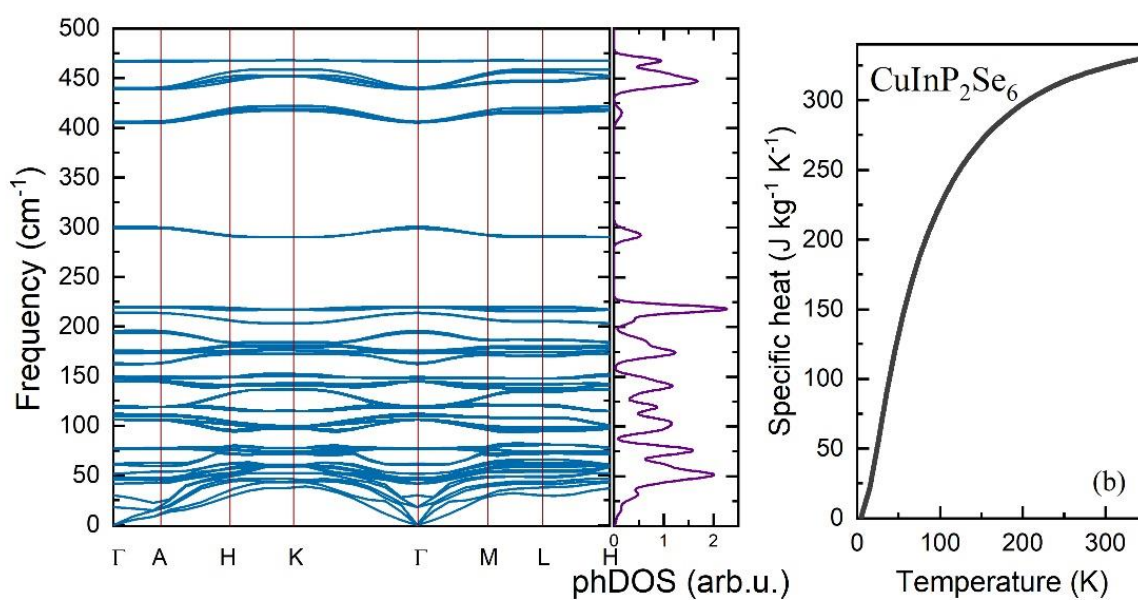
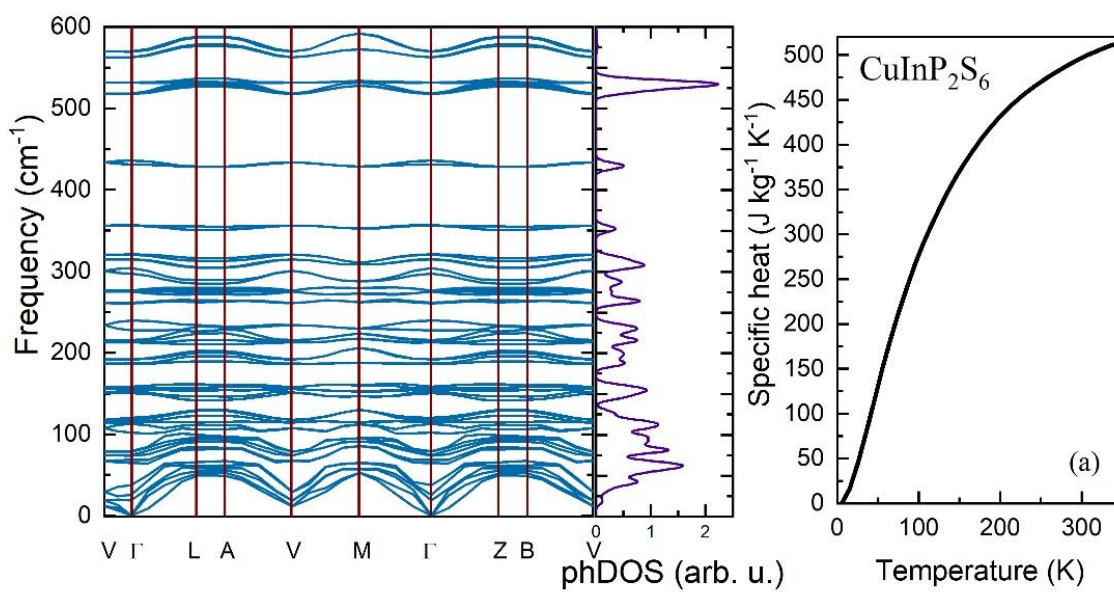


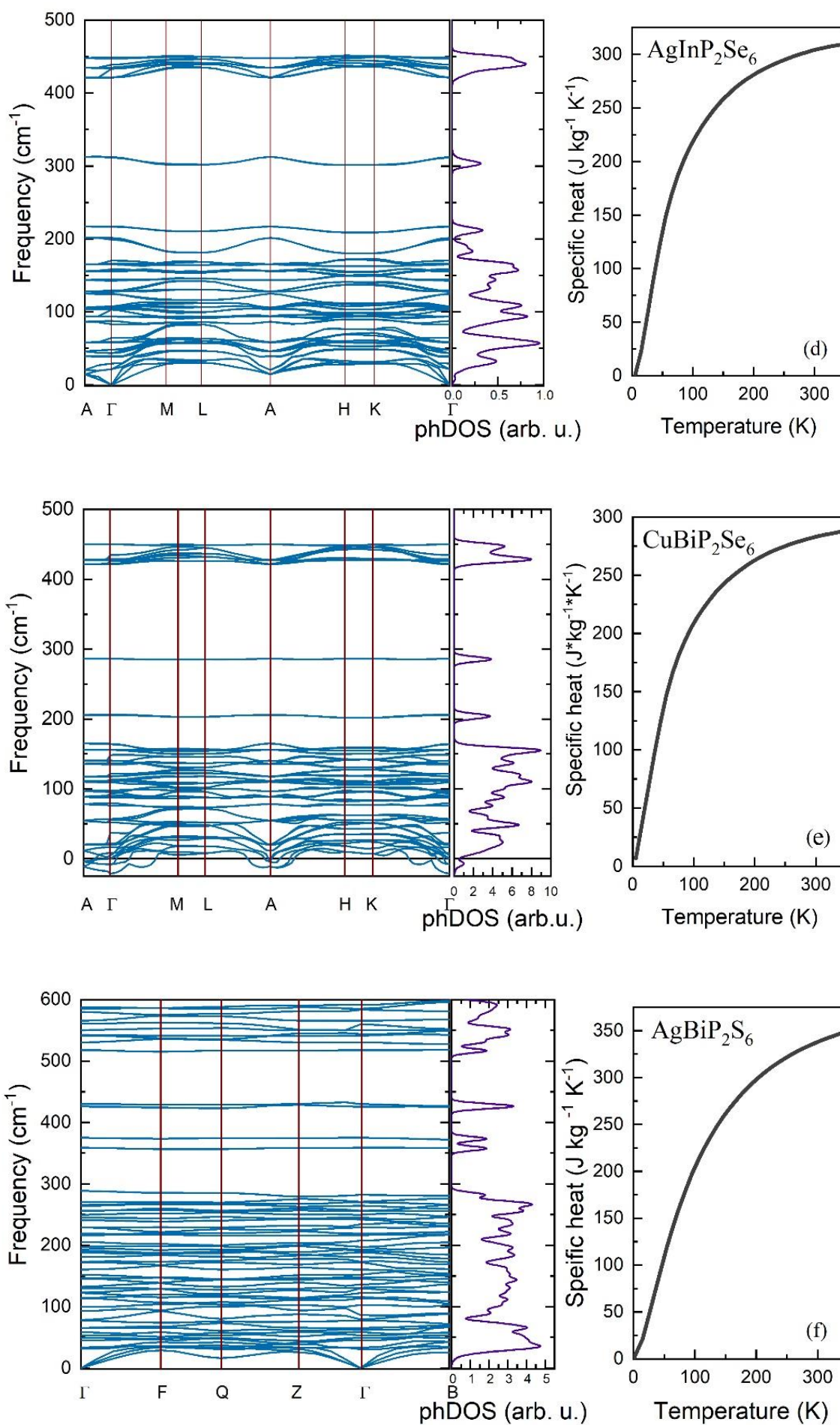
**Fig. 6.4.** Hysteresis of the PT at a rate of 75 mK/min in  $\text{CuBiP}_2\text{Se}_6$ , measured in the direction perpendicular to the layers

Finally,  $\text{AgBiP}_2\text{S}_6$  does not show any singularity in the thermal diffusivity curves, presenting a similar frustration of the ferroelectric ordering as in  $\text{AgInP}_2\text{S}_6$ . Interestingly, the crystal structure of  $\text{AgBiP}_2\text{S}_6$  is very different from  $\text{AgBiP}_2\text{Se}_6$  due to a bunch of reasons: a different coordination environment for Bi, the smaller size of S compared to Se, a tendency to stereochemically express the lone pair etc. [119]. In chapter 4 we have considered the ultrasonic velocity data in these compounds [143]. In that work authors have found a small singularity at about 220 K which was identified as a phase transition. In the detailed and high-resolution measurements presented here nothing of this sort has been found.

### 6.3.2. Heat Capacity

As the next step in our analysis, the molar heat capacity has been calculated as explained in section 6.2 for all samples. Figure 6.5 contains, the calculated phonon spectrum and phonon density of states as well as the calculated specific heats for them.





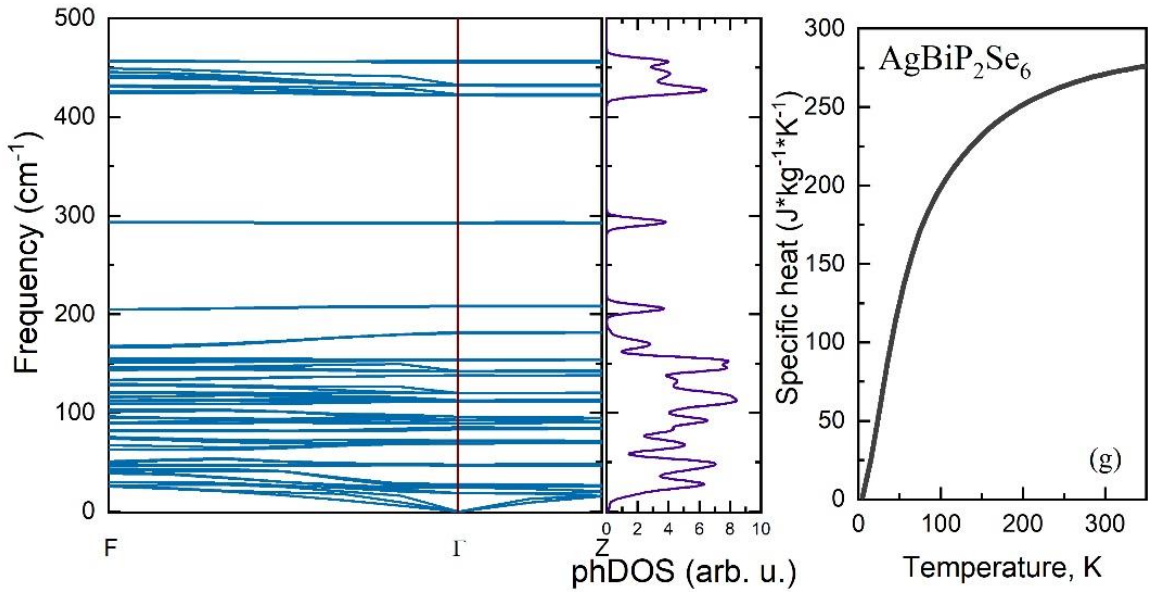


**Fig. 6.5.** Calculated phonon spectrum and phonon density of states (left) and calculated specific heat (right) using density-functional perturbation theory for  $\text{CuInP}_2\text{S}_6$  (a),  $\text{CuInP}_2\text{S}_6$  (b),  $\text{AgInP}_2\text{S}_6$  (c),  $\text{AgInP}_2\text{Se}_6$  (d),  $\text{CuBiP}_2\text{Se}_6$  (e),  $\text{AgBiP}_2\text{S}_6$  (f) and  $\text{AgBiP}_2\text{Se}_6$  (g) crystals.

### 6.3.3. Thermal Conductivity

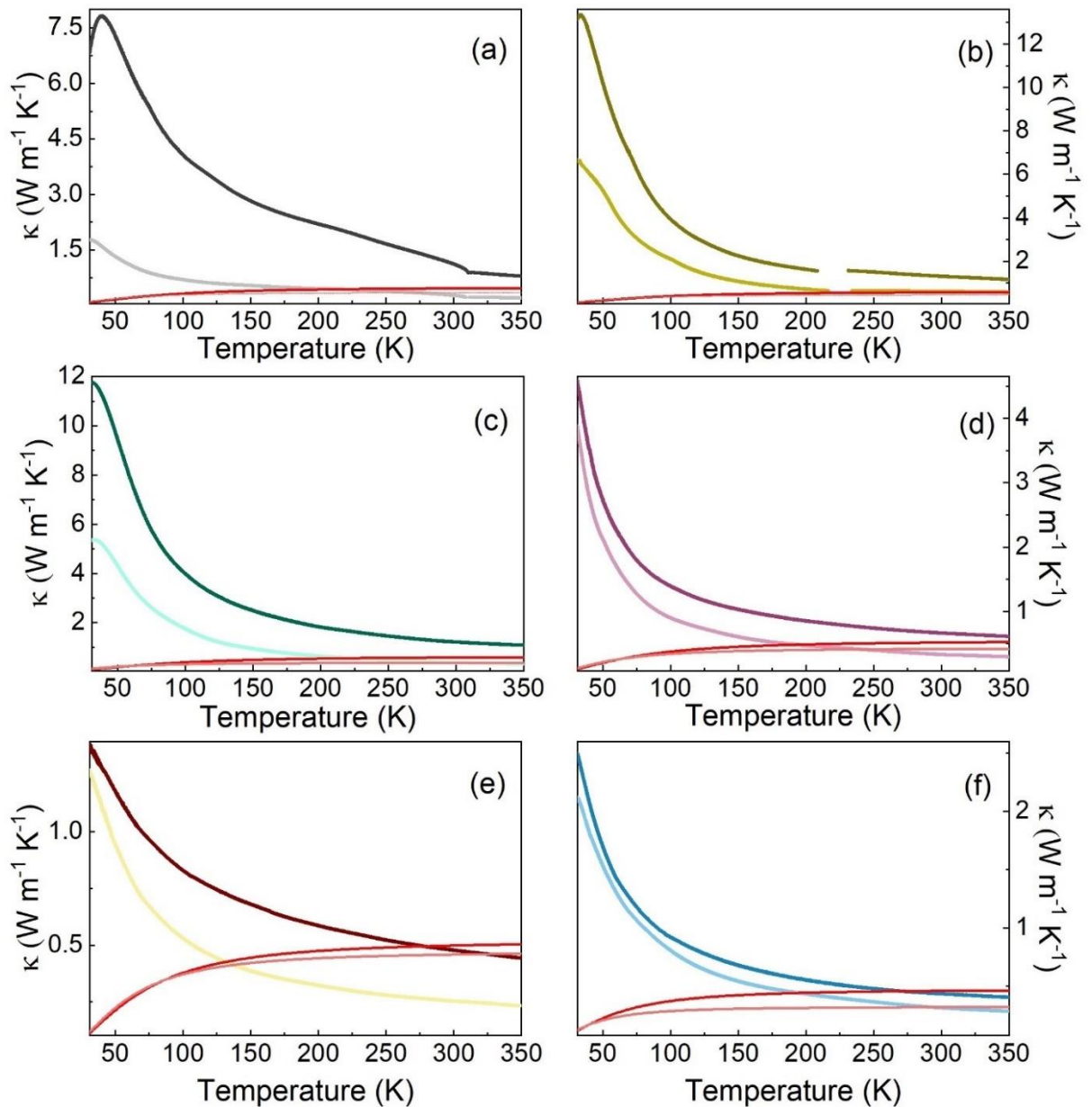
Figure 6.6 shows the thermal conductivity for all compounds studied in this work, calculated using eq. 6.2. There are some qualitative features shared by most of the compounds. In order to analyse their temperature dependency, the Debye temperatures for each compound have been calculated from the phonon dispersion spectra as

$$T_D = \frac{\hbar\omega_D}{k_B}, \quad (6.3)$$

where  $\hbar$  is the reduced Plank constant,  $k_B$  the Boltzmann constant and  $T_D$  the Debye frequency, for which the lowest optical branch has been taken. In the case of  $\text{CuInP}_2\text{S}_6$  ( $T_D = 129$  K),  $\text{CuInP}_2\text{Se}_6$  ( $T_D = 94$  K),  $\text{AgInP}_2\text{S}_6$  ( $T_D = 135$  K),  $\text{AgInP}_2\text{Se}_6$  ( $T_D = 80$  K),  $\text{CuBiP}_2\text{Se}_6$  ( $T_D = 42$  K),  $\text{AgBiP}_2\text{S}_6$  ( $T_D = 84$  K), and  $\text{AgBiP}_2\text{Se}_6$  ( $T_D = 64$  K), compounds, at middle temperature ranges, thermal conductivity decreases on heating closely following the law  $\kappa \sim T^{-1}$ , with exponents in the range 0.8 - 1.4 with the

exception of  $\text{AgBiP}_2\text{S}_6$  with the layers parallel to the heat flow which it is clearly flatter than the rest. This general behaviour confirms the dominant role of phonon scattering above the Debye temperature, softening the decrease, in general, at about a value double than that one.

At higher temperatures than  $T_D$ ,  $\kappa(T)$  dependence reflects the temperature dependence of the sound velocity and heat capacity. This behavior is valid only in the regime where the phonon mean free path exceeds the interatomic distance. In  $\text{CuBiP}_2\text{Se}_6$  compound the lattice thermal conductivity has already reached its lowest value of approximately  $0.20 \text{ W m}^{-1} \text{ K}^{-1}$  near 100 K, because the phonon mean free path is limited to the interatomic distance and cannot decrease further.



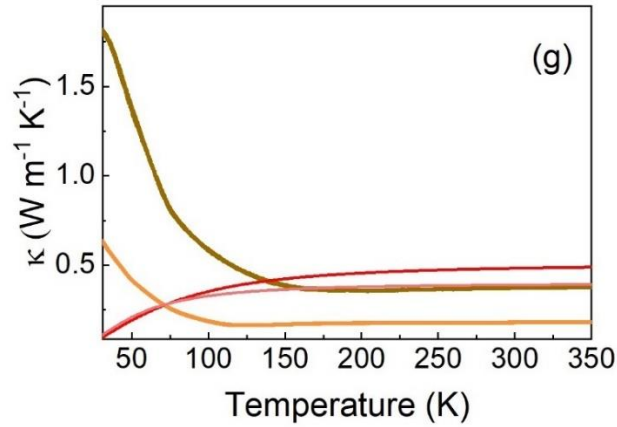


**Fig. 6.6.** Thermal conductivity  $\kappa$  as a function of temperature for: (a)  $\text{CuInP}_2\text{S}_6$ , (b)  $\text{CuInP}_2\text{Se}_6$ , (c)  $\text{AgInP}_2\text{S}_6$ , (d)  $\text{AgInP}_2\text{Se}_6$ , (e)  $\text{AgBiP}_2\text{S}_6$ , (f)  $\text{AgBiP}_2\text{Se}_6$  and (g)  $\text{CuBiP}_2\text{Se}_6$  2D layered ferroelectric compounds. Dark colour denotes that  $\kappa$  is measured along the layers while light implies that it is measured perpendicular to them

Near the Debye temperature and below, the biggest thermal conductivity is observed for  $\text{CuInP}_2\text{S}_6$ ,  $\text{CuInP}_2\text{Se}_6$  and  $\text{AgInP}_2\text{S}_6$  crystals. For these compounds, the biggest anisotropy of heat transport along and normally to the structural layer is also observed (fig. 6.7 (b)). For  $\text{AgInP}_2\text{Se}_6$  crystal and for all three Bi containing compounds with smaller thermal conductivity at low temperatures the thermal transfer anisotropy is also several times smaller.

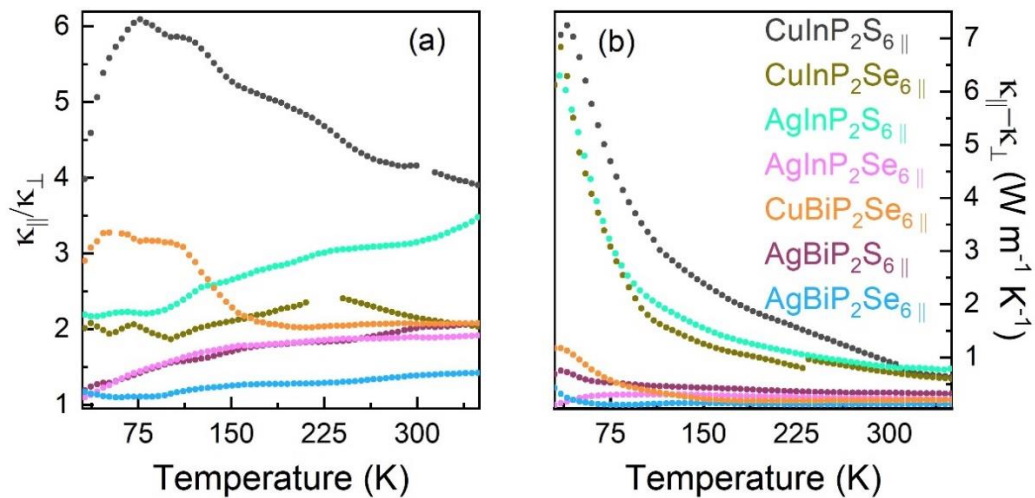


**Fig. 6.7.** Thermal conductivity anisotropic behavior: ratio (a) and the difference between  $\kappa_{||}$  and  $\kappa_{\perp}$

Where there are phase transitions in those compounds ( $\text{CuInP}_2(\text{S},\text{Se})_6$ ,  $\text{Ag}_{0.1}\text{Cu}_{0.9}\text{InP}_2(\text{S},\text{Se})_6$ ), there is a general decrease of the thermal conductivity values in the paraelectric phase with respect to the ferri(ferro)electric one, as the temperature is increased. The stark decrease in  $\text{CuInP}_2\text{S}_6$  is related to the fact that, in the paraelectric phase, the Cu ions occupy three non-equivalent sites [100]: Cu1 is quasitrigonal, in off-center positions, Cu2 is octahedral, located in the octahedron centers, Cu3 is almost tetragonal, penetrating into the interlayer space (fig. 6.8). For Cu1 there are two possible positions:  $\text{Cu1}^{up}$  is displaced upwards from the middle of the layer while  $\text{Cu1}^{down}$  is displaced downwards. This implies the presence of Cu1 dipoles that randomly flip between up and down state, yielding a macroscopically non polar configuration. At the ferrielectric phase ordering takes place as a cooperative freezing of these motions, with 90% of the Cu1 ions occupying the site  $\text{Cu1}^{up}$  [99]. This behavior is related to the second order Jahn–Teller effect of  $\text{Cu}^{1+}$  cations with  $3d^{10}$  electronic configuration [140]. Heat transfer by phonons is very efficiently blocked in the disordered, high temperature phase due to the reduction of the phonon mean free path by these hopping motions.

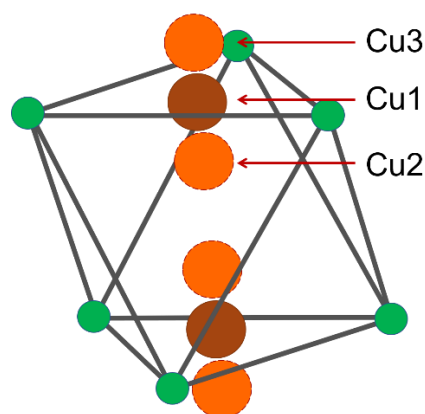


**Fig. 6.8.** The occupation of three “up”  $\text{Cu}^{1+}$  positions labeled Cu1, Cu2, Cu3 at paraelectric phase. The corresponding “down” positions are also shown

This scenario is more or less reproduced in the case of  $\text{CuInP}_2\text{Se}_6$  with the main difference that the off-center copper site is shifted from the layer midplane by a smaller distance than its equivalent in  $\text{CuInP}_2\text{S}_6$  ( $1.17 \text{ \AA}$  vs.  $1.58 \text{ \AA}$ ) [100]. The  $\text{In}^{3+}$  cations are also shifted but in opposite position and by only  $0.2 \text{ \AA}$  from the middle of

the layer, forming a second polar sublattice. Assuming that order-disorder takes place due to Cu hopping motions, the corresponding double well potential would be shallower in the selenide than in the sulphide, which would take the transition to a lower temperature. In the paraelectric phase, the disorder in the selenide is thus smaller, leading to a higher thermal conductivity than in the sulphide.

Figure 6.9 a shows the comparison of the thermal conductivities for pure  $\text{CuInP}_2\text{S}_6$  and  $\text{AgInP}_2\text{S}_6$  when figure 6.9 b demonstrates the difference of  $\kappa$  between  $\text{CuInP}_2\text{Se}_6$  and  $\text{AgInP}_2\text{Se}_6$ . Comparing figure 6.9 a and figure 6.9 b it is well seen that, in selenides the cation substitution severely reduces  $\kappa$ , while in sulphides  $\kappa$  is slightly higher in the case of  $\text{AgInP}_2\text{S}_6$  than in  $\text{CuInP}_2\text{S}_6$ .

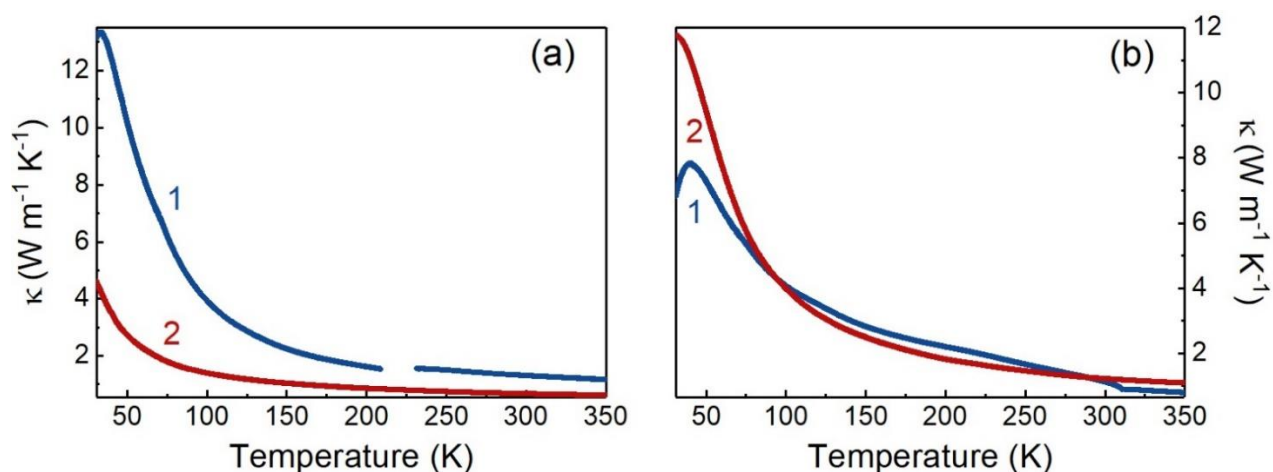


**Fig. 6.9.** Thermal conductivities for (1)  $\text{CuInP}_2\text{S}_6$  and (2)  $\text{AgInP}_2\text{S}_6$  (a) and (1)  $\text{CuInP}_2\text{Se}_6$  and (2)  $\text{AgInP}_2\text{Se}_6$  (b) measured in the direction perpendicular to the layers

The introduction of Bi has a very interesting consequence as in all three cases ( $\text{AgBiP}_2\text{S}_6$ ,  $\text{AgBiP}_2\text{Se}_6$ , and  $\text{CuBiP}_2\text{Se}_6$ ) there is a considerable reduction in the values of the thermal conductivity with respect to the indium doped counterparts, thus being candidates for applications where low or ultralow thermal conductivity is needed. Possibly, the reason is that the substitution of In by Bi affects the phonon mean free path because although they have a similar coordination environment,  $\text{Bi}^{3+}$  ion is bigger in size and has double mass. The extreme case is  $\text{CuBiP}_2\text{Se}_6$ . At room temperature, though Cu occupies a site with an octahedral coordination environment

of Se ions, the actual position of the copper ions is thought to be a disordered arrangement of various off-center positions [119], what would severely increase phonon scattering. As temperature is reduced from 350 K, thermal conductivity is more or less constant till the phase transition takes place, meaning that the disorder is well maintained even if the temperature is lowered; once the compound is in the ordered phase, its behaviour is similar to the rest, with thermal conductivity fulfilling the Eiken's law. Extremely low  $\kappa$  at low temperatures indicates that there could be a strong lattice anharmonicity in this compound. Obviously, the low thermal conductivity is mainly due to very short phonon free path (MFP) and hence, short lifetimes.

In order to obtain the values of MFP we used the well-known equations of the lattice thermal conductivity

$$\kappa_L = \frac{1}{3} C v \Lambda = \frac{1}{3} C v^2 \tau, \quad (6.4)$$

where  $\kappa_L$  is the lattice conductivity,  $C$  is volume heat capacity,  $v$  is average phonon velocity,  $\Lambda$  is phonon free pass and  $\tau$  is phonon life time. Therefore, MFP and phonon life time can be obtained as

$$\Lambda = \frac{3D}{v} \quad \text{and} \quad \tau = \frac{3D}{v^2}, \quad (6.5)$$

where  $D$  is the measured thermal diffusivity. The average phonon velocity can be calculated by the slopes of three acoustic phonon branches near the  $\Gamma$  point (Brillouin zone) taking into account the elastic modulus. For each direction, the sound velocity is averaged on the two transverse acoustic modes, ( $TA_1$  and  $TA_2$ ), and one longitudinal acoustic mode (LA) by means of the following equation:

$$\frac{3}{v^3} = \frac{1}{v_{TA_1}^3} + \frac{1}{v_{TA_2}^3} + \frac{1}{v_{LA_1}^3}. \quad (6.6)$$

Hence, the calculated average sound velocities for our compounds are follows:

**CuInP<sub>2</sub>S<sub>6</sub>** –  $v_{||} = 2750$  m/s and  $v_{\perp} = 2230$  m/s, **CuInP<sub>2</sub>Se<sub>6</sub>** –  $v_{||} = 2680$  m/s and  $v_{\perp} = 2330$  m/s, **AgInP<sub>2</sub>S<sub>6</sub>** –  $v_{||} = 2360$  m/s and  $v_{\perp} = 1600$  m/s, **AgInP<sub>2</sub>Se<sub>6</sub>** –  $v_{||} = 2260$  m/s

and  $v_{\perp} = 1910$  m/s, **CuBiP<sub>2</sub>Se<sub>6</sub>** –  $v_{\parallel} = 2280$  m/s and  $v_{\perp} = 2140$  m/s, **AgBiP<sub>2</sub>S<sub>6</sub>** –  $v_{\parallel} = 2000$  m/s and  $v_{\perp} = 1940$  m/s and **AgBiP<sub>2</sub>Se<sub>6</sub>** –  $v_{\parallel} = 2160$  m/s and  $v_{\perp} = 1830$  m/s.

And the result, MFPs and phonon life times as a function of temperature, are shown in fig. 6.10 and fig. 6.11 respectively.

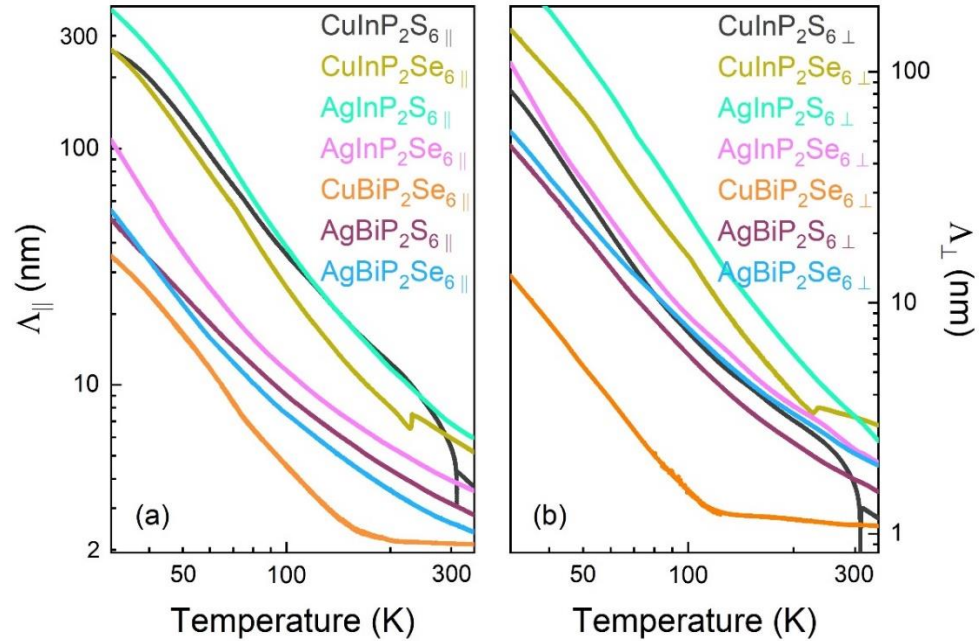


**Fig. 6.10.** Phonon mean free path  $\Lambda$  for  $M^{1+}M^{3+}P_2(S,Se)_6$  ( $M^{1+}$  - Cu, Ag;  $M^{3+}$  - In, Bi) in the parallel (a) and perpendicular (b) directions to the layers

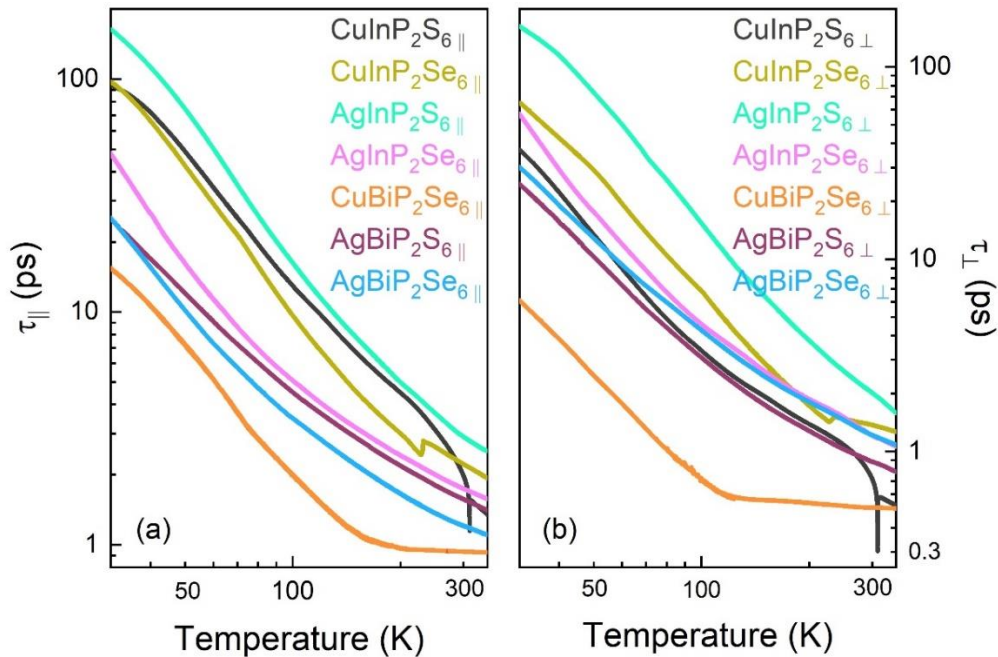


**Fig. 6.11.** Phonon life time  $\tau$  temperature dependence for  $M^{1+}M^{3+}P_2S(Se)_6$  layered crystals in the parallel (a) and perpendicular (b) directions to the layers

In general, we found that at high temperatures the phonon life times of all materials are very short, roughly ranging from 0.5 to 1.6 ps when heat is transferred normally the layers (fig. 6.11 a) and two times and two times longer (1 – 3 ps) along the layers (fig. 6.11 b). Obtained ultrashort phonon lifetimes could be explained of an essential role of phonon-phonon scattering and anharmonicity leading to outstanding thermal transport properties of investigated compounds.

In fig. 6.12 a, b, the MFPs at 130 K are compared as a function of  $T_D$ . In the case of heat transfer along the layers (fig. 6.12 a) the  $\Lambda(T_D)$  dependence is almost linear. For the case of heat being transferred along a direction normal to the structural layer plane (fig. 6.12 b), only for the  $\text{CuInP}_2\text{S}_6$  crystal the MFP deviates out of the general linear trend, to a lower value, what is related to an additional contribution to lattice anharmonicity that follows from second order Jahn – Teller (SOJT) effect inducing the ferrielectric phase transition. In dimensionless coordinates  $\Lambda/\Lambda_D$  vs  $T/T_D$  (Fig. 6.12 c), the dependencies for all compounds coincide, what gives evidence about the right values of the Debye temperatures to characterize the lattice anharmonicity in  $\text{M}'\text{M}''\text{P}_2\text{S}(\text{Se})_6$  compounds.

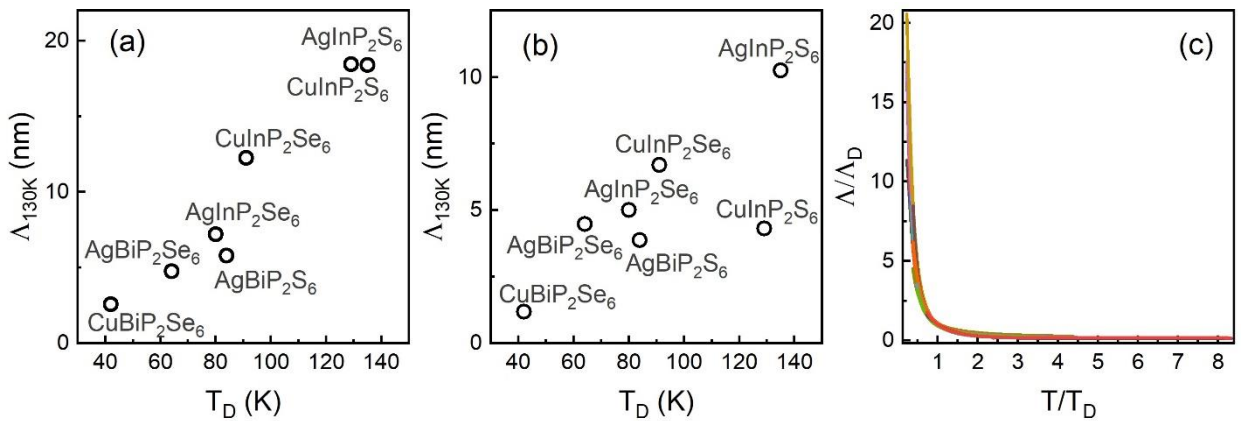


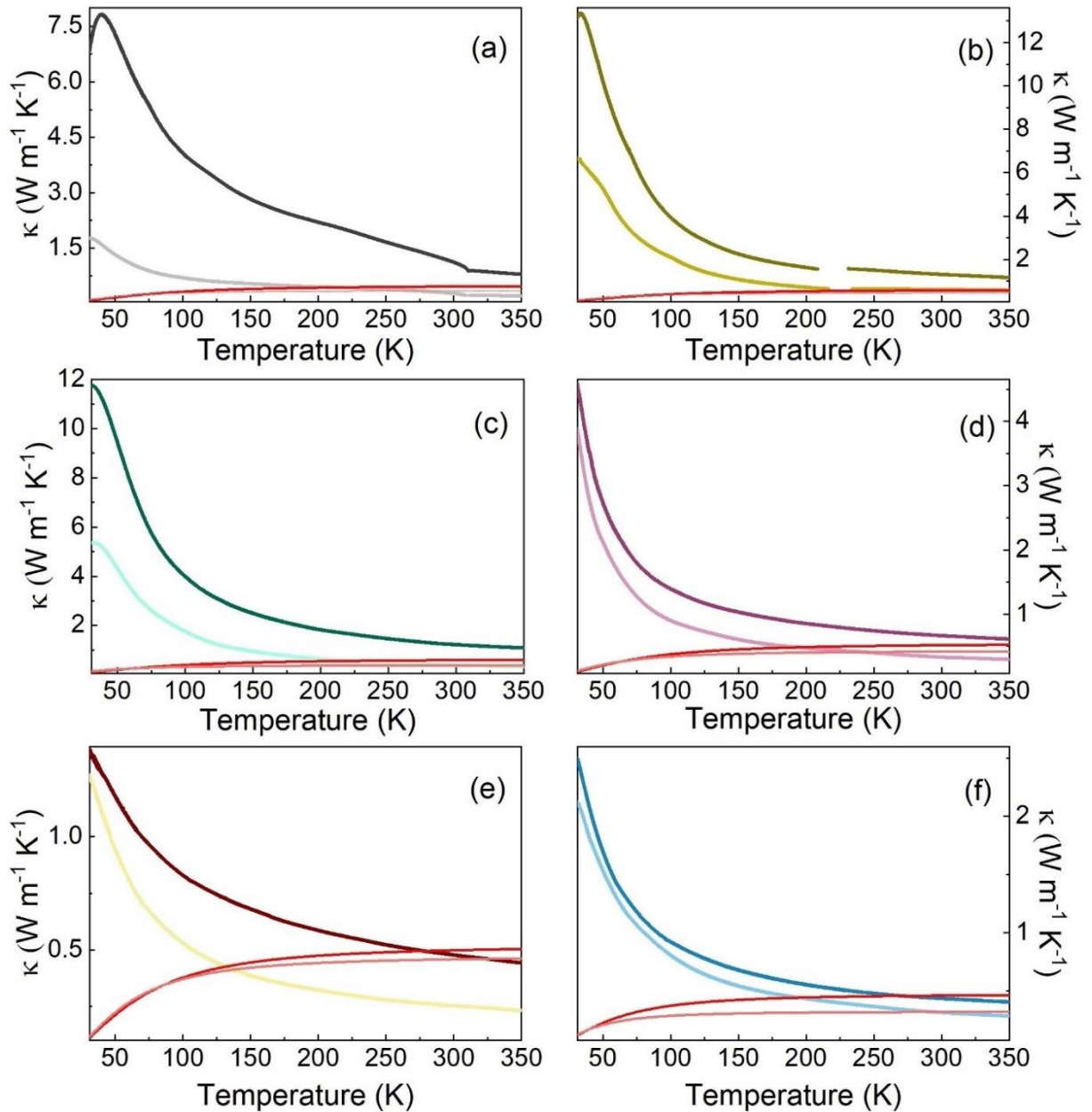
**Fig. 6.12.** The mean free path of heat transferring phonons at 130 K along layers (a) and normal to the layers (b) as a function of  $T_D$ . Normalized mean free path  $\Lambda/\Lambda_D$  vs normalized temperature  $T/T_D$  (c)

In order to estimate the minimal possible thermal conductivity  $\kappa_{min}$ , the equation which describes “an amorphous limit of thermal conductivity” for such type of crystals has been used, which can be written in the next form [211]:

$$\kappa_{\min} = \left(\frac{\pi}{6}\right)^{\frac{1}{3}} k_B n^{\frac{2}{3}} \sum_i \left[ c_i \left(\frac{T}{T_D}\right)^2 \int_0^{\frac{T_D}{T}} \frac{x^3 e^x dx}{(e^x - 1)^2} \right], \quad (6.7)$$

where  $T_D$  is the Debye temperature for each mode and can be found as  $T_D = v_i (\hbar / k_B) (6\pi^2 n)^{\frac{1}{3}}$ ,  $v_i$  is the average sound velocity,  $n$  the number of atoms,  $\hbar$  the reduced Plank constant, and  $k_B$  the Boltzmann constant.

The values of the measured thermal conductivities  $\kappa$  and the theoretical minimum thermal conductivities  $\kappa_{\min}$  for the different compounds are presented in fig. 6.15.



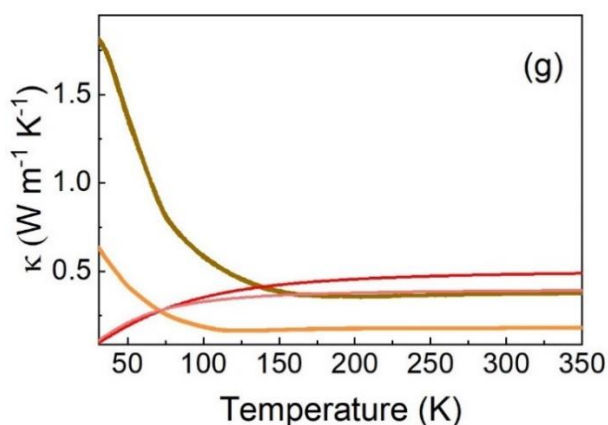


**Fig. 6.13.** Comparison of the measured thermal conductivity temperature dependence and the calculated minimal value (yellow lines) for  $M'M''P_2S(Se)_6$  layered crystals: (a)  $CuInP_2S_6$ ; (b)  $CuInP_2Se_6$ ; (c)  $AgInP_2S_6$ ; (d)  $AgInP_2Se_6$ ; (e)  $AgBiP_2S_6$ ; (f)  $AgBiP_2Se_6$ ; (g)  $CuBiP_2Se_6$ . Dark colour means that the thermal conductivity is measured along the layers while the light one means that it is measured normally to the structural layers

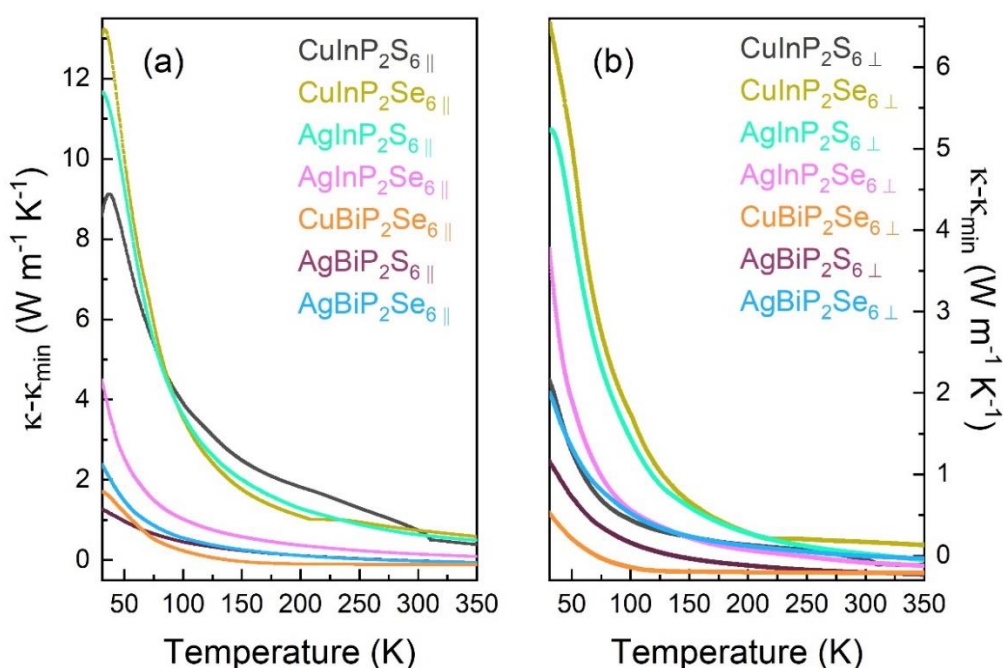


**Fig. 6.14** Temperature dependence of the difference between the measured and the calculated values of the thermal conductivity for  $M'M''P_2S(Se)_6$  layered crystals along the layers (a) and normal to the layers (b)

The difference among these values (fig. 6.14) increases on cooling. When heat is transferred along the layers, the  $\kappa - \kappa_{min}$  difference is clearly divided into two

groups: a high difference is found for  $\text{CuInP}_2\text{S}_6$ ,  $\text{CuInP}_2\text{Se}_6$  and  $\text{AgInP}_2\text{S}_6$  crystals while it is smaller for  $\text{AgInP}_2\text{Se}_6$ ,  $\text{AgBiP}_2\text{S}_6$ ,  $\text{AgBiP}_2\text{Se}_6$  and  $\text{CuBiP}_2\text{Se}_6$ . For the case of heat transport in the perpendicular direction to the structural layers, the  $\kappa - \kappa_{min}$  difference spreads between the biggest value for  $\text{CuInP}_2\text{S}_6$  and the smallest one for  $\text{CuBiP}_2\text{Se}_6$ . In fig. 6.15, the  $\kappa - \kappa_{min}$  difference as a function of  $T/T_D$  is shown for all investigated compounds, while Fig. 6.16 presents a comparison between the calculated  $\kappa_{min}$  and the measured  $\kappa$ , both of them at 350K.

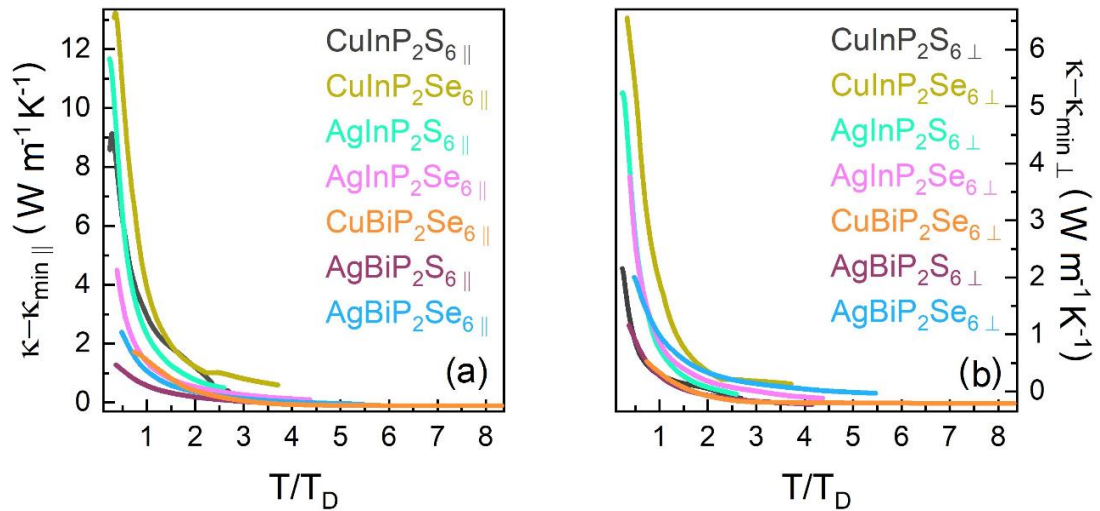


**Fig. 6.15.** Difference between the measured thermal conductivity  $\kappa$  and the calculated minimal value  $\kappa_{min}$  as a function of the dimensionless temperature  $T/T_D$  along the layers (a) and normal to the layers (b)

From the presented data, it follows that phonon Umklapp scattering is responsible for the low values of thermal conductivity above  $T_D$ . Figure 6.16 (a) demonstrates that for the case of heat transport along the structural layers at 350 K three compounds ( $\text{CuInP}_2\text{S}_6$ ,  $\text{CuInP}_2\text{Se}_6$  and  $\text{AgInP}_2\text{S}_6$ ) have a measured value of  $\kappa$  about two times bigger than  $\kappa_{min}$ . For another group ( $\text{AgBiP}_2\text{S}_6$ ,  $\text{AgBiP}_2\text{Se}_6$  and  $\text{CuBiP}_2\text{Se}_6$ ) the measured thermal conductivity is smaller than or equal to the calculated  $\kappa_{min}$ . Obviously, some additional structural disorder exists in the Bi containing compounds. The  $\text{CuBiP}_2\text{Se}_6$  crystal data especially demonstrates the presence of an additional mechanism of phonon scattering hindering heat transfer. Besides,  $\text{AgInP}_2\text{Se}_6$  crystal can be considered as an intermediate case between the more heat conductive and the more resistive groups of compounds, as the  $\kappa$  measured

in this case is a little bigger than  $\kappa_{min}$  at 350 K. In the case of  $\kappa_{\perp}$  (fig. 6.16 b) the measured thermal conductivity is smaller than or equal to the calculated  $\kappa_{min}$  for all the compounds except  $\text{CuInP}_2\text{S}_6$ .

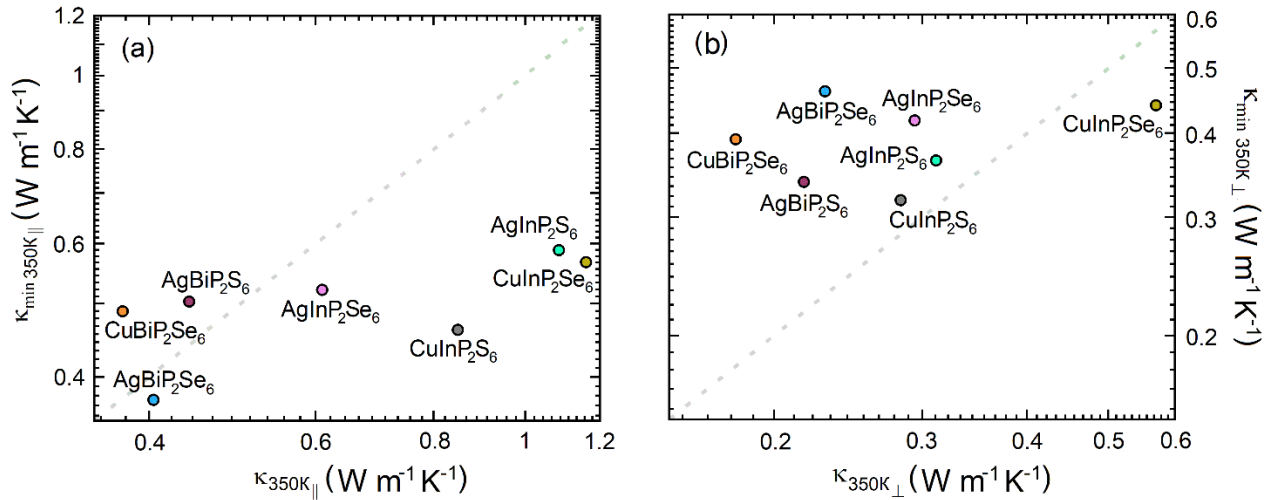


**Fig. 6.16.** Comparison of  $\kappa$  and  $\kappa_{min}$  at 350 K along the layers (a) and normal to the layers (b)

The excess in conduction,  $\kappa(T) - \kappa_{min}(T)$ , at temperatures  $T/T_D > 1$  is understood by considering the difference between Umklapp and Normal processes. However, as the temperature decreases below one half of the Debye temperature  $T_D$  (from about 42 K to 130 K), an increasingly greater fraction of thermally excited phonons have wave vectors shorter than one half of the distance to the Brillouin zone boundary. At  $T < T_D/2$  most phonon - phonon collisions are non - resistive Normal processes because the sum of the wave vectors of the interacting phonons fits within the first Brillouin zone. The number of Umklapp processes decreases with temperature below  $T_D/2$  so they can no longer limit  $\kappa(T)$  to  $\kappa_{min}(T)$ , leading to additional heat conduction compared to the case where  $T > T_D/2$ .

We conclude that, due to the extremely high anharmonicity in the studied layered crystals, the phonon thermal conductivity is limited to its minimum possible value where the mean free path equals the interatomic distance, by intrinsic phonon-phonon processes. At this point, it is interesting to understand why such a big difference exists in the thermal conductivity between the  $\text{AgInP}_2\text{S}_6$  and the  $\text{AgBiP}_2\text{S}_6$

crystals. Obviously, it is a direct consequence of the difference in the nature of the chemical bonding. In the selenide compound, the relatively low thermal conductivity arises from this layered crystal lattice vibrations, which create low frequency, localized optical phonons in the acoustic region and thus enable strong anharmonic phonon scattering.

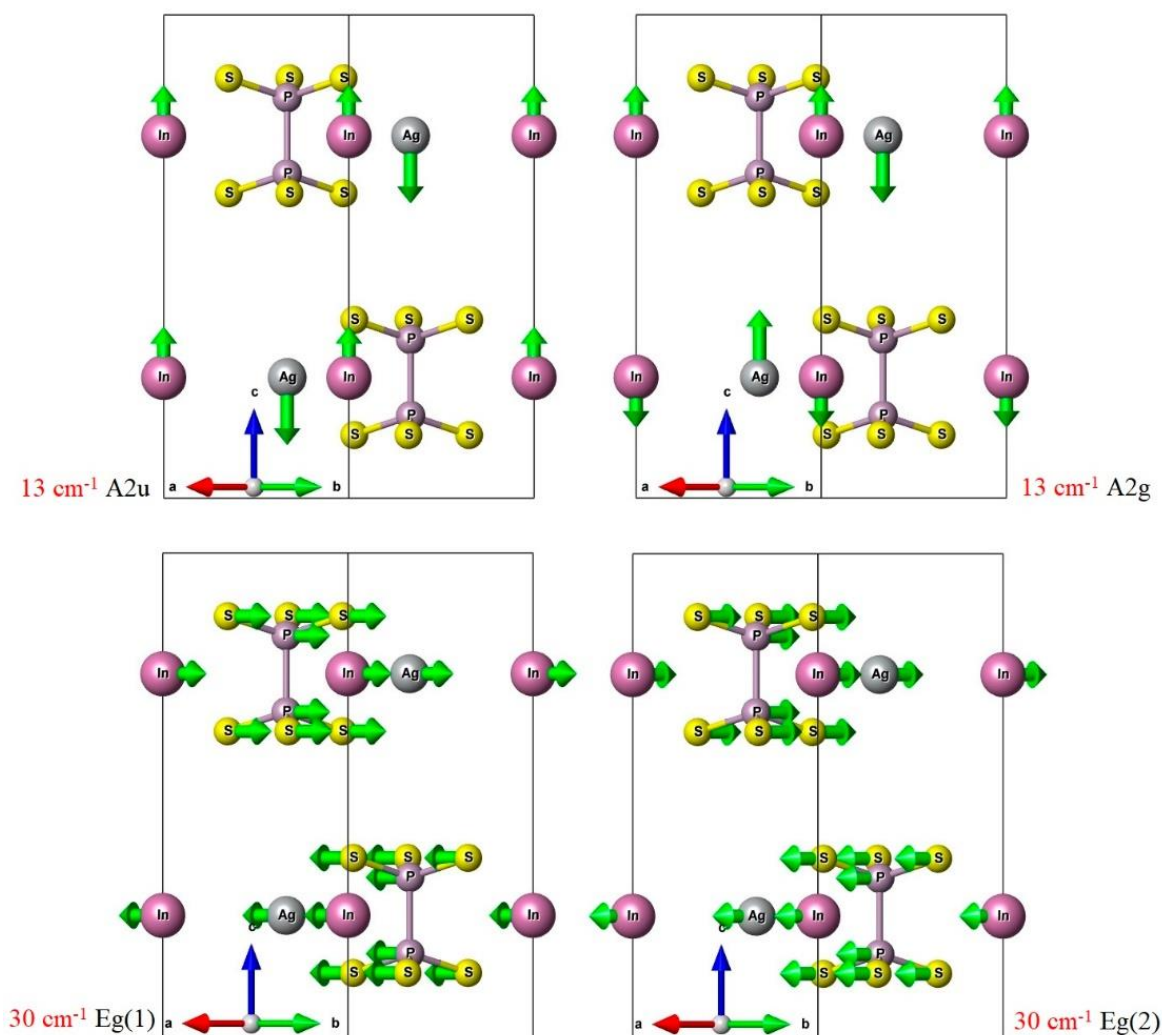


**Fig. 6.17.** Eigen vectors of lowest energy  $A_{2g}$ ,  $A_{2u}$ ,  $E_g$  optical modes at BZ center for  $\text{AgInP}_2\text{S}_6$  crystal

Fig. 6.17 and fig. 6.18 show atom-projected phonon density of states of  $\text{AgInP}_2\text{S}_6$  and  $\text{AgInP}_2\text{Se}_6$  layered crystals. Both compounds share the prominent feature of the presence of low-lying modes, cutting through the acoustic region (fig. 6.6 f, g). For  $\text{AgInP}_2\text{S}_6$ , the acoustic modes are attenuated near  $40\text{ cm}^{-1}$  towards the edge of Brillouin zone, and low-energy (near  $13\text{ cm}^{-1}$ )  $A_{2g}$  and  $A_{2u}$  symmetry optical

phonon modes are found in the acoustic region, both of which are mostly associated with vibrations of Ag atoms normally to the structural layers planes. At a little higher frequency (near  $30\text{ cm}^{-1}$ ), doubly degenerated  $E_g$  symmetry optical modes are also placed, which involve in-plane motions of silver and indium cations together with shifts of  $(P_2S_6)^{4-}$  anions. These phonon modes with approximately zero group velocity reflect the locality of vibrations of Ag atoms and confirm the relative weakness of covalent bonding Ag–S.

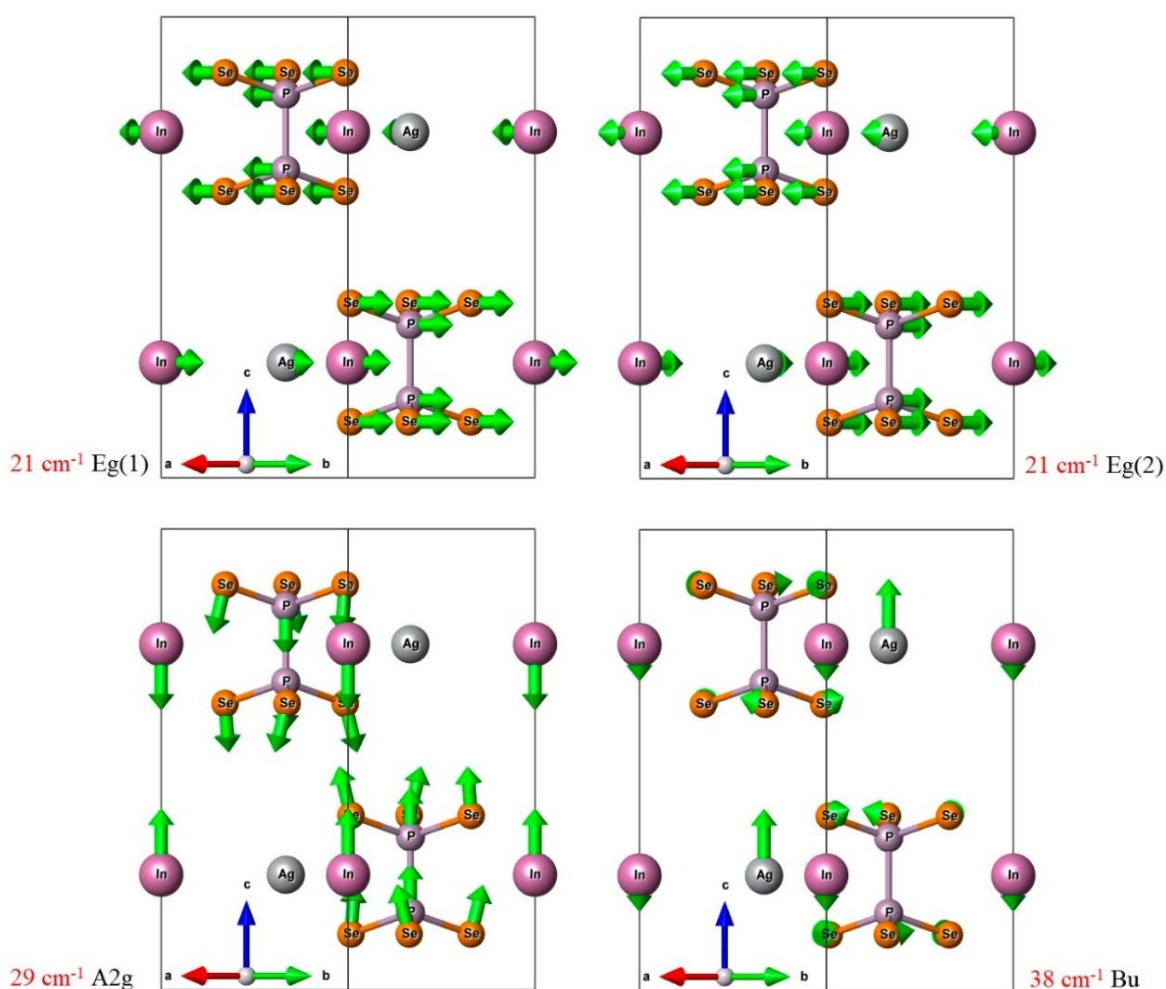


**Fig. 6.18.** Eigen vectors of lowest energy  $A_{2g}$ ,  $A_{2u}$ ,  $E_g$  optical modes at BZ center for  $AgInP_2Se_6$  crystal

In the case of  $AgInP_2Se_6$  crystal the lowest flat optical branches at BZ center have frequencies of  $21\text{ cm}^{-1}$  for  $E_g$  modes,  $29\text{ cm}^{-1}$  for  $A_{2g}$  mode and  $38\text{ cm}^{-1}$  for  $B_g$  mode (Fig. 6.18). For the selenium compound, the  $A_g$  mode frequency increases (from  $13\text{ cm}^{-1}$  in  $AgInP_2S_6$  crystal to  $29\text{ cm}^{-1}$  in  $AgInP_2Se_6$ ) as a result of a bigger

covalence of the Ag–Se bonds. Conversely, for the degenerate  $E_g$  modes on substitution of S by Se, the frequency decreases from  $30\text{ cm}^{-1}$  to  $21\text{ cm}^{-1}$  as a result of the bigger mass of the  $(\text{P}_2\text{Se}_6)^{4-}$  anions.

In addition to reducing group velocities, the lowest frequency localized optical modes act as scattering centers for low energy acoustic modes. Such resonant scattering further reduces the total lattice thermal conductivity and it is obviously more effective for the selenide crystal, with a bigger polarizability of the heavy  $(\text{P}_2\text{Se}_6)^{4-}$  anions. In more detail, a larger suppression of  $\kappa$  by the lower flat optical branch energy modes can originate from several reasons. The flat optical branch exhibits an anticrossing with acoustic phonon modes. This largely reduces the group velocity of the heat carrying acoustic phonons around the optical mode energy, which leads to the suppression of  $\kappa$ . The lower the frequency of the optical mode, the larger the effect, because the group velocity of acoustic phonons is larger at lower energy. The Umklapp scattering that suppresses  $\kappa$  can also be stronger with a lower energy of the optical branch, as lower optical modes must scatter higher acoustic phonons to create the same final phonons. Because acoustic phonons with higher energy have a higher density of states, the Umklapp scattering can be stronger.

Peculiarities of chemical bonding, such as the second order Jahn – Teller (SOJT) effect and a high deformability of the lone-pair electron charge density, can also limit the thermal conductivity in crystalline materials. It has already been shown [108] that in  $\text{CuInP}_2\text{S}_6$  and  $\text{CuInP}_2\text{Se}_6$  compounds the relaxational soft modes appeared due to the SOJT effect with participation of  $s$  and  $d$  orbitals of  $\text{Cu}^+$  cations and  $p$  orbitals of  $\text{S}(\text{Se})^{2-}$  anions. The  $\text{In}^{3+}$  cations in these ferrielectrics can also be involved in the SOJT effect by hybridization of their  $s$  and  $p$  electronic orbitals with sulfur or selenium anion  $p$  orbitals. But indium atoms in these compounds are strongly enough bounded by covalent interaction with the surrounding chalcogenide atoms. Related to the SOJT effect disordering at the transition, heating from the ferrielectric phase into the paraelectric one strongly suppresses the thermal conductivity, what is nicely seen in the case of  $\text{CuInP}_2\text{S}_6$  crystal (fig. 6.6 a).

In the case of  $\text{AgInP}_2\text{S}_6$  and  $\text{AgInP}_2\text{Se}_6$  compounds, the cations  $\text{Ag}^{1+}$  create stronger covalent bonds inside the chalcogenide octahedra preventing SOJT effect and the transition into a polar state when the temperature is lowered [134]. As was shown above, only for  $\text{AgInP}_2\text{Se}_6$  the strong phonon–phonon interaction is related to the crossing of the low energy optical branch with acoustic branches and therefore  $\kappa$  is reduced to the amorphous limit. But in  $\text{AgBiP}_2\text{S}_6$  and  $\text{AgBiP}_2\text{Se}_6$  compounds the physical origin of anharmonicity can also be traced to the existence of the stereochemically active  $s^2$  lone pair of  $\text{Bi}^{3+}$  cations. The  $s$  electron shell of Bi is easily deformed by lattice vibrations, resulting in a strong anharmonicity due to the nonlinear terms in the total energy associated with a large electronic response. Obviously, this electron lone pair is also related to the SOJT effect that may lead to the observed structural instability in  $\text{CuBiP}_2\text{Se}_6$  layered crystal [119]. The main idea behind the relationship between an electron lone pair and low  $\kappa$  is that as atoms approach one another during thermal agitation, the overlapping wave functions of the lone pair and nearby valence electrons will induce a nonlinear repulsive electrostatic force causing increased anharmonicity in the lattice. As the lone pair moves away from the nucleus, anharmonic interactions with adjacent atoms intensify and  $\kappa$  decreases. The highest degree of anharmonicity should thus be achieved when the electron lone pair is far removed from the nucleus, yet not participating in bonding. A similar situation was observed for the  $\text{Sn}_2\text{P}_2\text{S}_6$  crystal where  $\text{Sn}^{2+}$   $5s^2$  lone pair disordering induces the transition from the ferroelectric to the paraelectric phase and effectively suppress thermal conductivity [1, 189].

The electrostatic repulsion between the lone pair electrons and the neighboring chalcogen anions creates anharmonicity in the lattice, the strength of which is determined by the morphology of the lone pair orbital that is illustrated in fig. 6.19 for the  $\text{AgBiP}_2\text{S}_6$  layered crystal. It is seen that, as a result of Bi  $s$  orbitals stereoactivity, the electron density is presented at the top of the valence band in the case of  $\text{AgBiP}_2\text{S}_6$  crystal, but In  $s$  orbitals electron density is not observed at the top of  $\text{AgInP}_2\text{Se}_6$  valence band. This comparison gives evidence about the hybridization of Bi  $s$  orbitals with S  $p$  orbitals and Bi  $p$  orbitals. Such  $sp^2$  mixing induces the

stereoactivity of the Bi  $s^2$  lone pair which appears in the electronic charge space distribution for  $\text{AgBiP}_2\text{S}_6$  crystal, for which Bi  $s$  orbitals lay in the range  $-10.62 \div -10.49$  eV (fig. 6.20 b). Conversely, the space distribution for In  $s$  orbitals lying in the energetic range  $-6.44 \div -5.99$  eV (fig. 6.20 a) demonstrates their participation in the formation of In – Se covalence bonds.

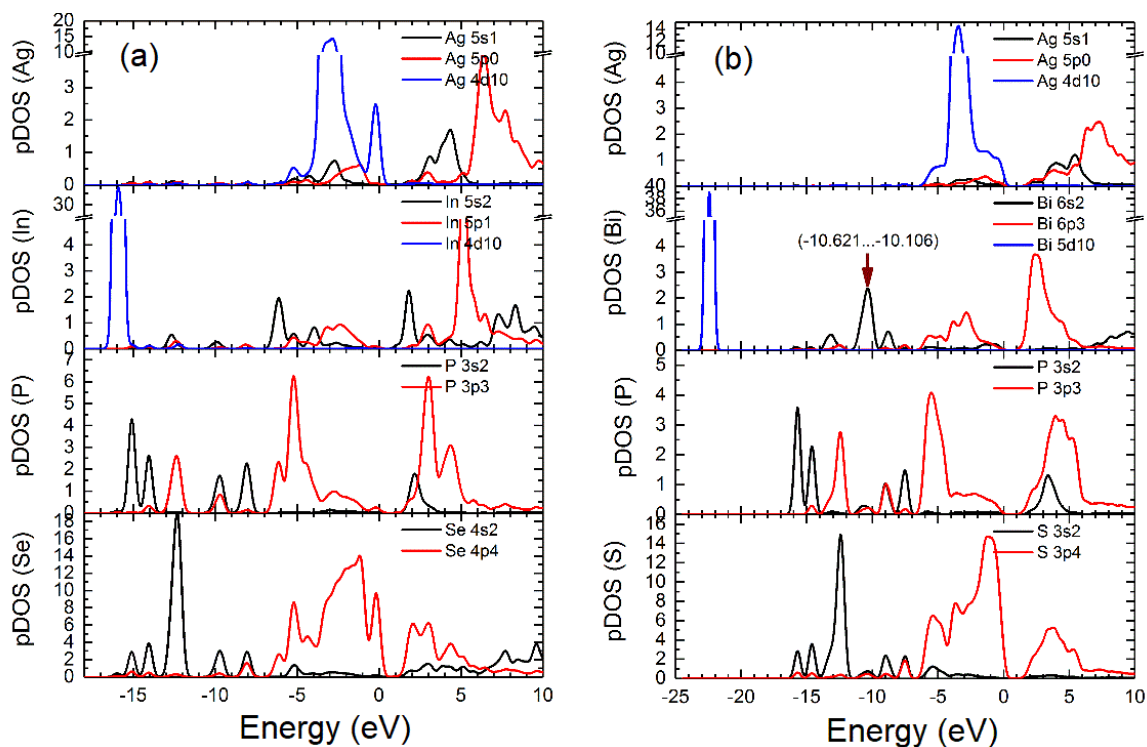


**Fig. 6.19.** Partial electron density of states for  $\text{AgInP}_2\text{Se}_6$  (a) and  $\text{AgBiP}_2\text{S}_6$  (b) crystals

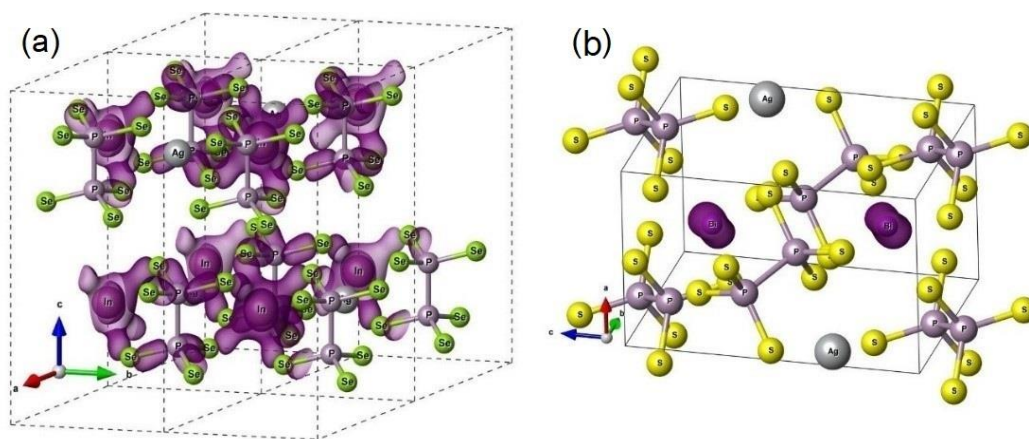


**Fig. 6.20.** Electron density space distribution for orbital laying in the energy range  $-6.44 \div -5.99$  eV of  $\text{AgInP}_2\text{Se}_6$  crystal valence band (a), and for orbital laying in the energy range  $-10.62 \div -10.49$  eV of  $\text{AgBiP}_2\text{S}_6$  crystal valence band (b)

Finally, we would like to discuss the interesting features observed for  $\text{CuBiP}_2\text{Se}_6$  layered crystal in the transition on cooling from the disordered phase into the modulated state, and further to the antiferroelectric phase.

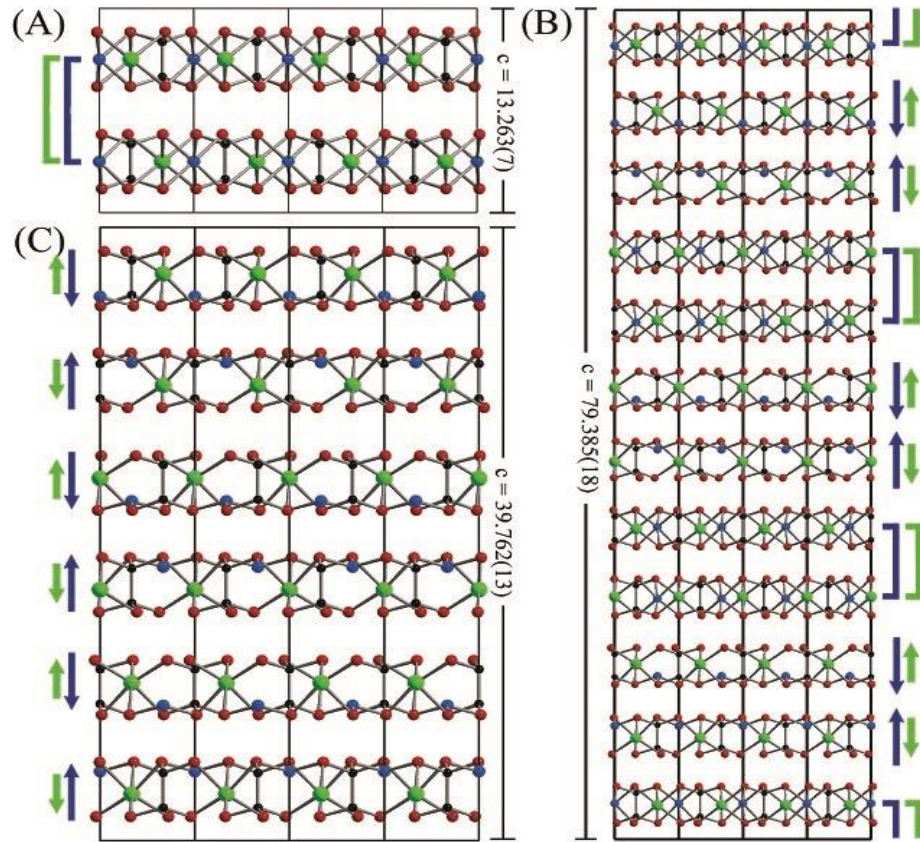


**Fig. 6.21.** The (A) 298 K (B) 173 K, and (C) 97 K structures of  $\text{CuBiP}_2\text{Se}_6$  viewed down the [110] direction. The direction of the displacement of the copper atoms has been indicated with an arrow. The copper atoms in the layers marked with a bracket have not yet ordered [119]

Let's consider the structure modulation and anisotropy of thermal conductivity. As follows from [119] (fig. 6.21), at temperatures higher than 173 K in the paraelectric phase the structure is centrosymmetric, averaged over time and periodical. However, the bismuth and copper atoms accomplish thermal relaxation displacements with the large amplitude which significantly dissipates the heat-bearing phonons (phonon packs) and reduces their mean free path (MFP) to a minimum. In the intermediate phase between 173 – 97 K, which is perpendicularly modulated to the structural layers, probably the wave packs are well propagated along

the layers (in this direction the structure is periodical, the copper and bismuth atoms in more localized positions are located). Nevertheless, heterogeneity (modulation) of the structure causes a minimal MFP (1 nm) across the layers. In antiferroelectric phase (below 97 K), the structure is periodical along and across the layers. Bismuth and copper are well localized and MFP depends on the phonon-phonon scattering only which increases at cooling. Therefore, the thermal diffusivity measurements probably confirm the intermediate structurally modulated phase in  $\text{CuBiP}_2\text{Se}_6$ .

In Fig. 6.6 (e) it is shown that the thermal conductivity of  $\text{CuBiP}_2\text{Se}_6$  along the layers (brown line) on heating decreases till the minimal value near 200 K. Above this temperature, in the disordered phase, the dependence  $\kappa(T)$  demonstrates a glassy – like behavior. Thermal conductivity normal to the structural layers (orange line), while heating, reaches the minimal value already near 100 K at the transition from the antiferroelectric phase to the intermediate modulated phase. The structural modulation of the intermediate phase is oriented normally to the structural layers. So, in the modulated phase, heat transport along the layers is similar to heat transfer in the antiferroelectric phase. Conversely, heat transport normal to the structural layers across the temperature interval of the modulated phase is similar to the observed heat conduction in the disordered high temperature phase. Figure 6.22 demonstrates the modulated phase in  $\text{CuBiP}_2\text{Se}_6$  crystal.

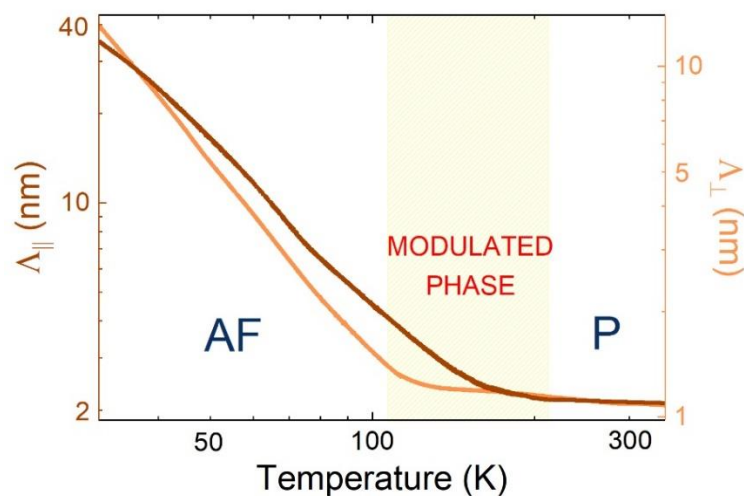


**Fig. 6.22.** Mean free path as a function of temperature of  $\text{CuBiP}_2\text{Se}_6$  in a direction perpendicular (orange) and parallel (brown) to the layers. Letters AF and P correspond to antiferroelectric and paraelectric phases respectively

#### 6.4. Conclusions

Thermal diffusivity has been measured on single crystals of the layered compounds  $\text{Cu}_{1-x}\text{Ag}_x\text{InP}_2(\text{S},\text{Se})_6$  with  $x = 0, 0.1, \text{ and } 1$ ,  $\text{AgBiP}_2(\text{S},\text{Se})_6$  and  $\text{CuBiP}_2\text{Se}_6$  in the wide temperature range 30 - 350K, exhibiting important thermal anisotropies, as well as different phase transitions depending on the particular ions present, confirming the different role played by them, which has been discussed on the basis of disorder, electronic hybridization, and the presence or absence of the second order Jahn Teller effect.

Heat capacity has been calculated through the evaluation of the phonon spectra using density-functional perturbation theory, and, through the combination of both variables.

Combining theoretically calculated heat capacity and experimentally measured thermal diffusivity, the temperature evolution of thermal conductivity has been analyzed for 2D metalthiophosphates and metalselenophosphates ferroelectrics, showing that heat is effectively transferred by phonons and that very low values can be found in several cases due to the enhancement of phonon scattering events, expressing a strong anharmonic behavior.

## Chapter 7. Experimental results and discussion on $(\text{Pb}_x\text{Sn}_{1-x})_2\text{P}_2(\text{Se}_y\text{S}_{1-y})_6$ ferroelectrics

### 7.1. Introduction

This chapter is focused on the critical behaviour study of the phase transitions in  $(\text{Pb}_x\text{Sn}_{1-x})_2\text{P}_2(\text{Se}_y\text{S}_{1-y})_6$  ferroelectric compounds. Here we consider the influence of Pb on the ferroelectric phase transitions (PT) and on their critical behaviour, selecting Se concentrations below and above the Lifshitz Point ( $y = 0.27$ ). According to chapter 5 of this PhD thesis, it is now well understood that Pb frustrates the ferroelectric transitions in  $(\text{Pb}_x\text{Sn}_{1-x})_2\text{P}_2\text{S}_6$  and  $(\text{Pb}_x\text{Sn}_{1-x})_2\text{P}_2\text{Se}_6$  as concentration is increased due to a weaker hybridization caused by a bigger difference between Pb 6s and S(Se) p states. The study of the critical behavior of the ferroelectric transitions in  $(\text{Pb}_x\text{Sn}_{1-x})_2\text{P}_2\text{S}_6$  evidenced that there is a crossover from a non-mean field model at  $x = 0.1$  to a mean-field one at  $x = 0.3$ . Besides, the continuous transition in  $(\text{Pb}_x\text{Sn}_{1-x})_2\text{P}_2\text{Se}_6$  ( $x = 0, 0.05$ ) was found to belong to the 3D-XY universality class, with the PT being smeared. Therefore, a higher increase of lead in the cation sublattice of  $(\text{Pb}_x\text{Sn}_{1-x})_2\text{P}_2(\text{Se}_y\text{S}_{1-y})_6$  is expected to smear the transitions and frustrate them till, at high enough concentrations, complete frustration takes place.

A very special case is the addition of Pb to the Lifshitz concentration compound  $(\text{Pb}_x\text{Sn}_{1-x})_2\text{P}_2(\text{Se}_{0.27}\text{S}_{0.78})_6$ , where it has been experimentally proven that there is a change from a Lifshitz point (LP) to a Tricritical Lifshitz point (TCLP) at a concentration of 5% Pb and to a first order character transition for higher concentrations [2, 191], in agreement with the theoretical predictions based on a Blume-Emery-Griffith (BEG) model with random field effects [80, 212]. After this model, there is an equivalency between the effects of applying an external pressure and introducing a chemical “pressure” with dopants (be them Se instead of S or Pb instead of Sn), and the appearance of a tricritical point (TCP) is predicted when the

consequence of any of these “pressures” is to reduce the critical temperature to a value lower than about 220 - 230K.

What is pending is to study the effect that the addition of Pb has on concentrations close to the Lifshitz point  $y = 0.27$  to check the possibility of new tricritical points for concentrations  $y < 0.27$  and/or frustration of the transitions for  $y > 0.27$ , which is precisely the aim of this study. This would allow, on the one hand, to contrast the validity of the theoretical models and, on the other, to have a deeper knowledge of how ferroelectric properties can be tuned with the addition of adequate dopants.

## 7.2. Samples, experimental techniques and fitting methods

Single crystals of the following concentrations have been grown by a vapor-transport method in a quartz tube using  $\text{SnI}_2$  as a transport reagent with the nominal concentrations of  $x = 0.1, 0.2, 0.3$  for  $(\text{Pb}_x\text{Sn}_{1-x})_2\text{P}_2(\text{Se}_{0.2}\text{S}_{0.8})_6$  and  $(\text{Pb}_{0.05}\text{Sn}_{0.95})_2\text{P}_2(\text{Se}_y\text{S}_{1-y})_6$  with  $y = 0.4, 0.5$ . All crystals were oriented in the (100) crystallographic direction and thin plane-parallel slabs (500 - 600  $\mu\text{m}$ ) were cut whose surfaces are perpendicular to that direction. Note that growing procedures were carried out using high-purity elements Sn (99.99%), Pb (99.99%), P (99.999%), S (99.99%) in atomic percentage.

A high-resolution *ac* photopyroelectric calorimeter has been used to measure the thermal diffusivity  $D$  by means of what is known as the back-detection configuration. The details of the technique and the experimental setup have been already explained in chapter 2. Thermal diffusivity is measured in the direction perpendicular to the sample surface which, in this case, is the direction (100). The phase transitions are signaled as dips on the thermal diffusivity curves and their precise shape has been provided by a controlled continuous temperature variation, slow enough when checking possible thermal hysteresis.

For the case of continuous transitions, the critical behavior is studied by means of the inverse of the thermal diffusivity, which behaves critically as the specific heat

$c_p$  if thermal conductivity  $\kappa$  does not present a singularity at the transition (as it happens in this ferroelectric family [43, 96, 213]), as they follow the equation

$$\frac{1}{D} = \frac{\rho c_p}{\kappa}, \quad (7.1)$$

where  $\rho$  is density.

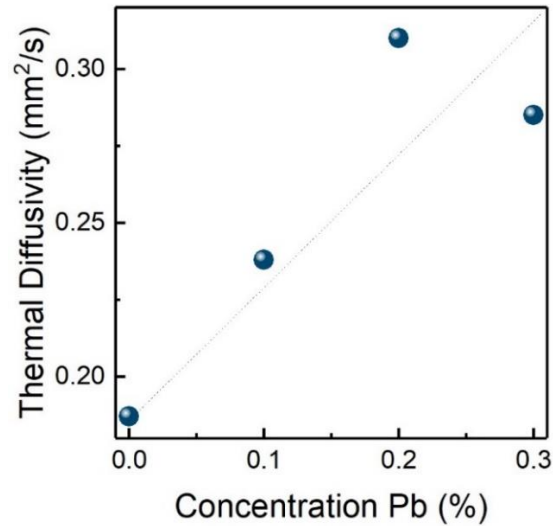
Therefore, the equation used to perform the fittings of the inverse of the thermal diffusivity at the second order phase transition has the same mathematical form as the one presented for specific heat in chapter 3 (Eq. 3.20)

$$\frac{1}{D} = B + Ct + A^\pm |t|^{-\alpha} \left(1 + E^\pm |t|^{0.5}\right) \quad (7.2)$$

where  $t = \frac{T - T_c}{T_c}$  is the reduced temperature,  $T_c$  the critical temperature and superscripts + and – stand for  $T > T_c$  and  $T < T_c$ , respectively; the linear term represents the regular contribution to the inverse of the thermal diffusivity, while the last term represents the anomalous contribution at the second order PT.

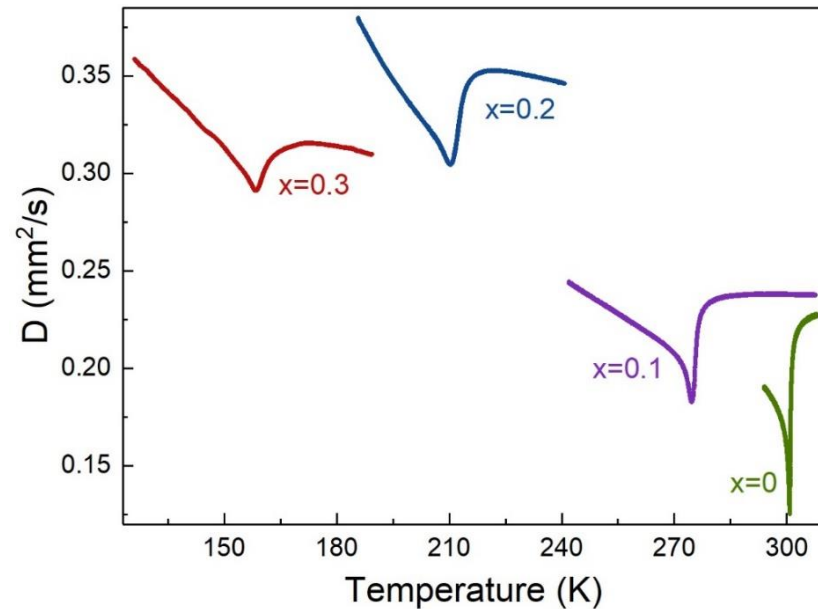
### 7.3. Experimental results and discussion

The measured thermal diffusivity of  $(\text{Pb}_x\text{Sn}_{1-x})_2\text{P}_2(\text{Se}_{0.2}\text{S}_{0.8})_6$  crystals at room temperature (295 K) confirms the fact that these ferroelectrics are poor thermal conductor materials, where heat is mainly transported by phonons. A slight substitution of tin by lead increases the thermal diffusivity from 0.187 to 0.311  $\text{mm}^2/\text{s}$  at 20 % lead, while at  $x = 0.3$  thermal diffusivity is 0.285  $\text{mm}^2/\text{s}$  which could happen due to the fluctuations in the concentration of a particular sample. This rising of D is surely due to the difference between the ionic radii of  $\text{Pb}^{2+}$  and  $\text{Sn}^{2+}$  ions, and as a consequence the bigger size of lead atoms affects the phonon scattering process and therefore the phonon mean free path is reduced (fig. 7.1).



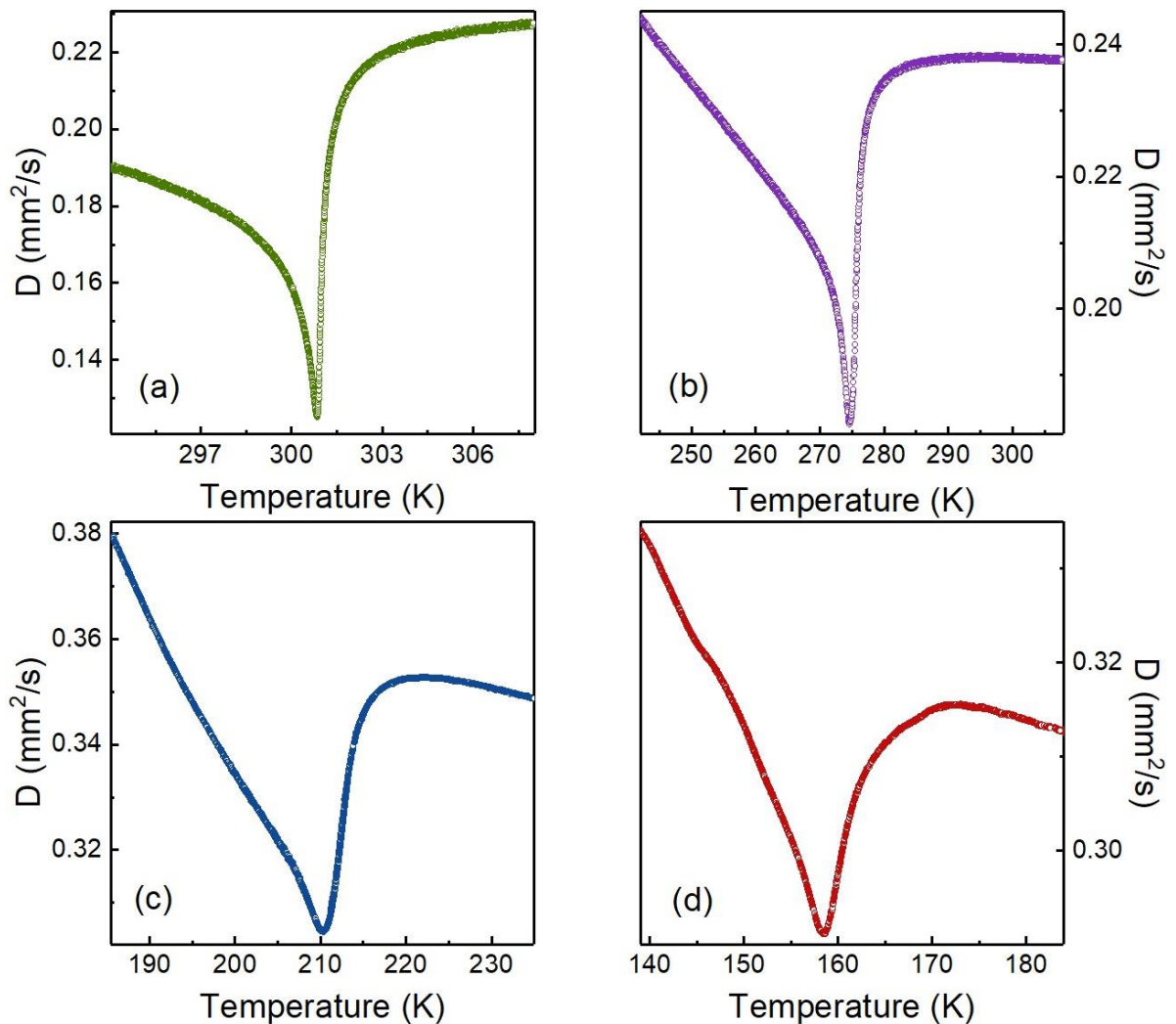
**Fig. 7.1.** Thermal diffusivity of  $(\text{Pb}_x\text{Sn}_{1-x})_2\text{P}_2(\text{Se}_{0.2}\text{S}_{0.8})_6$  mixed ferroelectrics along (100) crystallographic direction as a function of Pb contents at  $T = 295$  K. Data for  $x = 0$  has been taken from ref [43]

Figure 7.2 exhibits the thermal diffusivity values of  $(\text{Pb}_x\text{Sn}_{1-x})_2\text{P}_2(\text{Se}_{0.2}\text{S}_{0.8})_6$  with  $x = 0.1, 0.2, 0.3$  in the region where the PT takes place, having included the corresponding value for  $x = 0$  [43] for the sake of comparison (in all cases the orientation of the samples is the same).



**Fig. 7.2.** Thermal diffusivity as a function of temperature for  $(\text{Pb}_x\text{Sn}_{1-x})_2\text{P}_2(\text{Se}_{0.2}\text{S}_{0.8})_6$  with  $x = 0.1, 0.2, 0.3$  in the region where the ferroelectric phase transition takes place. Data for  $x = 0$  has been taken from ref. [43]

Figure 7.3 shows, in more detail, each PT. On the one hand, the addition of Pb, as expected, shifts the ferroelectric transition to lower temperatures, from  $T_c \approx 301$  K for  $x = 0$  to  $T_c \approx 275$  K for  $x = 0.1$ , to  $T_c \approx 211$  K for  $x = 0.2$  and to  $T_c \approx 157$  K for  $x = 0.3$ , with the thermal diffusivity values severely increasing from  $x = 0.1$  to  $x = 0.2$ . Concerning the character of the transitions, measurements have been performed on heating and on cooling with the result that  $x = 0, 0.1$  are continuous phase transitions while  $x = 0.2, 0.3$  have changed the character to first order, as they present thermal hysteresis. In these cases, there is a difference in the position of the PT ( $\Delta T = 0.8$  K for  $x = 0.2$ ,  $\Delta T = 0.3$  K for  $x = 0.3$ ) as well as in its shape on heating and cooling (well seen in fig.7.4).



**Fig. 7.3.** Phase transitions in detail for  $(\text{Pb}_x\text{Sn}_{1-x})_2\text{P}_2(\text{Se}_{0.2}\text{S}_{0.8})_6$  with  $x = 0.1$  (b), 0.2 (c), 0.3 (d). Data for  $x = 0$  (a) has been taken from ref. [43]

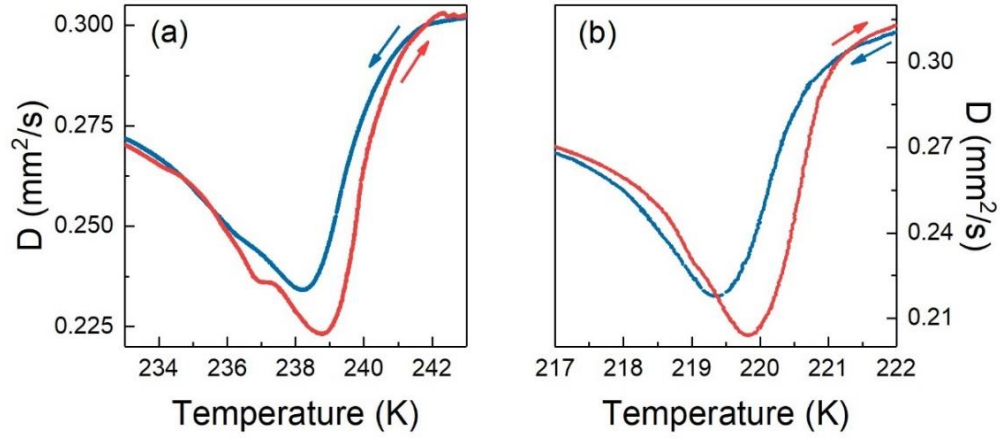


**Fig. 7.4.** Thermal diffusivity measured on heating and cooling at 30 mK/min showing the hysteresis for  $(\text{Pb}_x\text{Sn}_{1-x})_2\text{P}_2(\text{Se}_{0.2}\text{S}_{0.8})_6$  with  $x = 0.2, 0.3$

The results of the fitting for  $\text{Sn}_2\text{P}_2(\text{Se}_{0.2}\text{S}_{0.8})_6$  and  $(\text{Pb}_{0.1}\text{Sn}_{0.9})_2\text{P}_2(\text{Se}_{0.2}\text{S}_{0.8})_6$  accompanied with their corresponding deviation plots (the difference between each experimental and fitted value, divided by the experimental value, in percentage), where the difference in the width of the transition is clearly observed (an order of magnitude in reduced temperature)) are shown on fig. 7.5. The fitted parameters of the critical exponents  $\alpha$ , the ratios of the critical amplitude  $\frac{A^+}{A^-}$  and the critical temperatures  $T_c$  are collected in table 7.1. In the same table we have also included the temperature range  $t$  fitted and the determination coefficient  $R^2$ , which represents the quality of the fits. As seen from the graph both fits are very good, which is also confirmed by the high determination coefficient  $R^2$  ( $R^2 = 1$  the case for ideal fit) and the deviation plots. There is an evolution of the critical exponent  $\alpha$ , from the value of  $+0.147 \pm 0.004$  for  $x = 0$  (which does not correspond to any theorized universality class) to the value of  $+0.085 \pm 0.006$  for  $x = 0.1$ , with a very small deviation in this case. This tendency of  $\alpha$  to approach zero indicates that a mean field model is the closest universality class as Pb concentration is increased. As the transition has turned from second order to first order between  $x = 0.1$  and  $x = 0.2$ , a tricritical point is traversed but the critical exponent neither approaches the corresponding theoretical value  $(\frac{1}{2})$  nor points to any other class such as Lifshitz  $(\frac{1}{4})$  or Tricritical Lifshitz ( $\frac{1}{4}$ )

$\frac{9}{14}$ ). Besides, as it can be seen from fig.7.3, the transition is smeared instead of being sharpened, which is a common characteristic feature of a first order character.

Table. 7.1.

Result of the fitting of the inverse of thermal diffusivity  $1/D$  using equation 7.2. The parameters ( $\alpha$ ,  $A^+/A^-$ ,  $T_c$ ) are shown together with the fitted range and the coefficient of determination  $R^2$ . Data for  $\text{Sn}_2\text{P}_2(\text{Se}_{0.2}\text{S}_{0.8})_6$  has been taken from ref. [43]

Parameters	$\text{Sn}_2\text{P}_2(\text{Se}_{0.2}\text{S}_{0.8})_6$	$(\text{Pb}_{0.1}\text{Sn}_{0.9})_2\text{P}_2(\text{Se}_{0.2}\text{S}_{0.8})_6$
$\alpha$	$0.147 \pm 0.004$	$0.085 \pm 0.006$
$A^+/A^-$	0.66	0.92
$T_c$ , K	300.93	275.68
Fitted range $ t $ , $T_c < T$	$8.3 \times 10^{-3} - 3.1 \times 10^{-4}$	$5.1 \times 10^{-2} - 5 \times 10^{-3}$
Fitted range $ t $ , $T_c > T$	$7.6 \times 10^{-3} - 3 \times 10^{-5}$	$6.3 \times 10^{-2} - 5.8 \times 10^{-4}$
$R^2$	0.996	0.998

The fact that with  $x = 0.2$  the transition is already first order (and it keeps this character at  $x = 0.3$ ) tells us that, indeed, as it was predicted, once the PT falls below the range 210 - 230 K, tricriticality appears [2]. Let's analyse in some detail these theoretical predictions and what has been experimentally found prior to this work. The observed location of the TCPs at the same temperature level (210 – 240 K) for different mechanical or chemical impacts (on compression of  $\text{Sn}_2\text{P}_2\text{S}_6$  and at  $\text{S} \rightarrow \text{Se}$  or  $\text{Sn} \rightarrow \text{Pb}$  substitution [2, 174, 192, 214]) can be explained in the following way: On substitution of sulfur by selenium, the intercell interaction becomes weaker as a result of the stronger covalence of the chemical bonds [180, 215] but the stereoactivity of the  $\text{Sn}^{2+}$  cations and the form of the local potential remain almost unchanged. These factors determine the decrease of the transition temperature until the TCP is reached. For pure  $\text{Sn}_2\text{P}_2\text{S}_6$  crystal under pressure, the  $\text{Sn}^{2+}$  cations stereoactivity decreases, which reduces the depth of the side wells in the local three -

well potential. Due to this factor, at almost unchanged intercell interaction, the second order transition temperature goes down until the “tricritical temperature” and a first order ferroelectric transition line appears in the  $T - p$  diagram.

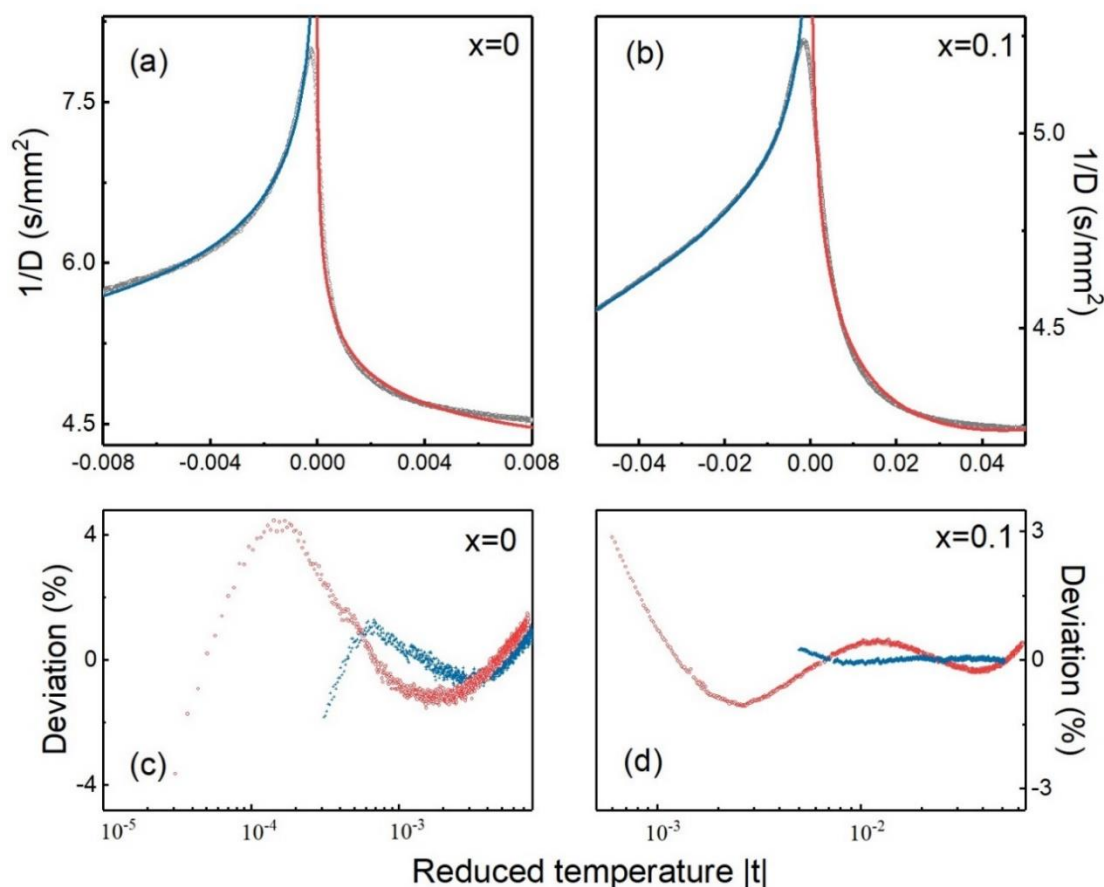


**Fig. 7.5.** Above: Results of the fitting of the inverse of the thermal diffusivity for  $(\text{Pb}_x\text{Sn}_{1-x})_2\text{P}_2(\text{Se}_{0.2}\text{S}_{0.8})_6$  with  $x = 0.1$  where the results for  $x = 0$  [43] have been included, for comparison. The points correspond to experimental measurements, the continuous lines to the fittings to equation 7.2. Below: Deviation curves for the fittings. Circles correspond to the fitting above the critical temperature, crosses to the ones below it

When substituting tin by lead, the sublattice of rather strongly stereoactive  $\text{Sn}^{2+}$  cations is diluted by weakly stereoactive  $\text{Pb}^{2+}$  cations, which also have a bigger ionic radius. A relatively small stereoactivity of the lead cations has been found according to GGA calculations [158], as the difference between S 3p orbitals energy and Sn 5s or Pb 6s orbitals energies increases nearly 1 eV from  $\text{Sn}_2\text{P}_2\text{S}_6$  to  $\text{Pb}_2\text{P}_2\text{S}_6$ . In addition to the dilution effect, the ionicity of the Sn - S chemical bonds increases [180, 215]

and the stereoactivity of the remaining  $\text{Sn}^{2+}$  cations decreases. The combined influence of the intercell interaction strengthening and the decrease of the stereoactivity of the two cation sublattices determines the decrease of the second order ferroelectric transition temperature down to the above mentioned “tricritical temperature”.

For pure  $\text{Sn}_2\text{P}_2\text{S}_6$  lattice compression, the observed  $T - p$  phase diagram can be related to the one predicted by the BEG model [190, 216]. With substitution of sulphur by selenium, the random field defects can appear, but their influence is small: no smearing of very sharp critical anomalies at the phase transitions was observed in the  $\text{Sn}_2\text{P}_2(\text{Se}_y\text{S}_{1-y})_6$  mixed crystals [43]. In the case of the substitution of tin by lead, strong random field defects appear due to hybridization of different electronic orbitals around the  $\text{Sn}^{2+}$  and  $\text{Pb}^{2+}$  cations. Such a complicated situation can be described by comparing the experimentally built  $T - x$  diagram with the diagram predicted by the diluted BEG model [80]. In such model, a segment of the former first order transition line (just below the TCP in the ideal system) becomes a disorder-induced continuous transition line. However, with further shift of the PT point down to lower temperatures, a clear first order transition nature is revealed.

Coming back to the results of this current work, the fact that the critical exponent points to a mean field model, instead to a tricritical universality class, is surely associated with randomness in the system, provoking the disappearance of the TCP, while the real first order nature is revealed when the temperature of the transition is further lowered.

After the experimental results and fittings, this is the case of  $(\text{Pb}_x\text{Sn}_{1-x})_2\text{P}_2(\text{Se}_{0.2}\text{S}_{0.8})_6$  where randomness provokes the rounding of the transition as well as the tendency to a mean field model where it should be leading to an exponent belonging to a Tricritical class. For  $x = 0.2$  and  $0.3$ , as the transition is lowered, the first order character is manifested.

Concerning the samples  $(\text{Pb}_{0.05}\text{Sn}_{0.95})_2\text{P}_2(\text{Se}_y\text{S}_{1-y})_6$  with Se concentration higher than the one corresponding to the Lifshitz point, figure 7.6 shows the thermal

diffusivity curves for  $y = 0.4, 0.5$ . The measurements have been performed in cooling/heating modes with different temperature rates ( $50 - 10$  mK/min) in order to check the character of the PT. Thermal diffusivity curves on heating and cooling for these crystals are depicted in fig. 7.7.

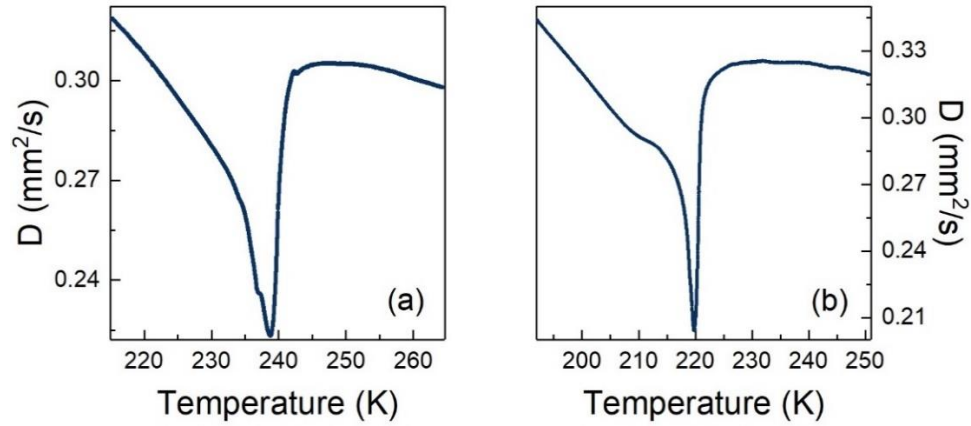


**Fig. 7.6.** Thermal diffusivity as a function of temperature for  $(\text{Pb}_{0.05}\text{Sn}_{0.95})_2\text{P}_2(\text{Se}_y\text{S}_{1-y})_6$  with  $y = 0.4$  (a) and  $0.5$  (b)

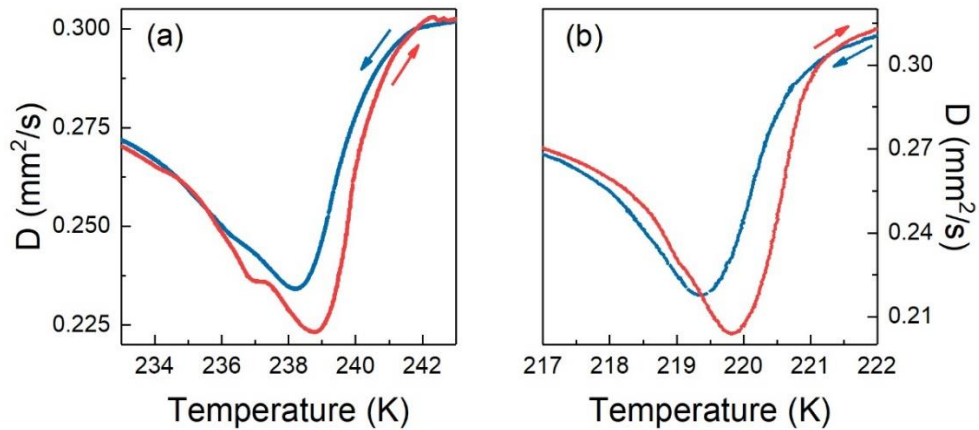


**Fig. 7.7.** Thermal diffusivity as a function of temperature for  $(\text{Pb}_{0.05}\text{Sn}_{0.95})_2\text{P}_2(\text{Se}_y\text{S}_{1-y})_6$  with  $y = 0.4$  (a) and  $0.5$  (b), measured on heating and cooling, showing the hysteretic behaviour

According to the phase diagram, in the samples without Pb there must be two transitions (the continuous one from the paraelectric phase to an incommensurate (IC) phase and the lower one to a ferroelectric phase, with a first order character). From the critical behaviour studies of  $\text{Sn}_2\text{P}_2(\text{S}_{1-x}\text{Se}_x)_6$  ferroelectric compounds [43] it was seen that, in thermal diffusivity, the two transitions were not clearly separated but for

very high Se concentrations. In particular,  $\text{Sn}_2\text{P}_2(\text{Se}_{0.4}\text{S}_{0.6})_6$  showed a sharp and thin dip where the two transitions were superimposed and with a first order character. The dip which appears now with Pb doping is placed at a lower temperature (about 20 K), it is much wider, rounder, with a clear structure and with hysteresis. The structure which appears in the dip, with a kink at about 237 K, could be due to the onset of the clear separation of the three phases induced by the presence of Pb.

In the case of  $y = 0.5$  (see Fig. 7.6) the dip goes to even lower temperature (another 20 K) and the two transitions are still superimposed but more separated, with a shoulder on the left and a dip on the right, with a hysteretic behaviour due to the fact that the two transitions are not well resolved yet (see Fig. 7.7). This means that the effect of lead is to reduce the critical temperature and better separate the two transitions, introducing a certain rounding. Hence, in all cases, ferroelectricity is hindered by the presence of Pb. The physical mechanism responsible for this behaviour is that Pb weakens the stereoactivity of the samples by obstructing the hybridization of the  $s$ - $p$  electron orbitals ( $s$  for Pb or Sn,  $p$  for S or Se) which activates the  $\text{Sn}^{2+} 5s^2$  lone pair formation. As explained in the introduction, there is a bigger difference between Pb 6s and S(Se)  $p$  states, as opposed to the difference between Sn 5s and S(Se)  $p$  states. Besides, the addition of Pb introduces randomness in the system which is the origin of the roundness in the transition as it happened in the case of  $(\text{Pb}_x\text{Sn}_{1-x})_2\text{P}_2(\text{Se}_{0.2}\text{S}_{0.8})_6$ . It would have been desirable to study the evolution of the PT in  $\text{Sn}_2\text{P}_2(\text{Se}_{0.4}\text{S}_{0.6})_6$  and  $\text{Sn}_2\text{P}_2(\text{Se}_{0.5}\text{S}_{0.5})_6$  with higher Pb contents but it has not been possible to grow single crystals of enough quality with these concentrations.

These results complement what was previously found and published concerning the effect that doping with Ge and Pb has on the Lifshitz point, which exists for  $\text{Sn}_2\text{P}_2(\text{Se}_{0.28}\text{S}_{0.72})_6$  [191]. Both ions affect the stereoactivity of the sample as the transition temperature is respectively increased or decreased, but only Pb provokes a significant change in the properties of the ferroelectric PT. In that work, it was found that the addition of 5% Pb changed the Lifshitz Point to a Tricritical Lifshitz Point, with further addition changing the character from second order to first order. In this study we have observed that the addition of Pb to  $\text{Sn}_2\text{P}_2(\text{Se}_y\text{S}_{1-y})_6$  for Se

concentrations lower to the one corresponding to the Lifshitz point also has the effect of turning the character of the transition from second to first order but without the formal apparition of a tricritical point. On the other hand, for Se concentrations higher than the Lifshitz point, the effect of Pb doping is to enhance the apparition of the intermediate, IC phase between the paraelectric and the ferroelectric phases.

#### 7.4. Conclusions

The effect of Pb doping in  $(\text{Pb}_x\text{Sn}_{1-x})_2\text{P}_2(\text{Se}_y\text{S}_{1-y})_6$  with Se concentrations slightly below and above the Lifshitz concentration has been studied. The theoretical prediction says that a tricritical point upon pressure application (chemical doping can have an equivalent effect to mechanical pressure) appears below 210 - 240 K. As a general rule, increasing lead concentration in the cation sublattice tends to frustrate the ferroelectric transition, lowering the critical temperature because it weakens the electron orbitals hybridization which is at the core of the stereoactivity of these systems. In the particular case of  $y = 0.2$ , the transition changes its character from second order to first order between  $x = 0.1$  and  $x = 0.2$ , fulfilling the predictions of the diluted Blume-Emery-Griffith model with randomness. This randomness prevents the apparition of a Tricritical Point and, instead, a mean field model is of application. In the case of  $y = 0.4, 0.5$ , Pb also promotes the separation of the paraelectric-incommensurate and the incommensurate-ferroelectric transitions in spite of the introduction of rounding.

## Chapter 8. Phase diagram of $(\text{Pb},\text{Sn})_2\text{P}_2(\text{Se},\text{S})_6$ ferroelectrics with multicritical points at coupling between polar and antipolar fluctuations

### 8.1. Introduction

Static and dynamic critical behavior of  $\text{Sn}_2\text{P}_2\text{S}_6$  type ferroelectrics and  $(\text{Pb}_x\text{Sn}_{1-x})_2\text{P}_2(\text{Se}_y\text{S}_{1-y})_6$  mixed crystals with line of tricritical points and line of Lifshitz points on the  $T - x - y$  phase diagram, which meet at the tricritical Lifshitz point, can be described in a combined BEG – ANNNI model. Such model considers first and second neighbor interactions for pseudospins in a local three-well potential. Below the temperature of tricritical Lifshitz point, the “chaotic” state accompanied by the coexistence of ferroelectric, metastable paraelectric and modulated phases is expected. In addition to the frustration of polar fluctuations near the Brillouin zone center, in  $\text{Sn}_2\text{P}_2\text{S}_6$  crystal the antipolar fluctuations also strongly develop in the paraelectric phase at cooling to continuous phase transition temperature  $T_0$ . Here, critical behavior can be described as a crossover between Ising and XY universality classes, what is expected near bicritical points with coupled polar and antipolar order parameters and competing instabilities in  $q -$  space.

### 8.2. Phase diagram with tricritical Lifshitz point

In order to build the  $t - \Delta - \lambda$  phase diagram for ferroelectrics in the system  $\text{Sn}(\text{Pb})_2\text{P}_2\text{S}(\text{Se})_6$ , we have used the Blume - Capel spin-1 Ising model (which is a simpler version of BEG model) with competing interactions [212, 217]. Such combined BC – ANNNI model displays a multicritical behavior such as tricriticality as well as the possibility of the presence of a LP. The tricritical Lifshitz point (TCLP) is predicted at the meeting points of TCPs and LPs lines [83, 218, 219]. In the used model [212] (as for original ANNNI model [220]) the relation between two

interactions is written in the form  $\lambda = -J_2/J_1$ , where  $J_1$  is the effective first neighbors' positive interaction and  $J_2$  is the negative coupling of next nearest neighbors. The paraelectric - ferroelectric second order transitions line can be found as [212]

$$\lambda = 1 - \frac{t}{1+0.5e^{\frac{\Delta}{t}}} \quad (8.1)$$

and from the paraelectric phase into a modulated one continuous transitions line

$$\lambda = \frac{t}{1+0.5e^{\frac{\Delta}{t}}} . \quad (8.2)$$

Here  $t = T/J_1$ , and  $\Delta = \delta/J_1$ . The parameter  $\delta$  is related to the single-ion terms [158, 190].

At  $\lambda = 0.25$  the paraelectric borders obtained from eq. (1) and eq. (2) meet at a LP. Considering the above-mentioned conditions, the line of LPs can be found by means of the following equation

$$\Delta = t_{LP} \ln\left(\frac{1-2t_{LP}}{t_{LP}}\right). \quad (8.3)$$

After reaching a value  $\Delta \simeq 0.231\dots$  the paraelectric borders begin to split and there is no LP anymore. Near this  $\Delta$  value the LPs line coincides with the TCPs line [220]. The calculated  $t - \Delta - \lambda$  phase diagram is depicted in Fig. 8.1.

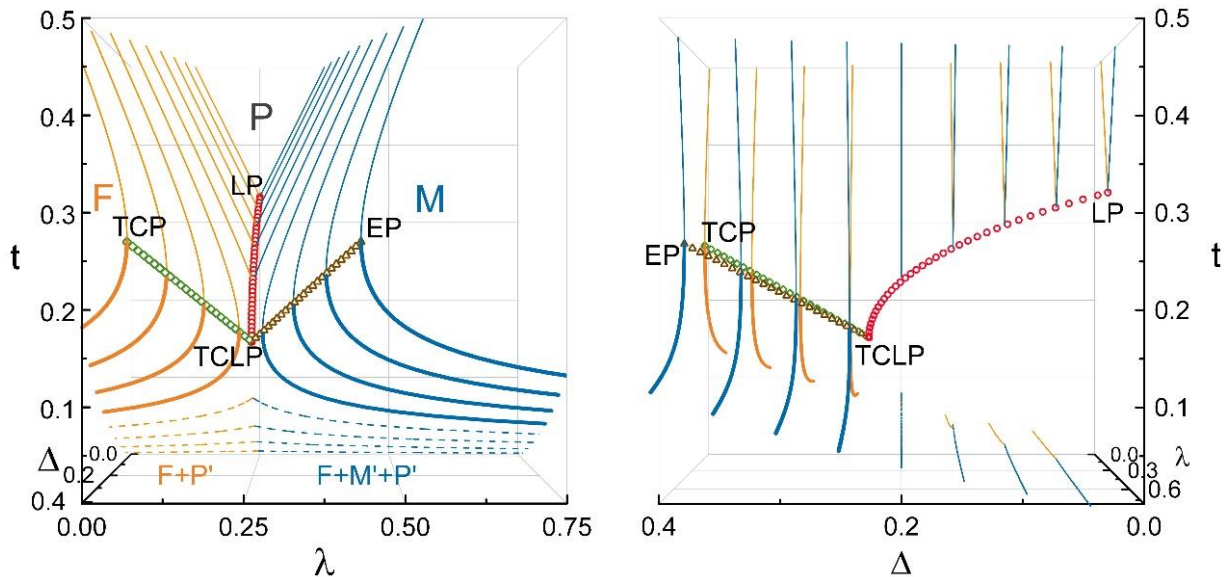


**Fig. 8.1.** Front (left) and side (right) view on calculated  $t - \Delta - \lambda$  diagram. Solid lines show paraelectric - ferroelectric (orange) and paraelectric - modulated (blue) borders, Lifshitz points line (red circles), tricritical points line (green

squares), end points (EP) line (brown triangles). Thin lines indicate the second order phase transitions while thick lines the first order ones. Letters F, P and M correspond to ferroelectric, paraelectric and modulated phases. The coexistence of ferroelectric and metastable paraelectric (F+P') and ferroelectric, metastable paraelectric and commensurate modulated phases (F+M+P') below the dashed lines are also shown

Let's compare the just obtained theoretical phase diagram with the experimentally determined temperature-concentration phase diagram for  $(\text{Pb}_x\text{Sn}_{1-x})_2\text{P}_2(\text{Se}_y\text{S}_{1-y})_6$  ferroelectric mixed crystals [56]. In order to do it we need to translate it into  $t - \Delta - \lambda$  coordinates. The experimentally observed TCLP for  $(\text{Pb}_{0.05}\text{Sn}_{0.95})_2\text{P}_2(\text{Se}_{0.28}\text{S}_{0.72})_6$  at  $T_{TCLP} \approx 259$  K [191], in  $t - \Delta - \lambda$  coordinates will correspond to the next position:  $t = 0.15825$ ,  $\Delta = 0.23105$ ,  $\lambda = 0.5$ . The LP with the composition  $\text{Sn}_2\text{P}_2(\text{Se}_{0.28}\text{S}_{0.72})_6$  at temperature  $T_{LP} \approx 284$  K [180] will lie on the line of LPs obtained from eq. 8.3 at  $t = 0.17345$ ,  $\Delta = 0.22997$ ,  $\lambda = 0.5$ . For mixed  $\text{Sn}_2\text{P}_2(\text{Se}_y\text{S}_{1-y})_6$  crystals in the framework of the ANNNI model, a linear variation of the  $\lambda$  parameter with composition  $x$  was assumed with the values 0.23, 0.25 and 0.30 for  $\text{Sn}_2\text{P}_2\text{S}_6$ ,  $\text{Sn}_2\text{P}_2(\text{Se}_{0.28}\text{S}_{0.72})_6$  and  $\text{Sn}_2\text{P}_2\text{Se}_6$ , respectively [56]. At the constant value  $\Delta = 0.22997$ , the coordinates for these concentrations on the  $t - \Delta - \lambda$  diagram are the following:  $t_0 = 0.20582$ ,  $\lambda = 0.23$  for  $\text{Sn}_2\text{P}_2\text{S}_6$  with  $T_0 = 337$  K;  $t_c = 0.13436$ ,  $\lambda_c = 0.30$ , and  $t_i = 0.11799$ ,  $\lambda_i = 0.30$  for  $\text{Sn}_2\text{P}_2\text{Se}_6$  with  $T_c = 220$  K,  $T_i = 193$  K [101].

At tin by lead substitution the shape of local three-well potential changes, and the coordinates of the TCP in the  $(\text{Pb}_{1-x}\text{Sn}_x)_2\text{P}_2\text{S}_6$  mixed crystals in mean-field approximation of BEG model [221] can be determined at condition of linear variation of  $\Delta$  in dependence of  $y$ , at unchanged intercell interactions. According to the earlier performed analysis for  $(\text{Pb}_{1-x}\text{Sn}_x)_2\text{P}_2\text{S}_6$  mixed crystals [158], the calculated  $t - \Delta$  diagram (at  $\lambda = 0.23$ ) is shown on Fig. 8.2. It was found that the TCP has coordinates  $t = 0.13436$ ,  $\Delta = 0.23577$ ,  $\lambda = 0.23$ .

As the inter-site interaction  $J_I$  is an almost unchanged quantity [158], we assume that, on increasing the lead concentration in  $(\text{Pb}_x\text{Sn}_{1-x})_2\text{P}_2\text{Se}_6$  mixed crystals

(with  $\lambda = 0.3$ ), the value of  $\Delta$  will change in the same way as in  $(\text{Pb}_x\text{Sn}_{1-x})_2\text{P}_2\text{S}_6$  solid solutions. Accordingly, the experimental phase diagram in  $t - \Delta - \lambda$  coordinates is presented in Fig. 8.3.

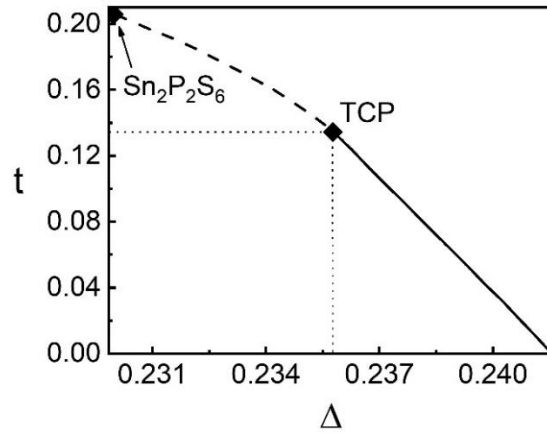


**Fig. 8.2.** Dependence of phase transition temperature on the single – ion term in dimensionless  $t - \Delta$  coordinates calculated in the mean-field approximation on the BEG model [158, 221]. Dashed and solid lines indicate second and first order transitions, respectively, that meet at the tricritical point

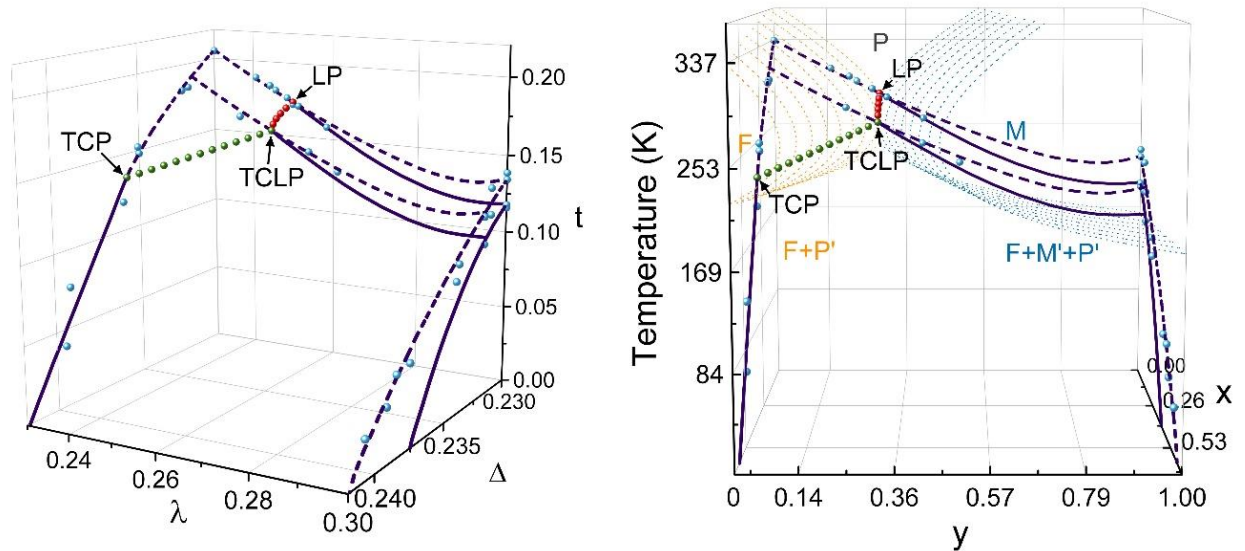


**Fig. 8.3.** Experimental phase diagram for  $(\text{Pb}_x\text{Sn}_{1-x})_2\text{P}_2(\text{Se}_y\text{S}_{1-y})_6$  ferroelectrics in  $t - \Delta - \lambda$  coordinates (left) and front view of both experimental and calculated phase diagrams in temperature - concentration  $T - x - y$  coordinates (right). Dashed and solid lines denote second order and first order phase transitions, respectively. Green and red spheres correspond to tricritical points line and Lifshitz points line, blue spheres to the calorimetric data [43, 96, 97, 98, 191, 198, 222]

From the calculated  $t - \Delta - \lambda$  diagram, it follows that the LPs line terminates at TCLP, and this multicritical point can be considered as a “Lifshitz end point”. The Lifshitz points line in TCLP splits into the tricritical points line and the end points (EP) line. At big  $\Delta$  parameter, the paraelectric - modulated critical line ends at the end point.

For high lead concentrations ( $x > 0.2$ ), at low temperatures a “chaotic” state can be observed [212]. This state presents a mixture of paraelectric, ferroelectric and modulated phases. Such peculiarity can be seen on the excess heat capacity  $\Delta C_p$  and anomalous temperature dependencies of dielectric susceptibility  $\varepsilon'$  in  $(\text{Pb}_x\text{Sn}_{1-x})_2\text{P}_2\text{Se}_6$  crystals, according to recent investigations [175, 223, 224, 225]. For small lead concentrations, there are clear anomalies of  $\Delta C_p(T)$  and  $\varepsilon'(T)$  at paraelectric – incommensurate ( $T_i$ ) and incommensurate – ferroelectric ( $T_c$ ) phase transitions (Fig. 8.4 and 8.5). However, for  $y \geq 0.2$  the  $\Delta C_p(T)$  and  $\varepsilon'(T)$  anomalies in the vicinity of the lock-in transition ( $T_c$ ) are strongly smeared. Such chaotization can be related to a synergy of frustration effects and nonlinearity of the system with the three-well local potential.

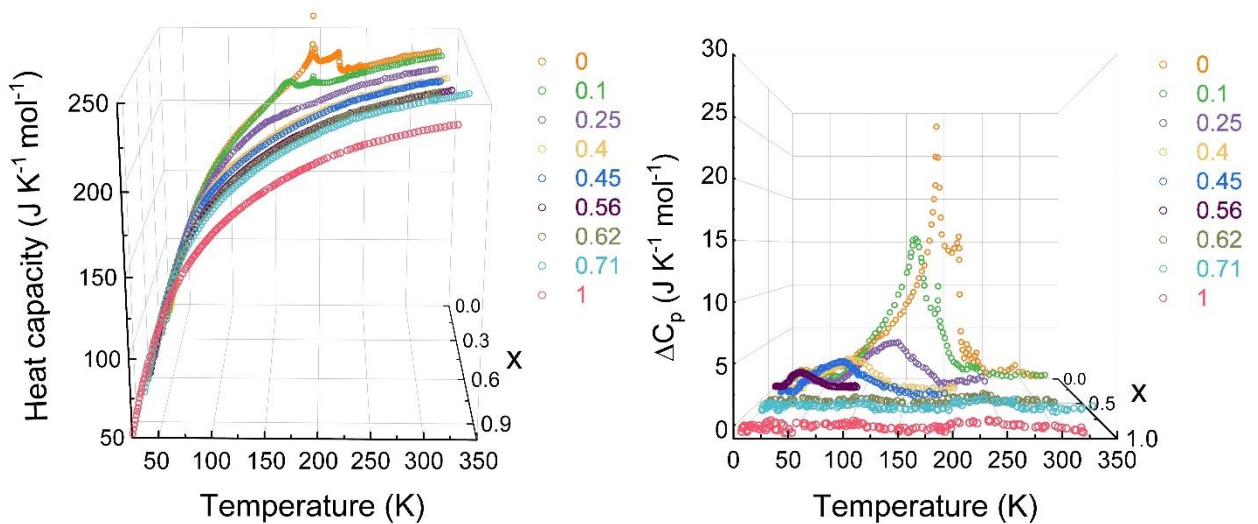


**Fig. 8.4.** Temperature dependence of heat capacity according to experimental data [175] (left) and related to the phase transition excess heat capacity (right) for  $(\text{Pb}_x\text{Sn}_{1-x})_2\text{P}_2\text{Se}_6$  crystals

Therefore, the ANNNI model with two structural sublattices reflects the main properties of ferroelectrics that are related to the LP and IC phase on their phase diagram. For the description of a presence of a TCP on the phase diagram of  $\text{Sn}_2\text{P}_2\text{S}_6$  family ferroelectrics, two structural sublattices were also considered in the frame of BEG model [190]. This three – state model is based on two order parameters – dipolar and quadrupolar ( $B_u$  and  $A_g$  symmetry variables in the case of  $\text{Sn}_2\text{P}_2\text{S}_6$ ) [1, 189]. Therefore, in addition to dipole–dipole inter-site coupling, the quadrupole – quadrupole interaction can also be important. In the case of two sublattices, taking into account the quadrupole – quadrupole interactions can complicate the topology of the temperature - pressure (composition) phase diagram. On such diagram, beside a TCP, another multicritical points might appear, such as a triple point, a critical end point, a bicritical point, and a tetracritical point.

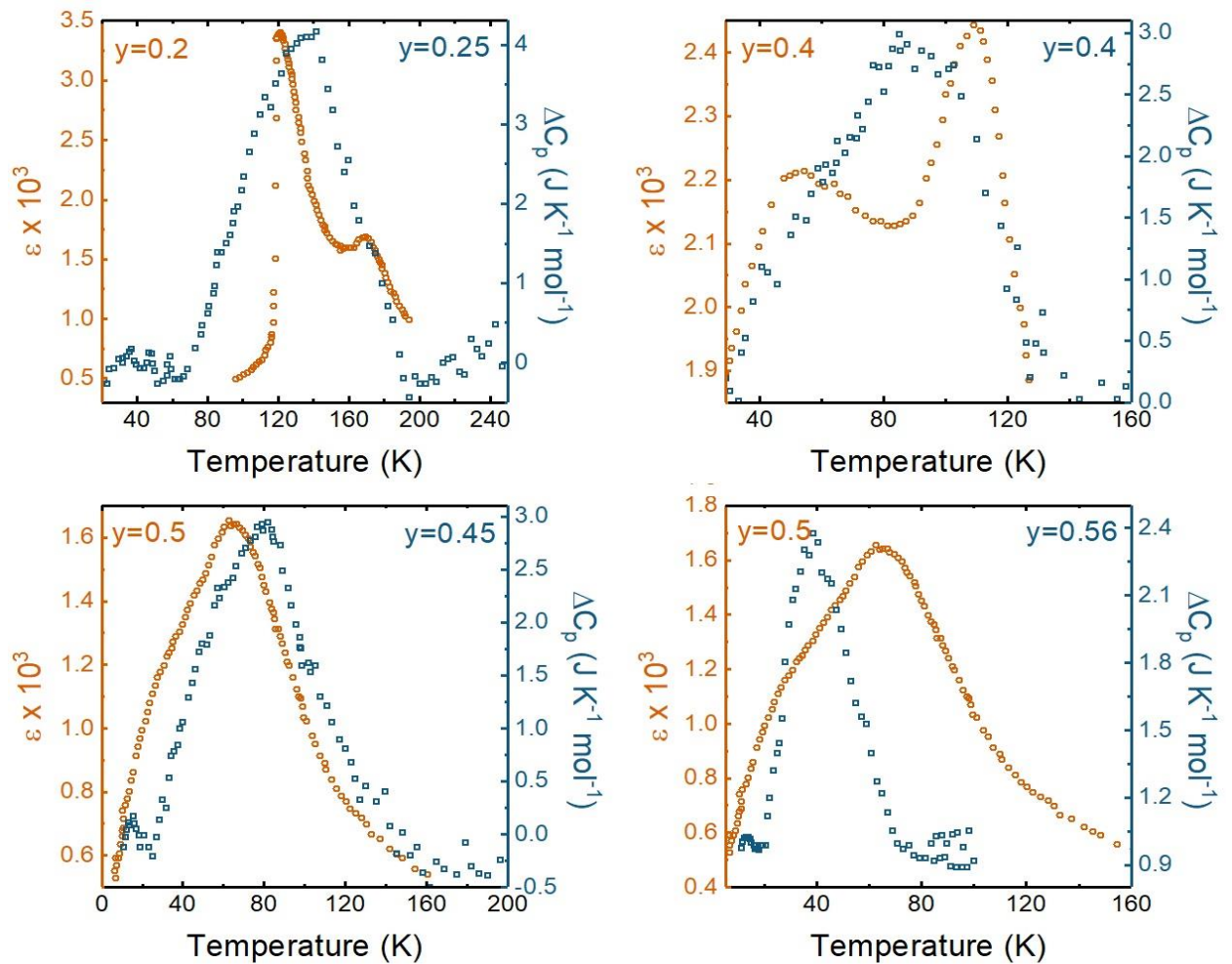


**Fig. 8.5.** Comparison of the anomalies for low frequency dielectric susceptibility (according to data [223, 224, 225]) and excess heat capacity

(according to data [175]) in the region of the phase transitions for  $(\text{Pb}_x\text{Sn}_{1-x})_2\text{P}_2\text{Se}_6$  crystals

### 8.3. Polar and antipolar fluctuations coupling

The above mentioned examples of possible complications of experimentally observed phase diagrams for objects with complex local potential for spontaneous polarization fluctuations demonstrate the proximity of the phase transitions to higher order multicritical points, like a tetracritical point, and give evidence of the importance of higher order invariants in the thermodynamic potential of the investigated ferroelectric crystals. Such possibility was earlier demonstrated [226, 227] when the incommensurate phase properties near lock – in transition into the ferroelectric phase in  $\text{Sn}_2\text{P}_2\text{Se}_6$  crystals were theoretically explained.

For  $\text{Sn}_2\text{P}_2\text{S}_6$  ferroelectrics, the experimental data of neutron scattering, dielectric susceptibility and hysteresis loops investigations present rich information about the complex character of the phase transitions. The neutron scattering data [185] show the presence of a flat lowest-energy transverse optical branch along  $q_y$  direction at 440 K in the paraelectric phase (Fig. 8.6 a). This phonon branch is polarized near [100] direction and softens at cooling. The polar soft optical mode, according to the submillimeter spectroscopy data near  $10^{12}$  Hz [228], contributes only  $\Delta\varepsilon' \simeq 10^3$  to the dielectric susceptibility maximum near  $T_0 \simeq 337$  K (Fig. 8.6 b). At frequency lowering till  $10^7$  Hz, the dielectric susceptibility near  $T_0$  rises to  $10^4 - 10^5$  (Fig. 8.6 c) [229], and at lower frequency obeys the Curie – Weiss law  $\varepsilon' = C(T - T_0)^{-1}$  with  $C \simeq 0.6 \cdot 10^5$  K.

On cooling in the paraelectric phase of  $\text{Sn}_2\text{P}_2\text{S}_6$  crystal, not only long wave polarization fluctuations are developed near the Brillouin zone center, which are proportional to the reciprocal of the polar soft optical mode (with  $B_u$  symmetry at  $q \leftrightarrow 0$ ) frequency square. Near the Brillouin zone edge, at  $q_y = \pi/b$ , also critical growth occurs for fluctuations of atomic motions that are related to the eigenvector of short length phonons from the soft optical branch  $B(q_y)$ . The development of the

aforementioned fluctuations was observed directly (Fig. 8.6 d) [230] by inelastic X – ray scattering at  $T_0 + 2$  K.

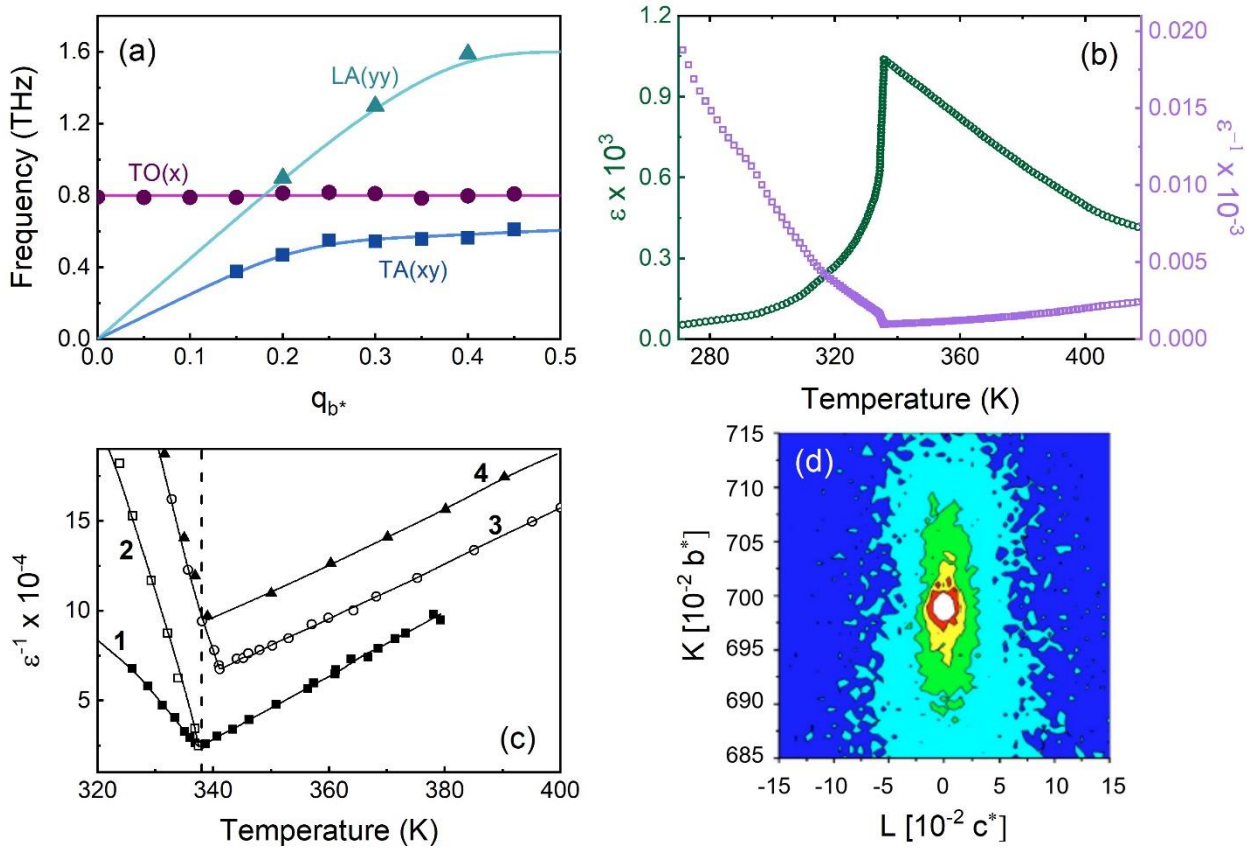


**Fig. 8.6.** Determined by neutron scattering at 440 K transverse soft optical TO(X), acoustic longitudinal LA(XX) and transverse TA(XY) phonon branches along  $q_y$  direction of  $\text{Sn}_2\text{P}_2\text{S}_6$  crystal monoclinic Brillouin zone [185] (a); temperature dependence of the dielectric susceptibility and his reciprocal from submillimeter soft optical mode contribution near the phase transition in  $\text{Sn}_2\text{P}_2\text{S}_6$  crystal [228] (b); comparison of the inverse of the dielectric susceptibility temperature dependence in  $\text{Sn}_2\text{P}_2\text{S}_6$  for 20 MHz (1), 4 GHz (2), 27 GHz (3) and submillimeter soft optical mode contribution (4) [229] (c); diffuse X – ray scattering at  $T_0 + 2$  K in the paraelectric phase of  $\text{Sn}_2\text{P}_2\text{S}_6$  crystal in the plane (0 K L) of Brillouin zone [230] (d)

The high value of the low frequency dielectric susceptibility on cooling to  $T_0$  is obviously related to crystal lattice anharmonicities. It was earlier supposed [1, 189] that the local three – well potential follows from a nonlinear interaction of polar  $B_u$  modes with fully symmetrical  $A_g$  modes (like  $A_g B_u^2 + A_g^2 B_u^2$ ) at the Brillouin

zone center. But on the matter of the soft optical mode flatness in  $q_y$  direction [232], the nonlinear phonon – phonon interaction can be obviously realized with the involvement of phonons from different points of the Brillouin zone. In the simplest approach, such possibility can be incorporated in QAO model [158, 231, 232, 233] that is based on a three – well on – site potential involving first and second neighbors inter-site interactions. Here we consider nonlocal interactions in  $q_y$  direction (instead of above considered frustration of  $J_1$  and  $J_2$  inter-site interactions that are related to the incommensurate phase appearance with modulation wave vector  $q_z$ ). The phase diagram calculated with such model contains a tetracritical point at which two second order transitions lines (from paraelectric into ferroelectric phase and between paraelectric and antipolar phases) intersect. It was found [231] that for  $\text{Sn}_2\text{P}_2\text{S}_6$  crystals below  $T_0$  coexistence of antipolar and ferroelectric phases can be presented.

The assumption that in  $\text{Sn}_2\text{P}_2\text{S}_6$  crystals the phase transition at  $T_0 \approx 337$  K is placed near the tetracritical point agrees with the previous discussion based on the BEG model, for which the phase diagram with a TCP can be complicated by the presence of bicritical or tetracritical points [236]. Thus, the critical behavior of  $\text{Sn}_2\text{P}_2\text{S}_6$  crystals near  $T_0 \approx 337$  requires special attention.

According to previous investigations on thermal diffusivity [96], which is proportional to the reciprocal of heat capacity, the critical behavior of  $\text{Sn}_2\text{P}_2\text{S}_6$  can be fitted with a good quality in the paraelectric phase to a model which considers the influence of both fluctuations and defects (combination of eqs. 3.8 and 3.11). On the other hand, below  $T_0$  the best fittings were found using a mean field Landau model (eq. 3.6). Such asymmetry is very strange, especially when it has been possible to describe the critical behavior of mixed crystals based on  $\text{Sn}_2\text{P}_2\text{S}_6$  using a single model for both phases. For  $\text{Sn}_2\text{P}_2(\text{Se}_y\text{S}_{1-y})_6$  solutions with increasing selenium concentration and approaching the LP ( $y \approx 0.28$ ), the critical anomalies are nicely described by exponents and ratios of critical amplitudes that belong to the Lifshitz universality class [43]. At tin by lead substitution in  $(\text{Pb}_{1-x}\text{Sn}_x)_2\text{P}_2\text{S}_6$  mixed crystals, the critical behavior is also satisfactorily described above and below  $T_0$  as a crossover from a clear non-mean field model at  $x = 0.1$  to a mean field one at  $x = 0.3$

[98]. For  $\text{Sn}_2\text{P}_2\text{Se}_6$  crystals, at the paraelectric to incommensurate second order phase transition the critical anomaly above and below  $T_i$  agrees with the predictions of the renormalization group theory for 3D – XY universality class [175]. At simultaneous substitution of chemical elements in cation and anion sublattices in  $(\text{Pb}_{1-x}\text{Sn}_x)_2\text{P}_2(\text{Se}_y\text{S}_{1-y})_6$  mixed crystals a TCLP has been found for  $x = 0.05$  and  $y = 0.28$  at  $T_c = 259.12$  K [191]. Here the tricritical Lifshitz universality class has been assigned by the obtained critical exponent  $\alpha = 0.64$  which is equal to the theoretical predicted one [69].

Why a critical behavior of  $\text{Sn}_2\text{P}_2\text{S}_6$  crystals can't be described satisfactorily in both temperature sides of  $T_0$ ? As was mentioned above, for pure  $\text{Sn}_2\text{P}_2\text{S}_6$  crystals below  $T_0$  the coexistence of antipolar (antiferroelectric like) and ferroelectric states is possible. This is manifested by the observation of double hysteresis loops and usual ferroelectric loops [231]. Considering the possibility of the coexistence of antipolar and ferroelectric phases below  $T_0$ , we reexamine previous experimental data [96] to check the contributions into a critical anomaly from two coexisting phases. We have used for the fittings equation 7.2. Fig. 8.7 (b) demonstrates the fittings together with the deviation plots (c) (difference between each experimental and fitted value, divided by the experimental value, in percentage). Fig. 8.7 (a) shows the comparison of the shapes of the anomalies in  $\text{Sn}_2\text{P}_2\text{S}_6$ ,  $(\text{Pb}_{0.2}\text{Sn}_{0.8})_2\text{P}_2\text{S}_6$  and  $\text{Sn}_2\text{P}_2(\text{Se}_{0.2}\text{S}_{0.8})_6$ .

The results of the fittings (Fig. 8.7 (b, c)) in  $\text{Sn}_2\text{P}_2\text{S}_6$  have shown a XY like behavior with the critical exponent  $\alpha = -0.0092 \pm 0.0008$  below  $T_0$  and Ising like one with  $\alpha = 0.1049 \pm 0.0066$  above  $T_0$ . Such value of the critical exponents, smaller than  $\alpha_{\text{ISING}}$  in the paraelectric phase and a little bigger than  $\alpha_{\text{XY}}$  below  $T_0$ , can be interpreted as a possible crossover in the critical behavior which earlier was predicted [234] for systems with two competing order parameters near a bicritical point on the phase diagram. The bicritical point can be originated instead of a tetracritical point if there is a strong enough coupling of two order parameters [235].

to the fitting below the critical temperature, red to the ones above it.

In any case, good fittings of thermal diffusivity in  $\text{Sn}_2\text{P}_2\text{S}_6$  crystal below  $T_0$  with negative value of critical index demonstrate its “cups” shape that is a characteristic of the antiferroelectric – like ordering and coincides with observed double hysteresis loops in  $\text{Sn}_2\text{P}_2\text{S}_6$  crystal below  $T_0$  [231].

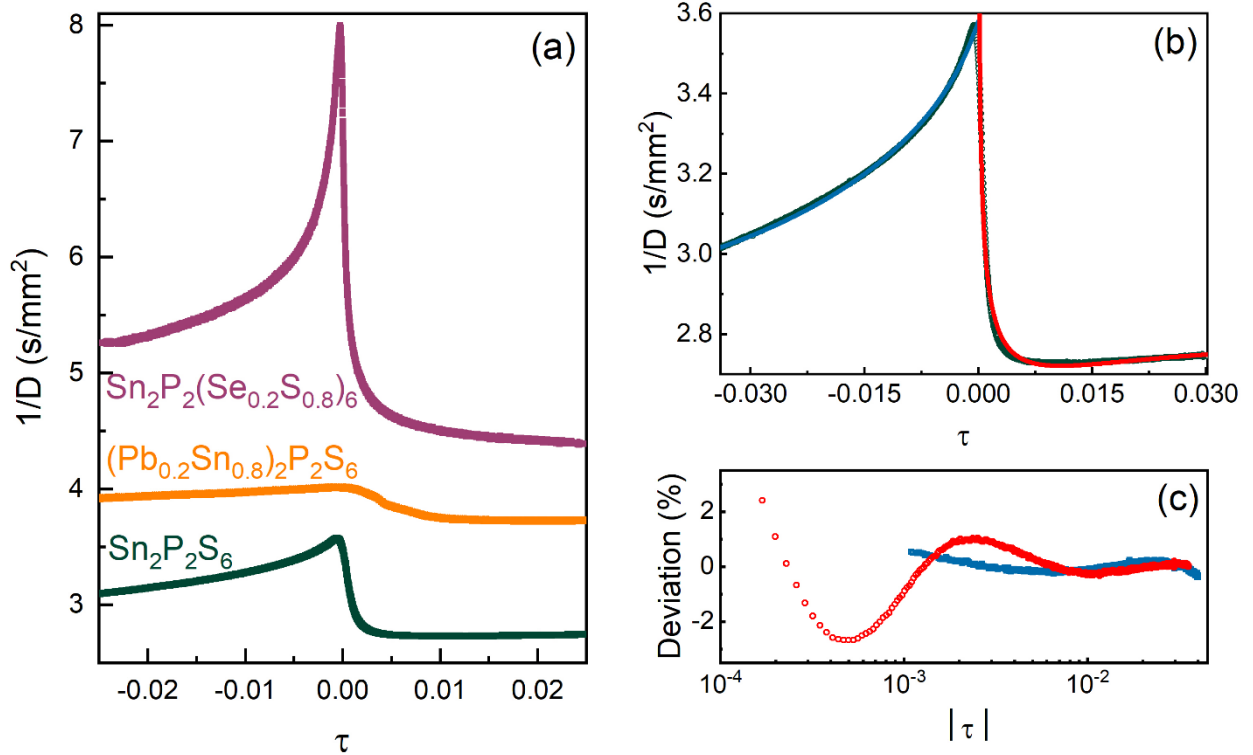


**Fig. 8.7.** Dependence of the inverse of thermal diffusivity measured in the [100] crystallographic direction in the vicinity of continuous phase transition in  $\text{Sn}_2\text{P}_2\text{S}_6$ ,  $(\text{Pb}_{0.2}\text{Sn}_{0.8})_2\text{P}_2\text{S}_6$  and  $\text{Sn}_2\text{P}_2(\text{Se}_{0.2}\text{S}_{0.8})_6$  crystals [43, 96, 98] (a); results of the fittings of the inverse of thermal diffusivity (b), deviation curves for the fittings (c). The points correspond to experimental measurements, the continuous lines to the fittings to Eq. (4). Blue color corresponds to the fitting below the critical temperature, red to the ones above it.  $\tau$  is reduced temperature

#### 8.4. Conclusions

Static and dynamic critical behavior of  $\text{Sn}_2\text{P}_2\text{S}_6$  type ferroelectrics and  $(\text{Pb}_x\text{Sn}_{1-x})_2\text{P}_2(\text{Se}_y\text{S}_{1-y})_6$  mixed crystals are governed by multicritical point presence on their phase diagram. At hydrostatic compression of  $\text{Sn}_2\text{P}_2\text{S}_6$  crystal or at tin by lead substitution in  $(\text{Pb}_x\text{Sn}_{1-x})_2\text{P}_2\text{S}_6$  mixed crystals the TCP can be reached, what is

described by the BEG model for a system with three-well local potential for pseudospin fluctuations. At sulfur by selenium replacement in  $\text{Sn}_2\text{P}_2(\text{Se}_y\text{S}_{1-y})_6$  solid solutions the LP is induced, what is explained by first and second neighbors short range interaction ratio changing in pseudospin ANNNI model. At simultaneous variation of chemical composition in cationic and anionic sublattices the lines of TCPs and LPs on  $T - x - y$  phase diagram meet at the TCLP, and this higher order multicritical point can be described in a combined BEG – ANNNI model [212]. Below the temperature of TCLP, which can be considered as the Lifshitz line end point, the “chaotic” state with coexisting ferroelectric and metastable paraelectric and modulated phases is possible. This expectation agrees with the concentration evolution of heat capacity [175] and dielectric susceptibility [225] temperature dependence in  $(\text{Pb}_x\text{Sn}_{1-x})_2\text{P}_2\text{Se}_6$  mixed crystals, which demonstrates a gradual lock-in transition smearing with growth of lead concentration.

In addition to the frustration of polar fluctuations near the center of the Brillouin zone, in  $\text{Sn}_2\text{P}_2\text{S}_6$  crystal the antipolar fluctuations also strongly develop in the paraelectric phase on cooling to the continuous phase transition temperature  $T_0$ . At this transition, the critical behavior according to the thermal diffusivity data [96] can be described as a crossover between Ising and XY universality classes, what is expected near a bicritical point with coupled polar and antipolar order parameters.

## Chapter 9. Ferroelectricity induced by germanium dopants in quantum paraelectrics $\text{Sn}(\text{Pb})_2\text{P}_2\text{S}(\text{Se})_6$

### 9.1. Introduction

In this chapter, we will consider how the introduction of germanium in the cation sublattice has an effect on the general shape of the phase diagram and on the possible responsibility to change the location and the ferroelectric properties of the transition. The dipole ordering in  $\text{Sn}(\text{Pb})_2\text{P}_2\text{S}(\text{Se})_6$  materials may be tuned by chemical substitution realizing a ferroelectric quantum phase transition and quantum glassy or relaxor type phenomena on different parts of the phase diagram. The introduction of Ge impurity increases the temperature of the phase transitions and enhances the stereoactivity of the cation subsystem [191, 198].

At low temperatures, a quantum critical behavior in  $\text{Pb}_2\text{P}_2\text{S}_6$  crystal can be established by the nonlinear coupling between polar and antipolar fluctuations. In this chapter we will consider the influence on dielectric and thermal properties induced by Ge impurity.

### 9.2. Samples and experimental techniques

Single crystals of  $(\text{Sn}_{0.95}\text{Ge}_{0.05})_2\text{P}_2(\text{Se}_{0.2}\text{S}_{0.8})_6$ ,  $(\text{Sn}_{0.95}\text{Ge}_{0.05})_2\text{P}_2(\text{Se}_{0.4}\text{S}_{0.6})_6$ ,  $(\text{Sn}_{0.95}\text{Ge}_{0.05})_2\text{P}_2(\text{Se}_{0.5}\text{S}_{0.5})_6$ ,  $(\text{Pb}_{0.7}\text{Sn}_{0.25}\text{Ge}_{0.05})_2\text{P}_2\text{S}_6$  and  $(\text{Pb}_{0.7}\text{Sn}_{0.25}\text{Ge}_{0.05})_2\text{P}_2\text{Se}_6$  were obtained by a chemical gas transport reaction with a small amount of carrier gas of  $\text{I}_2$ . High-purity elements Sn (99.99%), Pb (99.99%), P (99.999%), S (99.99%), Se (99.99%), and Ge (99.999%) in atomic percentage in required proportion were placed into the quartz tube. Thin slabs with their faces in monoclinic symmetry plane perpendicular to the (001) direction with the thickness of 500 – 550  $\mu\text{m}$  were cut for the thermal diffusivity measurements. The thermal diffusivity measurements have been performed using a high-resolution *ac* photopyroelectric calorimeter in the standard back detection configuration using a closed cycle helium cryostat. In order

to study the anomalies of the thermal diffusivity curves and to check possible temperature hysteresis, the rate of change of the temperature varied in the range of 100 - 10 mK / min. A detailed description of the experimental setups used during these investigations can be found in chapter 2.

In addition to the calorimetric measurements for  $\text{Pb}_2\text{P}_2\text{S}_6$ ,  $(\text{Pb}_{0.98}\text{Ge}_{0.02})_2\text{P}_2\text{S}_6$ ,  $(\text{Pb}_{0.7}\text{Sn}_{0.25}\text{Ge}_{0.05})_2\text{P}_2\text{S}_6$  and  $(\text{Pb}_{0.7}\text{Sn}_{0.25}\text{Ge}_{0.05})_2\text{P}_2\text{Se}_6$  crystals the dielectric measurements data have also been used [242]. In this case, monocrystal plates with a thickness of about 2 mm and plane parallel faces around 15 mm<sup>2</sup> with silver paste electrodes on polar (100) phases were prepared. The complex dielectric permittivity  $\varepsilon^* = \varepsilon' + i\varepsilon''$  was measured by a capacitance bridge HP4284A in the frequency range 10 kHz – 1 MHz. In order to study the temperature dependence of dielectric susceptibility the sample was placed in the He cryostat between the two copper conductors (contacts).

### **9.3. Thermal diffusivity anomalies in $(\text{Pb}_x\text{Sn}_{1-x})_2\text{P}_2(\text{Se}_y\text{S}_{1-y})_6$ chalcogenides with Ge impurity**

In  $\text{Sn}_2\text{P}_2(\text{Se}_{0.2}\text{S}_{0.8})_6$  the substitution of Ge 5% increases the critical temperature from 300.93 K to 307.13 K (fig. 9.1 a) as well as makes the anomaly slightly broader and brings some rounding. For the Lifshitz point composition  $\text{Sn}_2\text{P}_2(\text{Se}_{0.28}\text{S}_{0.72})_6$ , the critical index  $\alpha \approx 0.34$  and the critical amplitudes ratio  $A^+/A^- \approx 0.42$  were observed [43]. The introduction of Ge increases the critical temperature from 281.3 K to 284 K (Fig. 9.1 b) but changes neither the character of the transition nor the universality class, as it is uniaxial Lifshitz class with critical exponent  $\alpha \approx 0.25$  and  $A^+/A^- \approx 0.49$  [191]. Such values agree with the theoretical ones estimated for a Lifshitz system without considering strong dipolar interactions. In the case of the Lifshitz point in uniaxial ferroelectrics only small multiplicative corrections to mean field behavior are expected [69] in the critical region. Hence, both the critical exponent and the amplitude ratio values observed for the  $\text{Sn}_2\text{P}_2(\text{Se}_{0.28}\text{S}_{0.72})_6$  mixed crystal lead to the conclusion that long-range interactions do not have a strong influence on the critical behavior in this system. This can be related to the partial screening of the dipole -

dipole interaction by charge carriers in the  $\text{Sn}_2\text{P}_2(\text{Se}_y\text{S}_{1-y})_6$  ferroelectric semiconductors.

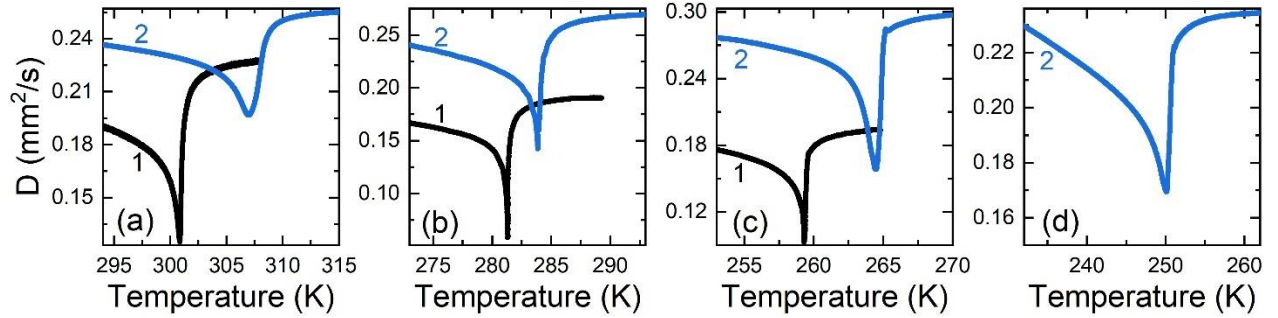


**Fig. 9.1.** Thermal diffusivity as a function of temperature for  $\text{Sn}_2\text{P}_2(\text{Se}_{0.2}\text{S}_{0.8})_6$  [43] and  $(\text{Sn}_{0.95}\text{Ge}_{0.05})_2\text{P}_2(\text{Se}_{0.2}\text{S}_{0.8})_6$  (a),  $\text{Sn}_2\text{P}_2(\text{Se}_{0.28}\text{S}_{0.72})_6$  [43] and  $(\text{Sn}_{0.95}\text{Ge}_{0.05})_2\text{P}_2(\text{Se}_{0.28}\text{S}_{0.72})_6$  (b) [191],  $\text{Sn}_2\text{P}_2(\text{Se}_{0.4}\text{S}_{0.6})_6$  [43] and  $(\text{Sn}_{0.95}\text{Ge}_{0.05})_2\text{P}_2(\text{Se}_{0.4}\text{S}_{0.6})_6$  (c),  $(\text{Sn}_{0.95}\text{Ge}_{0.05})_2\text{P}_2(\text{Se}_{0.5}\text{S}_{0.5})_6$  (d). Number 1 shows the samples without Ge while 2 demonstrates the crystals with Ge 5%

As already shown in Chapter 7, the introduction of Pb leads to a more obvious separation of the paraelectric and the ferroelectric phases. In the case of germanium, as we can see in Fig. 9.1 (c, d) this does not happen, although, as in the case of lead, the introduction of germanium leads to some rounding of anomalies. Unfortunately, the quality of  $\text{Sn}_2\text{P}_2(\text{Se}_{0.5}\text{S}_{0.5})_6$  crystal, where the separation may be more apparent, was quite bad, preventing it from being included in the fig. 9.1 d. Obviously, it would also be interesting to study the crystals with  $y = 0.6, 0.8$  selenium concentration.

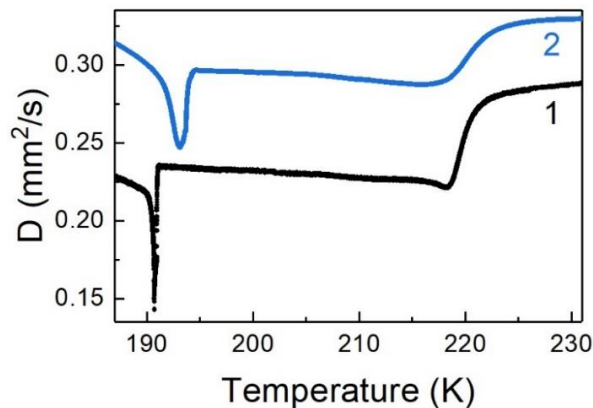


**Fig. 9.2.** Thermal diffusivity as a function of temperature for  $\text{Sn}_2\text{P}_2\text{Se}_6$  (1) and  $(\text{Sn}_{0.95}\text{Ge}_{0.05})_2\text{P}_2\text{Se}_6$  (2). Data for  $\text{Sn}_2\text{P}_2\text{Se}_6$  is taken from [43]

For  $(\text{Sn}_{0.95}\text{Ge}_{0.05})_2\text{P}_2\text{Se}_6$  crystal, the position of the transitions is almost unchanged, which can be interpreted as the fact that the amount of germanium is less than necessary (Fig. 9.2).

Overall, the results of the thermal diffusivity studies may indicate that germanium inhibits the splitting of the paraelectric and ferroelectric phases for the samples with a selenium concentration above  $y_{LP}$ .

#### 9.4. Quantum paraelectric state and critical behavior in $\text{Sn}(\text{Pb})_2\text{P}_2\text{S}(\text{Se})_6$ ferroelectrics

For  $\text{Pb}_2\text{P}_2\text{S}_6$  crystal the  $\varepsilon'(T)$  dependence [242] shows monotonic rise on cooling till 20 K with some flattening below 50 K (Fig. 9.3 a). At lead by germanium substitution (about 2%), a clear maximum of  $\varepsilon''(T)$  near 30 K (at 1 MHz frequency) is observed (Fig. 9.3 b). In order to describe the temperature dependencies of the dielectric susceptibility of quantum paraelectrics, the authors of work [242] have used Barrett's equation:

$$\varepsilon'(T) = \frac{C_{CW}}{\left(\frac{T_1}{2}\right) \coth\left(\frac{T_1}{2T}\right) - T_c} + \varepsilon_0, \quad (9.1)$$

where  $C_{CW}$  is the Curie-Weiss constant,  $T_c$  is the classical paraelectric Curie temperature,  $\varepsilon_0$  is a temperature independent constant and  $T_1$  is the dividing point between the low temperatures where quantum effects are important so  $\varepsilon(T)$  deviates from Curie-Weiss law, and the high temperature region where a classical approximation and Curie-Weiss law are valid [238].

In many cases,  $T_c \leq 0$  K, and the material does not undergo a ferroelectric phase transition at any finite temperature. When  $T_c$  is finite and  $T_c < T_1$ , the quantum fluctuations break the long range ferroelectric order and stabilize the quantum paraelectric state in the sample. Probable ferroelectric transition occurs at  $T_c$  [239]. According to dielectric data [216] of  $\text{Pb}_2\text{P}_2\text{S}_6$  (Fig. 9.3 a) deviation from Barrett's equation starts around 75 K. The obtained parameter values ( $T_1 = 190$  K and  $T_c = -$

370 K) for  $\text{Pb}_2\text{P}_2\text{S}_6$  crystal demonstrate that the material does not undergo a ferroelectric phase transition at any finite temperature.

As was mentioned in previous chapters, when lead substitutes tin in  $\text{Sn}_2\text{P}_2\text{S}_6$  type crystals, the hybridization of anion and cation sublattices electron orbitals becomes weaker, reducing the phase transition temperature. On the other hand, Ge dopant plays an opposite role: it enhances the total stereoactivity of the cation sublattice in the crystal. Small amount of impurities in quantum paraelectrics could induce ferroelectricity [240, 241]. So, it is possible that germanium impurities can affect quantum paraelectric state of  $\text{Pb}_2\text{P}_2\text{S}_6$ . Fig. 9.3 b shows the temperature dependence of the real part of dielectric susceptibility for  $(\text{Pb}_{0.98}\text{Ge}_{0.02})_2\text{P}_2\text{S}_6$  crystal and confirms a non-classical  $T^2$  behavior of the inverse dielectric susceptibility. For this, the temperature dependence of the real part of dielectric susceptibility for crystal doped by germanium is fitted by the Barret's equation 9.1 giving temperatures  $T_1 \approx 207$  K and  $T_c \approx 40$  K [242]. Since  $T_c < T_1$  for  $(\text{Pb}_{0.98}\text{Ge}_{0.02})_2\text{P}_2\text{S}_6$ , it could be concluded that the long-range ferroelectric order in the sample doped by Ge is broken due to quantum fluctuations below 207 K, and a probable ferroelectric transition occurs in the temperature region between 40 K and 80 K (Fig. 9.4). Doping with germanium obviously induces some disordering and decreases the real part of susceptibility below 80 K deviating from Barrett's fit (Fig. 9.3 b).

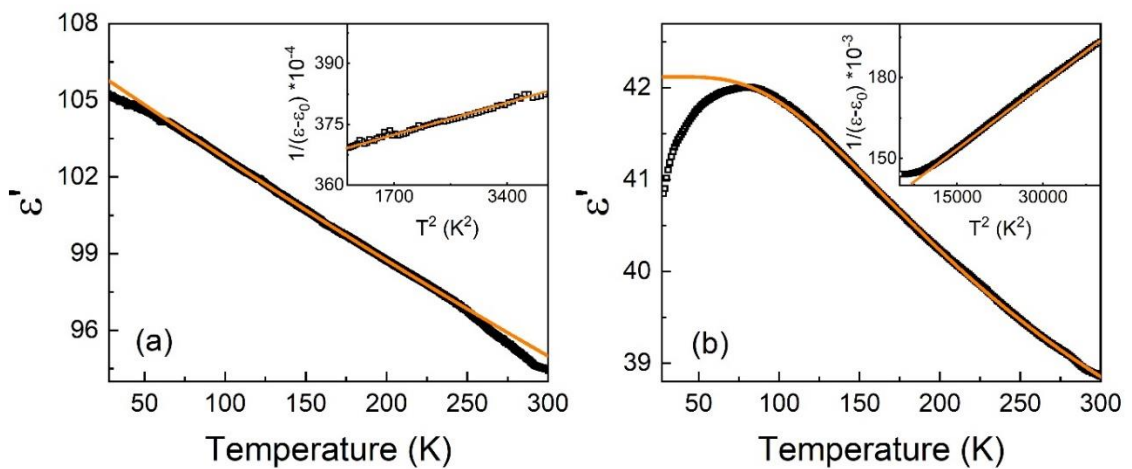


**Fig. 9.3.** Temperature dependence of the real part of the dielectric susceptibility for  $\text{Pb}_2\text{P}_2\text{S}_6$  crystal at 100kHz (a) and  $(\text{Pb}_{0.98}\text{Ge}_{0.02})_2\text{P}_2\text{S}_6$  at 10 kHz (b) [242]. The inset shows the  $\varepsilon(T)^{-1} \sim T^2$  behavior. Orange lines are the fitting of equation 9.1

The peak of the real part of the dielectric susceptibility is broad. Moreover, there are two peaks of the imaginary part of the dielectric susceptibility with a frequency dispersive behavior, and the temperatures of the loss peaks are around 50 K and 100 K at 100 kHz (Fig. 9.4). Obviously, this is related to compositional fluctuations in  $(\text{Pb}_{0.98}\text{Ge}_{0.02})_2\text{P}_2\text{S}_6$  crystal. Also, a fast-enough dynamics of local dipoles, and slower dynamics of noninteracting ones, or weakly interacting nanoclusters, can determine the broadness of the phase transition induced by Ge impurity with related frequency – temperature anomalous behavior of dielectric susceptibility that is similar to the one observed in the case of a crossover between dipole glass and ferroelectric relaxor [240, 241].

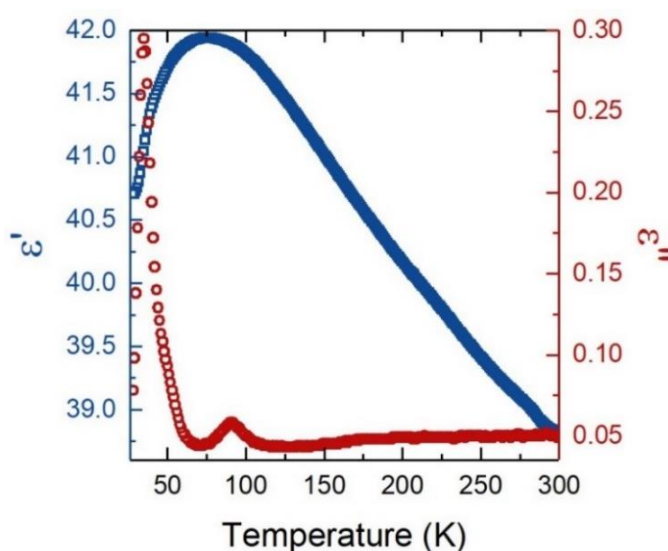


**Fig. 9.4.** Temperature dependence of dielectric susceptibility real  $\epsilon'$  (blue squares) and imaginary  $\epsilon''$  (red circles) parts at 100 kHz for  $(\text{Pb}_{0.98}\text{Ge}_{0.02})_2\text{P}_2\text{S}_6$  crystal

As was already found in [171], for  $(\text{Pb}_x\text{Sn}_{1-x})_2\text{P}_2\text{S}_6$  mixed crystals with compositions  $x \approx 0.61$  and  $x \approx 0.66$ , which are close to the transition at zero temperature from a polar phase ( $x < 0.7$ ) to a paraelectric one ( $x > 0.7$ ), the dielectric susceptibility demonstrates the quantum critical behavior with  $T_c \approx 35$  K and 20 K, respectively. Therefore, the study of crystals with higher concentrations of lead was necessary. The influence of Ge dopants on the quantum paraelectric state of  $\text{Pb}_2\text{P}_2\text{S}_6$  type compounds by studying  $(\text{Pb}_{0.7}\text{Sn}_{0.25}\text{Ge}_{0.05})_2\text{P}_2\text{S}_6$  and  $(\text{Pb}_{0.7}\text{Sn}_{0.25}\text{Ge}_{0.05})_2\text{P}_2\text{Se}_6$

samples has been investigated. In these crystals the  $\text{Sn}^{2+}$  sites were codoped with two different impurities ( $\text{Pb}^{2+}$  and  $\text{Ge}^{2+}$ ) which have very different influences on the phase transitions. It is important to realize that Sn substitution has the strongest effect because the ferroelectric phase transition is induced by the stereoactivity of the  $\text{Sn}^{2+}$  cation  $5s^2$  electron lone pair.

The temperature dependence of the real part of the dielectric susceptibility for  $(\text{Pb}_{0.7}\text{Sn}_{0.25}\text{Ge}_{0.05})_2\text{P}_2\text{S}_6$  and  $(\text{Pb}_{0.7}\text{Sn}_{0.25}\text{Ge}_{0.05})_2\text{P}_2\text{Se}_6$  crystals [242] is shown in Fig. 9.5. Susceptibility  $\epsilon'$  increases continuously with decreasing temperature from room temperature till 20 K. The dielectric losses have a maximum at low temperature, around 50 K at a frequency of 100 kHz. The inverse dielectric permittivity  $1/\epsilon(T)$  exhibits the expected non-classical  $T^2$  temperature dependence not only in the case of doped  $(\text{Pb}_{0.98}\text{Ge}_{0.02})_2\text{P}_2\text{S}_6$  sample (Fig. 9.3), but it is also observed in mixed crystals  $(\text{Pb}_{0.7}\text{Sn}_{0.25}\text{Ge}_{0.05})_2\text{P}_2\text{S}_6$  and  $(\text{Pb}_{0.7}\text{Sn}_{0.25}\text{Ge}_{0.05})_2\text{P}_2\text{Se}_6$  (Fig. 9.5). From this follows that the ferroelectric quantum critical behavior is relatively insensitive to quenched disorder in doped samples and mixed crystals.

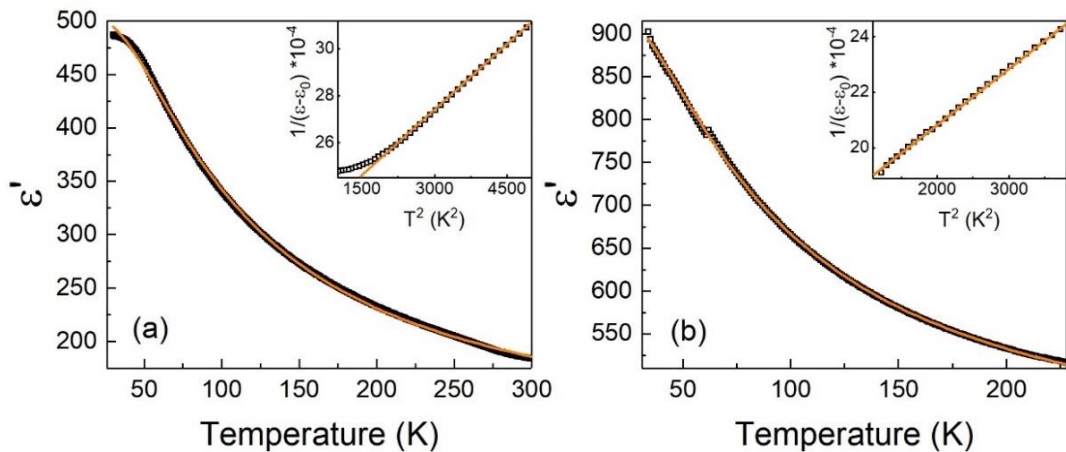


**Fig. 9.5.** Temperature dependence of dielectric susceptibility real part of  $(\text{Pb}_{0.7}\text{Sn}_{0.25}\text{Ge}_{0.05})_2\text{P}_2\text{S}_6$  (a) and  $(\text{Pb}_{0.7}\text{Sn}_{0.25}\text{Ge}_{0.05})_2\text{P}_2\text{Se}_6$  (b) at 10 kHz [242]; orange solid curve is the fitting according to the Barret's equation (1). The inset shows the reciprocal dielectric susceptibility as a function of the squared temperature

By fitting the experimental data [242] of Fig. 9.5 a to Barrett's equation (1) the next parameters were determined:  $T_l \approx 70$  K,  $T_c \approx -4$  K, and  $C_{CW} \approx 30670$  K. The observed temperature behavior of the dielectric susceptibility demonstrates that  $(\text{Pb}_{0.7}\text{Sn}_{0.25}\text{Ge}_{0.05})_2\text{P}_2\text{S}_6$  crystal obviously undergoes some inhomogeneous polar ordering at very low temperatures.

Similarly, the temperature dependence of the dielectric susceptibility  $\varepsilon'(T)$  for the  $(\text{Pb}_{0.7}\text{Sn}_{0.25}\text{Ge}_{0.05})_2\text{P}_2\text{Se}_6$  [242] crystal is shown in Fig. 9.5 b. On cooling from 300 till 20 K both  $\varepsilon'$  and  $\varepsilon''$  increase, their frequency dispersion appears below 70 K [242]. By fitting to the Barrett's equation 9.1 (Fig. 9.5 b) it was found that  $T_l \approx 55$  K,  $T_c \approx -6$  K, and  $C_{CW} \approx 34260$  K [242]. It is seen that in the selenide mixed crystal  $(\text{Pb}_{0.7}\text{Sn}_{0.3})_2\text{P}_2\text{Se}_6$  the germanium impurity induces inhomogeneous polar ordering at lower temperatures similarly to the case of the sulfide analogue.

As a whole, according to the results of the dielectric investigations, it can be concluded that  $\text{Pb}_2\text{P}_2\text{S}_6$  crystals exhibit a quantum paraelectric state. The introduction of small amounts of germanium dopant provokes the appearance of the ferroelectric phase. In mixed crystals a very inhomogeneous polar ordering (like dipole glassy or relaxor state) appears below approximately 70 K.

From the data obtained by the fittings we can see that the  $\varepsilon'(T)$  dependence of Eq. 9.1, considering quantum fluctuations for  $\text{Pb}_2\text{P}_2\text{S}_6$  compound, predicts the value of  $T_c$  in accordance with  $T_0(y)$  dependence for  $(\text{Pb}_y\text{Sn}_{1-y})_2\text{P}_2\text{S}_6$  mixed crystals (Fig. 1). At this, the value of  $T_l$  is strongly suppressed in mixed crystals – from 190 K in  $\text{Pb}_2\text{P}_2\text{S}_6$  and 207 K in the case of  $(\text{Pb}_{0.98}\text{Ge}_{0.02})_2\text{P}_2\text{S}_6$  to  $T_l \approx 70$  K in the solution with  $x = 0.7$ . Such decrease of the crossover temperature  $T_l$  from classic to quantum fluctuations behavior can be interpreted as the manifestation of quantum coherence destruction for the electronic component of spontaneous polarization fluctuations, that are determined by phosphorous cations  $\text{P}^{4+} + \text{P}^{4+} \leftrightarrow \text{P}^{3+} + \text{P}^{5+}$  charge disproportionation. The electronic contribution to spontaneous polarization is connected to the coherent state of polaronic excitons – small hole polarons in  $\text{SnPS}_3$  structural groups are coupled with small electronic polarons in nearest  $\text{SnPS}_3$  structural groups [158, 243]. Obviously such polaronic excitons are strongly bounded

by defects in mixed crystals what preserves the development of quantum fluctuations when lowering the temperature.

In Fig. 9.6 the temperature dependencies of real and imaginary parts of dielectric susceptibility are compared for  $(\text{Pb}_{0.7}\text{Sn}_{0.25}\text{Ge}_{0.05})_2\text{P}_2\text{S}_6$ ,  $(\text{Pb}_{0.98}\text{Ge}_{0.02})_2\text{P}_2\text{S}_6$  and  $\text{Pb}_2\text{P}_2\text{S}_6$  crystals [242] in comparison with data [171] for  $(\text{Pb}_{0.66}\text{Sn}_{0.34})_2\text{P}_2\text{S}_6$  and  $(\text{Pb}_{0.61}\text{Sn}_{0.39})_2\text{P}_2\text{S}_6$  mixed crystals. We can see that the dielectric anomalies induced by the germanium impurity are smeared similarly to the observed anomalies in the case of  $(\text{Pb}_x\text{Sn}_{1-x})_2\text{P}_2\text{S}_6$  solid solutions with lead concentration near the threshold value  $x_c = 0.7$ . In all three samples a complex thermal evolution of the provoked inhomogeneous polarization occurs on cooling below 70 K.

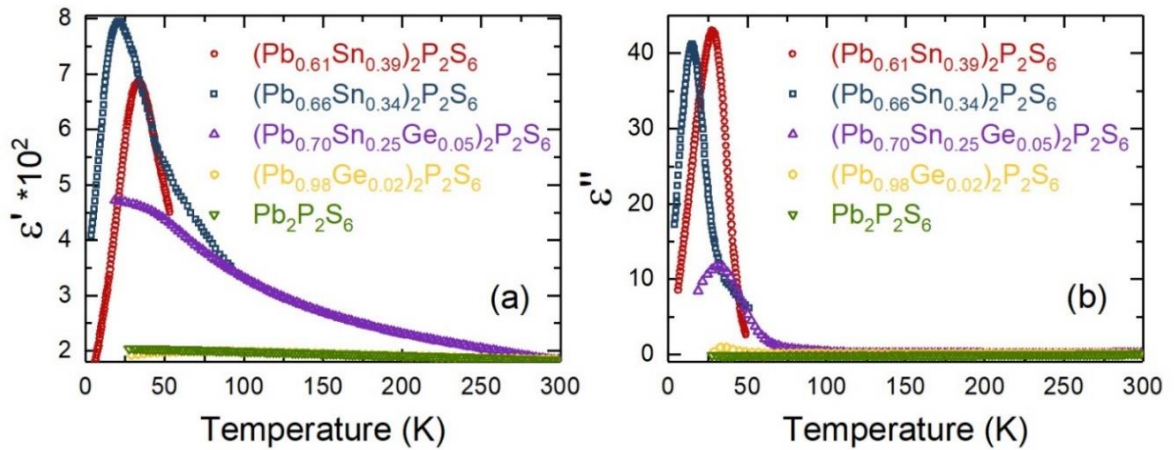


**Fig. 9.6.** Temperature dielectric susceptibility real (a) and imaginary (b) parts for crystals  $\text{Pb}_2\text{P}_2\text{S}_6$ ,  $(\text{Pb}_{0.98}\text{Ge}_{0.02})_2\text{P}_2\text{S}_6$ ,  $(\text{Pb}_{0.7}\text{Sn}_{0.25}\text{Ge}_{0.05})_2\text{P}_2\text{S}_6$  [242]. Data [171] for  $(\text{Pb}_{0.61}\text{Sn}_{0.39})_2\text{P}_2\text{S}_6$  and  $(\text{Pb}_{0.66}\text{Sn}_{0.34})_2\text{P}_2\text{S}_6$  mixed crystals are also shown for comparison

In fig. 9.7 (a) we present the experimental thermal diffusivity data for  $(\text{Pb}_{0.7}\text{Sn}_{0.25}\text{Ge}_{0.05})_2\text{P}_2\text{S}_6$  and  $(\text{Pb}_{0.7}\text{Sn}_{0.25}\text{Ge}_{0.05})_2\text{P}_2\text{Se}_6$  crystals. Thermal conductivity  $\kappa$  has been retrieved by eq. 6.2. In order to do it we have used the calculated heat capacities for  $(\text{Sn,Pb})_2\text{P}_2\text{S}_6$  crystals and the experimental heat capacity from [175]. In the case of  $(\text{Pb}_{0.7}\text{Sn}_{0.25}\text{Ge}_{0.05})_2\text{P}_2\text{S}_6$  mixed crystals the thermal conductivity temperature behavior (Fig. 9.7 b) is similar to the one observed in case of glassy materials, what demonstrates an effective phonon scattering in solid solutions with

sublattice of mixed tin and lead cations. The addition of germanium impurity induces the dipole glass state. Only a small contribution to thermal conductivity by germanium addition is observed in the temperature range from 50 K to 120 K. This has also been confirmed by additional studies of the temperature dependence of the real and imaginary parts of dielectric susceptibility at different frequencies (Fig. 9.8) of solid solutions with germanium [237]. Similar behavior is also observed for  $(\text{Pb}_{0.7}\text{Sn}_{0.25}\text{Ge}_{0.05})_2\text{P}_2\text{S}_6$  selenide solid solution.

With the introduction of germanium into the lattice of  $\text{Pb}_2\text{P}_2\text{S}_6$  crystal, the temperature dependence of the thermal conductivity in a wide temperature range coincides with Eiken's law, i.e. it is proportional to the inverse of temperature (Fig. 9.7 d). Such dependency gives evidence about the dominant role of three – phonon scattering processes in the thermal resistivity. In the case of  $\text{Sn}_2\text{P}_2\text{S}_6$  ferroelectric phase, the introduction of Ge impurity also improves  $\kappa \sim T^{-1}$  temperature dependence for the thermal conductivity.

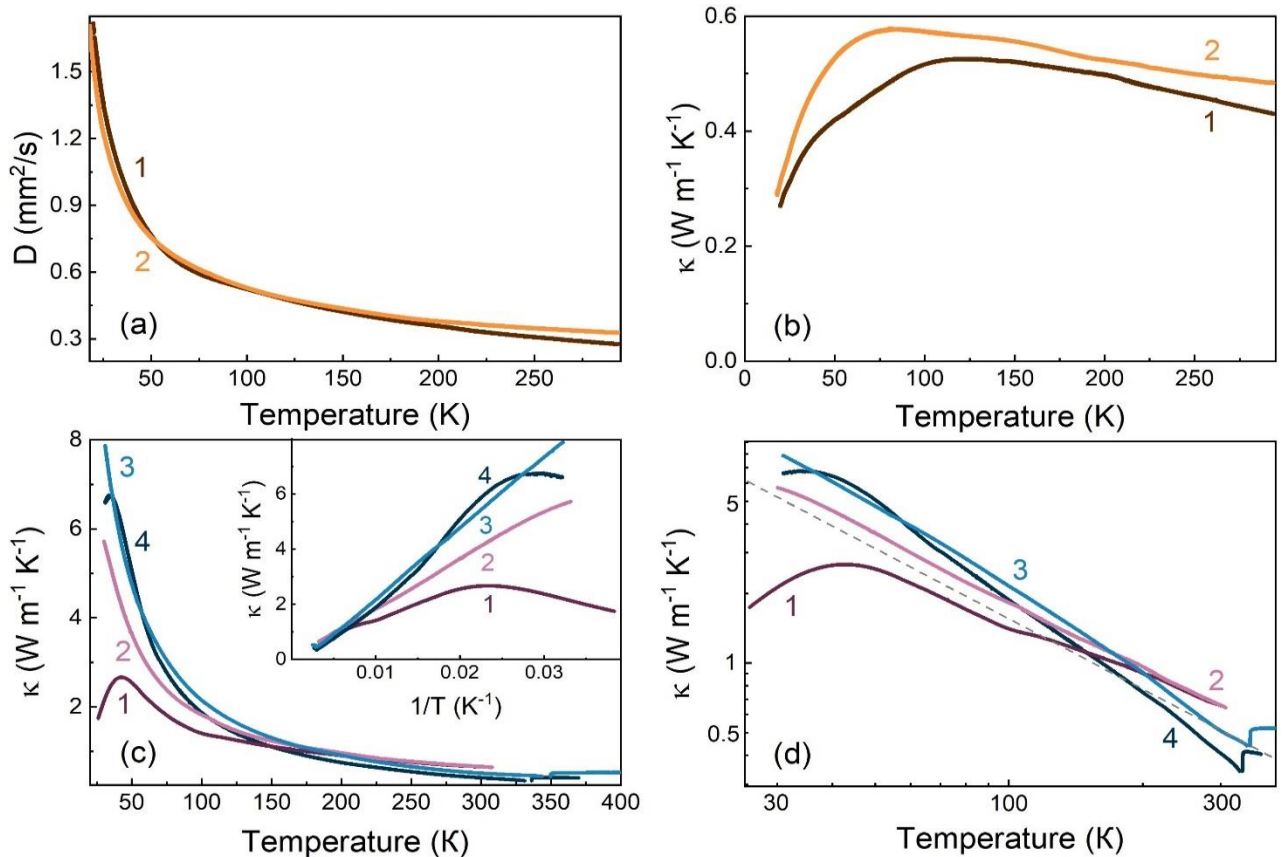


**Fig. 9.7** Temperature dependence of thermal diffusivity  $D$  for  $(\text{Pb}_{0.7}\text{Sn}_{0.25}\text{Ge}_{0.05})_2\text{P}_2\text{S}_6$  (1) and  $(\text{Pb}_{0.7}\text{Sn}_{0.25}\text{Ge}_{0.05})_2\text{P}_2\text{Se}_6$  (2), Temperature

dependence of thermal conductivity  $\kappa$  for  $\text{Pb}_2\text{P}_2\text{S}_6$  (1) ( $\text{Pb}_{0.98}\text{Ge}_{0.02}$ ) $_2\text{P}_2\text{S}_6$  (2), ( $\text{Sn}_{0.95}\text{Ge}_{0.05}$ ) $_2\text{P}_2\text{S}_6$  (3) and  $\text{Sn}_2\text{P}_2\text{S}_6$  (4) in normal (c) and logarithmic (d) coordinates. Inset: their  $\kappa(T^{-1})$  dependence. Grey dashed curve shows  $\kappa \sim T^{-1}$  behavior. Data for  $D$  is taken from [43, 96, 191]

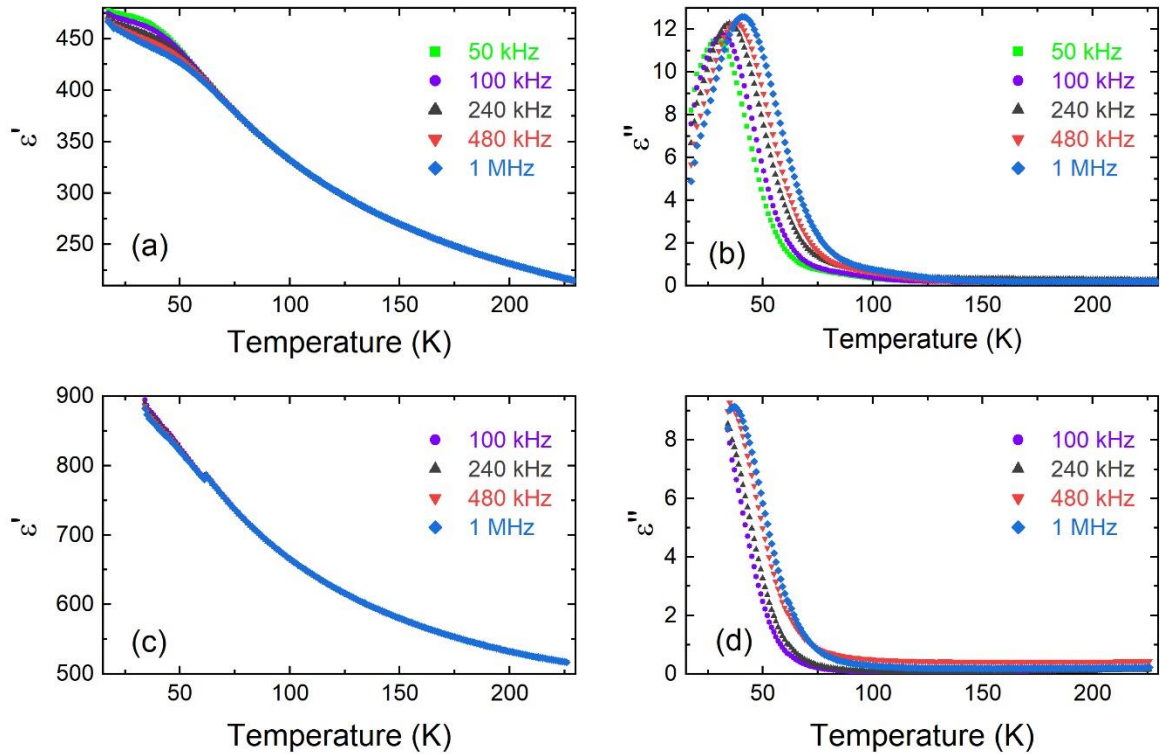


**Fig. 9.8.** Temperature dependence of the real and imaginary dielectric susceptibility at different frequencies for: ( $\text{Pb}_{0.7}\text{Sn}_{0.25}\text{Ge}_{0.05}$ ) $_2\text{P}_2\text{S}_6$  (a, b) and ( $\text{Pb}_{0.7}\text{Sn}_{0.25}\text{Ge}_{0.05}$ ) $_2\text{P}_2\text{Se}_6$  (c, d) crystals

For ( $\text{Pb}_{0.98}\text{Ge}_{0.02}$ ) $_2\text{P}_2\text{S}_6$  crystal the thermal conductivity at low temperatures is bigger than in the case of pure  $\text{Pb}_2\text{P}_2\text{S}_6$  crystal (Fig. 9.7 c, d). This is related to the induction of polar clusters of the ferroelectric phase when doping with Ge. The dielectric susceptibility of such clusters is smaller than the susceptibility of the paraelectric phase and the frequency of the lowest energy soft polar optical mode near the Brillouin zone center is elevated. The growth of the soft optical mode frequency diminishes the probability of the optical phonon resonance scattering by acoustic phonons [244, 245]. At low temperatures heat is transferred by acoustic and lowest frequency optical phonons. Acoustic phonons with small wave numbers are involved

mostly in normal scattering (N – process) that doesn't contribute to thermal resistivity. The phonons from the optical branch near the BZ center also participate in Umklapp scattering (U – process) by lattice imperfections, which provide an effective thermal resistivity. So, the hardening of the optical branch lowers the population of the optical phonons and increases the thermal conductivity of  $(\text{Pb}_{0.98}\text{Ge}_{0.02})_2\text{P}_2\text{S}_6$  crystal at very low temperatures (Fig. 9.7 c, d).

The explanation given above agrees with the comparison of the changes in the temperature dependencies of dielectric susceptibility and thermal conductivity induced by germanium (Fig. 9.9). On cooling below 100 K, the difference in thermal conductivity between  $(\text{Pb}_{0.98}\text{Ge}_{0.02})_2\text{P}_2\text{S}_6$  and  $\text{Pb}_2\text{P}_2\text{S}_6$  crystals rapidly rises, and oppositely – dielectric susceptibility of  $(\text{Pb}_{0.98}\text{Ge}_{0.02})_2\text{P}_2\text{S}_6$  crystal quickly lowers relatively to  $\text{Pb}_2\text{P}_2\text{S}_6$  crystal susceptibility. Such low temperature evolution of the dielectric susceptibility induced by germanium impurity reflects the hardening (frequency increase) of the lowest polar optic mode near the BZ center.

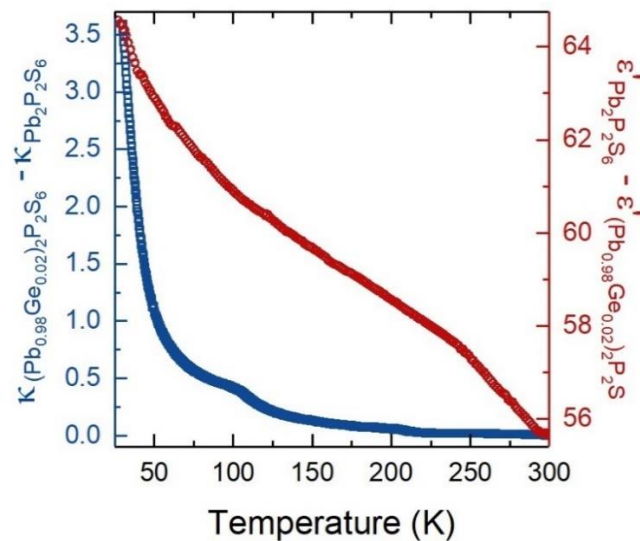


**Fig. 9.9.** Temperature dependence of thermal conductivity and dielectric susceptibility [242] difference for  $(\text{Pb}_{0.98}\text{Ge}_{0.02})_2\text{P}_2\text{S}_6$  and  $\text{Pb}_2\text{P}_2\text{S}_6$  crystals. Data for  $D$  is taken from [191]

As has already been told in chapter 8, in order to build a  $T - \Delta$  diagram for  $(\text{Pb}_x\text{Sn}_{1-x})_2\text{P}_2\text{S}_6$  crystals, the parameter  $\Delta$  depends on the change in the difference between the central and side minimum in the local potential, which occurs at the

change in tin/lead concentration in the cation. Thus, the quantum anharmonic oscillator model [158] can be used to determine the coordinate of the virtual “Ge<sub>2</sub>P<sub>2</sub>S<sub>6</sub>”, which allows us to determine the shape of the local potential. In this model, the real crystal lattice is represented as a system of one-dimensional interacting quantum anharmonic oscillators.

The local potentials of quantum anharmonic for Pb<sub>2</sub>P<sub>2</sub>S<sub>6</sub>, Sn<sub>2</sub>P<sub>2</sub>S<sub>6</sub> and virtual “Ge<sub>2</sub>P<sub>2</sub>S<sub>6</sub>” crystals, which were determined by a methodology described earlier [158], are shown in Fig. 9.10 a. They are characterized by the below listed frequency  $\omega_0$ , temperature  $T_x$  and values of zero-point energy  $E_0 = \frac{\hbar\omega_0}{2}$ :

$$\text{Pb}_2\text{P}_2\text{S}_6: \omega_0 \approx 47 \text{ cm}^{-1}, T_x \approx 72 \text{ K}, E_0 \approx 0.003 \text{ eV};$$

$$\text{Sn}_2\text{P}_2\text{S}_6: \omega_0 \approx 60 \text{ cm}^{-1}, T_x \approx 86 \text{ K}, E_0 \approx 0.004 \text{ eV};$$

$$\text{Ge}_2\text{P}_2\text{S}_6: \omega_0 \approx 80 \text{ cm}^{-1}, T_x \approx 115 \text{ K}, E_0 \approx 0.005 \text{ eV}.$$

The shape of the local potential favors an off - center displacement of Sn<sup>2+</sup> cations in Sn<sub>2</sub>P<sub>2</sub>S<sub>6</sub> or Pb<sup>2+</sup> cations in Pb<sub>2</sub>P<sub>2</sub>S<sub>6</sub> crystal lattice that induces a local electric dipole. The local dipoles at a given inter-cell interaction  $J$  cannot be ordered down to the lowest temperatures in the case of Pb<sub>2</sub>P<sub>2</sub>S<sub>6</sub> crystal, but here the ferroelectric ground states may be reached via chemical substitution of lead cations by tin or germanium cations.

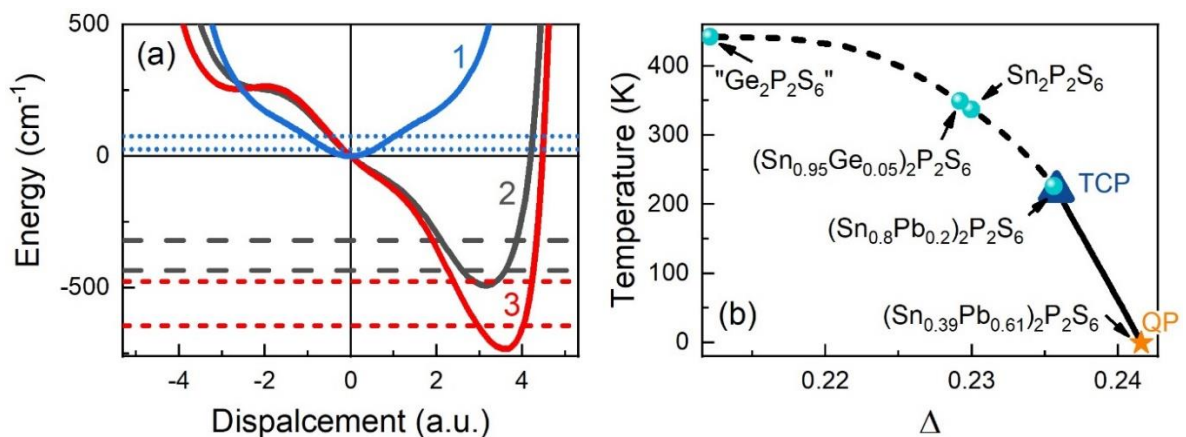


**Fig. 9.10.** The QAO local potentials at  $T = 0$  K and their lowest energy levels for crystals Pb<sub>2</sub>P<sub>2</sub>S<sub>6</sub> (1), Sn<sub>2</sub>P<sub>2</sub>S<sub>6</sub> (2) and for virtual crystal “Ge<sub>2</sub>P<sub>2</sub>S<sub>6</sub>” (3) (a). The phase transition temperature as a function of  $\Delta$ , calculated in the mean -

field approximation on the BEG model [158] (b). Solid line denotes first order and dashed one second order phase transitions. Blue triangle shows tricritical point, orange star shows quantum point

At low temperatures for ferroelectrics the quantum fluctuating electrical dipoles are coupled to the elastic steps of freedom. The quantum critical phase in three dimensional space  $d$  is evident by the fact that the dielectric susceptibility depends on both the static and dynamic (frequency dependent) properties of the system, which results for multiaxial ferroelectrics, like perovskite  $\text{SrTiO}_3$ , in a unity rise of effective dimension –  $d_{\text{eff}} = d + 1 = 4$  [246, 247]. In the uniaxial ferroelectrics apart from short range interactions, the long range anisotropic electrical dipole interactions provide a further unity increase in the effective dimension to  $d_{\text{eff}} = d + 2 = 5$  [248, 249].

For  $\text{SrTiO}_3$  below 25 K a nonmonotonic temperature dependence of the dielectric susceptibility arises from optic and acoustic phonon coupling (electrostriction) [250]. The upturn in the inverse susceptibility occurs when  $T$  is less than 10% of  $T_x$ , where  $T_x$  is the temperature associated with the soft transverse optical phonon frequency  $\omega$  at the Brillouin zone (BZ) center in the zero-temperature limit. This means that the fit of the dielectric susceptibility data to a quantum criticality model without taking into account the electrostrictive coupling is appropriate only for  $T > 0.1 * T_x$ . This condition is fulfilled for  $\text{Pb}_2\text{P}_2\text{S}_6$  crystal where  $0.1 T_x \approx 7$  K.

In Fig. 9.11 the measured dielectric susceptibility  $1/\epsilon'(T)$  over the range 27 – 80 K for  $\text{Pb}_2\text{P}_2\text{S}_6$  crystal in different temperature scales is shown. From the comparison of Fig. 9.11 a and Fig. 9.11 b, it is seen that  $1/\epsilon'$  varies as  $T^2$  in the region 27 - 80 K and doesn't satisfy the  $T^3$  quantum critical behavior. Above 80 K this crystal exhibits classical Curie-Weiss behavior (Fig. 9.11 c, d). We emphasize that for  $\text{Pb}_2\text{P}_2\text{S}_6$  crystal the critical exponent is close to  $\gamma = 2.0$ , that is calculated and observed for multiaxial quantum critical systems like  $\text{SrTiO}_3$  [246, 247], and does not follow the theoretically predicted for uniaxial ferroelectrics value  $\gamma = 3.0$  [248, 249] which have been experimentally found in the case of  $\text{BaFe}_{12}\text{O}_{19}$  and  $\text{SrFe}_{12}\text{O}_{19}$  crystals [248].

The  $1/T^2$  low temperature variation found for the dielectric susceptibility of  $\text{Pb}_2\text{P}_2\text{S}_6$  close to the quantum critical point instead of the expected uniaxial behavior of  $1/T^3$  can be explained at first glance by a screening phenomenon in semiconductor materials of the  $\text{Sn}(\text{Pb})_2\text{P}_2\text{S}(\text{Se})_6$  system which weakens the electric dipole interaction. Such explanation is seen as appropriate for the above discussed critical behavior near the Lifshitz point in  $\text{Sn}_2\text{P}_2(\text{Se}_{0.28}\text{S}_{0.72})_6$  mixed crystal, which agrees with the theoretically predicted for systems with short – range interactions [43, 191]. But, for  $\text{Pb}_2\text{P}_2\text{S}_6$  crystals at low temperatures, the electric conductivity is very small (below  $10^{-14} \text{ Ohm}^{-1} \text{ cm}^{-1}$  [251]) and screening effects can't be effective with a low concentration of the free charge carriers.

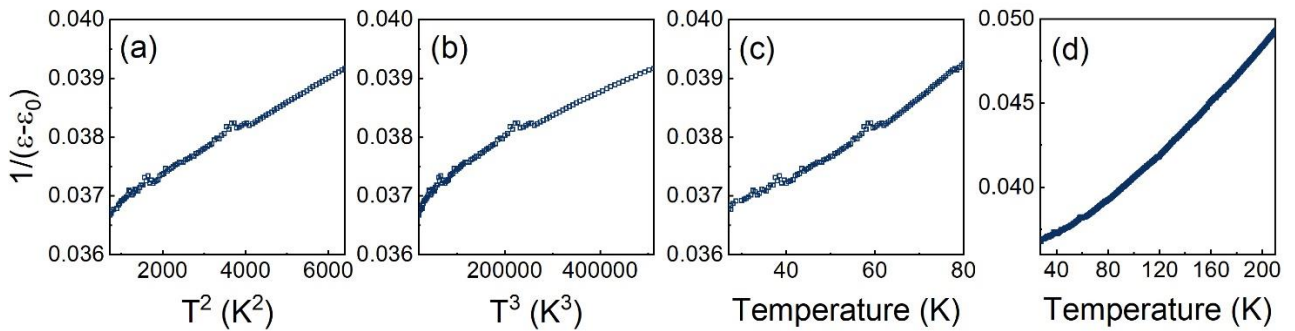


**Fig. 9.11.** Reciprocal dielectric susceptibility of  $\text{Pb}_2\text{P}_2\text{S}_6$  crystal as a function of temperature in different scales

As was already shown for  $\text{Sn}_2\text{P}_2\text{S}_6$  crystal in fig. 8.6 a, for  $\text{Pb}_2\text{P}_2\text{S}_6$  crystal (Fig. 9.12) the soft optic branch in the paraelectric phase is also flat: soft phonons frequency slightly changes with the increase of wave number and moves from the BZ center to the edge, where the crossing with acoustic phonon branches occurs [185]. On cooling to the continuous phase transition temperature  $T_0 \approx 337 \text{ K}$  for  $\text{Sn}_2\text{P}_2\text{S}_6$  crystal, in addition to the development of polar fluctuations near the BZ center, the antipolar fluctuations also strongly develop in the paraelectric phase. In the previous chapter we have shown that here the critical behavior can be described as a crossover between Ising and XY universality classes, what is expected near bicritical points with coupled polar and antipolar order parameters and competing instabilities in the reciprocal wave vectors space. A similar situation obviously exists in the quantum

paraelectric phase of  $\text{Pb}_2\text{P}_2\text{S}_6$  crystal, where on cooling down to 0 K the flat optic phonon branch softens across wide reciprocal space in Brillouin zone. Besides, the long wavelength polar fluctuations grow together with a development of short wavelength antipolar fluctuations and, therefore, their nonlinear coupling can modify the quantum critical behavior.

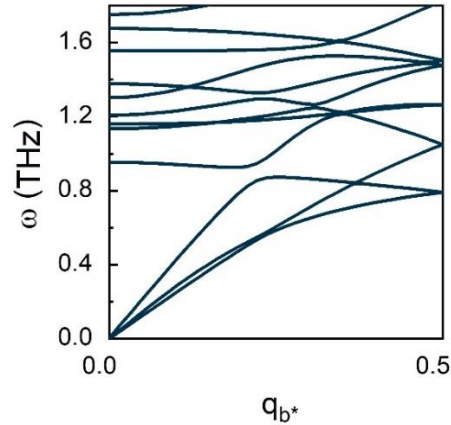


**Fig. 9.12.** Acoustic and soft optic phonon branches, calculated by GGA approach of DFT for  $\text{Pb}_2\text{P}_2\text{S}_6$  [158]

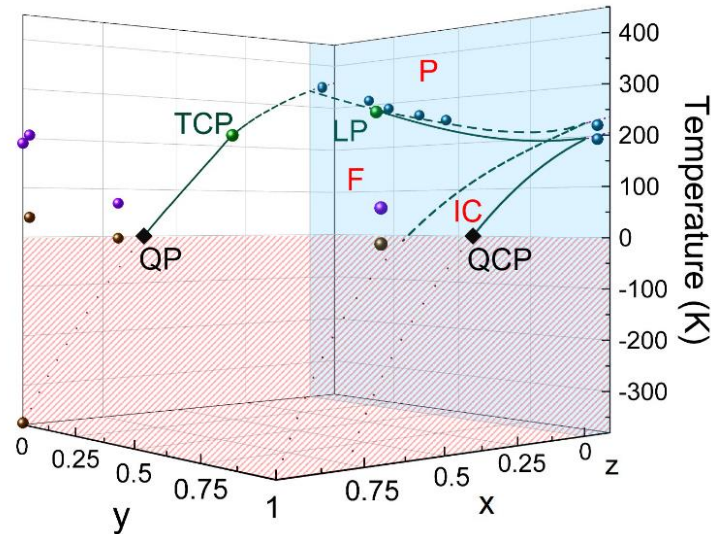


**Fig. 9.13.**  $T - x - y - z$  phase diagram for mixed crystals in  $\text{Sn}(\text{Pb})_2\text{P}_2\text{S}(\text{Se})_6$  system [56]. Dashed lines show the second order PTs, solid lines demonstrate the first order PTs. Blue spheres show the phase transitions in crystals with germanium according to data [191, 198] and own experimental data presented above. For crystals with quantum paraelectric state determined by equation 9.1 values of  $T_c$  (brown spheres) and  $T_l$  (violet triangles) are shown. Black rhombs denote quantum point (QP) and

quantum critical point (QCP). Paraelectric (P), ferroelectric (F) and incommensurate (IC) phases are also shown.

In Fig. 9.13 the  $T-x-y-z$  diagram for  $\text{Sn}(\text{Pb})_2\text{P}_2\text{S}(\text{Se})_6$  compounds is shown. Such diagram contains the information about the crystals with germanium. It is well seen that an increase in the Ge impurity decreases the width of the incommensurate phase. Our experimental data on  $(\text{Sn}_{0.95}\text{Ge}_{0.05})_2\text{P}_2(\text{Se}_{0.5}\text{S}_{0.5})_6$  crystal probably confirms it as at this concentration of selenium there is no any phase separation. In the cation sublattice germanium can only be introduced up to a certain quantity which corresponds to a solubility limit [200]. Thus, it is impossible to check it experimentally.

## 9.5. Conclusions

The dipole ordering temperature of  $\text{Sn}(\text{Pb})_2\text{P}_2\text{S}(\text{Se})_6$  materials may be tuned by chemical substitution realizing a ferroelectric quantum phase transition and quantum glassy or relaxor type phenomena in different parts of the phase diagram. The introduction of Ge impurity initiates several important phenomena: it increases the temperature of the phase transitions and improves the spontaneous polarization in the crystal; it doesn't shift the coordinate of the Lifshitz point  $y_{\text{LP}}$  in  $\text{Sn}_2\text{P}_2(\text{Se}_y\text{S}_{1-y})_6$  mixed crystals; it initiates a more pronounced critical anomaly in  $\text{Sn}_2\text{P}_2\text{S}_6$  crystals; it induces the appearance of a phase transition in the quantum paraelectric  $\text{Pb}_2\text{P}_2\text{S}_6$  and inhomogeneous polar ordering in  $(\text{Pb}_{0.7}\text{Sn}_{0.3})_2\text{P}_2\text{S}(\text{Se})_6$  crystals. The quantum fluctuations are destroyed in the mixed crystals, what follows from the comparison of the low temperature behavior of the thermal diffusivity and the complex dielectric susceptibility at different frequencies.

## Conclusions

In what follows, the most important results obtained in the study of the thermal properties and the critical behavior of the continuous second order PTs of  $MM'P_2(S,Se)_6$  ( $M, M' = Cu, Ag, In, Bi, Sn, Pb$ ) phosphorus chalcogenides by means of *ac* photopyroelectric calorimetry are presented:

1. It is found that in phosphorous layered crystals  $(Cu,Ag)^+(In,Bi)^{3+}P_2(Se,S)_6$ , at temperatures higher than the Debye temperature the thermal conductivity reaches extremely low values ( $\approx 0.2 \text{ W m}^{-1} \text{ K}^{-1}$ ) due to a strong anharmonicity of the crystal lattice caused by the relaxation of the lone electron pairs of stereoactive  $M^{3+}$  cations, the strong interaction between the soft optical and acoustic phonon branches, and the presence of a second order Jahn-Teller effect for copper cations. Significant thermal anisotropy was detected in the investigated layered ferroics, where the heat is transferred up to six times better along the structural layers than across them.
2. The thermal diffusivity data in  $CuBiP_2Se_6$  crystal confirm the presence of an intermediate structure-modulated phase between the low temperature antiferroelectric phase and the high temperature disordered one.
3. The substitution of copper by silver 10% in  $CuInP_2S_6$  changes the character of the PT from first order to second order. Such substitution also reduces the PT temperature by 30 K and frustrates the anomaly of thermal diffusivity, making it broader and shallower.
4. The results on the experimental research of thermal diffusivity for solids  $(Sn_{1-x}Pb_x)_2P_2(S_ySe_{1-y})_6$  with lead concentration  $x = 0.1, 0.2, 0.3$  and selenium  $y = 0.2$  indicate that the partial substitution of tin by lead (between  $x = 0.1$  and  $0.2$ ) has the consequence of changing the second-order PT line to a first-order PT line, which agrees with the theoretical predictions for the Blume-Emery-Griffiths

model, which describes the temperature-concentration (pressure) phase diagram for three-well potentials with spontaneous polarization fluctuations.

5. The obtained value of the critical exponent  $\alpha = 0.085$  for  $(\text{Sn}_{0.9}\text{Pb}_{0.1})_2\text{P}_2(\text{Se}_{0.2}\text{S}_{0.8})_6$  crystal indicates that the introduction of lead in the cationic sublattice leads to the appearance of strong random field defects which provoke the disappearance of the TCP; at decreasing the transition temperature to  $T_{TCP}$ , the nature of the first order PT is manifested. As a result, the critical behavior cannot be considered within the Tricritical universality class, and a Mean Field model is instead of application.
6. The topology of  $T - x - y$  phase diagram in the vicinity of tricritical Lifshitz point for  $(\text{Pb}_y\text{Sn}_{1-y})_2\text{P}_2(\text{Se}_x\text{S}_{1-x})_6$  solid solutions is established. Such diagram can be described with the combination of Blume-Emery-Griffiths model, which explains the TCP appearance at substitution of tin by lead in cationic sublattice, and the ANNNI model, which explains the appearance of Lifshitz point as well as the incommensurate phase at substitution of sulphur by selenium in anionic sublattice.
7. It is shown that the critical behavior of the anomaly of the inverse thermal diffusivity near the continuous PT in  $\text{Sn}_2\text{P}_2\text{S}_6$  crystal is well described as a crossover between Ising and XY universality classes, which is expected near a bicritical point with coupled polar and antipolar order parameters with the values:  $\alpha_{XY} = -0.0092 \pm 0.0008$  below  $T_0$  and  $\alpha_{ISING} = 0.1049 \pm 0.0066$  above  $T_0$ .
8. A substitution of the stereoactive tin cations by the more stereoactive germanium cations in  $(\text{Sn,Pb})_2\text{P}_2(\text{S,Se})_6$  compounds increases their thermal conductivity due to the increase of frequency of the lowest polar optic mode near BZ center which in turn diminishes the probability of the optical phonons resonance scattering by acoustic phonons. In  $(\text{Pb}_{0.7}\text{Sn}_{0.25}\text{Ge}_{0.05})_2\text{P}_2\text{S}(\text{Se})_6$  and  $(\text{Pb}_{0.7}\text{Sn}_{0.25}\text{Ge}_{0.05})_2\text{P}_2\text{S}(\text{Se})_6$  solid solutions germanium induces the dipole glass state in the temperature region of quantum fluctuations (at  $T < 50$  K).

## Bibliography

1. Glukhov K. Electronic Structure and Phase Transition in Ferroelectric  $\text{Sn}_2\text{P}_2\text{S}_6$  Crystal / K. E. Glukhov, K. V. Fedyo, Yu. M. Vysochanskii // International Journal of Molecular Sciences. – 2012. – V. 13(11). – P. 14356-14384.
2. Rushchanskii K. Ferroelectricity in  $(\text{Pb}_y\text{Sn}_{1-y})_2\text{P}_2\text{S}_6$  mixed crystals and random field BEG model / K. Z. Rushchanskii, R. M. Bilanych, A. A. Molnar, R. M. Yevych, A. A. Kohutych, S. I. Perechinskii, V. Samulionis, J. Banys, Y. M. Vysochanskii // Physica Status Solidi B. – 2016. – V. 253 No. 2. – P. 384-391.
3. Vysochanskii Yu. M. Raman spectroscopy study of the ferroelectricparaelectric transition in layered  $\text{CuInP}_2\text{S}_6$  / Yu. M. Vysochanskii, V. A. Stephanovich, A. A. Molnar, V. B. Cajipe, X. Bourdon // Physical Review B. – 1998. – V. 58, N 14. – P. 9119-9124.
4. Susner M. A. Metal Thio- and Selenophosphates as Multifunctional van der Waals Layered Materials / M. A. Susner, M. Chyasnovichyus, M. A. McGuire, P. Ganesh, P. Maksymovych // Advanced Materials. – 2017. – V. 29, I. 38. – P. 1602852(1–39).
5. Kleemann W. Magnetic and polar phases and dynamical clustering in multiferroic layered solid solutions  $\text{CuCr}_{1-x}\text{In}_x\text{P}_2\text{S}_6$  / W. Kleemann, V. V. Shvartsman, P. Borisov, J. Banys, Yu. M. Vysochanskii // Physical Review B. – 2011. – V. 84, – P. 094411(1–8).
6. Belianinov A.  $\text{CuInP}_2\text{S}_6$  Room Temperature Layered Ferroelectric / A. Belianinov, Q. He, A. Dziaugys, P. Maksymovych, E. Eliseev, A. Borisevich, A. Morozovska, J. Banys, Y. Vysochanskii, S.V. Kalinin // Nano Letters. – 2015. – V. 15, I. 6. – P. 3808-3814.
7. Wang F. Subthermionic field-effect transistors with sub-5 nm gate lengths based on van der Waals ferroelectric heterostructures / Feng Wang, Jia Liu, Wenhao

- Huang, Ruiqing Cheng, Lei Yin, Junjun Wang, Marshet Getaye Sendeku, Yu Zhang, Xueying Zhan, Chongxin Shan, Zhenxing Wang, Jun He // Science Bulletin. In press.
8. Howell J. R. Thermal Radiation Heat Transfer, 5th Edition / J. R. Howell, M. Pinar Menguc, R. Siegel // CRC Press, Taylor & Francis Group. – 2010. – P. 987.
  9. Levenspiel O. Engineering Flow and Heat Exchange / O. Levenspiel // Springer. – 1984. – P. 378.
  10. Carslaw H. S. Conduction of Heat in Solids / Carslaw H. S. Jaeger J. C. // London: Oxford University Press. – 1959. – P. 510.
  11. Salazar A. On thermal diffusivity / A. Salazar // European Journal of Physics. – 2003. – V. 24. – P. 351-358.
  12. Ioffe A.F. Physics of semiconductors / Ioffe A.F. // Academic Press inc. – 1960. – P. 436.
  13. Reissland J. A. The Physics of Phonons / J. A. Reissland // Wiley. – 1972. – P. 319.
  14. Feng T. Four-phonon scattering reduces intrinsic thermal conductivity of graphene and the contributions from flexural phonons / T. Feng, X. Ruan // Physical Review B. – 2018. – V. 97. – P. 045202(1-12).
  15. Ziman J.M. Electrons and Phonons: The Theory of Transport Phenomena in Solids / Ziman J.M. // Oxford: At the Clarendon Press. – 2001. – P. 576.
  16. Yang Q. S. Advanced heat transfer, 2nd edition / Q. S. Yang, B. Y. Pu // Shanghai Jiao Tong University Press. – 2001. (In Chinese)
  17. Rose A. Laser beam profile measurement by photothermal deflection technique / A. Rose, Y.-X. Nie, R. Gupta // Applied Optics. – 1986. – V. 25. – I. 11 – P. 1738-1741.
  18. Rose A. Pulsed photothermal deflection spectroscopy in a flowing medium: a quantitative investigation / A. Rose, R. Vyas, R. Gupta // Applied Optics. – 1986. – V. 24. – P. 4626-4643.

19. Bićanić D. Photoacoustic and Photothermal Phenomena III / D. Bićanić, // Photoacoustic and Photothermal Phenomena III. Springer Series in Optical Sciences. – 1992. – V. 69. – P. 732.
20. Thoen J. / Investigations of phase transitions in liquid crystals by means of adiabatic scanning calorimetry / J. Thoen, G. Cordoyiannis, C. Glorieux // Liquid Crystals – 2009. – V. 36. – P. 669-684.
21. Yao H. Nonadiabatic scanning calorimeter / H. Yao, K. Ema, C.W. Garland // Review of Scientific Instruments. – 1998. – V. 69. – P. 172-178.
22. Sullivan P. F. / Steady-state ac-temperature calorimetry / P.F. Sullivan, G. Seidel // Physical Review. – 1968. – V. 17. – No. 3. – P. 679-685.
23. Garland C.W. / High-resolution ac calorimetry and critical behavior at phase transitions / C.W. Garland // Thermochemica Acta. – 1985. – V. 88. – P. 127-142.
24. Birge N.O. / Specific-heat spectroscopy of the glass-transition / N.O. Birge, S.R. Nagel // Physical Review Letters. – 1985. – V. 54. – P. 2674-2677.
25. Huang C.C. / New experimental-technique for simultaneously measuring thermal-conductivity and heat-capacity / C.C. Huang, J.M. Viner, J.C. Novac // Review of Scientific Instruments. – 1985. – V. 56. – P. 1390-1393.
26. Mandelis A. / Theory of photopyroelectric spectroscopy of solids / A. Mandelis, M.M. Zver // Journal of Applied Physics. – 1985. – V. 57. – P. 4421-4430.
27. Zammit U. / Perspective: photopyroelectric effects and pyroelectric measurements: "Invited review article: photopyroelectric calorimeter for the simultaneous thermal, optical, and structural characterization of samples over phase transitions" / U. Zammit, M. Marinelli, F. Mercuri, S. Paoloni, F. Scudieri // Review of Scientific Instruments, – 2011. – V. 82. – No. 12. – P. 121101(1-4).
28. Mandelis A. Diffusion Waves and their Uses / Mandelis A // Physics Today. – 2000. – V. 53 – P. 29-34.

29. Mandelis A. Structure and the Reflectionless/Refractionless Nature of Parabolic Diffusion-Wave Fields / Mandelis A. Nicolaides L., Chen Y. – 2001. *Physical Review Letters*. – V. 87. – P. 020801(1-4).
30. Salazar A. / Energy propagation of thermal waves / A. Salazar // *European Journal of Physics*. – V. 2006. – V. 27. – No. 1. – P. 1349-1355.
31. Cattaneo C. A form of heat conduction equation which eliminates the paradox of instantaneous propagation / C. Cattaneo // *Comptes Rendus*. – 1958. – V. 247. – P. 431-433.
32. Almond D.P. / *Photothermal Science and Techniques* / D.P. Almond, P.M. Patel // Chapman & Hall. – 1996. – P. 241.
33. Massot M. Desarrollo y aplicación de la calorimetría fotopiroeléctrica al estudio de transiciones de fase / M. Massot // PhD thesis. – 2008. – P. 137.
34. Xu. Yu. Ferroelectric materials and their applications / Yu. Xu // Elsevier science Publishers. – 1991. – P. 406.
35. Hsu R. Synchrotron X-ray Studies of  $\text{LiNbO}_3$  and  $\text{LiTaO}_3$  / R. Hsu, E. N. Maslen, D. Du Boulay, N. Ishizawa // *Acta Crystallographica* – 1997. – V. B53. – P. 420-468.
36. Muralt P. Micromachined infrared detectors based on pyroelectric thin films / P. Muralt // Institute of Physics Publishing. *Reports on Progress in Physics*. – 2001 – V. 64. – P. 1339–1388.
37. Sullivan P.F. Steady-state ac-temperature calorimetry / P.F. Sullivan, G. Seidel // *Physical Review*. – 1968. – V. 17. No. 3. – P. 679-685.
38. Chirtoc M. Theory of the photopyroelectric method for investigation of optical and thermal materials properties / M. Chirtoc, G. Mihailescu // *Physical Review B*. – 1989. – V. 40. – P. 9606-9617.
39. Salazar A. / On the influence of the coupling fluid in photopyroelectric measurements / A. Salazar // *Review of Scientific Instruments*. – 2003. – V. 74. – No. 1. – P. 825-827.

40. Salazar A. / Overcoming the influence of the coupling fluid in photopyroelectric measurements of solid samples / A. Salazar, A. Oleaga // Review of Scientific Instruments. – 2012. – V. 83 – No. 1. – 014903(1-4).
41. Salazar A. On the influence of the coupling fluid in photopyroelectric measurements / A. Salazar // Review of Scientific Instruments. – 2003. – V. 74. – P. 825–827.
42. Delenclos S. A New Calibration Procedure for the Determination of Thermal Parameters and Their Temperature Dependence Using the Photopyroelectric Method / S. Delenclos, M. Chirtoc, A. Sahraoui, C. Kolinsky, J. Buisine // Analytical Sciences. – 2001. – V. 17. – P. s161-s164.
43. Oleaga A. Critical behavior near the Lifshitz point in  $\text{Sn}_2\text{P}_2(\text{S}_{1-x}\text{Se}_x)_6$  ferroelectric semiconductors from thermal diffusivity measurements / A. Oleaga, A. Salazar, A. Kohutych, Yu. Vysochanskii // Journal of Physics-Condensed Matter – 2011. – V. 23. – P. 025902(1-9).
44. Salazar A. On the piezoelectric contribution to the photopyroelectric signal / A. Salazar, A. Oleaga // Review of scientific instruments. – 2005. – V. 76. – P. 034901(1-4).
45. Landau L. D. Theoretical Physics. Statistical Physics / L. D. Landau, E. M. Lifshitz // Pergamon. Oxford. – 1980. – P. 544.
46. Landau L. On the Theory of Phase Transitions / Landau L. D. // Zh. Eksp. Teor. Fiz. – 1937. – V. 7. – P. 19–32.
47. Landau L. On the Theory of Phase Transitions / Landau L. D. // Phys. Z. Sowjet. – 1937. – V. 11 (545). – P. 26-35.
48. Landau L. D. On the Anomalous Absorption of Sound Near a Second-Order Phase Transition Point / L. D. Landau, I. M. Khalatnikov // Report of the Academy of Sciences of the USSR. – 1954. – V. 96. – P. 469-472.
49. Ginzburg V. L. The dielectric properties of crystals of seignettcelectric substances and of barium titanate / Ginzburg V. L. // Zh. Eksp. Teor. Fiz. – 1945. – V. 15. – P. 739-749.

50. Ginzburg V. L. Polarization and Piezoelectric Effect in BaTiO<sub>3</sub> Near the Ferroelectric Transition Point / Ginzburg V. L. // *Zh. Eksp. Teor. Fiz.* – 1949. – V. 19. – P. 36-41.
51. Ginzburg V.L. Some remarks on second order phase transitions and microscopic theory of ferroelectrics / V.L. Ginzburg // *Fiz. Tver. Tela.* – 1960. – V. 2. – P. 2031-2134.
52. Strukov B. A. Ferroelectric Phenomena in Crystals / Strukov B. A., Levanyuk A. P. // Springer-Verlag. – 1998. – P. 308.
53. Devonshire A. F. XCVI. Theory of barium titanate. Part I / Devonshire A. F. // *The London, Edinburgh, and Dublin Philosophical Magazine and Journal of Science.* – 1949. – V. 40. – P. 1040-1063.
54. Devonshire A. F. CIX. Theory of barium titanate. Part II / Devonshire A. F. // *The London, Edinburgh, and Dublin Philosophical Magazine and Journal of Science.* – 1951. – V. 42. – P. 1065-1079.
55. Valasek J. Piezo-Electric and Allied Phenomena in Rochelle Salt / Valasek J. // *Physical Review.* – 1921. – V. 17(4). – P. 475-481.
56. Vysochanskii Yu. M. Phase Transitions in Ferroelectric Phosphorous Chalcogenide Crystals / Yu. M. Vysochanskii, T. Janssen, R. Currat, R. Folk, J. Banys, J. Grigas, V. Samulionis // Vilnius University Publishing House. – 2006. – P. 453.
57. Khoma M. M. The mean-field analysis of Sn<sub>2</sub>P<sub>2</sub>(Se<sub>x</sub>S<sub>1-x</sub>)<sub>6</sub> thermodynamical properties in the paraelectric, incommensurate and ferroelectric phases / M. M. Khoma, A. A. Molnar, Yu. M. Vysochanskii // *Journal of Physical Studies.* – 1998. – V. 2. No. 4. – P. 524-535.
58. Levanyuk A. P. Defects and Structural Phase Transitions / A. P. Levanyuk, A. S. Sigov // Gordon and Breach Science Publishers. – 1988. – P. 222.
59. Isaverdiev A. A. Influence of defects on the properties of uniaxial ferroelectrics near the lifshitz point / A. A. Isaverdiev, N. Lebedev, A. P. Levanyuk, A. S. Sigov // *Ferroelectrics.* – 1991. – V. 117. – P. 135-139.

60. Isaverdiev A. A. Phase transition anomalies of physical properties of pyroelectrics and improper ferroelectrics with charged point defects / A. A. Isaverdiev, A. P. Levanyuk, A. S. Sigov // *Ferroelectrics*. – 1991. – V. 117. – P. 141-148.
61. Isaverdiyev A. Influence of point defects on the properties of ferroelectrics with one spontaneous polarization axis near the Lifshitz point / A. Isaverdiyev, N. Lebedev, A. Levanyuk, A. Sigov // *Fiz. Tverd. Tela*. – 1989. – V. 31. – P. 272-274.
62. Goldenfeld N. Lectures on Phase Transitions and the Renormalization Group, edited by David Pines / N. Goldenfeld // *Frontiers in Physics*. – 1992. – P. 420.
63. Fantoni R. Lectures on the renormalization group in statistical physics / R. Fantoni // *Universit`a Ca' Foscari Venezia*. – 2017. – P. 16.
64. Uzunov D. I. Introduction to the Theory of Critical Phenomena: Mean Field, Fluctuations and Renormalization / Dimo I. Uzunov // *World Scientific*. – 2010. – P. 673.
65. Guida R. Critical exponents of the N -vector model / R. Guida, J. Zinn-Justin // *Journal of Physics A: Mathematical and General*. – 1998. – V. 31. – No. 40. – P. 8103-8121.
66. Campostrini M. Critical behavior of the three-dimensional XY universality class / M. Campostrini, M. Hasenbusch, A. Pelisseto, P. Rossi, E. Vicari // *Physical Review B*. – 2001. – V. 63. – No. 21. – 214503(1-28).
67. Campostrini M. Critical exponents and equation of state of the three-dimensional Heisenberg universality class / M. Campostrini, M. Hasenbusch, A. Pelisseto, P. Rossi, and E. Vicari // *Physical Review B*. – 2002. – V. 65. – No. 3 – P. 144520(1-21).
68. Fisher M. E. Renormalization group in theory of critical behaviour / M. E. Fisher // *Reviews of Modern Physics*. – 1974. – V. 46. – No 4. – P. 597-616.
69. Folk R. Multicritical behavior in ferroelectrics / R. Folk // *Phase Transitions: A Multinational Journal*. – 1999. – V. 67. – No. 4. – P. 645-666.

70. Folk R. Critical dynamics: a field-theoretical approach / R. Folk, G. Moser // *Journal of Physics A: Mathematical and General*. 2006. – V. 39. No. 24. – P. 207-313.
71. Hohenberg P. Theory of dynamic critical phenomena / P. Hohenberg, B. Halperin // *Reviews of Modern Physics*. – 1977. – V. 49. – No 3. – P. 435-479.
72. Halperin B. Generalization of scaling laws to dynamical properties of a system near its critical point / B. Halperin, P. Hohenberg // *Physical Review Letters*. – 1967. – V. 19. – No. 12. – P. 700-703.
73. Halperin B. Renormalization-group treatment of critical dynamics of superfluid-helium, isotropic antiferromagnet, and easy-plane ferromagnet / B. Halperin, P. Hohenberg, E. Siggia // *Physical Review B*. – 1976. – V. 13. – No. 3. – P. 1299-1328.
74. Frey E. Critical-dynamics of magnets / E. Frey, F. Schwabl // *Advanced Physics*. – 1994. – V. 43. – No. 5. – 577-683.
75. Kadanoff L. Static phenomena near critical points - theory and experiment / L. Kadanoff, W. Götze, D. Hamblen, R. Hecht, E. Lewis, V. Palciauskas, M. Rayl, J. Swift // *Reviews of Modern Physics*. – 1967. – V. 39. – No. 2. – P. 395-431.
76. Lederman F. L. Experimental verification of scaling and test of the universality hypothesis from specific-heat data / F. L. Lederman, M. B. Salamon, L. W. Shacklette // *Physical Review B*. – 1974. – V. 9. – No. 7. – P. 2981-2988.
77. Pelisseto A. / Critical phenomena and renormalization-group theory / A. Pelisseto, E. Vicari // *Physics Reports*. – 2002. – V. 368. – No. 4. – P. 549-727.
78. Wilson K. The Renormalization Group and Critical Phenomena / Kenneth G. Wilson // *Reviews of Modern Physics*. – 1983. – V. 55. – No. 3. – P. 583-600.
79. Wilson K. The renormalization group and the  $\epsilon$  expansion / Kenneth G. Wilson, J. Kogut // *Physics Reports*. – 1974. – V. 12. – P. 75-199.
80. Falicov A. Tricritical and Critical End-Point Phenomena under Random Bonds / A. Falicov, A.N. Berker // *Physical Review Letters*. – 1996. – V. 76. – P. 4380-4383.

81. Wilson K. Critical Exponents in 3.99 Dimensions / K. Wilson, M. Fisher // *Physical Review Letters*. – 1972. – V. 28. – No 4. – P. 240-243.
82. Folk R. Lifshitz points in uniaxial ferroelectrics / R. Folk, G. Moser // *Physical Review B*. – 1993. – V. 47. – No. 21. – P. 13992-13997.
83. Abdel-Hadif A. Tricritical Lifshitz point in uniaxial ferroelectrics / A. Abdel-Hadif, R. Folk // *Physical Review B*. – 1996. – V. 54. – No. 6. – P. 3851-3860.
84. Dengler R. Renormalization group calculation of the critical exponents for the lifshitz tricritical point / R. Dengler // *Physical Letters*. – 1985. – V. 108A. – P. 269-271.
85. Nasser I. Specific-heat amplitude ratio near a Lifshitz point / I. Nasser, A. Abdel-Hady, R. Folk // *Physical Review B*. – 1997. – V. 56. – No. 1. – P. 154-160.
86. Pleimling M. Anisotropic Scaling and Generalized Conformal Invariance at Lifshitz Points / M. Pleimling, M. Henkel // *Physical Review Letters*. – 2001. – V. 87. – No. 12. – P. 125702(1-4).
87. Mo Z. Three-dimensional axial next-nearest-neighbor Ising model: A series investigation / Z. Mo, M. Ferer // *Physical Review B*. – 1991. – V. 43. – No. 13. – P. 10890-10904.
88. Garcia J. Accurate Monte Carlo critical exponents for Ising lattices / J. Garcia, J. A. Gonzalo // *Physica A*. – 2003. – V. 326. – P. 464-472.
89. Geldart D. J. W. Specific heat of nickel in the critical region / D. J. W. Geldart, G. Malmstrom // *Journal of Physics C Solid State Physics*. – 1982. – V. 15. – P. 5811-5819.
90. Kornblit A. Heat capacity of EuO near the Curie temperature / A. Kornblit, G. Ahlers // *Physical Review B*. – 1975. – V. 11. – No. 7. – P. 2678-2688.
91. Ahlers G. Universality of the specific heat of Heisenberg magnets near the critical temperature / G. Ahlers, A. Kornblit // *Physical Review B*. – 1975. – V. 12. – No. 5. – P. 1938-1946.

92. Vysochanskii Yu. Critical behaviour of uniaxial  $\text{Sn}_2\text{P}_2\text{S}(\text{Se})_6$  ferroelectrics / Yu. Vysochanskii, S. Perechinskii, V. Rizak, I. Rizak // *Ferroelectrics*. – 1993. – V. 143. – P. 59-66.
93. Molnar A. A. Relaxational change of the phase transition character in ferroelectrics-semiconductor / A. A. Molnar, Yu. M. Vysochanskii, A. A. Horvat, Yu. S. Nakonechnii // *Ferroelectrics*. – 1995. – V. 174. – P. 41-49.
94. Kohutych A. Sound behavior near the Lifshitz point in proper ferroelectrics / A. Kohutych, R. Yevych, S. Perechinskii, V. Samulionis, J. Banys, Yu. Vysochanskii // *Physical Review B*. – 2010. – V. 82. I. 5. – P. 054101(1-10).
95. Vysochanskii Y. M. Birefringence investigations of the  $\text{Sn}_2\text{P}_2(\text{Se}_x\text{S}_{1-x})_6$  uniaxial ferroelectrics behaviour near the lifshitz point / Y. M. Vysochanskii, V. V. Mitrovcij, A. A. Grabar, S. I. Perechinskii, S. F. Motrja, J. Kroupa // *Ferroelectrics*. – 2000. – V. 237. – P. 193-200.
96. Oleaga A. Thermal diffusivity and critical behaviour of uniaxial ferroelectric  $\text{Sn}_2\text{P}_2\text{S}_6$  / A. Oleaga, A. Salazar, M. Massot, and Y. M. Vysochanskii // *Thermochimica Acta*. – 2007. – V. 459. – P. 73-79.
97. Shvalya V. Thermal diffusivity and 3D-XY critical behavior of ferroelectric semiconductors  $(\text{Pb}_x\text{Sn}_{1-x})_2\text{P}_2\text{Se}_6$  / V. Shvalya, A. Oleaga, A. Salazar, A. A. Kohutych, Yu. M. Vysochanskii // *Journal of Physics and Chemistry of Solids*. – 2016. – V. 88. – P. 78–84.
98. Shvalya V. Critical behaviour study of ferroelectric semiconductors  $(\text{Pb}_x\text{Sn}_{1-x})_2\text{P}_2\text{S}_6$  from thermal diffusivity measurements / V. Shvalya, A. Oleaga, A. Salazar, A. A. Kohutych, Yu. M. Vysochanskii // *Thermochimica Acta*. – 2015. – V. 617. – P. 136–143.
99. Dziaugys A. Dipolar glass phase in ferrielectrics:  $\text{CuInP}_2\text{S}_6$  and  $\text{Ag}_{0.1}\text{Cu}_{0.9}\text{InP}_2\text{S}_6$  crystals / A. Dziaugys, J. Banys, J. Macutkevicius, R. Sobiestianskas, Yu. Vysochanskii // *Physica Status Solidi A*. – 2010. – V. 207. – P. 1960-1967.

100. Maisonneuve V. Ferrielectric ordering in lamellar  $\text{CuInP}_2\text{S}_6$  / V. Maisonneuve, V.B. Cajipe, A. Simon, R. Von Der Muhll, J. Ravez // *Physical Review B*. – 1997. – V. 56. – P. 10860-10868.
101. Vysochanskii Yu. M. Phase transitions in  $\text{CuInP}_2(\text{Se}_x\text{S}_{1-x})_6$  layered crystals / Yu. M. Vysochanskii, A. A. Molnar, M. I. Gurzan, V. B. Cajipe // *Ferroelectrics*. – 2001. – V. 257. – P. 147-154.
102. Dziaugys A. Phase transitions in  $\text{CuBiP}_2\text{Se}_6$  crystals / A. Dziaugys, J. Banys, J. Macutkevic, Yu. Vysochanskii, I. Pritz, M. Gurzan // *Phase Transitions*. – 2011. – V. 84: 2. – P. 147-156.
103. Dziaugys A. Conductivity spectroscopy of new  $\text{AgInP}_2\text{S}_6$  crystals / A. Dziaugys, J. Banys, J. Macutkevic and Yu. Vysochanskii // *Integrated Ferroelectrics*. – 2009. – V. 103. – P. 52-59.
104. Banys J. Dielectric and ultrasonic investigation of phase transition in  $\text{CuInP}_2\text{S}_6$  crystals / J. Banys, J. Macutkevic, V. Samulioniz, A. Brilingas, Y. Vysochanskii // *Phase Transition*. – 2004. – V. 77. – P. 345-358.
105. Studenyak I. P. Phase transitions and optical absorption edge in  $\text{CuInP}_2\text{Se}_6$  layered ferrielectrics / I. P. Studenyak, O. A. Mykajlo, V. O. Stephanovich, M. I. Gurzan, Y. M. Vysochanskii, V. B. Cajipe // *Physica Status Solidi A*. – 2003. – V. 198. – P. 487-494.
106. Wang X. Second-harmonic generation in quaternary atomically thin layered  $\text{AgInP}_2\text{S}_6$  crystals / X. Wang, K. Du, W. Liu, P. Hu, X. Lu, W. Xu, C. Kloc, Q. Xiong // *Applied Physics Letters*. – 2016. – V. 109. – P. 123103(1-5).
107. Mengwei S. Ferroelectric Field-Effect Transistors Based on  $\text{MoS}_2$  and  $\text{CuInP}_2\text{S}_6$  Two-Dimensional Van der Waals Heterostructure / S. Mengwei, P.Y. Liao, G. Qiu, Yu. Duan, P.D. Ye // *ACS Nano*. – 2018. – V. 12, I. 7. – P. 6700-6705.
108. Liubachko V. Anisotropic thermal properties and ferroelectric phase transitions in layered  $\text{CuInP}_2\text{S}_6$  and  $\text{CuInP}_2\text{Se}_6$  crystals / V. Liubachko, V. Shvalya, A. Oleaga, A. Salazar, A. Kohutych, A. Pogodin and Yu. M. Vysochanskii, *Journal of Physics and Chemistry of Solids*. – 2017. – V. 111. – P. 324-327.

109. Zheng Yi. Wafer-scale graphene/ferroelectric hybrid devices for low-voltage electronics / Yi Zheng, Guang-Xin Ni, Sukang Bae, Chun-Xiao Cong, Orhan Kahya, Chee-Tat Toh, Hye Ri Kim, Danho Im, Ting Yu, Jong Hyun Ahn, Byung Hee Hong, Barbaros Özyilmaz // *EPL (Europhysics Letters)*. –2011. – V. 93 (1). – P. 17002(1-4).
110. Hyeon Jun Hwang. Ferroelectric polymer-gated graphene memory with high speed conductivity modulation / Hyeon Jun Hwang, Jin Ho Yang, Young Gon Lee, Chunhum Cho, Chang Goo Kang, Soo Cheol Kang, Woojin Park, Byoung Hun Lee // *L. Nanotechnology* – 2013. – V. 24 (17). – P. 175202(1-6).
111. Lee S. General trends observed in the substituted thiophosphate family. Synthesis and structure of silver scandium thiophosphate,  $\text{AgScP}_2\text{S}_6$ , and cadmium iron thiophosphate,  $\text{CdFeP}_2\text{S}_6$  / S. Lee, P. Colombet, G. Ouvrard, R. Brec // *Inorganic Chemistry* – 1988. – V. 27. – P. 1291-1294.
112. Pfitzner A. Synthesis and Structure Determination of  $\text{AgScP}_2\text{Se}_6$ ,  $\text{AgErP}_2\text{Se}_6$  and  $\text{AgTmP}_2\text{Se}_6$  / A. Pfitzner, S. Seidlmayer // *Zeitschrift für anorganische und allgemeine Chemie*. – 2009. – V. 635. – P. 704-707.
113. Maisonneuve V. Room-temperature crystal structure of the layered phase  $\text{Cu}^{\text{I}}\text{n}^{\text{III}}\text{P}_2\text{S}_6$  / V. Maisonneuve, M. Evain, C. Payen, V.B. Cajipe, P. Molinié // *Journal of Alloys and Compounds*. – 1995. – V. 218. – P. 157-164.
114. Ouili Z. Crystal structure of a new lamellar compound:  $\text{Ag}_{12}\text{In}_{12}\text{PS}_3$  / Z. Ouili, A. Leblanc, P. Colombet // *Journal of Solid State Chemistry*. – 1987. – V. 66. – P. 86-94.
115. Colombet P. Structural aspects and magnetic properties of the lamellar compound  $\text{Cu}_{0.50}\text{Cr}_{0.50}\text{PS}_3$  / P. Colombet, A. Leblanc, M. Dannot, J. Rouxel // *Journal of Solid State Chemistry*. – 1982. – V. 41, I. 2. – P. 174-184.
116. Maisonneuve V. Low-temperature neutron powder diffraction study of copper chromium thiophosphate ( $\text{CuCrP}_2\text{S}_6$ ): observation of an ordered, antipolar copper sublattice / V. Maisonneuve, V. B. Cajipe, C. Payen // *Chemistry of Materials*. – 1993. – V. 5(6). – P. 758-760.

117. Colombet P. Coordinance inhabituelle de l'argent dans un sufur lamellaire a sous- reseau magnetique 1D: le compose  $\text{Ag}_{0.5}\text{Cr}_{0.5}\text{PS}_3$  / P. Colombet, A. Leblanc, M. Danot, J. Rouxel // *Nouveau Journal de Chimie.* – 1983. – V. 7. – P. 333-338.
118. Pfeiff R. Quaternary selenodiphosphates (IV):  $\text{M}^{\text{I}}\text{M}^{\text{III}}[\text{P}_2\text{Se}_6]$ , ( $\text{M}^{\text{I}} = \text{Cu}, \text{Ag}$ ;  $\text{M}^{\text{III}} = \text{Cr}, \text{Al}, \text{Ga}, \text{In}$ ) / R. Pfeiff, R. Kniep // *Journal of Alloys and Compounds.* – 1992. – V. 186. – P. 111-133.
119. Gave M. A. On the Lamellar Compounds  $\text{CuBiP}_2\text{Se}_6$ ,  $\text{AgBiP}_2\text{Se}_6$  and  $\text{AgBiP}_2\text{S}_6$ . Antiferroelectric Phase Transitions Due to Cooperative  $\text{Cu}^+$  and  $\text{Bi}^{3+}$  Ion Motion / M.A. Gave, D. Bilc, S.D. Mahanti, J.D. Breshears, M.G. Kanatzidis // *Inorganic Chemistry.* – 2005. – V. 44, I. 15. – P. 5293–5303.
120. Bercha D.M. Vibronic interaction in crystals with the Jahn-Teller centers in the elementary energy bands concept / D.M. Bercha, S.A. Bercha, K.E. Glukhov, M. Sznajder // *Condensed Matter Physics.* – 2015. – V. 18. No 3. – P. 33705(1-17).
121. Simon A. Paraelectric-Ferroelectric Transition in the Lamellar Thiophosphate  $\text{CuInP}_2\text{S}_6$  / A. Simon, J. Ravez, V. Maisonneuve, C. Payen, V. B. Cajipe // *Chemistry of Materials.* – 1994. – V. 6. – P. 1575-1580.
122. Durand E. Split model description of the copper site distribution in the new layered (2D) copper vanadium phosphorus sulfide ( $\text{CuIVIIIIP}_2\text{S}_6$ ) phase / E. Durand, G. Ouvrard, M. Evain, R. Brec // *Inorganic Chemistry.* – 1990. – V. 29. I. 24. – P. 4916-4920.
123. Néel L. Antiferromagnetism and Ferrimagnetism / Louis Néel // *Proceedings of the Physical Society A.* – 1952. – V. 65. No 11. – P. 859. The term is used in analogy with “ferrimagnetism,” a term suggested by L. Ne’el to describe magnetic behavior similar to that of ferrites which contain two unequal and oppositely directed magnetic sublattices.
124. Burdett J. K. From three- to four-coordination in copper(I) and silver(I) / Burdett J. K., Eisenstein O. // *Inorganic Chemistry.* – 1992. – V. 31. – P. 1758-1762.

125. Wei S. H. Off-Center Atomic Displacements in Zinc-Blende Semiconductor / Wei S. H., Zhang S., Zunger A. // *Physical Review Letters*. – 1993. – V. 70. – P. 1639-1642.
126. Fagot-Revurat Y. Interplay between electronic and crystallographic instabilities in the low-dimensional ferroelectric  $\text{CuInP}_2\text{Se}_6$  / Y. Fagot-Revurat, X. Bourdon, F. Bertran, V. B. Cajipe, and D. Malterre // *Journal of Physics: Condensed Matter*. – 2003. – V. 15. – P. 595-602.
127. Bercha D.M. Electron-Phonon Interaction as a Mechanism of Phase Transition in the  $\text{CuInP}_2\text{S}_6$  Crystal / D.M. Bercha, S.A. Bercha, K.E. Glukhov, M. Sznajder. *Acta Physica Polonica A*. – 2014. – V. 126. – P. 1143-1145.
128. Bourdon X. Copper sublattice ordering in layered  $\text{CuMP}_2\text{Se}_6$  ( $M=\text{In,Cr}$ ) / X. Bourdon, V. Maisonneuve, V.B. Cajipe, C. Payen, J.E. Fischer // *Journal of Alloys and Compounds*. – 1999. – V. 283. – P. 122–127.
129. Vysochanskii Yu. M. Dielectric measurement study of lamellar  $\text{CuInP}_2\text{Se}_6$ : successive transitions towards a ferroelectric state via an incommensurate phase? / Yu. M. Vysochanskii, A. A. Molnar, M. I. Gurzan, V. B. Cajipe, X. Bourdon // *Solid State Communications*. – 2000. – V. 115. – P. 13–17.
130. Dziaugys A. Anisotropy effects in thick layered  $\text{CuInP}_2\text{S}_6$  and  $\text{CuInP}_2\text{Se}_6$  crystals / A. Dziaugys, J. Banys, J. Macutkevicius, Y. Vysochanskii // *Phase Transition*. – 2013. – V. 86. – P. 878-885.
131. Macutkevicius J. Electrical conductivity of layered  $\text{CuInP}_2(\text{S}_x\text{Se}_{1-x})_6$  crystals / J. Macutkevicius, J. Banys, Y. Vysochanskii // *Physica Status Solidi B*. – 2015. – V. 252. – P. 1773-1777.
132. Dziaugys A. Piezoelectrically active domain walls in layered ferroelectric  $\text{CuInP}_2\text{Se}_6$  / A. Dziaugys, K. Kelley, J. A. Brehm, A. Puretzky, T. Feng, S. Neumayer, M. Chyashnikov, E. A. Eliseev, J. Banys, Yu. Vysochanskii, F. Ye, B. Chakoumakos, M. A. McGuire, S. V. Kalinin, G. Panchapakesan, S. T. Pantelides, N. Balke, A. N. Morozovska, P. Maksymovych // *Wiley-VCH*. – Preprint. – P. 1-32.

133. Dziaugys A. Dielectric Properties of New  $\text{AgInP}_2\text{Se}_6$  Crystals / A. Dziaugys, J. Banys, J. Macutkevic, Ju. Vysochanskii // *Ferroelectrics*. – 2009. – V. 391(1). – P. 151-157.
134. Babuka T. Structural, electronic, vibration and elastic properties of the layered  $\text{AgInP}_2\text{S}_6$  semiconducting crystal – DFT approach / T. Babuka, K. Glukhov, Y. Vysochanskii, M. Makowska-Janusik // *RSC Advances*. – 2018. – V. 8. – P. 6965(1-13).
135. Villars P. Pauling File in: *Inorganic Solid Phases*, SpringerMaterials (online database), Springer, Heidelberg (ed.) SpringerMaterials  $\text{AgIn}[\text{P}_2\text{Se}_6]$  Crystal Structure / Villars P. // Springer-Verlag. – 2016.
136. Samulioniz V. Piezoelectric and Ultrasonic Studies of New Lamellar Crystals of  $\text{CuInP}_2\text{S}_6$  Type / V. Samulioniz, J. Banys, A. Dziaugys, M. I. Gurzan, I. P. Pritz, Y. Vysochanskii // *Ferroelectrics*. – 2011. – V. 419. – P. 97-102.
137. Xu Bo. Monolayer  $\text{AgBiP}_2\text{Se}_6$ : an atomically thin ferroelectric semiconductor with out-plane polarization / Bo Xu, Hui Xiang, Yidong Xia, Kun Jiang, Xiangang Wan, Jun He, Jiang Yin, Zhiguo Liua // *Nanoscale*. – 2017. – V. 9. – P. 8427-8434.
138. Shusta V. S. Dielectric properties of  $\text{CuInP}_2\text{S}_6$  crystals under high pressure / V. S. Shusta, I. P. Prits, P. P. Guranich, E. I. Gerzanich, A. G. Slivka // *Condensed Matter Physics*. – 2007. – V. 10. No. 1(49). – P. 91-94.
139. Džiaugys A. Dielectric and ultrasonic studies of new  $\text{Ag}_{0.1}\text{Cu}_{0.9}\text{InP}_2\text{S}_6$  layered ferroelectric compound / A. Džiaugys, J. Banys, V. Samulionis, Y. Vysochanskii // *Ultragarsas*. – 2008. – V. 63. No.3. – P. 7-10.
140. Macutkevic J. Broadband dielectric spectroscopy of  $\text{CuInP}_2\text{Se}_6$  crystals / J. Macutkevic, J. Banys, Yu. Vysochanskii // *Physica Status Solidi (a)*. – 2009. – V. 206, – P. 167-172.
141. Macutkevic J. Asymmetric phase diagram of mixed  $\text{CuInP}_2(\text{S}_x\text{Se}_{1-x})_6$  crystals / J. Macutkevic, J. Banys, R. Grigalaitis, Yu. Vysochanskii // *Physical Review B*. – 2008. – V. 78. – P. 064101(1-9).

142. Samulionis V. Piezoelectric and elastic properties of layered materials of  $\text{Cu}(\text{In,Cr})\text{P}_2(\text{S,Se})_6$  system / V. Samulionis, J. Banys, Yu. Vysochanskii // *Journal of Electroceramics*. – 2009. – V.22. – P. 192–197.
143. Samulionis V. Ultrasonic and Piezoelectric Studies of Phase Transitions in Two-Dimensional  $\text{CuInP}_2\text{S}_6$  Type Crystals / V. Samulionis, J. Banys, Y. Vysochanskii // *Ferroelectrics*. – 2009. – V. 379. – P. 69–76.
144. Samulionis V. Piezoelectric and Ultrasonic Studies of Mixed  $\text{Ag}_x\text{Cu}_{1-x}\text{InP}_2(\text{S,Se})_6$  Layered Crystals / V. Samulionis, J. Banys, Y. Vysochanskii, *Materials Science Forum*. – 2010. V. 636-637. – P. 398-403.
145. Beley L.M. Thermodynamic Properties of Ferroelectric Crystals  $\text{CuInP}_2(\text{Se}_x\text{S}_{1-x})_6$  / L.M. Beley // PhD thesis. Uzhhorod. – 2007.
146. Moriya K. The Heat Capacity of  $\text{CuInP}_2\text{Se}_6$ , a Layer-Structured Selenodiphosphate / K. Moriya, N. Kariya, I. Pritz, Yu. M. Vysochanskii, A. Inaba, T. Matsuo // *Ferroelectrics*. – 2007. – V. 346. – P. 143-148.
147. Grabar A. A. Photorefractive Materials and Their Applications, V.2 “Photorefractive effects in  $\text{Sn}_2\text{P}_2\text{S}_6$ ” / A. A. Grabar, M. Jazbinšek, A. N. Shumelyuk, Yu. M. Vysochanskii, G. Montemezzani, P. Günter // Springer. Springer Series in Optical Sciences. – 2007. – V. 114. – P. 327-362.
148. Mys O. On the acoustooptic efficiency of  $\text{Pb}_2\text{P}_2\text{Se}_6$  crystals. Acoustic and thermal studies / O. Mys, I. Martynyuk-Lototska, A.M. Kostruba, A. Grabar, R. Vlokh // *Ukrainian Journal of Physical Optics*. – 2012. – V. 13. – P. 177-182.
149. Ovsyannikov S. V. Tuning the electronic and vibrational properties of  $\text{Sn}_2\text{P}_2\text{Se}_6$  and  $\text{Pb}_2\text{P}_2\text{S}_6$  crystals and their metallization under high pressure / S. V. Ovsyannikov, N. V. Morozova, I. V. Korobeinikov, V. Haborets, R. Yevych, Yu. Vysochanskii, V. V. Shchennikov // *Dalton Transactions*. – 2017. – V. 46. – P. 4245-4258.
150. Voroshilov Yu. Peculiarities of structure and phase transitions in crystals  $\text{Sn}(\text{Pb})_2\text{P}_2\text{S}(\text{Se})_6$  / Voroshilov Yu., Vysochanskii Yu., Grabar A., Potorii M., Pritz I., Rizak V., Seykovskaya L., Slivka V., Yatsenko A. // – 1990. *Ukr. Fiz. Zh.* – V. 35. – P. 71-75.

151. Voroshilov Yu. Crystalstructure of  $\text{Sn}_2\text{P}_2\text{Se}_6$  / Yu. Voroshilov, M. Potorii, L. Seykovskaya, A. Yatsenko, I. Pritz // *Kristallografiya* – 1988. – V. 33. – No. 5. – P. 1282-1283.
152. Dittmar G. Die Struktur des Di-Zinn-Hexathiohypo-diphosphats  $\text{Sn}_2\text{P}_2\text{S}_6$  / G. Dittmar, H. Shafer // *Zs. Naturforsch.* – 1974. – V. 296. – P. 312-317.
153. Carpentier C. D. Vapour growth and crystal data of the thio (seleno) hypodiphosphates  $\text{Sn}_2\text{P}_2\text{S}_6$ ,  $\text{Sn}_2\text{P}_2\text{Se}_6$ ,  $\text{Pb}_2\text{P}_2\text{S}_6$ ,  $\text{Pb}_2\text{P}_2\text{Se}_6$  and their mixed crystals / C. D. Carpentier, R. Nitsche // *Materials Research Bulletin.* – 1974. – V. 9. – P. 401-410.
154. Scott B. High temperature crystal structure and DSC of  $\text{Sn}_2\text{P}_2\text{S}_6$  B. Scott, M. Pressprich, R.D. Willit, D.A. Cleary J. *Solid State Chem.* – 1992. – V. 96. – P. 294-300.
155. Kuepper K. Electronic structure of  $\text{Sn}_2\text{P}_2\text{S}_6$  / K. Kuepper, B. Schneider, V. Caciuc, and M. Neumann, A. V. Postnikov, A. A. Grabar, Yu. M. Vysochanskii // *Physical Review B.* – 2003. – V. 67. – P. 115101(1-7).
156. Curro G.M. An X-ray photoemission spectroscopy study of the  $\text{Sn}_2\text{P}_2\text{S}_6$  monoclinic II phase G.M. Curro, V. Grasso, F. Neri, L. Silipigni // *Nuovo Cimento D.* – 1998. – V. 20. – P. 1163-1170.
157. Baltrunas D. Temperature investigations of the ferroelectric crystals  $\text{Sn}_2\text{P}_2\text{S}_6$  and  $\text{Sn}_2\text{P}_2\text{Se}_6$  by means of  $^{119}\text{Sn}$  Mössbauer spectroscopy / D. Baltrunas, A. Grabar, K. Mazeika, Y. Vysochanskii // *Journal of Physics: Condensed Matter.* – 1999. – V. 11. – P. 2983-2992.
158. Yevych R. Valence fluctuations in  $\text{Sn}(\text{Pb})_2\text{P}_2\text{S}_6$  ferroelectrics / R. Yevych, V. Haborets, M. Medulych, A. Molnar, A. Kohutysh, A. Dziaugys, Ju. Banys, Yu. Vysochanskii // *Low Temperature Physics.* – 2016. – V. 42. No. 12. – P. 1155-1162.
159. Enjalbert R. Structural study of the ferroelectric instability in  $\text{Sn}_2\text{P}_2\text{Se}_6$  / R. Enjalbert, J. Galy, Yu. Vysochanskii, A. Ouedraogo, P. Saint-Gregoire // *European Physical Journal B.* – 1999. – V. 8. – P. 169-177.

160. Gomonnay A. The splitting of phase transitions in ferroelectric solid solutions of  $\text{Sn}_2\text{P}_2(\text{Se}_x\text{S}_{1-x})_6$  / A. Gomonnay, A. Grabar, Yu. Vysochanskii, A. Belyaev, V. Machulin, M. Gurzan, V. Slivka // *Fiz. Tv. Tela.* –1981. – V. 23. – No. 12. – P. 3602-3606.
161. Barsamian T. Incommensurate phase in proper ferroelectric  $\text{Sn}_2\text{P}_2\text{Se}_6$  / T. Barsamian, S. Khasanov, V. Shekhtman, Yu. Vysochanskii, V. Slivka // *Fiz. Tv. Tela.* – 1985. – V. 27. – No. 11. – P. 3327-3331.
162. Barsamian T. Diffraction analysis of incommensurate phases in crystals of quasi-binary system  $\text{Sn}_2\text{P}_2(\text{S}_{1-x}\text{Se}_x)_6$  / T. Barsamian, S. Khasanov, V. Shekhman // *Ferroelectrics.* – 1993. – V. 138. – No. 1. – P. 63-77.
163. Israel R. Crystal structures of di-tinhexa(seleno)hypodiphosphate,  $\text{Sn}_2\text{P}_2\text{Se}_6$ , in the ferroelectric and paraelectric phase / R. Israel, R. Gelder, J. Smits, P. Beurskens, S. W. H. Eijt, T. Rasing, H. van Kempen, M. Maior, S. Motrija // *Z. Kristallographie.* – 1998. – V. 213. – P. 34-41.
164. Vysochanskii Yu. M. Concentration dependencies of temperatures and character of phase transitions in  $(\text{Pb}_y\text{Sn}_{1-y})_2\text{P}_2\text{S}_6$  and  $(\text{Pb}_y\text{Sn}_{1-y})_2\text{P}_2\text{Se}_6$  / Yu. M. Vysochanskii, M. I. Gurzan, M. M. Maior, S. F. Motrja, S. I. Perechinskii, M. V. Potorij, L. A. Salo, M. M. Khoma, V. Yu. Slivka, Yu. V. Voroshilov // *Soviet physics, Solid state.* – 1984. – V. 23. No.3. – P. 858-864.
165. Villars P. Pauling File in: *Inorganic Solid Phases*, SpringerMaterials (online database), Springer, Heidelberg (ed.) SpringerMaterials  $\text{Pb}_2\text{P}_2\text{S}_6$  ( $\text{PbPS}_3$  ht) Crystal Structure / Villars P. // Springer-Verlag. – 2016.
166. Xu Ya. Role of Stoichiometry in the Growth of Large  $\text{Pb}_2\text{P}_2\text{Se}_6$  Crystals for Nuclear Radiation Detection / Yadong Xu, Xu Fu, Hongjian Zheng, Yihui He, Wenwen Lin, Kyle M. McCall, Zhifu Liu, Sanjib Das, Bruce W. Wessels, Mercuri G. Kanatzidis // *ACS Photonics.* – 2018. – V. 5. – P. 566-573.
167. Becker R. Kristallstruktur und Schwingungsspektren des Di-BleiHexathiohypodiphosphates  $\text{Pb}_2\text{P}_2\text{S}_6$  / R. Becker, W. Brockner // *Z. Naturforsch.* – 1983. – V. 38a. – P. 874-879.

168. Prits I. Phase equilibria in the Pb-P-S(Se) systems / I. Prits, M. Potorii, Y. Voroshilov / *Ukrainskii Khimichnyi Zhurnal*. – 1989. – V. 55. – No. 2. – P. 25-27.
169. Gerzanich E. I. Optical properties of  $A_2^{IV}B_2^VC_6^{VI}$  ferroelectrics-semiconductors the effect of temperature and hydrostatic pressure / Gerzanich E. I. // *Ukr. J. Phys. Opt.* – 2008. – V. 9. – No. 3. – P. 129-163.
170. Slivka A. G. Effect of isomorphous substitution and external hydrostatic pressure on the fundamental optical absorption edge of  $\text{Sn}(\text{Pb})_2\text{P}_2\text{S}(\text{Se})_6$  crystals / Slivka A. G., Gerzanich E. I., Shusta V. S. and Guranich P. P. // *Izv. Vuzov. Ser. Fiz.* – 1999. – V. 9. – P. 23–28.
171. Moriya K. Dielectric Studies of Ferroelectric Phase Transitions in  $\text{Pb}_{2x}\text{Sn}_{2(1-x)}\text{P}_2\text{S}_6$  Single Crystals / K. Moriya, K. Iwauchi, M. Ushida, A. Nakagawa, K. Watanabe, S. Yano, S. Motojima, Y. Akagi // *Journal of the Physical Society of Japan*. – 1995. – V. 64, No. 5. – P. 1775-1784.
172. Barsamian T. K. Incommensurate phase in proper ferroelectric  $\text{Sn}_2\text{P}_2\text{Se}_6$  / T. K. Barsamian, S. S. Khasanov, V. S. Shekhtman, Y. M. Vysochanskii, V. Y. Slivka // *Ferroelectrics*. – 1986. – V. 67. – P. 47-54.
173. Vysochanskii Yu. M. Influence of defects and conductivity on the Phase Transitions and the domain structure properties in ferroelectric-semiconductors  $\text{Sn}_2\text{P}_2\text{S}(\text{Se})_6$  / Yu. M. Vysochanskii, A. A. Molnar, M. M. Khoma // *Ferroelectrics*. – 1999. – V. 223. – P. 19-26.
174. Vysochanskii Yu. M. The tricritical Lifshitz point on the phase diagram of  $\text{Sn}_2\text{P}_2(\text{Se}_x\text{S}_{1-x})_6$  ferroelectrics / Yu. M. Vysochanskii, M. M. Mayor, V. M. Rizak, V. Yu. Slivka, M. M. Khoma // *Sov. Phys. JETP*. – 1989. – V. 68. No. 4. – P. 782-787.
175. Moriya K. Ferroelectric Phase Transitions in  $\text{Pb}_{2x}\text{Sn}_{2(1-x)}\text{P}_2\text{Se}_6$  System / K. Moriya, T. Yamada, K. Sakai, S. Yano, S. Baluja, T. Matsuo, I. Pritz, Y. M. Vysochanskii. // *Journal of Thermal Analysis and Calorimetry*. – 2002. – V. 70. – P. 321-328.

176. Moriya K. Low-temperature thermal properties of  $\text{Pb}_2\text{P}_2\text{Se}_6$  and  $\text{Pb}_{1.424}\text{Sn}_{0.576}\text{P}_2\text{Se}_6$  / K. Moriya, T. Yamada, S. Baluja, T. Matsuo, I. Pritz d, Yu. M. Vysochanskii // *Thermochimica Acta.* – 2003. – V. 403. – P. 153-160.
177. Major M. The heat capacity and linear expansion of crystals  $\text{Sn}_2\text{P}_2(\text{Se}_x\text{S}_{1-x})_6$  in the field of phase transitions / M. Major, B. Koperles, B. Savchenko, M. Gurzan, O. Morozova, N. Korda // *Fiz. Tver. Tela.* – 1983. – V. 25. – P. 214-223.
178. Moriya K. Ferroelectric Phase Transitions in  $\text{Sn}_2\text{P}_2\text{S}_6$  and  $\text{Sn}_2\text{P}_2\text{Se}_6$  Crystals, / K. Moriya, K. Iwauchi, M. Ushida, A. Nakagawa, K. Watanabe, S. Yano, S. Motojima, Y. Akagi // *Journal of the Physical Society of Japan.* – 1998. – V. 67, No. 10. – P. 3505-3511.
179. Vysochanskii Yu. The model of phase transitions in  $\text{Sn}_2\text{P}_2\text{S}_6$  ferrosemiconductor and their lattice dynamics / Yu. Vysochanskii, V. Slivka, Yu. Voroshilov // *Fiz. Tverd. Tela,* 1979. – V. 21. – № 8. – P. 2402-2408.
180. Vysochanskii Yu. M. Lifshitz point on the state diagram of ferroelectrics / Yu. M. Vysochanskii, V. Yu. Slivka// *Usp. Fiz. Nauk.* – 1992. – V. 162. No. 2. – P. 139-160.
181. Bilanych R. M. Elastic properties of  $(\text{Pb}_y\text{Sn}_{1-y})_2\text{P}_2\text{S}_6$  solid solutions / R. M. Bilanych, R. M. Yevych, A. A. Kohutyach, S. I. Perechinskii, I. M. Stoika, Yu. M. Vysochanskii // *Central European Journal of Physics.* – 2014. – V. 12. – P. 611-614.
182. Kohutyach A. Acoustic attenuation in ferroelectric  $\text{Sn}_2\text{P}_2\text{S}_6$  crystals / A. Kohutyach, R. Yevych, S. Perechinskii, Yu. Vysochanskii // *Central European Journal of Physics.* – 2010. – V. 8. No. 6. – P. 905-914.
183. Rushchanskii K. Z. Observation of nonequilibrium behavior near the Lifshitz point in ferroelectrics with incommensurate phase / K. Z. Rushchanskii, A. Molnar, R. Bilanych, R. Yevych, A. Kohutyach, Yu. M. Vysochanskii // *Physical Review B.* – 2016. – V. 93. I. 1. – P. 014101(1-12).
184. Vysochanskii Yu.M. Phase transitions in crystals  $\text{Sn}_2\text{P}_2\text{S}_6$  / Yu. M. Vysochanskii, M.M. Maior, B.M. Koperles, M.I. Gurzan // *Fiz. Tverd. Tela.* – 1984. – V. 26. No. 3. – P. 690-695.

185. Eijt S. W. H. Soft modes and phonon interactions in  $\text{Sn}_2\text{P}_2\text{Se}_6$  studied by means of neutron scattering / S. W. H. Eijt, R. Currat, J. E. Lorenzo, P. SaintGrégoire, S. Katano, T. Janssen, B. Hennion, Y. M. Vysochanskii // *Journal of Physics: Condensed Matter*. – 1998. – V. 5. – P. 169–178.
186. Vysochanskii Yu. M. Critical behavior of  $\text{Sn}_2\text{P}_2(\text{Se}_x\text{S}_{1-x})_6$  uniaxial ferroelectrics near the Lifshitz point / Yu. M. Vysochanskii, V. G. Furtsev, M. M. Khoma, A. A. Grabar, M. I. Gurzan, M. M. Maior, S. I. Perechinskii, V. M. Rizak, V. Yu. Slivka // *Journal of Experimental and Theoretical Physics*. – 1986. – V. 91. No. 4. – P. 1384-1390.
187. Rizak. I. M. Lifshitz points line on the state diagram  $(\text{Pb}_y\text{Sn}_{1-y})_2\text{P}_2(\text{Se}_x\text{S}_{1-x})_6$  / I. M. Rizak, V. M. Rizak, M. I. Gurzan, S. I. Perechinskii, Yu. Vysochanskii, V. Yu. Slivka // *Ukr. Fiz. J.* – 1993. – V. 38. No. 5. – P. 67-70.
188. Michelson A.P. Phase diagrams near the Lifshitz point. I. Uniaxial magnetization / A.P. Michelson // *Physical Review B*. – 1977. – V. 16. – P. 577-584.
189. Rushchanskii K. Ferroelectricity, nonlinear dynamics and relaxation effects in monoclinic  $\text{Sn}_2\text{P}_2\text{S}_6$  / K. Rushchanskii, Yu. Vysochanskii, D. Strauch // *Physical Review Letters*. – 2007. – V. 99. – P. 207601(1-4).
190. Blume M. Ising Model for the  $\lambda$  Transition and Phase Separation in He3 -He4 Mixtures / M. Blume, V.J. Emery, R.B. Griffiths // *Physical Review A*. – 1971. – V. 4. I. 3 – P. 1071-1077.
191. Oleaga A. In search of a tricritical Lifshitz point in  $\text{Sn}_2\text{P}_2(\text{S}_{1-x}\text{Se}_x)_6$  doped with Pb, Ge: A critical behavior study / A. Oleaga, V. Shvalya, A. Salazar, I. Stoika, Yu. M. Vysochanskii // *Journal of Alloys and Compounds*. – 2017. – V. 694. – P. 808-814.
192. Ondrejko P. An x-ray scattering study of  $\text{Sn}_2\text{P}_2\text{S}_6$ : absence of incommensurate phase up to 1 GPa / P. Ondrejko, M. Guennou, M. Kempa, Y. Vysochanskii, G. Garbarino, J. Hlinka // *Journal of Physics: Condensed Matter*. – 2013. – V. 25. No. 11. – P. 115901(1-5).

193. Andersson O. Tricritical Lifshitz point in the temperature-pressure-composition diagram for  $(\text{Pb}_y\text{Sn}_{1-y})_2\text{P}_2(\text{Se}_x\text{S}_{1-x})_6$  ferroelectrics / O. Andersson, O. Chobal, I. Rizak, V. Rizak // *Physical Review B*. – 2009. – V. 80. – P. 174107(1-5).
194. Zapeka B. Critical Behavior of  $\text{Sn}_2\text{P}_2\text{S}_6$  and  $\text{Sn}_2\text{P}_2(\text{Se}_{0.28}\text{S}_{0.72})_6$  Crystals under High Hydrostatic Pressures / Zapeka B., Kostyrko M., Martynyuk-Lototska I. and Vlokh R. // *Philosophical Magazine*. – 2015. – V. 95. – I.4. – P. 382-393.
195. Shvalya V. / Electron-phonon anharmonicity and low thermal conductivity in phosphorous chalcogenide ferroelectrics / V. Shvalya, A. Oleaga, A. Salazar, A. Kohutych, Yu. M. Vysochanskii // *Material Express*. – 2017. – V. 7. – No. 5. – P. 361-368.
196. Baltrunas D. / Mossbauer spectroscopy of the phase transitions in the ferroelectric system  $\text{Sn}(\text{Pb})_2\text{P}_2\text{S}(\text{Se})_6$  / D. Baltrunas, K. Mazeika, Yu. Vysochanskii, A. Grabar, V. Slivka // *Ferroelectrics*. – 1995. – V. 165. – P. 359-368.
197. Mys O. / Thermal expansion of  $\text{Pb}_2\text{P}_2\text{Se}_6$  crystals / O. Mys, I. Girnyk, A. Grabar, I. Martynyuk-Lototska, M. Kostyrko, R. Vlokh // *Ukr. J. Phys. Opt.* – 2013. – V. 14. – No. 4. – P. 219-224.
198. Shvalya V. Influence of dopants on the thermal properties and critical behavior of the ferroelectric transition in uniaxial ferroelectric  $\text{Sn}_2\text{P}_2\text{S}_6$  / V. Shvalya, A. Oleaga, A. Salazar, I. Stoika and Yu. M. Vysochanskii // *Journal of Materials Science*. – 2016. – V. 51. – P. 8156-8167.
199. Grigas J. XPS of Impurities Influence on Electronic Structure of  $\text{Sn}_2\text{P}_2\text{S}_6$  Ferroelectrics / J. Grigas, E. Talik, K. Glukhov, K. Fedyo, I. Stoika, M. Gurzan, I. Prits, A. Grabar, Yu. Vysochanskii // *Ferroelectrics* – 2011. – V. 418. – P. 134-142.
200. Maior M. M. Effect of Germanium Doping on Pyroelectric and Piezoelectric Properties of  $\text{Sn}_2\text{P}_2\text{S}_6$  Single Crystal / M. M. Maior, M. I. Gurzan, Sh. B. Molnar, I. P. Prits, Yu. M. Vysochanskii // *IEEE Transactions on Ultrasonics, Ferroelectrics, and Frequency Control*. – 2000. – V. 47. – P. 877-880.
201. Potorii M. V. Phase equilibrium in systems involving tetra-type compounds  $\text{Me}^I\text{Me}^{III}\text{P}_2\text{S}_6(\text{Se}_6)$ , where  $\text{Me}^I$  – Cu, Ag;  $\text{Me}^{III}$  – In, Cr. / M. V. Potorii, P. M. Mylian,

- S. F. Motria, V. V. Tovt, S. M. Hasynets // *Physics and chemistry of solid state.* – 2015. – V. 16, No 2. – P. 327-334.
202. Altomare A. A new tool for crystal structure determination and refinement / A. Altomare, M. C. Burla, M. Camalli, B. Carrozzini, G. Cascarano, C. Giacovazzo, A. Guagliardi, A.G.G. Moliterni, G. Polidori, R. Rizzi // *Journal of Applied Crystallography.* – 1999. – V. 32. – P. 115-119.
203. Altomare A. EXPO2013: A kit of tools for phasing crystal structure from powder data / A. Altomare, C. Cuocci, C. Giacovazzo, A.G.G. Moliterni, R. Rizzi, N. Corriero, A. Falcicchio // *Journal of Applied Crystallography.* – 2013. – V. 46. – P. 1231-1235.
204. Kohn W. Self-Consistent Equations Including Exchange and Correlation Effects / W. Kohn, L. J. Sham // *Physical Review Journals A.* – 1965. – V. 140. – P. 1133-1138.
205. Gonze X. Recent developments in the ABINIT software package / X. Gonze, F. Jollet, F. Abreu Araujo, D. Adams, B. Amadon, T. Applencourt, C. Audouze, J. M. Beuken, J. Bieder, A. Bokhanchuk, E. Bousquet, F. Bruneval, D. Caliste, M. Côté, F. Dahm, F. Da Pieve, M. Delaveau, M. Di Gennaro, J.W.Zwanziger // *Computer Physics Communications.* – 2016. – V. 205. – P. 106-131.
206. Lee Ch. Ab initio calculation of the thermodynamic properties and atomic temperature factors of SiO<sub>2</sub>  $\alpha$ -quartz and stishovite / Ch. Lee, X. Gonze // *Phys. Rev. B.* – 1995. – V. 51. – P. 8610-8613.
207. Perdew J. P. Generalized Gradient Approximation Made Simple / J. P. Perdew, K. Burke, and M. Ernzerhof // *Physical Review Letters.* – 1996. – V. 77. – P. 3865-3868.
208. Monkhorst H. J. Special points for Brillouin-zone integrations / H. J. Monkhorst, J. D. Pack // *Physical Review B.* – 1976. – V. 13. – P. 5188-5192.
209. Gonze X. First-principles responses of solids to atomic displacements and homogeneous electric fields: Implementation of a conjugate-gradient algorithm / X. Gonze // *Physical Review B.* – 1997. – V. 55 – P. 10337-10354.

210. Maradudin A. A. Theory of Lattice Dynamics in the Harmonic Approximation. 2nd Edition / Maradudin A. A., Montroll E. W., Weiss G. H., Ipatova I. P. // Academic Press. – 1971. – P. 708.
211. Cahill D. Lower limit to the thermal conductivity of disordered crystals / D. Cahill, S. Watson, R. Pohl // Physical Review B. – 1992. – V. 46. – No. 10. – P. 6131-6140.
212. Tomé T. Modulated phases and chaotic behavior in a spin-1 ising-model with competing interactions / T. Tomé, R. Salinas // Physical Review A. – 1989. – V. 39. – P. 2206-2213.
213. Rizak V.M. On the origin of the anomalies in the temperature dependences of thermal conduction in  $\text{Sn}_2\text{P}_2\text{S}_6$ -like crystals at the phase transitions / V.M. Rizak, K. Al'-Shoufi, I.M. Rizak, Yu. Vysochanskii, V.Yu Slivka // Ferroelectrics. – 1997. – V. 192. – P. 177-185.
214. Ondrejko P. Neutron scattering study of ferroelectric  $\text{Sn}_2\text{P}_2\text{S}_6$  under pressure / P. Ondrejko, M. Kempa, Y. Vysochanskii, P. Saint-Gregoire, P. Bourges, K.Z. Rushchanskii, J. Hlinka // Physical Review B. – 2012. – V. 86. – P. 224106(1-8).
215. Baltrūnas D. Manifestation of the Ferroelectric Phase Transition in the Mössbauer Parameters of the System  $(\text{Sn}_x\text{Pb}_{1-x})_2\text{P}_2\text{S}_6$  / D. Baltrūnas, R. Mikaitis, V.Yu. Slivka, Yu.M. Vysochanskii // Physica Status Solidi A. – 1990. – V. 119. – P. 71-75.
216. Ekiz C. Metastable and unstable states of the Blume-Capel model obtained by the cluster variation method and the path probability method / C. Ekiz, M. Keskin, O. Yalcin // Physica Status Solidi A. – 2001. – V. 293. – P. 215-232.
217. Jensen P. J. Properties of a spin-1 system with competing interactions and reentrant magnetic behavior / P. J. Jensen, K. A. Penson, K. H. Bennemann // Physical Review B. – 1987. – V. 35. – No. 13. – P. 7306-7309.

218. Aharony A. Novel Lifshitz tricritical point and critical dynamics / Aharony, A., Domany, E., Hornreich, R. M., Schneider, T., Zannetti M. // *Physical Review B*. – 1985. – V. 32. – No. 5. – P. 3358–3360.
219. Tonchev N. S. On the tricritical Lifshitz behaviour / Tonchev N. S., Uzunov D. I. // *Physica A: Statistical Mechanics and Its Applications*. – 1985. – V. 134. – P. 265-273.
220. Selke W. The ANNNI model – Theoretical analysis and experimental application / W. Selke // *Physics Reports*. – 1988. – V. 170. – I. 4. – P. 213-264.
221. Rice T. M. Real-Space and  $k \rightarrow$ Space Electron Pairing in  $\text{BaPb}_{1-x}\text{Bi}_x\text{O}_3$  / Rice T. M., Sneddon L. // *Physical Review Letters* – 1981. – V. 47. – P. 689–692.
222. Oleaga A. Inducing a Tricritical point in  $\text{Sn}_2\text{P}_2(\text{Se}_y\text{S}_{1-y})_6$  ferroelectrics by Pb addition / A. Oleaga, V. Liubachko, A. Salazar, Yu. Vysochanskii // *Thermochimica Acta*. – 2019. – V. 675. – P. 38–43.
223. Penning F. C. A sensitive capacitance thermometer at low temperature for use in magnetic fields up to 20 T / Penning F. C., Maior M. M., Wiegers S. A. J., van Kempen H., Maan J. C. // *Review of Scientific Instruments*. – 1996. – V. 67. – P. 2602–2605.
224. Maior M. M. New dielectric material for low temperature thermometry in high magnetic fields / Maior M. M., Molnar S. B., Vysochanski, Y. M., Gurzan, M. I., van Loosdrecht P. H. M., van der Linden P. J. E. M., van Kempen H. // *Applied Physics Letters*. – 1993. – V. 62. – P. 2646–2648.
225. Vysochanskii Yu. Influence of cation and anion replacing on anomalous hysteresis of dielectric susceptibility in crystals  $\text{Sn}_2\text{P}_2\text{S}_6$  / Yu. Vysochanskii, M. Mayor, V. Slivka, M. Gurzan // *Fiz.Tv. Tela*. – 1985. – V. 27. – No. 5. – P. 1560-1562.
226. Korda V. Y. A possible generalization of the phenomenological theory of phase transitions in type II ferroelectrics with incommensurate phase / Korda V. Y., Berezovsky S. V., Molev A. S., Korda L. P., Klepikov V. F. *Physica B: Condensed Matter*. – 2012. – V. 407. – P. 3388–3393.

227. Korda V. Y. On importance of higher non-linear interactions in the theory of type II incommensurate systems / Korda V. Y., Berezovsky S. V., Molev A. S., Korda L. P., & Klepikov V. F. // *Physica B: Condensed Matter*. – 2013. – V. 425. – P. 31–33.
228. Volkov A. A. Low frequency modes in infrared spectra of  $\text{Sn}_2\text{P}_2\text{S}_6$  crystal / Volkov, G. V. Kozlov, N. I. Afanasjeva, A. A. Grabar, Yu. M. Vysochanskii, V. Yu. Slivka // *Fiz. Tverd. Tela*. – 1983. – V. 25. – P. 2575-2578.
229. Grigas, J. Microwave Dielectric Spectroscopy of Ferroelectrics / Grigas, J. // *Ferroelectrics*. – 2009. – V. 380. – I. 1. – P. 113–121.
230. Hlinka J. Two-length-scale behavior near the ferroelectric phase transition of  $\text{Sn}_2\text{P}_2\text{S}_6$  / Hlinka J., Currat R., de Boissieu M., Livet F., & Vysochanskii Y. M. // *Physical Review B*. – 2005. – V. 71. – P. 052102(1-4).
231. Zamaraitė I. Double hysteresis loops in proper uniaxial ferroelectrics / I. Zamaraitė, R. Yevych, A. Dziaugys, A. Molnar, J. Banys, S. Svirskas, Yu. Vysochanskii // *Physical Review Applied*. – 2018. – V.10. I.3. – P. 034017(1-7).
232. Yevych R. Nonlinear dynamics of ferroelectrics with three-well local potential / R. Yevych, M. Medulych, Yu. Vysochanskii // *Condensed Matter Physics*. – 2018. – V. 21. No 2. – P. 23001(1–8).
233. Yevych R. Description of lattice anharmonicity observed in ferroelectrics with unusual three-well local potential / R. Yevych, Yu. Vysochanskii // *Condensed Matter Physics*. – 2018. – V. 21. No 3. – P. 33001(1–6).
234. Kosterlitz J. M. Bicritical and tetracritical points in anisotropic antiferromagnetic systems / Kosterlitz J. M., Nelson D. R., Fisher M. E. // *Physical Review B*. – 1976. – V. 13. – P. 412–432.
235. Folk R. Field theory of bicritical and tetracritical points. I. Statics / Folk R., Holovatch Y., Moser G. // *Physical Review E*. – 2008. – V.78. – P. 041124(1-14).
236. Hoston W. Multicritical phase diagrams of the Blume-Emery-Griffiths model with repulsive biquadratic coupling / Hoston, W., Berker, A. N. // Hoston, W., & Berker, A. N. Multicritical phase diagrams of the Blume-Emery-Griffiths model with

- repulsive biquadratic coupling. *Physical Review Letters*. – 1991. – V. 67. – No. 8. – P. 1027–1030.
237. Zamaraitė I. Quantum paraelectric state and critical behavior in  $\text{Sn(Pb)}_2\text{P}_2\text{S(Se)}_6$  ferroelectrics / I. Zamaraitė, V. Liubachko, R. Yevych, A. Oleaga, A. Salazar, A. Dziaugys, J. Banys, Yu. Vysochanskii // *Physical Review B*. under revision. – 2020. – V. . – P.
238. Wang C. L. Burns temperature and quantum temperature scale / C. L. Wang, M. L. Zhao // *Journal of Advanced Dielectrics*. – 2011. – V. 1. – P. 163 - 167.
239. Barman N. Incipient ferroelectric to a possible ferroelectric transition in  $\text{Te}^{4+}$  doped calcium copper titanate ( $\text{CaCu}_3\text{Ti}_4\text{O}_{12}$ ) ceramics at low temperature as evidenced by Raman and dielectric spectroscopy / N. Barman, P. Singh, C. Narayana, K. B. R. Varma // *AIP Advances*. – 2017. – V. 7. – P. 035105(1-7).
240. Bednorz J. G.  $\text{Sr}_{1-x}\text{Ca}_x\text{TiO}_3$ : An XY Quantum Ferroelectric with Transition to Randomness / J. G. Bednorz, K. A. Muller // *Physical Review Letters*. – 1984. – V. 52, – P. 2289 – 2292.
241. Ang C. Phonon-coupled impurity dielectric modes in  $\text{Sr}_{1-1.5x}\text{Bi}_x\text{TiO}_3$  / Chen Ang, Zhi Yu. // *Physical Review B*. – 2000. – V. 61. – P. 11363 – 11366.
242. Zamaraitė I. Quantum paraelectricity and induced ferroelectricity by germanium doping of  $(\text{Pb}_y\text{Sn}_{1-y})_2\text{P}_2\text{S(Se)}_6$  single crystals / I. Zamaraitė, A. Dziaugys, Yu. Vysochanskii, J. Banys // *Lithuanian Journal of Physics*. – 2020. – V. 60. – P. 125 – 131.
243. Vysochanskii Yu. Ferroelectricity and polarons in  $\text{Sn}_2\text{P}_2\text{S}_6$  crystals / Yu. Vysochanskii, A. Molnar, R. Yevych, K. Glukhov, M. Medulych // *Ferroelectrics*. – 2012. – V. 440. – P. 31 - 41.
244. Martelli V. Thermal Transport and Phonon Hydrodynamics in Strontium Titanate / V. Martelli, J. Larrea Jim'enez, M. Continentino, E. Baggio-Saitovitch, K. Behnia // *Physical Review Letters*. – 2018. – V. 120. – P. 125901(1-6).

245. Huber W. H. Electric field dependence of the thermal conductivity of quantum paraelectrics / W. H. Huber, L. M. Hernandez, A. M. Goldman // *Physical Review B*. – 2000. – V. 62. – P. 8588 – 8591.
246. Fujishita H. Quantum Paraelectric States in  $\text{SrTiO}_3$  and  $\text{KTaO}_3$ : Barrett Model, Vendik Model, and Quantum Criticality / H. Fujishita, S. Kitazawa, M. Saito, R. Ishisaka, H. Okamoto, T. Yamaguchi // *Journal of the Physical Society of Japan*. – 2016. – V. 85. – P. 074703(1-8).
247. Rytz D. Dielectric susceptibility in quantum ferroelectrics / D. Rytz, U. T. Hochli, H. Bilz // *Physical Review B*. – 1980. – V. 22. – P. 359 – 364.
248. Rowley S. E. Uniaxial ferroelectric quantum criticality in multiferroic hexaferrites  $\text{BaFe}_{12}\text{O}_{19}$  and  $\text{SrFe}_{12}\text{O}_{19}$  / S. E. Rowley, Yi-Sheng Chai, Shi-Peng Shen, Young Sun, A. T. Jones, B. E. Watts, J. F. Scott // *Scientific Report*. – 2016. – V. 6. – P. 25724(1-5).
249. Rowley S. E. Quantum criticality in a uniaxial organic Ferroelectric / S. E. Rowley, M. Hadjimichael, M. N. Ali, Y. C. Durmaz, J. C. Lashley, R. J. Cava, J. F. Scott // *Journal of Physics: Condensed Matter*. – 2015. – V. 27. – P. 395901(1-7).
250. Rowley S. E. Ferroelectric quantum criticality / Rowley S. E., Spalek L. J., Smith R. P., Dean M. P. M., Itoh M., Scott J. F., Lonzarich G. G., Saxena S. S // *Nature Physics*. – 2014. – V. 10. – P. 367–372.
251. Rizak V. M. Electric conduction of  $\text{Sn}(\text{Pb})_2\text{P}_2\text{S}(\text{Se})_6$ -like crystals / V. M. Rizak, A. A. Bokotey, I. M. Rizak, K. Al'-Shoufi, V. Yu. Slivka // *Ferroelectrics*. – 1997. – V. 192. – P. 149-154.

## Summary in Spanish / Resumen en Castellano

### “Transporte térmico y transiciones de fase en calcogenuros fosforosos $MM'P_2(S,Se)_6$ ( $M, M' = Cu, Ag, In, Bi, Sn, Pb$ )”

Esta tesis doctoral se ha realizado en el marco de un acuerdo de cotutela internacional entre la Uzhgorod National University, Uzhgorod, Ucrania y la Universidad del País Vasco-Euskal Herriko Unibertsitatea, habiendo realizado el estudiante Vitalii Liubachko una estancia en la UPV/EHU de un total de 19 meses, en dos fases separadas en el tiempo (10 meses más otros 9) con el soporte económico de la Unión Europea a través del programa ERASMUS MUNDUS ACTIVE (primer período de estancia) y de la UPV/EHU a través de una beca del programa de cotutelas internacionales (segundo período de estancia). El resto del tiempo el trabajo se ha desarrollado en Ucrania.

Los materiales objeto de estudio son dos familias de calcogenuros fosforosos, una de multiferroicos que se disponen en capas bidimensionales  $M^{1+}M^{3+}[P_2X_6]^{4-}$  ( $M^{1+} = Cu, Ag; M^{3+} = In, Bi; X = S, Se$ ) y otra de calcogenuros tridimensionales  $(Pb_xSn_{1-x})_2P_2(Se_yS_{1-y})_6$ . En el caso de los materiales en capas, el objetivo principal es estudiar sus propiedades térmicas en función de la temperatura (de 20 a 350 K) focalizando la atención sobre la posibilidad de obtener conductividades térmicas ultrabajas. En el caso de los tridimensionales, estudiar también la evolución de las propiedades térmicas para, en este caso, analizar el comportamiento crítico de las transiciones de fase ferroeléctricas y su evolución con las sustituciones de Sn por Pb. También se ha analizado este comportamiento si se añaden ligeros dopajes de Ge.

El interés del estudio tanto experimental como teórico de las propiedades físicas de cristales calcogenuros con estructura *bulk* o en capas y que presentan polarización espontánea tiene importancia, en primer lugar, desde el punto de vista del avance en la Física de la Materia Condensada y, en segundo, por sus posibles aplicaciones en

la creación de una tecnología de fabricación de materiales ferroicos de baja dimensionalidad para integrarlos en heteroestructuras con materiales tipo grafeno que puedan ser utilizados esencialmente en nuevos elementos funcionales biestables para electrónica de ultra-alta densidad y alta velocidad.

Los dos primeros capítulos de la memoria son capítulos que contextualizan el trabajo experimental que se describe en los capítulos 6 al 9. El **capítulo uno** contiene una descripción general de los procesos de transferencia de calor, introduciendo las definiciones de las variables térmicas que se van a manejar en la memoria. El **capítulo dos** describe con todo detalle las técnicas experimentales utilizadas y su fundamento teórico. La técnica básica utilizada ha sido calorimetría fotopiroeléctrica *ac* y en todos los casos se han utilizado monocristales de alta calidad para los estudios.

El **capítulo tres** desarrolla la teoría del comportamiento crítico de transiciones de fase continuas (segundo orden), empezando por la teoría clásica de Landau y las correcciones aplicadas a la misma con el fin de considerar fenómenos tales como fluctuaciones del parámetro de orden, presencia de interacciones dipolares fuertes, contribución añadida de defectos cargados, etc. Se describen los límites de esta teoría clásica y se pasa a describir la teoría moderna del comportamiento crítico, basada en el desarrollo de los hamiltonianos que incluyan las interacciones relevantes en la transición y la obtención por diferentes métodos (el más relevante de los cuales es la teoría de grupos de renormalización) del comportamiento singular de diferentes variables físicas, como el calor específico o la difusividad térmica. Se obtienen así las diferentes clases de universalidad, donde cada una tiene un conjunto particular de exponentes críticos, susceptibles de ser evaluados experimentalmente. Así, una vez que obtengamos las curvas experimentales, las ajustaremos a los diferentes modelos teóricos con el fin de extraer conclusiones sobre los mecanismos físicos relevantes en la transición. La magnitud experimental utilizada para dichos ajustes ha sido en todos los casos el inverso de la difusividad térmica, cuyo comportamiento crítico es análogo al del calor específico en estos materiales. Se

plantea también en este capítulo el estado del arte del comportamiento crítico de la familia  $(\text{Pb}_x\text{Sn}_{1-x})_2\text{P}_2(\text{Se}_y\text{S}_{1-y})_6$ .

Las peculiaridades de la estructura cristalina, la influencia en las propiedades físicas de la sustitución de átomos en las redes catiónica y aniónica de los tio y selenofosfatos bidimensionales  $\text{M}^{1+}\text{M}^{3+}[\text{P}_2\text{X}_6]^{4-}$  han sido considerados en el **capítulo cuatro**. La segunda parte de este capítulo está dedicada a la descripción de las propiedades físicas de cristales en capas bidimensionales, a saber dieléctricas, piezoeléctricas, ultrasónicas y térmicas.

El **capítulo cinco** contiene una breve revisión de las propiedades físicas (térmicas, ópticas, elásticas, acústicas y dieléctricas) de las soluciones sólidas cristalinas  $(\text{Pb},\text{Sn})_2\text{P}_2(\text{Se},\text{S})_6$ , lo que permite describir el muy complejo diagrama de fases temperatura-concentración. Con el fin de entender mejor la evolución del carácter de la transición de fase al sustituir elementos químicos en las subredes aniónica y catiónica, se han considerado tres diagramas de fase independientes para  $\text{Sn}_2\text{P}_2(\text{Se}_y\text{S}_{1-y})_6$ ,  $(\text{Pb}_x\text{Sn}_{1-x})_2\text{P}_2\text{S}_6$  and  $(\text{Pb}_x\text{Sn}_{1-x})_2\text{P}_2\text{Se}_6$ . Se ha prestado especial atención a los puntos multicríticos que aparecen en el diagrama de fases, dependiendo del cambio, bien en la composición química, bien en la presión. Se ha considerado la influencia del Pb en la posición de la temperatura de la transición ferroeléctrica así como en la forma de las anomalías críticas en los cristales  $\text{Sn}_2\text{P}_2\text{S}_6$  y  $\text{Sn}_2\text{P}_2\text{Se}_6$ . Por último, se han presentado los estudios sobre propiedades físicas en  $\text{Sn}_2\text{P}_2\text{S}_6$  dopado con Ge.

Los restantes cuatro capítulos están dedicados a la presentación de resultados y a la interpretación de los mismos. Así, el **capítulo seis** está dedicado a los materiales bidimensionales en capas  $\text{M}^{1+}\text{M}^{3+}[\text{P}_2\text{X}_6]^{4-}$ , donde se ha estudiado el efecto en sus propiedades térmicas de la sustitución de átomos en las subredes aniónica y cationica, encontrando además una anisotropía muy significativa en dichas propiedades, sean medidas sobre las capas bidimensionales o perpendiculares a ellas. Además, se han estudiado con detalle las transiciones de fase ferroeléctricas en las composiciones que las presentan. Se han desarrollado cálculos teóricos de espectros de fonones para cada cristal estudiado, utilizando teoría de densidad

funcional (functional density theory), obteniendo la capacidad calorífica que, combinada con la difusividad térmica medida, nos ha permitido extraer la conductividad térmica desde baja temperatura hasta por encima de temperatura ambiente en todos los casos, obteniendo valores ultrabajos que han sido justificados por la presencia de una fuerte anarmonicidad de la red cristalina creada por la relajación de los pares de electrones aislados de los cationes estereoactivos  $M^{3+}$ , la fuerte interacción entre las ramas de fonones ópticas y acústicas y por la presencia de un efecto Jahn-Teller secundario de los cationes de cobre,

En el caso particular de  $CuBiP_2Se_6$ , los datos de difusividad térmica confirman la presencia de una fase intermedia modulada entre la fase antiferroeléctrica de baja temperatura y la fase desordenada a alta temperatura. También se ha observado que la sustitución de cobre por plata en un 10% en  $CuInP_2S_6$  cambia el carácter de la transición de fase de primer orden a segundo orden, reduciendo la temperatura crítica en 30 K y frustrando la anomalía crítica en la difusividad térmica, haciéndola más ancha y menos picuda.

En el **capítulo siete** se presentan, en primer lugar, las curvas de difusividad térmica en función de la temperatura para  $(Pb_xSn_{1-x})_2P_2(Se_{0.2}S_{0.8})_6$  con  $x = 0.1, 0.2, 0.3$  y para  $(Pb_{0.05}Sn_{0.95})_2P_2(Se_yS_{1-y})_6$  con  $y = 0.4, 0.5$ . Se ha considerado la sustitución de estaño por plomo con el fin de intentar obtener un punto tricrítico. Los exponentes críticos obtenidos tras el ajuste de las curvas se han comparado con las diferentes clases de universalidad aplicables a ferroeléctricos. Al incrementar la concentración de Pb en  $(Pb_xSn_{1-x})_2P_2(Se_{0.2}S_{0.8})_6$  se ha comprobado una tendencia al cambio desde la clase de universalidad Lifshitz hacia el modelo de Campo Medio en lugar de a una clase de universalidad tricrítica, lo que ha sido explicado sobre la base del modelo Blume-Emery-Griffiths model (modelo BEG) con influencia de defectos de campo aleatorio. Dicho modelo describe el diagrama de fases temperatura-concentración-presión para el caso de potenciales de tres pozos con fluctuaciones de la polarización espontánea.

El **capítulo ocho** está dedicado al comportamiento crítico de  $Sn_2P_2S_6$ , que puede ser descrito como un “crossover” entre las clases de universalidad Ising y XY,

lo que es esperable cerca de puntos bicríticos con parámetros de orden polar y antipolar acoplados e inestabilidades que compiten en el espacio  $q$ . Se ha propuesto un diagrama de fases mejorado  $T - x - y$  para los ferroeléctricos  $\text{Sn}(\text{Pb})_2\text{P}_2\text{S}(\text{Se})_6$  que combina una línea de puntos de Lifshitz, una línea de puntos tricríticos y un punto de Lifshitz tricrítico. Este complejo diagrama de fases puede ser descrito en un modelo BEG-ANNI combinado. Aquí es esperable la presencia de un estado “caótico” acompañado de la coexistencia de una fase ferroeléctrica, otra paraeléctrica metastable y una tercera modulada.

Por último, el **capítulo nueve** está dedicado a las propiedades térmicas y dieléctricas de cristales  $(\text{Pb}_y\text{Sn}_{1-y})_2\text{P}_2(\text{Se},\text{S})_6$  dopados con Ge. Se presenta la dependencia de la difusividad térmica con la temperatura para  $(\text{Sn}_{0.95}\text{Ge}_{0.05})_2\text{P}_2(\text{Se}_{0.2}\text{S}_{0.8})_6$ ,  $(\text{Sn}_{0.95}\text{Ge}_{0.05})_2\text{P}_2(\text{Se}_{0.4}\text{S}_{0.6})_6$ ,  $(\text{Sn}_{0.95}\text{Ge}_{0.05})_2\text{P}_2(\text{Se}_{0.5}\text{S}_{0.5})_6$ ,  $(\text{Pb}_{0.7}\text{Sn}_{0.25}\text{Ge}_{0.05})_2\text{P}_2\text{S}_6$  y  $(\text{Pb}_{0.7}\text{Sn}_{0.25}\text{Ge}_{0.05})_2\text{P}_2\text{Se}_6$ . La dependencia de las susceptibilidades dieléctricas con la temperatura ha sido analizada usando el modelo de Barrett, mostrando la presencia de un estado paraeléctrico cuántico en  $\text{Pb}_2\text{P}_2\text{S}_6$ . También se ha obtenido la conductividad térmica para los cristales con Ge y se ha comparado con la de las mismas muestras sin dopar. La presencia de germanio incrementa la conductividad térmica debido al incremento de la frecuencia del menor modo óptico polar cerca del centro de la zona de Brillouin lo que, a su vez, reduce la probabilidad de que haya scattering resonante de los modos ópticos por los acústicos. En el caso de  $(\text{Pb}_{0.7}\text{Sn}_{0.25}\text{Ge}_{0.05})_2\text{P}_2\text{S}(\text{Se})_6$  y  $(\text{Pb}_{0.7}\text{Sn}_{0.25}\text{Ge}_{0.05})_2\text{P}_2\text{S}(\text{Se})_6$  se ha demostrado que la presencia de Ge induce un estado vítreo dipolar, de acuerdo con los datos de susceptibilidad dieléctrica.

La memoria finaliza con la exposición de las **conclusiones** principales derivadas del estudio completo, resumiendo, recogiendo y relacionando las conclusiones planteadas al final de las discusiones desarrolladas en cada uno de los cuatro capítulos (seis a nueve) que contienen el trabajo de investigación realizado.

Todo este trabajo ha dado lugar a 5 publicaciones en revistas del Journal Scitation Index y una más está ya enviada (en el momento de redactar esta memoria)

y en proceso de revisión. Además, se han presentado siete comunicaciones en congresos internacionales y otras cinco en nacionales.